

**A Thesis Submitted for the Degree of PhD at the University of Warwick**

**Permanent WRAP URL:**

<http://wrap.warwick.ac.uk/99641>

**Copyright and reuse:**

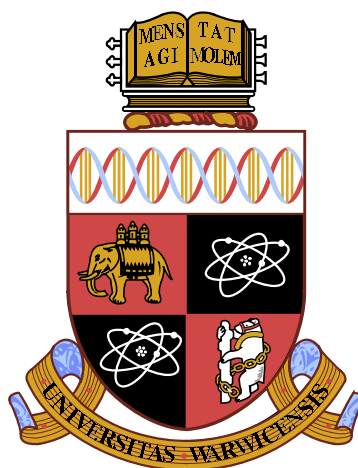
This thesis is made available online and is protected by original copyright.

Please scroll down to view the document itself.

Please refer to the repository record for this item for information to help you to cite it.

Our policy information is available from the repository home page.

For more information, please contact the WRAP Team at: [wrap@warwick.ac.uk](mailto:wrap@warwick.ac.uk)



# Investigating Interactions Using Solid State NMR: Applications to Biomolecular Complexes

by

Carl Johan Wilhelm Öster

Thesis

Submitted to the University of Warwick

for the degree of

Doctor of Philosophy

Supervised by Dr. Józef R. Lewandowski

Department of Chemistry

August 2017



# Table of Contents

TABLE OF CONTENTS .....	1
LIST OF TABLES .....	2
LIST OF FIGURES .....	3
ACKNOWLEDGEMENTS .....	5
DECLARATIONS .....	6
ABSTRACT .....	9
<b>1. INTRODUCTION .....</b>	<b>10</b>
1.1 GB1:IGG COMPLEX.....	10
1.2 ANTIMICROBIAL RESISTANCE.....	11
1.2.1 <i>Peptidoglycan</i> .....	11
1.2.2 <i>Antibiotics binding to Lipid II</i> .....	14
1.3 NMR .....	18
1.3.1 <i>Basic theory</i> .....	18
1.3.2 <i>Biological assemblies in NMR</i> .....	25
1.3.3 <i>Protein dynamics</i> .....	29
1.4 NMR STRUCTURE CALCULATIONS.....	33
1.4.1 <i>Resonance assignments in solution and solid state</i> .....	34
1.4.2 <i>CYANA libraries</i> .....	38
1.4.3 <i>Structure calculations using UNIO-ATNOS CANDID</i> .....	42
1.5 REFERENCES.....	44
<b>2 CHARACTERIZATION OF PROTEIN-PROTEIN INTERFACES IN LARGE COMPLEXES BY SOLID STATE NMR SOLVENT PARAMAGNETIC RELAXATION ENHANCEMENTS .....</b>	<b>51</b>
2.1 ABSTRACT.....	51
2.2 INTRODUCTION .....	52
2.3 RESULTS AND DISCUSSION .....	54
2.3.1 <i>Overview of the different sPRE approaches</i> .....	54
2.3.2 <i>sPREs: solution vs. crystal</i> .....	57
2.3.3 <i>sPREs in GB1:IgG complex</i> .....	61
2.3 CONCLUSIONS .....	70
2.4 EXPERIMENTAL SECTION.....	71
2.5 ACKNOWLEDGEMENTS .....	76
2.6 REFERENCES.....	77
2.7 SUPPORTING INFORMATION .....	82
2.7.1 <i>Results and Discussion</i> .....	82
2.6.2 <i>References</i> .....	100
<b>3. INTERMOLECULAR INTERACTIONS AND PROTEIN DYNAMICS BY SSNMR .....</b>	<b>101</b>
3.1 ABSTRACT.....	101
3.2 INTRODUCTION AND DISCUSSION .....	101
3.3 ACKNOWLEDGEMENTS .....	110
3.4 REFERENCES.....	111
3.5 SUPPLEMENTARY INFORMATION .....	113
3.5.1 <i>Experimental Section</i> .....	113

3.5.2 3D GAF model including spinning frequency dependent expressions for $R_{1\rho}$ .....	125
3.5.2 References .....	127
<b>4. ACCELERATED EXPERIMENTS FOR PROBING MICROSECOND EXCHANGE IN LARGE PROTEIN COMPLEXES IN THE SOLID STATE .....</b>	<b>129</b>
4.1 ABSTRACT.....	129
4.2 INTRODUCTION AND DISCUSSION .....	129
4.3 ACKNOWLEDGEMENTS .....	138
4.4 REFERENCES.....	138
4.5 SUPPLEMENTARY INFORMATION .....	141
4.5.1 Experimental Section .....	141
4.5.2 Results and Discussion .....	144
4.5.3 References .....	160
<b>5 INVESTIGATION OF TEIXOBACTIN-LIPID II INTERACTIONS USING SOLUTION AND SOLID STATE NMR.....</b>	<b>161</b>
5.1 ABSTRACT.....	161
5.2 INTRODUCTION AND DISCUSSION .....	161
5.3 REFERENCES.....	167
5.4 SUPPLEMENTARY INFORMATION .....	168
5.4.1 Experimental Section .....	168
5.4.2 Results and Discussion .....	172
5.4.3 References .....	181

## List of Tables

<b>TABLE 1.1.</b> PROPERTIES IMPORTANT FOR NMR.....	19
<b>SI TABLE 2.1.</b> $^{15}\text{N}$ $R_1$ RATES FOR GB1 <sub>FREE</sub> WITH VARYING CONCENTRATION OF Gd(DTPA-BMA) .....	87
<b>SI TABLE 2.2.</b> $^{15}\text{N}$ $R_1$ RATES FOR GB1 <sub>FREE</sub> WITH VARYING CONCENTRATION OF Gd(DTPA-BMA) .....	88
<b>SI TABLE 2.3.</b> $^{15}\text{N}$ $R_1$ RATES FOR GB1 <sub>CRYST</sub> WITH 0 AND 2 MM Gd(DTPA-BMA) .....	89
<b>SI TABLE 2.4.</b> $^{15}\text{N}$ $R_1$ RATES FOR GB1 <sub>IGG</sub> WITH VARYING CONCENTRATIONS OF Gd(DTPA-BMA) .....	90
<b>SI TABLE 2.5.</b> $^{15}\text{N}$ $R_{1\rho}$ RATES AT 10 KHZ NUTATION FREQUENCY FOR GB1 <sub>IGG</sub> WITH VARYING CONCENTRATIONS OF Gd(DTPA-BMA) .....	91
<b>SI TABLE 2.6.</b> $^1\text{H}$ $R_1$ RATES FOR GB1 <sub>IGG</sub> WITH 0 AND 100 MM Cu(EDTA).....	91
<b>SI TABLE 2.7.</b> EXPERIMENTAL $^{15}\text{N}$ SPRE VALUES FOR GB1 <sub>FREE</sub> , GB1 <sub>CRYST</sub> AND GB1 <sub>IGG</sub> AND $^1\text{H}$ SPRES FOR GB1 <sub>IGG</sub> .....	92
<b>SI TABLE 2.8.</b> PREDICTED $^{15}\text{N}$ SPRE VALUES FOR GB1 <sub>FREE</sub> , GB1 <sub>CRYST</sub> , GB1 <sub>IGG</sub> AND GB1 IN COMPLEX WITH IGG FRAGMENTS .....	93
<b>SI TABLE 2.9.</b> PREDICTED $^1\text{H}$ PRE VALUES FOR GB1 <sub>FREE</sub> , GB1 <sub>IGG</sub> AND GB1 IN COMPLEX WITH IGG FRAGMENTS.....	95
<b>SI TABLE 2.10.</b> RELAXATION DELAYS USED AND TOTAL EXPERIMENTAL TIME FOR $R_1$ MEASUREMENTS OF GB1 <sub>FREE</sub> AND GB1 <sub>CRYST</sub> .....	96
<b>SI TABLE 2.11.</b> RELAXATION DELAYS AND SPIN-LOCK LENGTHS AND TOTAL EXPERIMENTAL TIME USED FOR $R_1$ AND $R_{1\rho}$ MEASUREMENTS OF GB1 <sub>IGG</sub> .....	96
<b>SI TABLE 2.12.</b> RESULT OF FITTING OF EXPERIMENTAL $\Delta\text{SPRES}$ AGAINST $\Delta\text{SPRES}$ BACK-CALCULATED.....	97
<b>SI TABLE 2.13.</b> PREDICTED $^1\text{H}$ SPRES FOR GB1 <sub>IGG</sub> BASED ON MODIFIED MODELS .....	97
<b>SI TABLE 2.14.</b> PREDICTED $^1\text{H}$ SPRES FOR GB1 <sub>IGG</sub> BASED ON MODIFIED MODELS WITH AN ADDITIONAL INTERACTION SITE .....	99
<b>TABLE 4.1.</b> RESULTS FROM RD FITS FOR GB1 <sub>DIA</sub> AND GB1 <sub>PRE</sub> .....	133
<b>SI TABLE 4.1.</b> RESULTS FROM RD FITS OF INDIVIDUAL RESIDUES FOR GB1 <sub>DIA</sub> .....	153



<b>SI TABLE 4.2.</b> RESULTS FROM RD FITS OF ALL RESIDUES COMBINED FOR GB1 <sub>DIA</sub> .....	154
<b>SI TABLE 4.3.</b> RESULTS FROM RD FITS OF THE B REGION COMBINED FOR GB1 <sub>DIA</sub> .....	155
<b>SI TABLE 4.4.</b> RESULTS FROM RD FITS OF THE A REGION COMBINED FOR GB1 <sub>DIA</sub> .....	155
<b>SI TABLE 4.5.</b> RESULTS FROM RD FITS OF INDIVIDUAL RESIDUES FOR GB1 <sub>PRE</sub> .....	156
<b>SI TABLE 4.6.</b> RESULTS FROM RD FITS OF ALL RESIDUES COMBINED FOR GB1 <sub>PRE</sub> .....	156
<b>SI TABLE 4.7.</b> RESULTS FROM RD FITS OF THE B REGION COMBINED FOR GB1 <sub>PRE</sub> .....	157
<b>SI TABLE 4.8.</b> RESULTS FROM RD FITS OF THE A REGION COMBINED FOR GB1 <sub>PRE</sub> .....	157
<b>SI TABLE 4.9.</b> RESULTS FROM RD FITS OF INDIVIDUAL RESIDUES FOR GB1 IN COMPLEX WITH IgG.....	158
<b>SI TABLE 4.10.</b> RESULTS FROM RD FITS OF ALL RESIDUES COMBINED FOR GB1 IN COMPLEX WITH IgG .....	158
<b>SI TABLE 4.11.</b> RESULTS FROM RD FITS OF RESIDUES EXPECTED TO BIND THE Fc FRAGMENT OF IgG COMBINED FOR GB1 IN COMPLEX WITH IgG .....	159
<b>SI TABLE 4.12.</b> RESULTS FROM RD FITS OF RESIDUES EXPECTED TO BIND THE Fab FRAGMENT OF IgG COMBINED FOR GB1 IN COMPLEX WITH IgG .....	159
<b>SI TABLE 4.13.</b> NUMBER OF SPIN-LOCK LENGTHS, NUTATION FREQUENCIES AND TOTAL DURATION OF EACH EXPERIMENT. .....	159
<b>SI TABLE 4.14.</b> STATISTICAL ANALYSIS OF RD FITS FOR ALL SAMPLES. ....	159
<b>SI TABLE 5.1.</b> RESULTS FROM STRUCTURE CALCULATION OF [U- <sup>13</sup> C, <sup>15</sup> N] TEIXOBACTIN IN D <sub>38</sub> DPC MICELLES IN SOLUTION. ....	174
<b>SI TABLE 5.2.</b> CHEMICAL SHIFTS FOR [U- <sup>13</sup> C, <sup>15</sup> N]TEIXOBACTIN IN D <sub>38</sub> DPC MICELLES, SOLUTION NMR AT 25 °C .....	175
<b>SI TABLE 5.3.</b> CHEMICAL SHIFTS FOR [U- <sup>13</sup> C, <sup>15</sup> N]TEIXOBACTIN IN D <sub>38</sub> DPC MICELLES, SOLUTION NMR AT 37 °C.....	176
<b>SI TABLE 5.4.</b> CHEMICAL SHIFTS FOR [U- <sup>13</sup> C <sup>15</sup> N]TEIXOBACTIN IN COMPLEX WITH LIPID II IN D <sub>38</sub> DPC MICELLES, SOLID STATE NMR AT 39 ± 2 °C.....	177
<b>SI TABLE 5.5.</b> RESULTS FROM Kd FITS WITH A 2:1 RATIO OF TEIXOBACTIN:LIPID 2 .....	178
<b>SI TABLE 5.6.</b> COMPARISON OF Kd FITS WITH DIFFERENT RATIOS OF TEIXOBACTIN:LIPID II. ....	180

## List of Figures

<b>FIGURE 1.1.</b> SCHEMATIC DRAWING OF PEPTIDOGLYCAN.....	12
<b>FIGURE 1.2.</b> PEPTIDOGLYCAN SYNTHESIS PATHWAY .....	14
<b>FIGURE 1.3.</b> SCHEMATIC MODEL AND CHEMICAL STRUCTURE OF LIPID II. ....	16
<b>FIGURE 1.4.</b> (ZEEMAN SPLITTING FOR A SPIN ½ NUCLEI AND LARMOR PRECESSION AROUND THE $B_0$ FIELD. ....	20
<b>FIGURE 1.5.</b> CROSS POLARIZATION EXPERIMENT.....	23
<b>FIGURE 1.6.</b> MAGIC ANGLE SPINNING .....	25
<b>FIGURE 1.7.</b> 2D H-N CORRELATION SPECTRA FOR 4 DIFFERENT SAMPLES	
<b>FIGURE 1.8.</b> EXAMPLES OF TIME SCALES OF DYNAMIC PROCESSES IN PROTEINS AND RELAXATION MEASUREMENTS TO OBTAIN INFORMATION ON THEM. ....	30
<b>FIGURE 1.9.</b> SCHEMATIC DRAWING OF 2D ASSIGNMENT SPECTRA USED IN SOLUTION NMR. ....	35
<b>FIGURE 1.10.</b> EXAMPLE STRIPS FROM SOLUTION NMR 3D ASSIGNMENT SPECTRA FOR [U- <sup>13</sup> C, <sup>15</sup> N]TEIXOBACTIN IN DPC MICELLES. ....	36
<b>FIGURE 1.11.</b> EXAMPLE STRIPS FROM ASSIGNMENT SPECTRA OF [U- <sup>13</sup> C, <sup>15</sup> N]TEIXOBACTIN IN A SEDIMENTED COMPLEX WITH NATURAL ABUNDANCE LIPID II IN DEUTERATED DPC MICELLES.....	37
<b>FIGURE 1.12.</b> STRUCTURE OF CYANA LIBRARY ENTRY. ....	40
<b>FIGURE 1.13.</b> STEPWISE EXPLANATION FOR HOW TO CREATE CYANA LIBRARY ENTRIES .....	42
<b>FIGURE 2.1.</b> EXPERIMENTAL <sup>15</sup> N $R_1$ SOLVENT PRES FOR GB1 .....	59
<b>FIGURE 2.2.</b> EXAMPLES OF LINEAR FITS FOR SPRES FOR GB1 IN A COMPLEX WITH IgG.....	62
<b>FIGURE 2.3.</b> <sup>15</sup> N $\Delta$ SPRES FOR GB1 <sub>IgG</sub> .....	64
<b>FIGURE 2.4.</b> <sup>1</sup> H $R_1$ RELAXATION RATES, <sup>1</sup> H $R_1$ SPRES AND <sup>1</sup> H $R_1$ $\Delta$ SPRES FOR GB1 <sub>IgG</sub> .....	65

<b>FIGURE 2.5.</b> EXPERIMENTAL $\Delta$ SPRES VS. $\Delta$ SPRES PREDICTED FROM GB1:IGG MODELS .....	68
<b>SI FIGURE 2.1.</b> COMPARISON BETWEEN EXPERIMENTAL AND PREDICTED $^{15}\text{N}$ SPRES FOR GB1 IN COMPLEX WITH IGG. .	83
<b>SI FIGURE 2.2.</b> COMPARISON BETWEEN EXPERIMENTAL AND PREDICTED $^1\text{H}$ SPRES FOR GB1 FREE IN SOLUTION AND GB1 IN COMPLEX WITH IGG .....	84
<b>SI FIGURE 2.3.</b> EXAMPLES OF LINEAR FITS USED TO EXTRACT $^{15}\text{N}$ SPRES .....	85
<b>SI FIGURE 2.4.</b> MODEL OF GB1 IN COMPLEX WITH IGG USED FOR CALCULATIONS OF THEORETICAL SPRES. ....	86
<b>SI FIGURE 2.5.</b> SECONDARY CHEMICAL SHIFTS FOR GB1 FREE IN SOLUTION AND GB1 IN COMPLEX WITH IGG.....	86
<b>FIGURE 3.1.</b> $^{15}\text{N}$ $R_1$ AND $R_{1\rho}$ RELAXATION RATES FOR GB1 IN A COMPLEX WITH IGG AND IN A GB1 CRYSTAL. ....	103
<b>FIGURE 3.2.</b> RESIDUES CLEARLY EXHIBITING CHEMICAL EXCHANGE ON THE MS TIME SCALE IN CRYSTALLINE GB1 AND IN GB1 IN COMPLEX WITH IGG. ....	106
<b>FIGURE 3.3.</b> $^{15}\text{N}$ $R_{1\rho}$ RATES FOR GB1 IN COMPLEX WITH IGG MEASURED AT VARYING MAS SPEED AND VISUALIZATION OF THE OVERALL 3D GAF MOTION OF GB1 IN THE COMPLEX WITH IGG .....	109
<b>FIGURE S3.1.</b> PULSE SEQUENCE USED FOR MEASURING $^{15}\text{N}$ $R_{1\rho}$ RATES IN THE GB1:IGG COMPLEX.....	116
<b>FIGURE S3.2.</b> ASSIGNED 2D $^{15}\text{N}$ - $^1\text{H}$ SPECTRUM OF DEUTERATED (FULL-PROTONATED AT EXCHANGEABLE SITES) [U- $^{13}\text{C}$ , $^{15}\text{N}$ ]GB1 IN COMPLEX WITH NATURAL ABUNDANCE FULL-LENGTH HUMAN IGG.....	117
<b>FIGURE S3.3.</b> ASSIGNED 2D $^{15}\text{N}$ - $^1\text{H}$ SPECTRUM OF DEUTERATED (FULL-PROTONATED AT EXCHANGEABLE SITES) CRYSTALLINE [U- $^{13}\text{C}$ , $^{15}\text{N}$ ]GB1. ....	118
<b>FIGURE S3.4.</b> SIMULATED $^{15}\text{N}$ $R_{1\rho}$ RATES FOR OVERALL ANISOTROPIC MOTION OF GB1 ABOUT THREE DIFFERENT MOTIONAL AXES .....	119
<b>FIGURE S3.5.</b> $^{15}\text{N}$ $R_{1\rho}$ RELAXATION DISPERSION CURVES MEASURED ON CRYSTALLINE GB1.....	122
<b>FIGURE S3.6.</b> DIFFERENCES BETWEEN THE $^{15}\text{N}$ $R_{1\rho}$ RELAXATION RATES MEASURED AT 2.5 KHZ AND 17 KHZ SPIN-LOCK FIELDS FOR GB1 IN COMPLEX WITH IGG .....	123
<b>FIGURE S3.7.</b> COMPARISON OF HELIX PACKING IN GB1 CRYSTAL AND GB1 IN COMPLEX WITH IGG .....	124
<b>FIGURE S3.8.</b> COMPARISON OF $^{15}\text{N}$ $R_{1\rho}$ RATES MEASURED AT 56 AND 39 KHZ SPINNING FREQUENCIES MEASURED FOR CRYSTALLINE GB1 AT 10 KHZ NUTATION FREQUENCY. ....	127
<b>FIGURE 4.1.</b> $^{15}\text{N}$ $R_{1\rho}$ RELAXATION DISPERSION FOR CRYSTALLINE GB1.....	131
<b>FIGURE 4.2.</b> $^{15}\text{N}$ $R_{1\rho}$ RELAXATION DISPERSION PROFILES FOR GB1 IN COMPLEX WITH IGG .....	134
<b>FIGURE 4.3.</b> MICROSECOND EXCHANGE IN CRYSTALLINE GB1 AND GB1 IN A COMPLEX WITH IGG .....	135
<b>SI FIGURE 4.1.</b> RELAXATION DISPERSION PROFILES FOR GB1 <sub>DIA</sub> AT 16.4 T. ....	146
<b>SI FIGURE 4.2.</b> RELAXATION DISPERSION PROFILES FOR GB1 <sub>DIA</sub> AT 14.1 T. . ....	147
<b>SI FIGURE 4.3.</b> RELAXATION DISPERSION PROFILES FOR GB1 <sub>PRE</sub> AT 16.4 T. ....	148
<b>SI FIGURE 4.4.</b> RELAXATION DISPERSION PROFILES FOR GB1 <sub>PRE</sub> AT 14.1 T.....	149
<b>SI FIGURE 4.5.</b> RELAXATION DISPERSION PROFILES FOR GB1 IN COMPLEX WITH IGG, WITH 5 mM Gd(DTPA-BMA) AS PARAMAGNETIC RELAXATION ENHANCEMENT AGENT, MEASURED AT 20 T. ....	150
<b>SI FIGURE 4.6.</b> RELAXATION DISPERSION PROFILES FOR GB1 IN COMPLEX WITH IGG, WITH 2 mM Gd(DTPA-BMA) AS PARAMAGNETIC RELAXATION ENHANCEMENT AGENT, MEASURED AT 16.4 T. ....	151
<b>SI FIGURE 4.7.</b> GB1 STRUCTURES WITH RESIDUES COLORED BASED ON RELAXATION DISPERSION PROFILES OF GB1 <sub>DIA</sub> AND GB1 <sub>PRE</sub> . ....	152
<b>SI FIGURE 4.8.</b> GB1 STRUCTURES WITH RESIDUES COLORED BASED ON RELAXATION DISPERSION PROFILES OF GB1 IN COMPLEX WITH IGG. ....	153
<b>FIGURE 5.1.</b> COMPARISON BETWEEN A SOLUTION NMR STRUCTURE OF TEIXOBACTIN IN DPC MICELLES WITH A CRYSTAL STRUCTURE OF TEIXOBACTIN ANALOGUE AC- $\Delta_{1-5}$ ARG $_{10}$ -TEIXOBACTIN AND RESULTS FROM KD FITS OF A 2:1 TEIXOBACTIN:LIPID II BINDING MODE.....	163
<b>FIGURE 5.2.</b> COMAPRISON OF CHEMICAL SHIFTS BETWEEN TEIXOBACTIN IN SOLUTION AND TEIXOBACTIN IN COMPLEX WITH LIPID II IN SOLID STATE. ....	165
<b>SI FIGURE 5.1.</b> $^1\text{H}$ - $^{15}\text{N}$ SOLID STATE NMR SPECTRUM OF [U, $^{13}\text{C}$ , $^{15}\text{N}$ ]TEIXOBACTIN IN COMPLEX WITH NATURAL ABUNDANCE LIPID II IN D <sub>38</sub> DPC MICELLES. ....	173
<b>SI FIGURE 5.2.</b> $^1\text{H}$ - $^{13}\text{C}$ SOLID STATE NMR SPECTRUM OF [U- $^{13}\text{C}$ , $^{15}\text{N}$ ] TEIXOBACTIN IN COMPLEX WITH NATURAL ABUNDANCE LIPID II IN D <sub>38</sub> DPC MICELLES. ....	174

## Acknowledgements

During my PhD I have had the opportunity to work together with many great scientists, both at the University of Warwick and externally and I am grateful for everything I have learned and all the help I have got. First I would like to thank Józef Lewandowski for his great supervision. I consider myself lucky to have had a dedicated supervisor who was always available for discussion. I would also like to thank the other members of the Lewandowski group especially Jonathan Lamley for teaching me how to run solid state NMR experiments and Simone Kosol for teaching me how to produce isotope labelled proteins, helping me with solution NMR experiments and for great collaborations on the solvent PRE project. Also thanks to Angelo Gallo for help with solution NMR and Trent Franks for help with pulse programs for solid state NMR experiments.

I also appreciate the regular discussions with my additional supervisors Steven Brown, David Roper and Christopher Dowson, providing expertise in solid state NMR and microbiology. During my PhD I also had the opportunity to spend some time in other labs which was very helpful for my skills developments. I thank Torsten Herrmann and Yusuke Nishiyama for welcoming me in their labs. Large thanks to all the co-authors on my papers. Thanks also to the UK 850 MHz solid state NMR facility, for the opportunity to conduct experiments there and for their generous grant allowing me to present my data at the ICMRBS in Kyoto, Japan and thanks to Dinu Iuga, facility manager at the UK 850 MHz solid state NMR facility for all the help. I would also like to acknowledge the SCI Messel travel grant, which also supported my travel to the ICMRBS. Funding from the European Union under a Marie Curie Initial Training Network FP7-PEOPLE-2012-ITN Grant Agreement Number 316630 CAS-IDP is acknowledged. I am also grateful to Alison Rodger and Naomi Grew for all their work with the Marie Curie initial training network, and all the other Marie Curie fellows in my network.

## Declarations

All experimental chapters are results of collaborations. My contributions to the work are stated in this section. My supervisor, Józef Lewandowski, was of course involved in all the projects and made significant contributions to all aspects from planning experiments to analysing data and writing the manuscripts. Chapter 2 has been accepted for publication in *Journal of the American Chemical Society*. In chapter 2, I produced the isotopically labelled GB1 together with Simone Kosol. I acquired, processed and analysed all the solid state NMR experiments except for the  $^1\text{H}$   $R_1$  measurements with 100 mM CuEDTA which was acquired by Jonathan Lamley. I have also proposed a new parameter called difference solvent paramagnetic relaxation enhancement ( $\Delta\text{sPRE}$ ) and theoretical treatment of the data for identifying protein-protein interactions based on the difference in solvent accessibility measured in isolated protein in solution and in a sample with protein-protein interactions in solid state. Simone Kosol measured the solution NMR experiments and Christoph Hartlmüller and Tobias Madl performed the PRE predictions. Chapter 3 is published in *Angewandte Chemie* and was led by a previous PhD student in our group, Jonathan Lamley. I was involved originally by assisting in packing solid state NMR rotors and acquiring data as part of my training. I also assisted in data analysis, making figures and editing the manuscript. After Jonathan left the group I performed most of the additional experiments and data analysis required for publication. My main contributions to the paper were the site specific  $^{15}\text{N}$   $R_{1\rho}$  measurements at varying MAS speeds and site specific  $^{15}\text{N}$   $R_1$  measurements for GB1 in the complex with IgG. An early version of this manuscript was included in Jonathan Lamley's PhD thesis. However, the final version is significantly different and includes more data that I acquired. The isotopically labelled GB1 used in chapter 3 was provided by Stephan Grzesiek and co-workers at the University of Basel. In chapters 4 and 5 I have conducted all the experiments and data analysis. The isotopically labelled GB1 used in chapter 4 was from the same batch that I produced together with Simone Kosol, used in chapter 2. The teixobactin used in chapter 5 was provided by Kim Lewis at Northeastern

University and Dallas Hughes at Novobiotics (US). Lipid II was provided by the David Roper and Christopher Dowson groups at the School of Life Sciences, University of Warwick. In order to perform structure calculations of molecules with non-proteinogenic residues I have produced a large library for the molecular dynamics software CYANA that was used in the structure calculations in chapter 5. This library can deal with modified amino acid containing standard peptide bonds but also residues containing other types of bonds, such as glycosidic bonds between sugar molecules. The 0.81 mm probes used in chapters 2 (for 850 MHz spectrometer) and 5 (for 600 MHz spectrometer) were developed by Ago Samoson and co-workers in Estonia. The 0.81 mm probe for the 600 MHz spectrometer belongs to our group and was an experimental probe in which development our group was involved. I have spent a lot of time optimising the sample preparations, and general procedures for running of this probe. For all chapters, except chapter 3, I wrote the original manuscripts, which were subsequently edited collaboratively with the co-workers. As will be made clear in the thesis I have during my PhD gained experience in preparing samples for and running NMR experiments, mainly in the solid state but also in solution, to investigate structures and dynamics of proteins, protein complexes, small peptides, cell wall fragments and complexes of peptides and cell wall fragments. I have also learned how to calculate 3D structures of biomolecules based on NMR data, and gained further understanding in how the structure calculation software work to be able to incorporate non-proteinogenic residues. During my PhD I also contributed the following published papers;

*Solid-State NMR of a Protein in a Precipitated Complex with a Full-Length Antibody*, Lamley, J.M., Iuga, D., Öster, C., Sass, H.J., Rogowski, M., Oss, A., Past, J., Reinhold, A., Grzesiek, S., Samoson, A., Lewandowski, J.R. *J. Am. Chem. Soc.* **2014** 136 (48):16800–16806.

*Protein residue linking in a single spectrum for magic-angle spinning NMR assignment*, Andreas LB, Stanek J, Le Marchand T, Bertarello A, Cala-De Paepe D, Lalli D, Krejčíková M, Doyen C, Öster C, Knott B, Wegner

S, Engelke F, Felli IC, Pierattelli R, Dixon NE, Emsley  
L, Herrmann T, Pintacuda G. *J Biomol NMR* **2015** 62 (3) 253-61

In these publications, my contributions were minor and they are  
therefore not included in the thesis.

## **Abstract**

Solid state NMR is a powerful method to obtain information on structure and dynamics of proteins, protein complexes, and other biomolecular assemblies, that due to solubility and size limitations cannot be achieved by other methods. This thesis is dedicated to the use of proton detected solid state NMR experiments at fast (60-100 kHz) magic angle spinning speeds to probe biomolecular structure, dynamics and intermolecular interactions. We used solvent paramagnetic relaxation enhancements to (i) speed up experiments and (ii) measure solvent accessibility to map protein – protein interfaces. Further we use nuclear spin relaxation measurements to obtain information on protein dynamics in a small protein in two different ensembles; crystalline and precipitated in a > 300 kDa complex. We also apply a combined solution and solid state NMR approach to investigate the interactions between possibly the most promising antibiotic lead in modern time, teixobactin, and arguably the most exciting bacterial target, lipid II. Our most important results include a new method for probing protein-protein interactions using solvent paramagnetic relaxation enhancements, the first site specific dynamics measurements spanning a wide range of time scales obtained in a large protein complex using as little as 8 nanomoles of isotopically labelled material, the use of solvent paramagnetic relaxation enhancements to enable measurements of conformational exchange in a large protein complex and finally we have identified important conformational changes involved in the binding of teixobactin to cell wall precursor lipid II.

## **1. Introduction**

The following chapter provides theoretical basis for understanding the experimental chapters 2-5. Chapter 2 discusses characterisation of protein – protein interfaces using solvent paramagnetic relaxation enhancements. Chapters 3-4 concern protein dynamics in large protein complexes and chapter 5 interactions between an antibiotic and a bacterial cell wall precursor. The common theme in all the experimental chapters is that they include the use of solid state NMR to obtain vital information about interactions in biomolecular complexes. In chapters 2-4 the complex studied is a > 300 kDa protein – antibody complex formed between the B1 domain of bacterial Protein G (GB1) and human immunoglobulin G (IgG), in chapter 5 it is the complex formed between an antibiotic, teixobactin, and a cell wall precursor, lipid II. This introduction includes information regarding bacterial cell walls, solid state NMR of biomolecules and structure determination by NMR in solution and in solid state. More specific information related to the experimental work conducted is provided in each experimental chapter. The introduction gives more general descriptions of important information that is not included in the experimental chapters, i.e. information that is vital to understand how the results were obtained but not suitable for inclusion in publications. The original aim of my PhD project was to obtain structural information on bacterial cell walls or on cell wall fragments involved in the cell wall synthesis and how antibiotics can inhibit the synthesis of cell walls. In order to achieve this I worked a lot on methods development for solid state NMR approaches on large complexes, e.g. the GB1:IgG complex.

### **1.1 GB1:IgG complex**

The B1 domain of Protein G (GB1) has been used as a model protein in solution and solid state NMR method developments for decades due to its stable fold and large yields in protein production. The solution NMR structure of GB1 was solved already in 1991<sup>1</sup>. For solid state NMR applications it is also beneficial that it is easy and straight-forward to obtain microcrystals of GB1 yielding NMR spectra with high resolution,



leading to that it was one of the first protein structures solved by solid state NMR<sup>2-4</sup>. However, there is also a biological interest for GB1; the binding to IgG antibodies. Protein G is produced by group G and C streptococci as a part of the bacterial defence strategy against antibodies that enables bacteria to escape detection by the host immune system.<sup>5</sup> The high affinity between GB1 and IgG is commonly exploited in numerous biotechnological applications such as immunosorbent assays or affinity purification of antibodies. IgG antibodies are used in a range of therapeutic applications such as cancer treatment and treatments of infectious diseases. Antibody-based drugs are one of the fastest growing classes of protein therapeutics and of these unmodified IgG antibodies are the most common.<sup>6</sup> Solution NMR and X-Ray crystallography has been used to study interactions between domains of Protein G and fragments of IgG but only with solid state NMR is it possible to investigate interactions with full length IgG. See chapter 2 for more details on interactions between GB1 and IgG and chapters 3-4 for details on the dynamics of GB1 in complex with IgG.

## **1.2 Antimicrobial resistance**

Antimicrobial resistance (AMR) is a global threat resulting in hundreds of thousands of deaths each year. At the same time the development of new antibiotics has been slow and there is an urgent need for new antibiotics that can tackle bacteria that have acquired resistance against current last resort antibiotics. If these issues are not tackled the estimated deaths caused by AMR are expected to overtake cancer and according to the O'Neill report<sup>7</sup> 10 million people will die each year from AMR in 2050. Strategies for obtaining new antimicrobial agents include identifying good targets, which are conserved between different strains of bacteria and not present in human cells. Such a target is the cell wall building block lipid II, which is considered in the work presented here.

### *1.2.1 Peptidoglycan*

Bacterial cell wall consists of peptidoglycan, which as the name suggests is made up of peptides and sugars. Peptidoglycan is an essential part of bacterial cells. Its main task is to maintain the integrity of the cell by

withstanding turgor pressure. If the peptidoglycan is damaged or if the synthesis of peptidoglycan is interrupted the cell will be destroyed. This has of course been widely utilized in antibiotics design. In fact penicillin, which was discovered by Alexander Fleming in the famous accidental growth of mould incident<sup>8</sup>, is inhibiting the synthesis of peptidoglycan in bacteria. Although it took around 35 years from the initial discovery until it was discovered that penicillin works by inhibiting transpeptidation (see Fig.1.2) in the peptidoglycan synthesis<sup>9,10</sup>. Peptidoglycan is also responsible for keeping a certain cell shape and functions as a scaffold for anchoring other cell envelope components such as proteins and teichoic acids. It is closely involved in cell division and cell growth.<sup>11</sup> Figure 1.1 shows a schematic drawing of peptidoglycan.

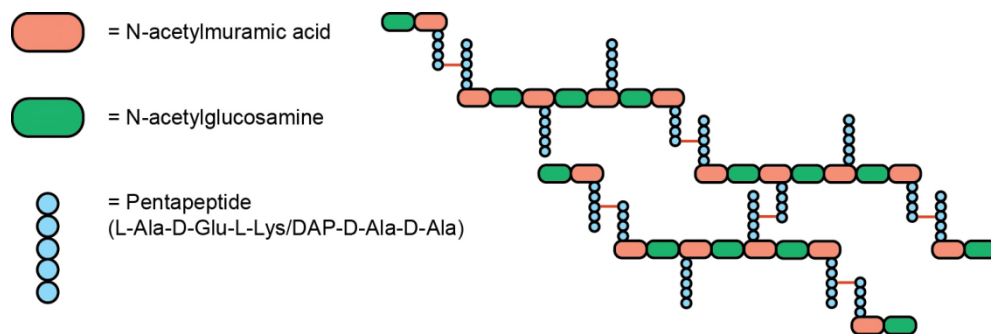


**Figure 1.1.** Schematic drawing of peptidoglycan. Red lines indicate peptide links connecting glycan strands.

Peptidoglycan is composed of linear glycan strands that are connected through peptide links (red lines in Fig. 1.1). The glycan strands consist of alternating N-acetylglucosamine (NAG, green in Fig. 1.1) and N-acetylmuramic acid (NAM, orange in Fig. 1.1) connected through  $\beta$ -1-4 bonds.<sup>11</sup> The glycan strands can be modified in different ways; N-deacetylation, N-glycolylation, O-acetylation,  $\delta$ -lactam formation, attachment of surface polymers and formation of 1-6 anhydro ring.<sup>12</sup> There are no bacteria known to have completely unmodified glycan strands. Modifications affect how the host cells recognize pathogenic bacteria and it can also result in resistance against host defence mechanisms. An example is that N-deacetylation has been shown to increase resistance against lysozyme by making the peptidoglycan a much worse substrate for the enzyme. The actual effect of the different

modifications is not very well understood, even though some enzymes responsible for modifications have been identified.<sup>12</sup>

The peptide links are formed between peptide stems situated on the NAM residue of each disaccharide. The peptide stem varies between different species but the most common is L-Ala-D-Glu-DAP(diaminopimelic acid)/L-Lys-D-Ala-D-Ala. Variations in this peptide sequence can result in resistance against antibiotics, which is the case for bacteria that have obtained resistance against vancomycin (discussed below in section 1.1.2). The peptide link is usually established between the carboxyl group in the amino acid at position 4 and the amino group in the diamino acid at position 3.<sup>11</sup> In most gram negative bacteria it is a direct cross-link and in most gram positive bacteria it has an interpeptide bridge. Two of the most studied bacteria when it comes to peptidoglycan are the gram negative *Escherichia coli* and the gram positive *Staphylococcus aureus*. These two differ in peptide cross links as *E. coli* has a direct 3-4 cross link while *S. aureus* has a 3-4 pentaglycine bridge. The length of the interpeptide bridge can vary between 1 and 7 amino acids and there are many different amino acids present in different bacteria. Also the degree of cross-linkage varies. In *E. coli* approximately 20% of the peptide stems are involved in cross-linkage whereas in *S. aureus* it is more than 90%.<sup>11</sup> All these different variations in peptidoglycan structure may be important for how bacteria respond to antimicrobial agents and more understanding of peptidoglycan and the synthesis of peptidoglycan is important for the development of new antibiotics.

Figure 1.2 shows a schematic drawing of the peptidoglycan biosynthesis pathway adapted from a recent review by Teo and Roper<sup>13</sup>. The potential of disturbing the synthesis of peptidoglycan by attacking this biosynthesis pathway makes it interesting to study and many of the enzymes involved have been identified as potential targets for antibiotics. However, perhaps the most interesting target is not an enzyme but the cell wall precursor lipid II since it is highly conserved between different bacteria and difficult to modify.

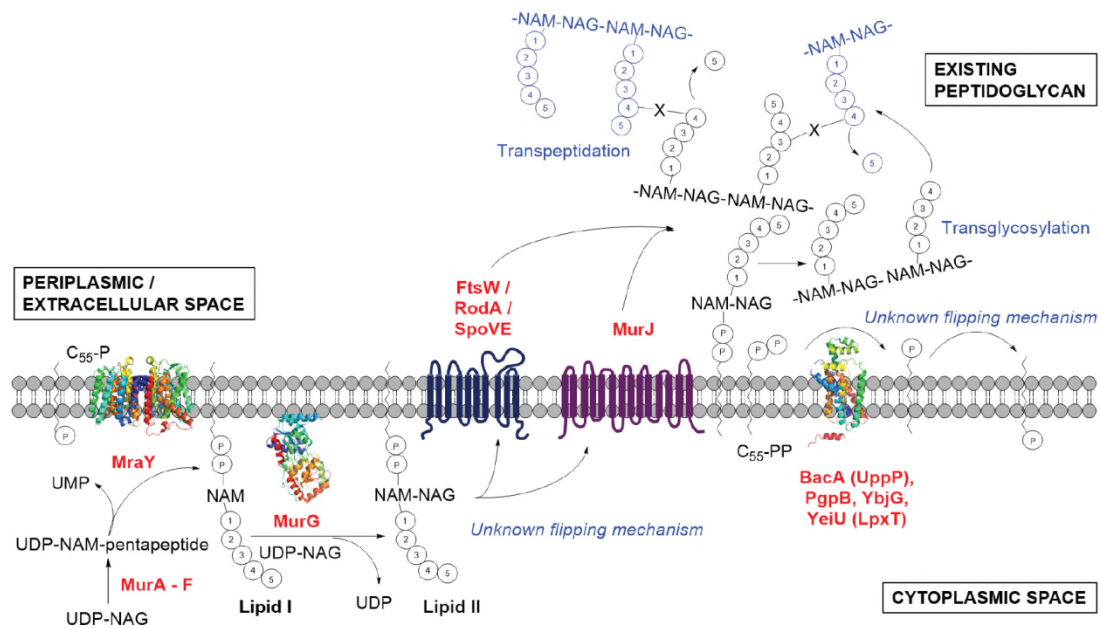


**Figure 1.2.** Peptidoglycan synthesis pathway<sup>13</sup>

Lipid II consists of the general building blocks of peptidoglycan (shown in figure 1.1), linked through a pyrophosphate group and a carrier lipid (undecaprenyl pyrophosphate) attached to the membrane (the chemical structure of lipid II is shown in figure 1.3).

### 1.2.2 Antibiotics binding to Lipid II

Antibiotics that inhibit the cell wall synthesis are the most popular type of antibiotics and, as mentioned before, lipid II is an excellent target to focus on. There are many different types of lipid II binders including; glycopeptides, defensins, lantibiotics and nonribosomally synthesised peptides (e.g depsipeptides), recently reviewed by Oppedisjk *et al*<sup>14</sup>. Glycopeptides are peptides that contain residues with glycans attached to the side chains. The only lipid II binding antibiotic currently in clinical use is the glycopeptide vancomycin. Vancomycin binds the D-Ala – D-Ala at the C-terminus of the peptide stem of lipid II by the formation of five hydrogen bonds. Vancomycin was in clinical use for more than 30 years before resistance was detected, which highlights the importance of lipid II binding antibiotics. The resistance towards vancomycin was obtained from the change of the D-Ala – D-Ala to D-Ala – D-Lac or D-Ala – D-Ser in the peptide stem of lipid II, resulting in only four hydrogen bonds

being formed leading to almost a 1000 fold decrease in affinity<sup>15</sup>. This substitution has been seen in *Lactobacillus casei* naturally and in Enterococci with acquired resistance to vancomycin<sup>11</sup>. Since vancomycin binds the peptide stem it can also bind mature peptidoglycan, which vancomycin intermediate *Staphylococcus aureus* (VISA) has taken advantage of by making a thicker peptidoglycan layer leading to that most vancomycin will bind to the mature peptidoglycan rather than lipid II. Other parts of lipid II such as the sugars and pyrophosphate are more conserved between bacteria. Especially the carrier lipid, undecaprenyl pyrophosphate is very important in the peptidoglycan synthesis pathway and is not present in mature peptidoglycan. Hence, antibiotics that bind to the sugars and/or undecaprenyl pyrophosphate of lipid II have the potential, if they become commercially available, to be used for a long time before (if ever) antimicrobial resistance will emerge. For this reason many of the antibiotics that have been studied more carefully recently are those that are believed to interact with that part. In fact, the antibiotic nisin, which interacts with the pyrophosphate group and possibly parts of the lipid tail has been used for more than 40 years in the food industry without any resistance being detected. Figure 1.3a shows suggested binding sites for different interesting lipid II binding antibiotics. The chemical structure of lipid II is shown in figure 1.3b.

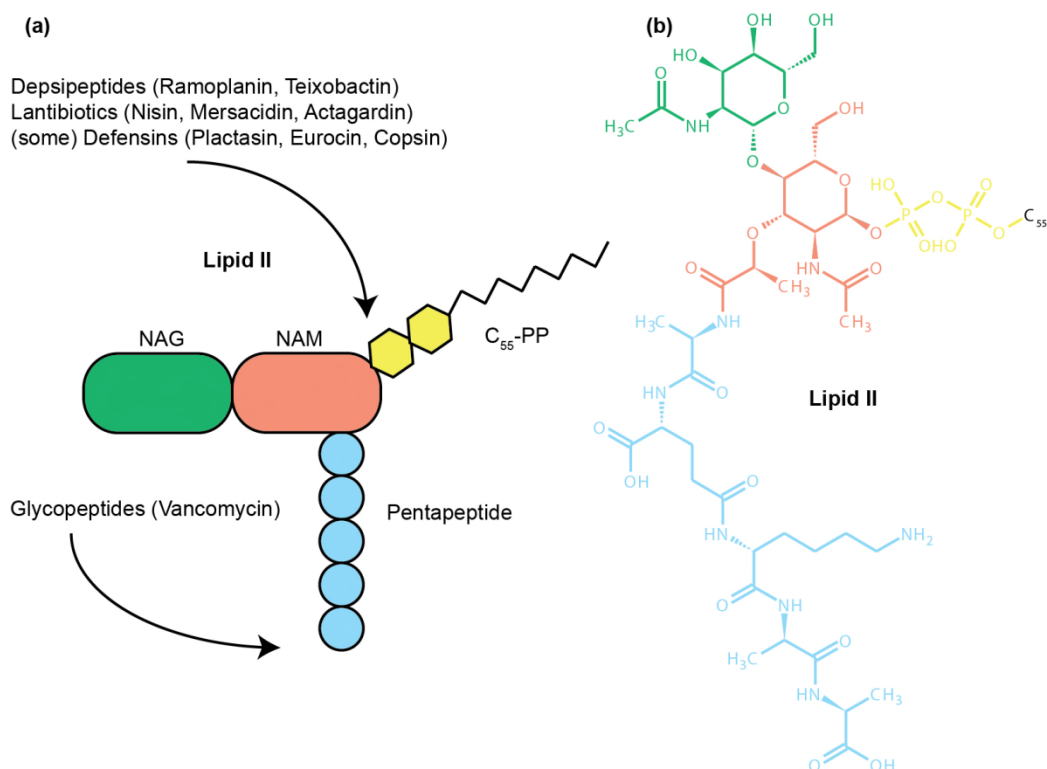


**Figure 1.3.** (a) Schematic model of lipid II with binding sites for different types of antibiotics indicated. (b) chemical structure of lipid II. The lipid tail is represented by C<sub>55</sub> as it contains 55 carbons.

A novel lipid II binding mode was identified for nisin from solution NMR measurements of a nisin – lipid II complex<sup>16</sup>. In this binding mode a pyrophosphate cage is formed by intermolecular hydrogen bonds between backbone amides of nisin in the N-terminus lanthionine ring and the pyrophosphate group of lipid II. The N-terminal lanthionine ring is conserved in many lantibiotics and it is likely that the same binding mode occurs in other lantibiotics. A lanthionine ring is formed by bonds between side-chains of modified alanines where the  $\beta$ -carbons are cross-linked with a sulfur atom in between. Nisin belongs to the class A lantibiotics which are characterized by an elongated structure. They actually have two killing modes, where the binding of lipid II through the pyrophosphate cage mode represents the first step, the second step is a pore formation resulting from insertion of the elongated peptide into the membrane. Each of those modes would be sufficient to kill bacteria but the combined mode makes the class A lantibiotics even more efficient. Class B lantibiotics, like mersacidin, works by binding lipid II leading to the accumulation of cell wall precursors and inhibition of

transglycosylation. Class B lantibiotics undergo substantial conformational changes in different environments and when binding lipid II. This behaviour was shown in an NMR study where conformational changes were detected when the sample solution was changed from a methanol/water solution to a membrane environment (dodecylphosphocholine (DPC) micelles) and then again when Lipid II was present<sup>17</sup>. Such conformational changes could be important for how the antibiotic enters the cell and reaches the membrane where lipid II is located.

An example of an interesting depsipeptide is ramoplanin, which is a cyclic lipoglycopeptide. Ramoplanin inhibits peptidoglycan synthesis by blocking transglycosylation upon binding to Lipid II. The mode of action of ramoplanin seems to be similar as mersacidine, in both cases they accumulate cell wall precursors inhibiting the formation of peptidoglycan, and even though the chemical structure is very different between the two antibiotics their 3D structures are very similar and they both undergo conformational changes upon binding to lipid II<sup>18</sup>.

Defensins are found in mammals, invertebrates and plants where they function as host defence peptides. A very interesting defensin is plectasin<sup>19</sup>, which was shown by NMR to form hydrogen bonds with the pyrophosphate of lipid II and blocking synthesis of peptidoglycan in a similar way as mersacidine and ramoplanin. In that study several other defensins binding lipid II were isolated from fungi, maggots and mussels

<sup>20</sup>.

In many structural studies of antibiotics NMR has been an indispensable technique. However, in some studies it was noted that antibiotics – lipid II complexes form large soluble aggregates, making solution NMR unusable. In the case of ramoplanin it formed fibrillar structures<sup>18</sup> that resulted in severe broadening of the spectra. To prevent fibrillation non-physiological solvents, such as DMSO, had to be used. In our approach to study the teixobactin – lipid II complex, which also formed large soluble aggregates, we took advantage of the fact that in solid state NMR the

size dependent tumbling of molecules is not present. This study is presented in chapter 5.

### **1.3 NMR**

The main technique used in the work presented in this thesis is NMR. Depending on the sample investigated the experiments were performed in solution or in solid state. Most of the samples were not suitable for solution NMR due to size implications but in the cases where applicable, solution NMR gave important information: It was used to obtain solvent accessibility for isolated GB1 in chapter 2 and to solve the 3D structure of teixobactin in membrane mimics in chapter 5. This section is mostly focused on solid state NMR, but the information is valid for solution NMR as well and important aspects where the techniques differ are pointed out.

#### *1.3.1 Basic theory*

In this section a few important theoretical aspects of NMR will be briefly discussed. The NMR interactions are described by quantum mechanics and it is beyond the scope of this thesis to go into a full description of the physics required to explain it properly. Some important theoretical aspects will be introduced but the explanations will be left out. This section is based on information that can be found in the NMR text books written by Malcolm H. Levitt<sup>21</sup>, James Keeler<sup>22</sup>, Melinda J. Duer<sup>23</sup>, Gordon S. Rule and Kevin T. Hitchens<sup>24</sup>.

First of all, it is important that the nuclei investigated are NMR active, that is they have a spin angular momentum. All nuclei that have an odd mass number have spin angular momentum since they have an unpaired proton. The nuclei commonly occurring in proteins are hydrogen, carbon, nitrogen and oxygen. All of these have isotopes that are NMR active (table 1.1). As can be seen in the table also nuclei with even mass number can have a spin angular momentum, that is if they have an odd charge. Nuclei that have spin angular momentum have a non-zero spin number. Nuclei with even number of protons and neutrons have spin number 0, and hence no spin angular momentum.



**Table 1.1.** Properties important for NMR of different isotopes of the most common nuclei in proteins.

Nucleus	Spin	Abundance (%)	$\gamma$ (MHz / T)
$^1\text{H}$	$\frac{1}{2}$	99.98	42.57697
$^2\text{H}$	1	0.0015	6.535857
$^3\text{H}$	$\frac{1}{2}$	0	45.41486
$^{13}\text{C}$	$\frac{1}{2}$	1.108	10.70842
$^{14}\text{N}$	1	99.63	3.077738
$^{15}\text{N}$	$\frac{1}{2}$	0.37	-4.31628
$^{17}\text{O}$	$\frac{5}{2}$	0.037	-5.77398

For hydrogen the most abundant isotope is  $^1\text{H}$ , which also has the largest gyromagnetic ratio ( $\gamma$ ) of all nuclei used for NMR.  $^3\text{H}$  has a larger  $\gamma$ , but it is radioactive and not naturally abundant so it is not often used in NMR. For carbon, where the most abundant isotope is  $^{12}\text{C}$ , which is a spin 0 isotope, typically it is necessary to introduce  $^{13}\text{C}$  (natural abundance  $^{13}\text{C}$  can be used for smaller compounds) and  $^{15}\text{N}$  is introduced instead of  $^{14}\text{N}$  (which is quadrupolar and can be measured but is generally not used in proteins) for NMR applications. Oxygen would be very useful but since  $^{16}\text{O}$  is spin 0 and the NMR active  $^{17}\text{O}$  is spin 5/2 and hence has a quadrupolar moment it is not often used in protein NMR (though it is still an active area of method development).

The first interaction in NMR that needs to be considered when a sample is put in a static magnetic field ( $B_0$ ) is called the Zeeman interaction, which describes how spins are split into quantum states with different energy levels (Figure 1.4a). For nuclei with spin  $I$  the number of energy levels is  $2I+1$ . Spin  $\frac{1}{2}$  nuclei have then two energy levels, generally called  $E_\alpha$  and  $E_\beta$ , where the difference in energy between the two states is defined as the Larmor frequency:

$$\nu_0 = \frac{\omega_0}{2\pi} = \frac{\gamma \times B_0}{2\pi} \quad (1.1)$$

in Hz,  $\gamma$  is the gyromagnetic ratio ( $\text{rad s}^{-1} \text{T}^{-1}$ ) and  $B_0$  the static magnetic field (T). The  $2\pi$  is used to convert from  $\text{rad s}^{-1}$  to Hz. The spins are said to precess around the  $B_0$  field at the Larmor frequency (figure 1.4b). NMR magnets are often referred to by their  $^1\text{H}$  Larmor frequency in MHz.

The population ratio between the energy levels is described by Boltzmann distribution:

$$\frac{p_\alpha}{p_\beta} = e^{\frac{-\gamma\hbar B_0}{kT}} \quad (1.2)$$

where  $\hbar$  is Plancks constant divided by  $2\pi$ ,  $k$  is the Boltzmann constant and  $T$  is the temperature.

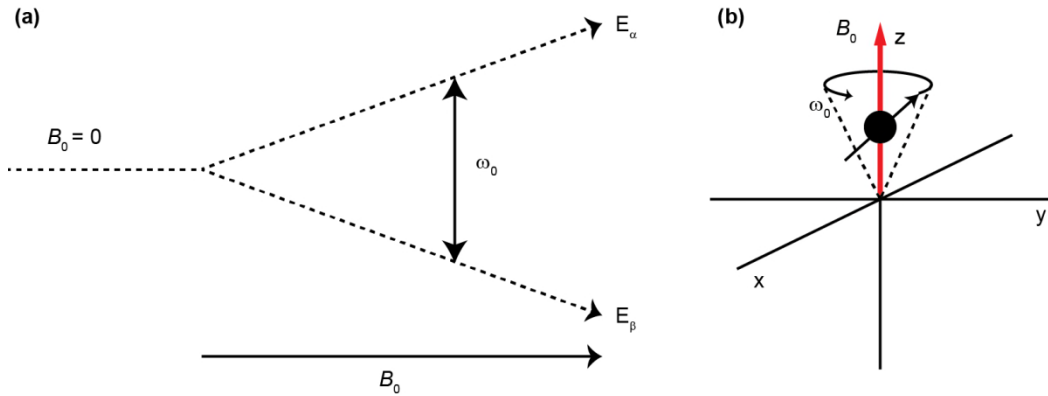


**Figure 1.4.** (a) Zeeman splitting for a spin  $\frac{1}{2}$  nuclei. The difference between the energy levels is the Larmor frequency. (b) Larmor precession around the  $B_0$  field.

The Boltzmann distribution is important since the NMR signal partly depends on that the populations of the energy levels are different and the quantity of the difference can be changed by changing the gyromagnetic ratio, the  $B_0$  field and the temperature. Higher magnetic field gives higher signal, higher gyromagnetic ratio gives higher signal and lower temperature gives higher signal, although for proteins there is normally not much room for changing the temperature to make any difference.

In a one pulse experiment a  $\pi/2$  radiofrequency pulse is applied at the Larmor frequency of the nuclei of interest with a certain nutation frequency

$$\omega_1 = \gamma \times B_1 \quad (1.3)$$

creating a local magnetic field  $B_1$ . The spins will be rotated from the z-axis and precess at the Larmor frequency in the xy plane. The precession results in an oscillating magnetic field, which, in accordance to Faradays law, induces a current in a coil in the NMR probe recorded as the free

induction decay (FID). The FID is then Fourier transformed into a time domain axis and plotted as intensity versus frequency.

Before moving on to experiments correlating different nuclei a few more interactions need to be introduced. So far the interactions (described by Hamiltonians in quantum mechanics) have been external; interactions between the magnetic field and the spins and interactions between radiofrequency pulses and the spins, but there are also internal interactions. The internal Hamiltonians are interactions of spins with the local electronic environment (chemical shift), with each other (dipolar and scalar couplings) and with electric field gradients (quadrupolar couplings). For spin  $\frac{1}{2}$  nuclei, which are considered in all experiments here, no quadrupolar interactions are present. The internal interactions can have parts that are isotropic (independent of orientation with respect to  $B_0$ ) and anisotropic (dependent of orientation with respect to  $B_0$ ). Dipolar couplings are anisotropic and consist of both homonuclear and heteronuclear couplings in a sample with more than one nucleus. To fully describe the dipolar couplings it would be necessary to involve quantum mechanics, but for the purpose of this thesis it is sufficient to present the dipolar couplings as:

$$D \propto \gamma_1 \gamma_2 r^{-3} (3 \cos^2 \theta - 1) \quad (1.4)$$

where  $r$  is the distance between the coupled spins and  $\theta$  is the angle formed between the spins and the  $B_0$  field. The chemical shift depends on the Larmor frequency and chemical shielding based on the electronic environment around the spin. The chemical shift can be described as:

$$\delta = \gamma B_0 (1 - \sigma) \quad (1.5)$$

where  $\sigma$  is the chemical shielding. The isotropic chemical shift (i.e. the component of chemical shift that is independent of the orientation with respect to  $B_0$ ) is simply the Larmor frequency determined from the local magnetic field that each spin feels as a combination between the static field and the field produced by surrounding electrons. The magnetic field created by the electrons around a nucleus is not uniform so there will be an anisotropic part to the chemical shift, which just as for the dipolar

couplings is proportional to the second Legendre polynomial  $\frac{1}{2}(3\cos^2\theta - 1)$ . Scalar couplings, or J-couplings as they are normally referred to, are isotropic and give rise to J-splittings in NMR spectra. Since they are much weaker than dipolar couplings and chemical shift anisotropy the line widths reachable in solid state NMR typically are broader than the J-splittings so they are often ignored. However, with recent methodological advances and improvements in resolution J-couplings receive more attention in the solid state.

Line broadening is caused by the effect of anisotropic interactions on the  $T_2$  relaxation time, which represents the loss of coherence in the transverse plane due to spin-spin interactions. Further information on relaxation is given in section 1.3.3. There are two main ways of removing unwanted broadening caused by the interactions described above; rotating the sample and decoupling. In solution NMR the molecules tumble freely and sample all orientations leading to that anisotropic interactions are averaged to 0. J-couplings, which are isotropic, are still present but can be removed by decoupling. Heteronuclear J-couplings are weak and easily removed by applying a weak radio frequency field on, for example, the  $^{13}\text{C}$  channel during  $^1\text{H}$  detection. Homonuclear J-couplings, however, are more complicated to remove and lead to J-splitting normally seen in solution NMR experiments. As mentioned above, in solid state NMR the lines are often not sufficiently narrow to observe J-splittings. To remove anisotropic interactions in solid state NMR the sample is mechanically rotated at the magic angle ( $\theta = 54.74^\circ$ ), where  $\frac{1}{2}(3\cos^2\theta - 1) = 0$ . For the magic angle spinning (MAS)<sup>25,26</sup> to efficiently average out the anisotropic interaction the spinning speed needs to be much faster than the strength of the interaction (in Hz).

As mentioned above the Boltzmann distribution is important for the sensitivity of an NMR experiment, the increase in  $\gamma$  to increase the sensitivity is taken advantage of in the cross-polarization (CP)<sup>27</sup> experiment, in solid state NMR, where magnetization from the higher  $\gamma$  nuclei, often  $^1\text{H}$ , can be transferred to lower  $\gamma$  nuclei ( $^{13}\text{C}$  or  $^{15}\text{N}$  in proteins) to increase the signal. Figure 1.5 shows the pulse sequence of a

CP experiment and what happens to the magnetization during the experiment.

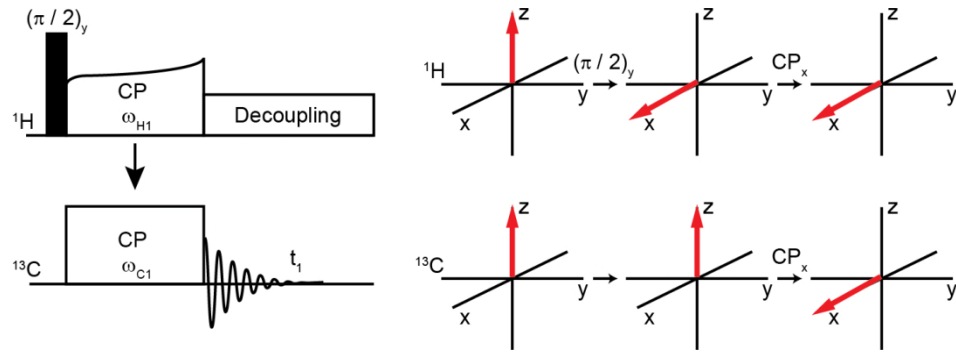


**Figure 1.5.** Cross polarization experiment. Left, block diagram of the pulse sequence. Right, magnetization transfer showed on xyz coordinates.

First a  $\pi/2$  pulse is applied to the  $^1\text{H}$  channel, which causes the magnetization to go into the xy plane. In this example the pulse was applied about the y axis leading to magnetization along x. The CP transfer is made up of spin-lock pulses at both channels simultaneously causing the magnetization to precess around x at the same nutation frequency for both nuclei as long as the pulse is on. Now the strong heteronuclear dipolar couplings will cause magnetization to transfer between the excited  $^1\text{H}$  spins and the  $^{13}\text{C}$  spins. Once the pulse is turned off the spins will precess around the x-axis at the Larmor frequency and the FID can be recorded on the  $^{13}\text{C}$  channel, while heteronuclear decoupling is applied to the  $^1\text{H}$  channel. For the transfer to work the nutation frequencies need to be equal for both channels so that the Hartmann – Hahn condition is fulfilled:

$$\omega_{H1} = \omega_{C1} \quad (1.6)$$

This is valid in static samples, but when MAS is employed making the dipolar couplings time dependent the Hartmann-Hahn matching condition becomes:

$$\omega_{H1} \pm \omega_{C1} = n\omega_{rot}, n = 1, 2 \quad (1.7)$$

If the magnetization transfer would be 100% efficient the signal could be increased by a factor of  $\gamma_1/\gamma_2$ , compared to an experiment with direct excitation of the lower  $\gamma$  nuclei, which is approximately 4 if  $\gamma_1$  is  $^1\text{H}$ ,  $\gamma_2$  is

$^{13}\text{C}$  and 10 if  $\gamma_1$  is  $^1\text{H}$ ,  $\gamma_2$  is  $^{15}\text{N}$ . CP experiments can also be repeated quicker since the repetition delay depends on the  $T_1$  relaxation time (see section 1.3.3) of the excited nuclei and the spins need to return to equilibrium before the next experiment can be started.  $T_1$ s for protons are much shorter than  $T_1$ s for lower gamma nuclei (e.g.  $^{13}\text{C}$  and  $^{15}\text{N}$ ) leading to higher signal to noise ratio in the same time (signal to noise ratio increases by  $\sqrt{n}$ , where  $n$  = number of repetitions).

In most NMR experiments it is desirable to obtain as narrow lines as possible, especially in protein NMR since the spectra typically contain many signals and if the peaks are too broad it is difficult to assign which peaks belong to which atom in the protein. To achieve narrow lines when using MAS it is important that the rotor angle is set properly. There are several options for what type of sample is used to set the angle depending on the spinning speed. The probes that were used in this work were 1.3 mm probes that have operational MAS speeds up to 60 kHz and 0.81 mm probes with operational MAS speeds up to 100 kHz. The probe sizes refer to the outer diameter of the rotors used in the specific probe. In this fast spinning regime the magic angle can be set using a [ $^{13}\text{C}'$ ] labelled alanine sample since the spinning speeds are much higher than the strengths of the anisotropic interactions in this sample. Figure 1.6a shows a schematic drawing of MAS and 1.6b shows CP spectra of [ $^{13}\text{C}'$ ]alanine obtained at 60 kHz MAS with the magic angle slightly off, anisotropic interactions causing line broadening (red) and the magic angle set correctly, anisotropic interactions sufficiently averaged out (blue). Not only is the peak narrower when the magic angle is set properly, the maximum intensity is also higher. Overall, the line width also depends on inhomogeneous broadening, which depends on how well the sample is recrystallised. In our laboratory, for a well-crystallised [ $^{13}\text{C}'$ ]alanine sample the  $^{13}\text{C}$  line width in the case where the magic angle is properly adjusted is  $< 20$  Hz.

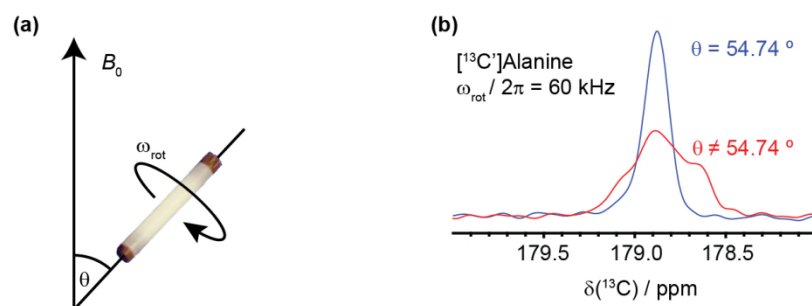


**Figure 1.6.** Magic angle spinning. (a) NMR rotor with the angle towards the static magnetic field indicated. (b)  $^1\text{H} - ^{13}\text{C}$  CP spectra of  $[^{13}\text{C}]$ alanine with the magic angle set correctly (blue line) and the magic angle set incorrectly (red line).

It can be noted in the spectra in Figure 1.6b that the chemical shift ( $\delta$ ) is presented in ppm, parts per million. This is the general convention of how chemical shifts are presented as spectra can then easily be compared between experiments acquired at different  $B_0$  fields. The chemical shifts in ppm are calculated as:

$$\delta = \frac{\omega_0^{\text{sample}} - \omega_0^{\text{ref}}}{\omega_0^{\text{ref}}} \times 10^6 \quad (1.8)$$

where  $\omega_0^{\text{ref}}$  is the chemical shift of a reference material. In protein NMR the reference used is often DSS (2,2-dimethyl-2-silapentane-5-sulfonic acid) as it is soluble in aqueous solutions and does not interact with biological samples. It can be put into the rotor in solid state NMR or the sample tube in solution NMR together with the protein sample. The  $^1\text{H}$  chemical shift of DSS is only very slightly affected by the temperature in the sample (at least in the range of temperatures suitable in protein NMR) further making it suitable as a reference. Referencing is then easily done by recording a 1 pulse  $^1\text{H}$  experiment and setting the peak originating from the DSS sample to 0 ppm. References for  $^{13}\text{C}$  and  $^{15}\text{N}$  can then be calculated indirectly from the  $^1\text{H}$  reference by using IUPAC recommended ratios<sup>28,29</sup>.

### 1.3.2 Biological assemblies in NMR

A main benefit of solid state NMR towards other techniques such as solution NMR and X-Ray crystallography is what type of samples can be used. Solution NMR requires soluble stable proteins that tumble free in the solution fast enough to average out the anisotropic interactions.

However, large molecules tumble slowly, which results in efficient transverse relaxation causing severe broadening of the lines so that no or little information can be extracted from the spectra. Solution NMR therefore suffers from strong size limitations for larger molecules (>40 kDa). The size of molecules accessible to solution NMR can be sometimes extended by using a number of methodological tricks such as deuteration and TROSY type techniques but it is difficult in general. X-ray crystallography requires good quality diffracting crystals and membrane proteins or molecules with large internal motions or highly flexible domains are notoriously difficult to crystallize. With solid state NMR it is in principle possible to study any kind of biological molecules and assemblies independent of the size and there are several different ways of preparing the samples before they are put into the NMR rotors. Very good resolution is achieved from microcrystalline proteins, without the need for the same kind of quality crystals as in X-ray crystallography. No long-range order is required, however the sample needs to be homogenous since inhomogeneous broadening can severely limit the possibility of obtaining good quality spectra. Samples can also be precipitated, sedimented by ultracentrifugation, freeze dried, or analysed in the form of fibrils. In many cases proteins packed into NMR rotors can be stable for months and even years.

Solid state NMR has become an important technique for studying protein assemblies<sup>30-39</sup>. The main areas of interest for large complexes or assemblies are fibrils, virus capsids and membrane proteins. Recent developments in solid state NMR of membrane proteins have been reviewed by Ladizhansky<sup>40</sup>. Quinn and Polenova<sup>41</sup> have reviewed developments in solid state NMR on structure and dynamics of protein complexes and other biomolecular assemblies (e.g. virus capsids). Of specific interest to this thesis is the use of proton detection to study protein complexes and biomolecular assemblies. Regarding membrane proteins and fibrils it was first shown by Linser *et al.* that high quality spectra could be obtained using proton detection of Alzheimer's disease  $\beta$ -amyloid peptide (fibrils) and membrane proteins.<sup>42</sup> Further work in method developments lead to fast experiments to achieve assignments



and structural information using proton detection on these types of complicated samples as shown for example in ref. 43. Recent developments of fast spinning MAS probes and high field NMR magnets enable high resolution site specific information requiring only a few nanomoles of labelled material (e.g. as demonstrated for GB1 in complex with IgG<sup>36</sup>).

In the work presented in this thesis three different types of sample preparations were used; microcrystalline protein, precipitated protein – protein complex and a sedimented sample of cell wall bound antibiotic. Figure 1.7 shows  $^1\text{H}$ - $^{15}\text{N}$  correlation spectra of samples prepared using these different methods, including both perdeuterated crystalline [ $\text{U-}^{13}\text{C}, ^{15}\text{N}$ ]GB1 with 100% of exchangeable protons back-exchanged (a) and fully protonated crystalline [ $\text{U-}^{13}\text{C}, ^{15}\text{N}$ ]GB1 (b). Figure 1.7c shows a spectrum of 100% back-exchanged perdeuterated [ $\text{U-}^{13}\text{C}, ^{15}\text{N}$ ]GB1 in a precipitated complex with full length natural abundance human Immunoglobulin G (IgG) antibody and (d) shows a sedimented complex of [ $\text{U-}^{13}\text{C}, ^{15}\text{N}$ ]teixobactin with natural abundance lipid II in deuterated dodecylphosphocholine (DPC) micelles. All solid state experiments considered in this thesis are acquired with proton detection. For proton detected experiments it is important to use fast MAS as strong  $^1\text{H}$ - $^1\text{H}$  dipolar couplings will otherwise lead to broad lines, just like in solution NMR if a protein tumbles too slowly. How fast the spinning needs to be depends mainly on how dense the proton network is. In most experiments considered here samples with only protons on exchangeable sites are considered (i.e mostly amide protons). For 100% back-exchanged perdeuterated samples 60 kHz MAS is sufficient to obtain high quality spectra suitable for structure determinations and dynamics measurements, but for the samples that are fully protonated 90-100 kHz MAS is used to get high quality spectra. For large protein complexes or other biological assemblies only containing small amounts of labelled material it is often useful to add a solvent paramagnetic relaxation enhancement agent to the sample<sup>44</sup>. As mentioned previously regarding CP experiments the  $T_1$  relaxation time of the excited nuclei determines how fast an experiment can be repeated (recycle delay). The addition of

a paramagnetic agent to the sample will shorten the  $T_1$  relaxation time and hence speed up the acquisition. As an example the spectrum of GB1 in complex with IgG (fig 1.7c) was recorded with 288 scans and a recycle delay of 2 s, which took around 14 h, but the addition of 2 mM gadolinium diethylenetriaminepentaacetic acid bismethylamide (Gd(DTPA-BMA)) as paramagnetic relaxation enhancement agent allowed for a recycle delay of 0.6 s and a spectrum with similar signal to noise ratio could then be acquired in 3.5 h. Solvent paramagnetic relaxation enhancements were used to speed up experiments in chapters 4 and 5 and to probe intermolecular interfaces in chapter 2. For a more detailed explanation of this phenomenon, see chapter 2.

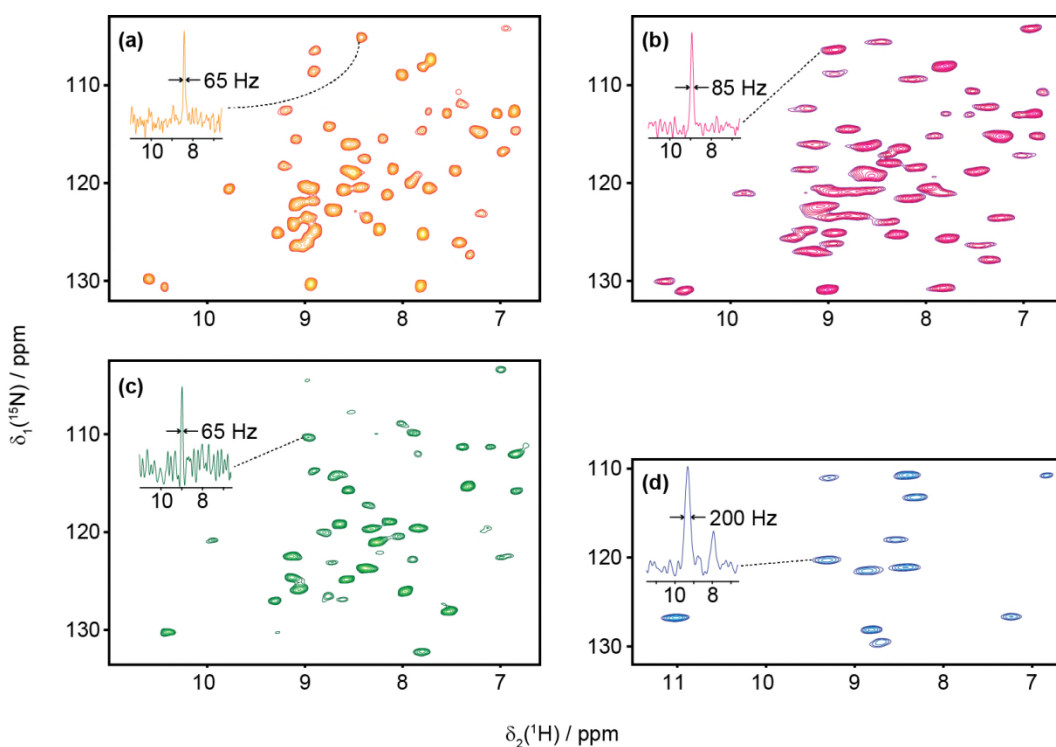


**Figure 1.7.** 2D  $^1\text{H}$ - $^{15}\text{N}$  correlation spectra for 4 different samples, with 1D slices showing examples of average  $^1\text{H}$  linewidths included. (a) Crystalline  $[\text{U-}^2\text{H}, ^{13}\text{C}, ^{15}\text{N}]$  GB1, back-exchanged in 100%  $\text{H}_2\text{O}$ . Spectrum acquired at 700 MHz  $^1\text{H}$  Larmor frequency with 60 kHz MAS. (b) Crystalline  $[\text{U-}^{13}\text{C}, ^{15}\text{N}]$  GB1. Spectrum acquired at 600 MHz  $^1\text{H}$  Larmor frequency with 100 kHz MAS (c) Precipitated complex consisting of  $[\text{U-}^2\text{H}, ^{13}\text{C}, ^{15}\text{N}]$  GB1, back-exchanged in 100%  $\text{H}_2\text{O}$ , and natural abundance full length human antibody IgG. Spectrum acquired at 700 MHz  $^1\text{H}$  Larmor frequency with 60 kHz MAS. (d) Sedimented complex consisting of  $[\text{U-}^{13}\text{C}, ^{15}\text{N}]$  teixobactin and natural abundance lipid II in deuterated DPC micelles. Spectrum acquired at 600 MHz  $^1\text{H}$  Larmor frequency with 90 kHz MAS.

A comparison between fully protonated GB1 (fig. 1.7b) and GB1 with only exchangeable protons (fig. 1.7a) illustrates the effect on proton line widths of diluting the proton network with deuterium. Even at 100 kHz

MAS the proton lines are broader in the fully protonated GB1 sample (1.7b) compared to the 100 % back-exchanged deuterated GB1 sample at 60 kHz MAS in 1.7a. According to simulations by Böckmann *et al.* spinning speeds of up to 250 kHz would be required to obtain the same line widths in a fully protonated sample as in a 100% back-exchanged perdeuterated sample at 100 kHz MAS<sup>45</sup>. There are currently probes that can spin at 100 kHz and above available from the 3 main probe developers (reported operational MAS speeds in brackets); Bruker 0.7 mm (111 kHz), JEOL 0.75 mm (100 kHz), Samoson 0.81 mm (100 kHz), Samoson 0.6 mm (130 kHz) and Samoson 0.5 mm (150 kHz).

### 1.3.3 Protein dynamics

Proteins are not static but move around constantly and are involved in motions spanning several magnitudes of time scales. NMR is a versatile tool for accessing information on motion at atomic resolution. Relaxation measurements in solution can be used for motions on picosecond to nanosecond time scales, limited by the tumbling of the molecules, which generally occur on nanoseconds timescale. It is also possible to access information on the nanosecond – millisecond motions in solution using alternative methods such as residual dipolar couplings or exchange methods. Figure 1.8 shows examples of dynamic processes occurring in proteins and which timescales relaxation measurements in solution and solid state NMR can pick up.

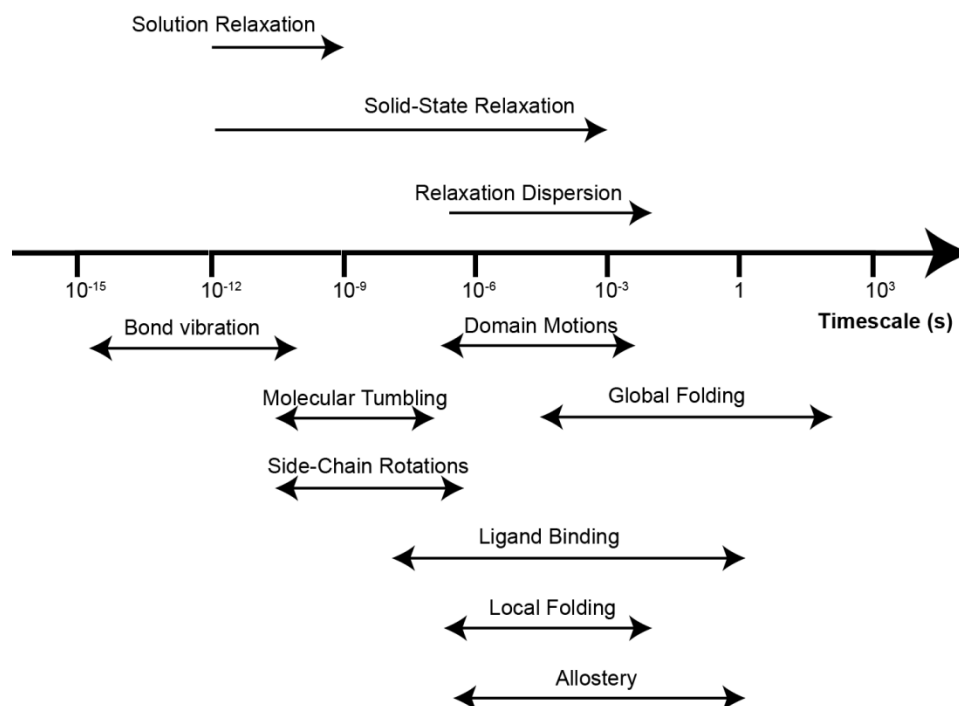


**Figure 1.8.** Examples of time scales of dynamic processes in proteins and relaxation measurements to obtain information on them.

In solid state NMR where molecules generally don't tumble, relaxation measurements can be used to characterize time scales and amplitude of motion spanning from picoseconds – milliseconds. In this work three types of relaxation measurements were used;  $R_1$ ,  $R_{1\rho}$  and  $R_{1\rho}$  relaxation dispersion.

To understand how these measurements relate to protein dynamics it is useful to first introduce the longitudinal ( $R_1=1/T_1$ ) and transverse ( $R_2=1/T_2$ ) relaxation rates. Excited nuclear spins will return to equilibrium through these relaxation processes. Longitudinal relaxation refers to the loss of z magnetization and transverse relaxation refers to the loss of coherence of xy magnetization. Generally, relaxation processes occur through anisotropic interactions; chemical shift anisotropy (CSA) and dipolar couplings (also quadrupolar interactions but they are not considered here). CSA results in local magnetic fields that depend on bond vector orientations relative to the static magnetic field. When a protein rotates relative to the  $B_0$  field and/or the bond vector rotates relative to the protein backbone, the local magnetic field will change with time, which produces an oscillating field that can stimulate relaxation.

Through space dipolar couplings between pairs of nuclear spins depend on both distance between the spins and orientation towards the  $B_0$  field (see equation 1.4). The distance and the orientation may change with time and thus leads to local magnetic field oscillations, which just as the CSA stimulates nuclear relaxation. In solution NMR, information on protein motion can then indirectly be obtained from measuring  $R_1$  and  $R_2$  relaxation rates. In order to quantify the ps-ns dynamics of a protein in solution heteronuclear NOEs (Nuclear Overhauser Effects) are generally also measured. The heteronuclear NOEs occur due to dipolar interactions between  $^1\text{H}$  and a hetero atom ( $^{15}\text{N}$  or  $^{13}\text{C}$ ), and as mentioned above dipolar interactions stimulate nuclear relaxation due to protein motions at ps-ns timescales. Site specific measurements of these three parameters can give a full characterization of ps-ns motions in a protein in solution.<sup>46</sup>

In the solid state however, to extract information on dynamics from relaxation rates, coherent effects also need to be considered. The discussion below about effects of coherent contributions to  $R_1$ ,  $R_2$  and  $R_{1\rho}$  relaxation are based on a review by Lewandowski<sup>47</sup>. Spin diffusion is a coherent effect, originating from the incomplete averaging of a strong network of dipolar couplings, i.e. it is difficult to extract information on protein dynamics from relaxation measurements unless spin diffusion is properly suppressed. For site specific measurements of  $R_1$  relaxation rates, which are measured by following the magnetization aligned with the static magnetic field as a function of relaxation delay, spin diffusion will cause magnetization transfer between different sites leading to average relaxation rates over several sites and no site specific information. Since spin diffusion is caused by anisotropic dipolar couplings it can be suppressed. In proteins the strongest dipolar couplings are caused by protons, so diluting the proton network is an efficient way of suppressing spin diffusion. Fast MAS will also suppress spin diffusion as it depends on the term  $\frac{1}{2}(3\cos^2\theta - 1)$ . Generally, a combination of diluting the proton network with deuterium and using fast MAS is used to measure site specific  $R_1$  relaxation rates in proteins. Applying strong radio frequency pulses can also suppress spin diffusion but is generally not helpful as in order to achieve sufficient suppression

very strong radio frequency pulses would have to be used, which could heat up the sample and damage the equipment. For  $^{15}\text{N}$   $R_1$  relaxation measurements, which are studied in chapters 2 and 3, the variant of spin diffusion one needs to worry about is proton-driven spin diffusion (PDS) and it is assisted by  $^1\text{H}$ - $^{15}\text{N}$  dipolar couplings. It has been shown that even in fully protonated proteins PDS is sufficiently suppressed to allow site specific  $^{15}\text{N}$   $R_1$  measurements already at 20 kHz MAS<sup>48-50</sup>. The strength of the dipolar couplings depend on the gyromagnetic ratios of the coupled nuclei leading to that it is more difficult to suppress spin diffusion for  $^{13}\text{C}$  than for  $^{15}\text{N}$  and even more difficult for  $^1\text{H}$ . We investigate the use of  $^1\text{H}$   $R_1$  measurements with 100 kHz MAS, not to measure dynamics, but to study protein – protein interfaces in chapter 2.

While  $R_1$  relaxation rates report on dynamics at picosecond – nanosecond time scales  $R_2$  report on dynamics on nanoseconds – millisecond motions.  $R_2$  relaxation is called spin – spin relaxation or transverse relaxation and occur due to decay of magnetization in the xy-plane, perpendicular to the static magnetic field. An important challenge when measuring  $R_2$  relaxation rates is that coherent effects dominate the decay rates, in particular dipolar dephasing, which originates from strong  $^1\text{H}$ - $^1\text{H}$  dipolar couplings. As mentioned earlier  $^1\text{H}$ - $^1\text{H}$  dipolar couplings are the most difficult to suppress and even if fast MAS (> 60 kHz) and a high degree of deuteration (10% back-exchange of exchangeable protons) is applied it is very challenging to measure  $R_2$  relaxation rates in proteins. It is though possible to measure  $R_{1\rho}$  relaxation to get information on nanosecond – millisecond motion.  $R_{1\rho}$  relaxation rates are measured by following the decay of magnetization under a spin-lock field. For  $^{15}\text{N}$   $R_{1\rho}$  measurement the coherent contributions can be sufficiently suppressed by a > 10 kHz spin-lock pulse and > 45 kHz MAS even in fully protonated proteins<sup>47</sup>. In chapter 3,  $R_1$  and  $R_{1\rho}$  relaxation are investigated and related to protein motion for the protein GB1 in crystals and in a precipitated complex with IgG.

Relaxation dispersion is a method used to study conformational exchange and provide information on short lived conformational states and thereby report on local structure. These motions occur on microsecond –

millisecond timescales and are measured by quantifying  $R_2$  or  $R_{1\rho}$  relaxation rates at varying spin-lock frequencies. However as the spin-lock field strength needs to be varied and one cannot rely on the spin-lock to help suppressing dipolar dephasing, higher levels of deuteration and/or faster MAS speed needs to be applied compared to standard  $R_{1\rho}$  relaxation measurements. Ma *et al.* showed that dipolar dephasing was sufficiently suppressed with 39.5 kHz MAS in a 50% back-exchanged perdeuterated crystalline sample of the small protein ubiquitin.<sup>51</sup> In chapter 4 we show that we can access microsecond motion in the small protein GB1 in a > 300 kDa complex with full length human IgG.

#### **1.4 NMR structure calculations**

NMR, both in solution and in solid state, is a powerful tool for solving structures of biomolecules. Traditionally this is a very time consuming process but recent developments in NMR instrumentation and automation of structure calculation software have significantly shortened the time it takes from the first NMR experiments until a final structure can be determined. In order to determine a structure using NMR it is required to assign resonances relating to the atoms of the protein and to obtain distance restraints. In solution NMR the distance restraints are typically obtained from 2D and/or 3D NOESY (Nuclear Overhauser Effect Spectroscopy) experiments. This is often supplemented with torsion angle restraints, that for example can be calculated from the chemical shifts using the software TALOS+<sup>52</sup>. It is also possible to add restraints obtained from other types of NMR experiments and if there is information available from other sources that would aid the calculation it can also be added. There are several different software packages available for structure calculations as compared in the Critical Assessment of Automated Structure Determination of Proteins from NMR Data (CASD NMR)<sup>53</sup>, some of which use the traditional method described here and some of which calculate the structure based on chemical shifts.

Before the fast MAS frequencies that are currently available could be achieved, structure calculations in solid state NMR were often relying on

$^{13}\text{C}$ - $^{13}\text{C}$  distances rather than the  $^1\text{H}$ - $^1\text{H}$  distances commonly used in solution NMR. However with MAS speeds of 100 kHz and above it is now possible to use a similar approach as in solution NMR which has been demonstrated with fully protonated proteins<sup>54</sup> and a combination of 100% back exchanged perdeuterated protein for  $^1\text{H}^{\text{N}}$ - $^1\text{H}^{\text{N}}$  distance restraints and partly labelled protein for distance restraints between methyl groups<sup>55</sup>. In the work presented here UNIO ATNOS-CANDID, with CYANA as molecular dynamics software was used for the structure calculation of teixobactin presented in chapter 5.

#### *1.4.1 Resonance assignments in solution and solid state*

There are several different approaches to obtain full chemical shift assignments of proteins and peptides. For smaller peptides (up to around 20-30 residues), it might be sufficient to use 2D experiments with unlabelled material in solution. Figure 1.9 shows the approach for assignments using 2D spectra. The  $^1\text{H}$ - $^1\text{H}$  COrelation Spectroscopy (COSY) experiment gives a walk through each residue, where the cross-peaks that show up are coupled. The diagonal shows peaks of the protons with itself. The example in the figure is alanine, where the first diagonal peak from the top is  $\text{H}\beta$ - $\text{H}\beta$ , following the dotted line leads to  $\text{H}\beta$ - $\text{H}\alpha$ , horizontally to the diagonal is  $\text{H}\alpha$ - $\text{H}\alpha$ , following the dotted line vertically leads to  $\text{H}\alpha$ - $\text{H}^{\text{N}}$  and finally vertical to the diagonal shows  $\text{H}^{\text{N}}$ - $\text{H}^{\text{N}}$ . The same information can be obtained from the  $^1\text{H}$ - $^1\text{H}$  Total COrelation Spectroscopy (TOCSY) experiment, but in a TOCSY all correlations between spins in a spin system is shown for each proton. This approach doesn't give any interresidue information, which has to be obtained from interresidual  $\text{H}^{\text{N}}$ - $\text{H}^{\text{N}}$  peaks in  $^1\text{H}$ - $^1\text{H}$  NOESY spectra. If a peptide chain contains many residues of the same amino acid unambiguous sequential assignments becomes difficult.



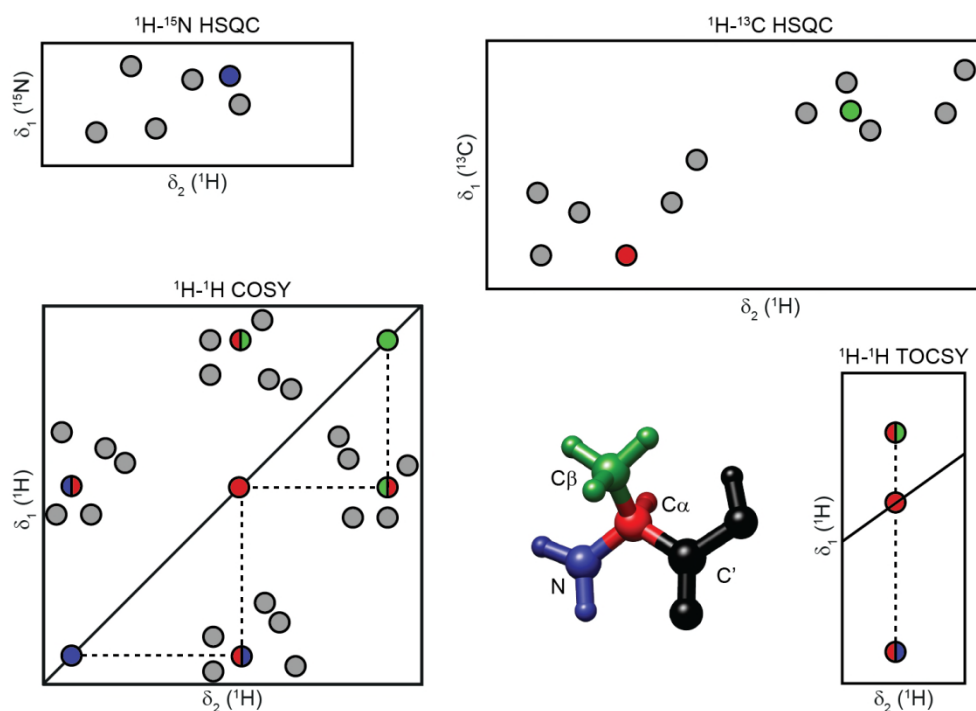


**Figure 1.9.** Schematic drawing of 2D assignment spectra used in solution NMR. Peaks resulting from alanine are highlighted in the figure.

If labelling is possible the assignment becomes easier, as 3D experiments can be recorded. Figure 1.10 shows an approach based on a combination of two 3D experiments. CBCANH gives the correlations between the NH group of residue  $n$  and the  $C\alpha$  (positive peaks, red-yellow in fig1.10) and  $C\beta$  (negative peaks, green-blue in fig 1.10) from residues  $n$  and  $n-1$ , while CACB(CO)NH only gives the peaks between an NH group of residue  $n$  and the  $C\alpha$  and  $C\beta$  from residue  $n-1$ . With these two experiments a backbone walk through the peptide chain to achieve assignments for all N,  $H^N$ ,  $C\alpha$  and  $C\beta$  can be performed. It is often required, in larger systems or if the peptide chain contains many similar residues, to acquire additional spectra connecting the  $C'$  to  $H^N$  as the chemical shift dispersion of  $C'$  is often larger than that of  $C\alpha$ . In this respect it should also be mentioned that it is useful to assign atoms that are not directly needed for the structure calculation (e.g.  $C'$ ) since chemical shifts also contain structural information in itself (which is discussed in chapter 5). If a 3D hCCH TOCSY is acquired as well, the  $H\alpha$ ,  $H\beta$  and side chain carbons and protons can also be assigned.

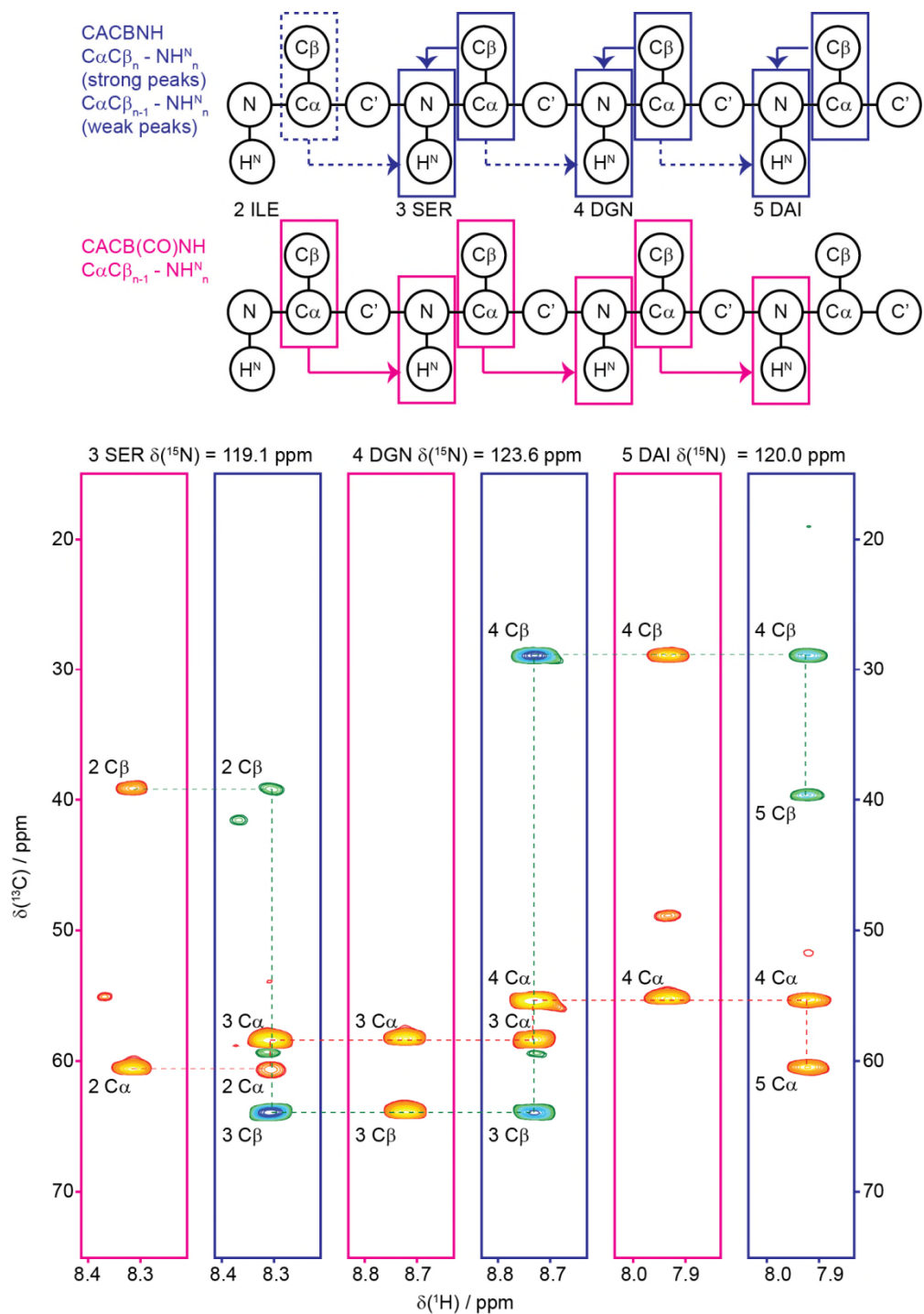


**Figure 1.10.** Example strips from solution NMR 3D assignment spectra for  $[\text{U-}^{13}\text{C}, ^{15}\text{N}]$ teixobactin in DPC micelles. Spectra acquired at 700 MHz  $^1\text{H}$  Larmor frequency. DGN = D-Glutamine, DAI = D-allo-Isoleucine. The colour gradient from red to yellow represents the intensities of positive peaks. The colour gradient from green to blue represents the intensities of negative peaks.

In proton detected experiments in the solid state similar 3D experiments can be recorded. In figure 1.11 example strips of the assignment spectra for  $[\text{U-}^{13}\text{C}, ^{15}\text{N}]$ teixobactin in complex with natural abundance lipid II are shown. The experiments hCANH and hCONH are purely based on CP

transfers whereas the hCOCAHA uses dipolar recoupling enhanced by amplitude modulation (DREAM)<sup>56</sup> transfer between C' and C $\alpha$ . The DREAM also transfers to the C $\beta$  from the C' (however the spectrum was folded and therefore only C $\alpha$  was considered in this case), and hence also gives the assignments for C $\beta$  and H $\beta$ .

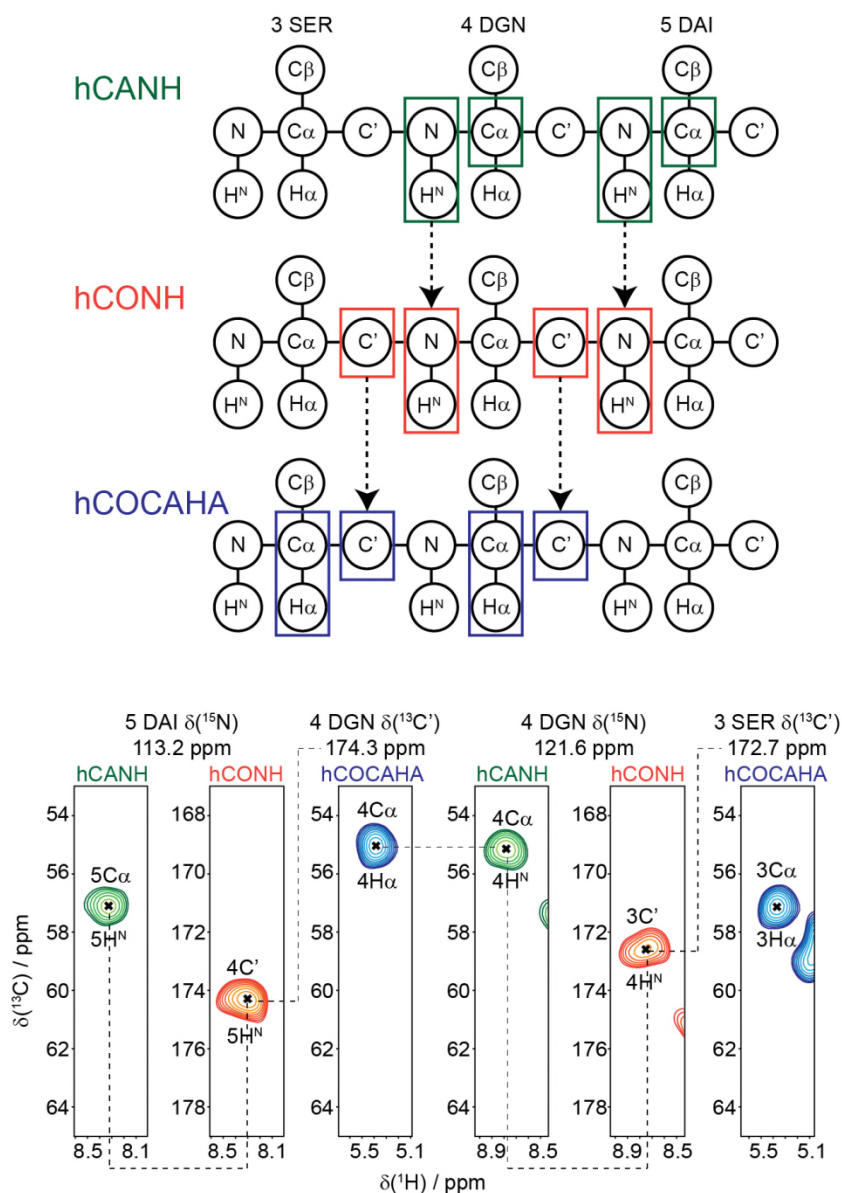


**Figure 1.11.** Example strips from assignment spectra of [U- $^{13}\text{C}$ ,  $^{15}\text{N}$ ]teixobactin in a sedimented complex with natural abundance lipid II in deuterated DPC micelles. Spectra acquired at 600 MHz  $^1\text{H}$  Larmor frequency with 90 kHz MAS. DGN = D-glutamine, DAI = D-*allo*-isoleucine.

DREAM is a type of dipolar recoupling sequence. In contrast to the CP transfer that recouples heteronuclear dipolar couplings, DREAM recouples

homonuclear dipolar couplings by fulfilling the double quantum HOmonuclear ROtary Resonance (HORROR) condition:

$$\omega_1 = \frac{\omega_{rot}}{2} \quad (1.9)$$

where  $\omega_1$  is the nutation frequency of the adiabatic pulse in the DREAM experiment. Another homonuclear recoupling technique called radio frequency driven recoupling (RFDR)<sup>57</sup> is used to obtain  $^1\text{H} - ^1\text{H}$  distance restraints, similar to NOESY in solution NMR. In an RFDR experiment a train of rotor synchronized  $n$  pulses is applied on the  $^1\text{H}$  channel to recouple the homonuclear dipolar couplings, the longer the train of pulses is the further the magnetization is transferred.

#### 1.4.2 CYANA libraries

When calculating a 3D structure based on NMR data it is necessary to use a molecular dynamics software. CYANA performs molecular dynamics calculations using torsion angle dynamics<sup>58</sup>. The degrees of freedom are based on the number of torsion angles, which are much smaller than the Cartesian coordinates and hence CYANA is much faster than molecular dynamics software that uses Cartesian space dynamics.

Many lipid II binders contain peptides with non-standard amino acid residues and in order to perform structure calculations on these kinds of molecules library entries for a molecular dynamics software need to be produced. In order to produce library entries for non-standard residues it is necessary to understand how CYANA libraries work. Torsion angles are defined in CYANA library files following a tree structure with a base rigid body that is fixed in space and  $n$  rigid bodies that are connected by  $n$  rotatable bonds. The rigid base is the amino acid backbone starting at the N-terminus, it then branches out and terminates at the end of the side-chains and C-terminus<sup>58</sup>. The CYANA library files are built as shown in figure 1.12a. The first line contains the short name of the residue, in this example ALA (alanine), followed by the number of torsion angles (4), the number of atoms (14), the first atom included in the residue (3) which means that atom 1 and 2 belong to the previous residue in the polypeptide chain. The last number of the first line represents the last

atom included in the residue (13), which means that atom number 14 belongs to the next residue in the chain. The peptide bonds are defined like this, so that each entry in the library representing a standard amino acid starts with C and O of the previous residue and ends with N of the following residue. The second line in the library entry defines the first torsion angle, which for all standard amino acids is  $\omega$  (OMEGA). Each angle is defined by exactly 4 atoms and for side chain angles also a fifth atom is included which represents the last atom being affected by changing the angle. For  $\omega$  the 4 atoms defining it are  $C_{n-1}$  (2),  $O_{n-1}$  (1),  $N_n$  (3) and  $H_n$  (4), since it is a backbone torsion angle the fifth number is 0. Continuing down the library entry we see the other three torsion angles of alanine  $\phi$  (PHI),  $\chi_1$ (CHI1) and  $\psi$  (PSI), where  $\chi_1$  is the only side chain torsion angle and hence has a non-zero entry as the fifth number (11) representing HB3 of the methyl group. Any of the HB atoms could be used here or QB, the pseudo atom which is positioned at the centre of the HB1, HB2 and HB3 atoms. Pseudo atoms are used to represent groups of protons that are connected to the same heavy atom or symmetrical protons in aromatic rings. Pseudo atoms can also be used for methyl groups that are connected to the same carbon, such as in valine or leucine. After the angles are defined all the atoms are defined, first the number of the atom, then name, then the atom type, the coordinates, which other atoms it is bonded to and the last number indicates the corresponding pseudo atom (0 for atoms where there is no corresponding pseudo atom).<sup>58</sup>

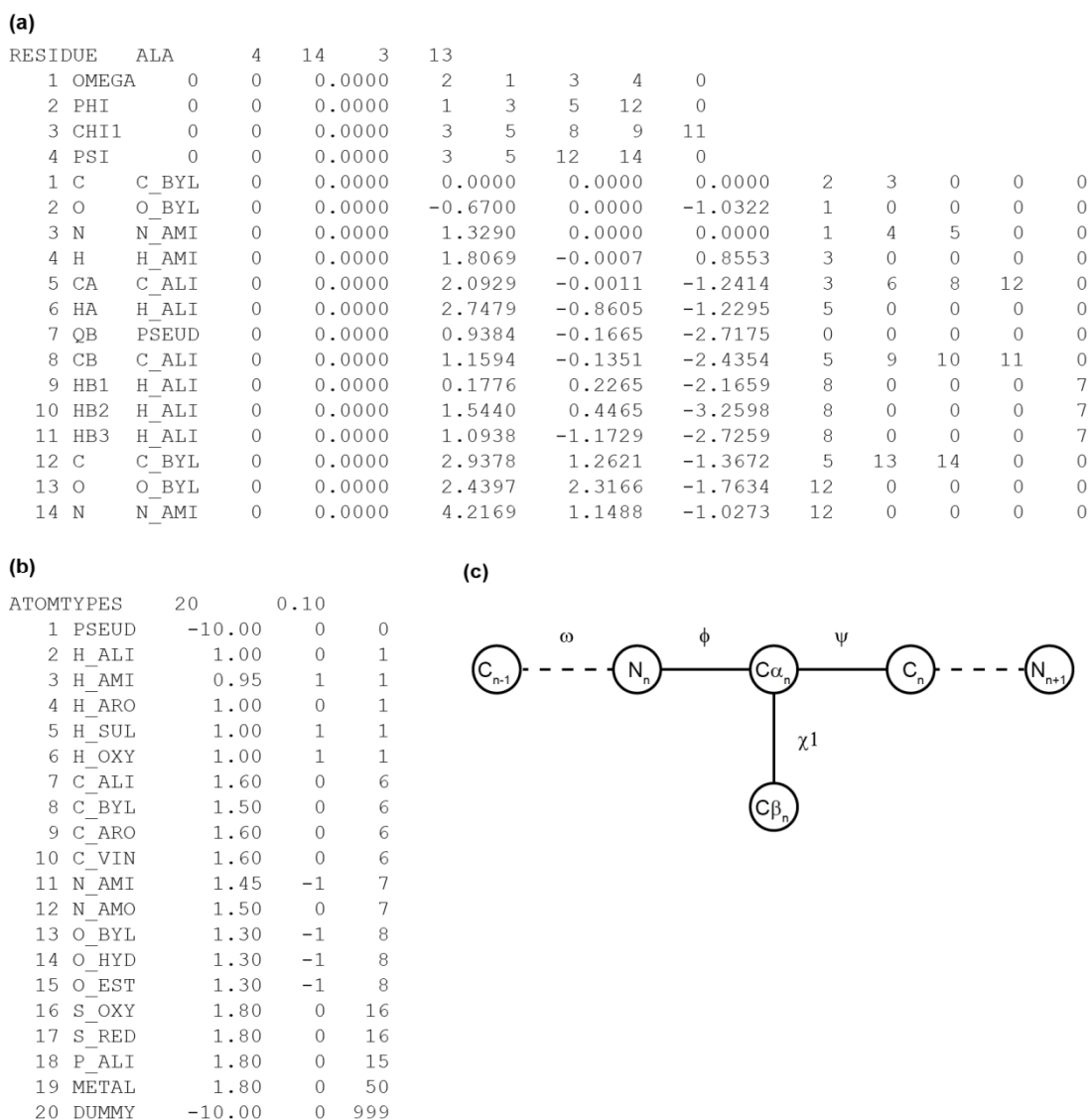
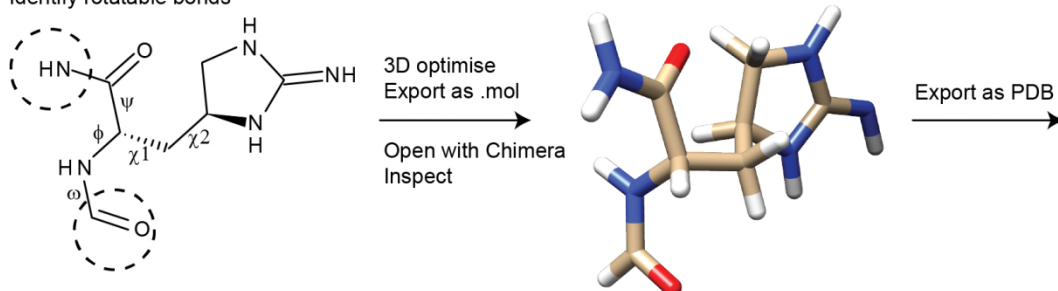


**Figure 1.12.** Structure of CYANA library entry<sup>58</sup>. (a) example of library entry for the amino acid alanine. (b) Definition of atom types used in Cyana. (c) Tree structure of alanine.

The different atom types used in CYANA are shown in figure 1.12b. As CYANA doesn't use a complete physical force field the atom type only specifies the repulsion radius, whether or not an atom can be involved in a hydrogen bond (0 for no, 1 for protons that can form hydrogen bonds and -1 for hydrogen bond acceptors). The last column in figure 1.12b is for which chemical element the atom is (1 for hydrogen, 6 for carbon etc.). Figure 1.12c shows a schematic view of how the torsion angles are defined for alanine. Each angle is defined by two atoms before the angle and two atoms after, as described in the example of the OMEGA angle above.<sup>58</sup>

The standard CYANA library includes all standard amino acid residues, RNA bases and DNA bases but if structure calculations with non-standard residues are to be performed, library entries for these have to be produced. Recently a software called Cylib<sup>59</sup> was released. Cylib can convert any molecular topology description from the PDB Chemical Component Dictionary (CCD) into CYANA library entries. This makes it much easier to perform structure calculations of peptides containing non-standard residues as it is tedious process to produce library entries manually. There are however cases where Cylib doesn't work; (i) if there is no entry in the PDB CCD or (ii) if the connection between residues is not a standard peptide bond. In these cases an entry has to be created manually. Figure 1.13 shows the steps needed to prepare a new library entry. Here L-*allo*-enduracidine was used as example, which is an unusual amino acid present in teixobactin. The first step is to obtain starting coordinates and connections for all the atoms in the new residue. This can be done by drawing it in any molecule drawing software and convert it into a 3D drawing. Then it needs to be saved in a format that UCSF Chimera<sup>60</sup> can read, for example as a mol file. If there is an available 3D structure of the residue or a similar residue this first step can be skipped and one can download the 3D structure and add the overlapping atoms to the connecting residues (in dotted circles at the top of Figure 2), which can be done in UCSF Chimera. The file should then be saved as a PDB file, which can be read by MOLMOL<sup>61</sup> and a file containing coordinates and connections can be created. The final step is to manually rearrange and rename the atoms, add angles, pseudo atoms and add atom types. It is important that the atoms and angles are arranged according to the tree structure of CYANA library files.

Draw chemical structure including connecting atoms  
Identify rotatable bonds



Open with MOLMOL  
-CalcBond, -WriteLib

RESIDUE	UNK		0	27	1	27	0						
1 N1	N		0	0.0000	20.5550	-9.9190	-0.8910	2	3	0	0	0	0
2 H3	H		0	0.0000	21.0410	-10.8540	-0.8760	1	0	0	0	0	0
3 C6	C		0	0.0000	19.2750	-9.8560	-1.1120	1	4	26	0	0	0
4 N4	N		0	0.0000	18.5040	-10.9730	-1.3330	3	5	6	0	0	0
...													
...													
...													
24 H7	H		0	0.0000	16.8690	-8.4730	-2.3970	23	0	0	0	0	0
25 H8	H		0	0.0000	16.5180	-8.5590	-0.6190	23	0	0	0	0	0
26 N3	N		0	0.0000	18.5830	-8.6650	-1.1420	3	23	27	0	0	0
27 H9	H		0	0.0000	19.0430	-7.7320	-0.9760	26	0	0	0	0	0

Open with text editor

-Rearrange and rename atoms, -Remove any extra atoms, -Add atom types, -Add pseudo atoms, -Add angles

RESIDUE	END	5	26	3	25								
#L-allo-Enduracidine													
1 OMEGA		0	0	0.0000	2	1	3	4	0				
2 PHI		0	0	0.0000	1	3	5	24	0				
3 CHI1		0	0	0.0000	3	5	6	7	22				
4 CHI2		0	0	0.0000	5	6	7	19	19				
5 PSI		0	0	0.0000	3	5	24	26	0				
1 C	C_BYL	0	0.0000	14.1720	-13.0140	-1.8850	2	3	0	0	0	0	0
2 O	O_BYL	0	0.0000	14.6650	-13.5210	-0.9010	1	0	0	0	0	0	0
3 N	N_AMI	0	0.0000	14.1980	-11.6420	-2.0430	1	4	5	0	0	0	0
4 H	H_AMI	0	0.0000	13.7880	-11.2530	-2.9320	3	0	0	0	0	0	0
...													
...													
...													
21 HB3	H_ALI	0	0.0000	16.5470	-12.0350	-1.1950	6	0	0	0	0	22	
22 QB	PSEUD	0	0.0000	16.6185	-11.3680	-0.5840	0	0	0	0	0	0	0
23 HA	H_ALI	0	0.0000	14.3710	-11.1130	0.0000	5	0	0	0	0	0	0
24 C	C_BYL	0	0.0000	14.4340	-9.3490	-1.2390	5	25	26	0	0	0	0
25 O	O_BYL	0	0.0000	15.3180	-8.5680	-1.5050	24	0	0	0	0	0	0
26 N	N_AMI	0	0.0000	13.1270	-8.9050	-1.1980	24	0	0	0	0	0	0

**Figure 1.13.** Stepwise explanation for how to create Cyana library entries for non-standard amino acids. Here with L-*allo*-enduracidine as example.

#### 1.4.3 Structure calculations using UNIO-ATNOS CANDID

With (almost) complete chemical shift assignments and functioning molecular dynamics software the final consideration for structure calculations is distance restraints. Generally, NOESY spectra are used for this since NOE transfer is based on dipolar couplings, which are distance



dependent and the intensity of the cross-peaks in NOESY spectra will be proportional to the distance between two protons.

To obtain distance restraints from NOE spectra in solution NMR the chemical shifts of the two protons involved in the cross peak needs to be unambiguously assigned. As the chemical shift range of protons in proteins is fairly small < 15 ppm and the accuracy of which NOE cross peaks can be measured is limited it is very difficult to unambiguously assign the peaks. By using 3D HSQC-NOESY spectra, which are resolved through an additional  $^{13}\text{C}$  or  $^{15}\text{N}$  chemical shift, it becomes easier than for 2D  $^1\text{H}$  –  $^1\text{H}$  NOESY experiments but is still very challenging. NOESY spectra can also be quite noisy and contain artefacts making the process even more challenging. Traditionally picking and assigning NOE cross peaks was an iterative process where a preliminary 3D structure was calculated from a limited amount of unambiguously assigned peaks. The preliminary 3D structure was then used to identify more peaks. Luckily, due to a lot of effort into software development it is now much easier and faster to perform NMR structure calculations. There are several software packages that can achieve high quality 3D structures of proteins with unassigned peak lists from NOESY spectra compared in the CASD-NMR<sup>53</sup>. Of the software packages tested in that study only two submitted results based on raw spectra as input, UNIO and Ponderosa. Using raw spectra as input is very appealing as it eliminates time consuming and error prone peak picking. As previously mentioned UNIO ATNOS-CANDID was used for the structure calculation of teixobactin presented chapter 5.

UNIO includes different algorithms for backbone assignments (MATCH)<sup>62</sup>, side-chain assignments (ATNOS-ASCAN)<sup>63,64</sup> and NOE assignments and structure calculations (ATNOS-CANDID)<sup>63,65</sup>. In a structure calculation with UNIO ATNOS-CANDID in combination with a molecular dynamics software (CYANA or other) the traditional method is performed automatically in a much less error prone fashion. The software performs the calculation in a way so that in the first cycle ATNOS picks peaks based only on the chemical shift list containing resonance assignments supplied by the user, similar to how a manual peak picking would be attempted. The validated peaks are sent to CANDID which assigns them

and transforms them into distance restraints for CYANA and a preliminary structure is calculated. This structure is then used by ATNOS to identify more peaks and by CANDID to assign them and add more distance restraints for the next structure calculation, the structure based criteria for peak validation in ATNOS is loosened up, while the acceptance for NOE assignment and distance restraints by CANDID is tightened. Generally 7 cycles are performed in a standard structure calculation using UNIO ATNOS-CANDID.

Two important elements that were incorporated in CANDID are network anchoring and constraint-combination. In network anchoring the assignment for each NOE cross-peak is weighted by how well it fits in a network including all other NOE assignments. This works because any network of correct NOE cross-peak assignments can be seen as a self-consistent set. Constraint combination is used to combine several distance restraints into one in order to reduce the risk of artefacts influencing the structure calculation. This is especially important for long-distance restraints that have a larger impact on the structure calculation.<sup>65</sup>

The same procedure works in solid state NMR, but RFDR spectra are normally used instead of NOESY. There are however not yet any published structures calculated from solid state NMR data where raw spectra have been used as input. A few structures have recently been published using the "solution NMR" approach in UNIO with unassigned peak lists from spectra of fully protonated proteins in solid state NMR<sup>54</sup>.

## 1.5 References

- (1) Gronenborn, A.; Filpula, D.; Essig, N.; Achari, A.; Whitlow, M.; Wingfield, P.; Clore, G. *Science* (80-. ). **1991**, 253 (5020), 657.
- (2) Frericks Schmidt, H. L.; Sperling, L. J.; Gao, Y. G.; Wylie, B. J.; Boettcher, J. M.; Wilson, S. R.; Rienstra, C. M. *J. Phys. Chem. B* **2007**, 111 (51), 14362.
- (3) Franks, W. T.; Wylie, B. J.; Schmidt, H. L. F.; Nieuwkoop, A. J.;

- Mayrhofer, R.-M.; Shah, G. J.; Graesser, D. T.; Rienstra, C. M. *Proc. Natl. Acad. Sci. U. S. A.* **2008**, *105* (12), 4621.
- (4) Zhou, D. H.; Shea, J. J.; Nieuwkoop, A. J.; Franks, W. T.; Wylie, B. J.; Mullen, C.; Sandoz, D.; Rienstra, C. M. *Angew. Chemie - Int. Ed.* **2007**, *46* (44), 8380.
- (5) Björck, L.; Kronvall, G. *J. Immunol.* **1984**, *133* (2), 969.
- (6) Carter, P. J. *Exp. Cell Res.* **2011**, *317* (9), 1261.
- (7) O'Neill, J. *Rev. Antimicrob. Resist.* **2014**, <https://amr-review.org>
- (8) Fleming, A. *Br. J. Exp. Pathol.* **1929**, *10* (31), 226.
- (9) Wise, E. M.; Park, J. T. *Proc. Natl. Acad. Sci. U. S. A.* **1965**, *54* (1), 75.
- (10) Tipper, D. J.; Strominger, J. L. *Proc. Natl. Acad. Sci. U. S. A.* **1965**, *54* (4), 1133.
- (11) Vollmer, W.; Blanot, D.; de Pedro, M. a. *FEMS Microbiol. Rev.* **2008**, *32* (2), 149.
- (12) Vollmer, W. *FEMS Microbiol. Rev.* **2008**, *32* (2), 287.
- (13) Teo, A.; Roper, D. *Antibiotics* **2015**, *4* (4), 495.
- (14) Oppedijk, S. F.; Martin, N. I.; Breukink, E. *Biochim. Biophys. Acta - Biomembr.* **2016**, *1858* (5), 947.
- (15) Bugg, T. D. H.; Wright, G. D.; Dutka-Malen, S.; Arthur, M.; Courvalin, P.; Walsh, C. T. *Biochemistry* **1991**, *30* (43), 10408.
- (16) Hsu, S.-T. D.; Breukink, E.; Tischenko, E.; Lutters, M. A. G.; de Kruijff, B.; Kaptein, R.; Bonvin, A. M. J. J.; van Nuland, N. A. J. *Nat. Struct. Mol. Biol.* **2004**, *11* (10), 963.
- (17) Hsu, S. T. D.; Breukink, E.; Bierbaum, G.; Sahl, H. G.; De Kruijff, B.; Kaptein, R.; Van Nuland, N. A. J.; Bonvin, A. M. J. J. *J. Biol. Chem.* **2003**, *278* (15), 13110.

- (18) Cudic, P.; Kranz, J. K.; Behenna, D. C.; Kruger, R. G.; Tadesse, H.; Wand, A. J.; Veklich, Y. I.; Weisel, J. W.; McCafferty, D. G. *Proc. Natl. Acad. Sci. U. S. A.* **2002**, 99 (11), 7384.
- (19) Mygind, P. H.; Fischer, R. L.; Schnorr, K. M.; Hansen, M. T.; Sönksen, C. P.; Ludvigsen, S.; Raventós, D.; Buskov, S.; Christensen, B.; De Maria, L.; Taboureau, O.; Yaver, D.; Elvig-Jørgensen, S. G.; Sørensen, M. V.; Christensen, B. E.; Kjaerulff, S.; Frimodt-Møller, N.; Lehrer, R. I.; Zasloff, M.; Kristensen, H.-H. *Nature* **2005**, 437 (7061), 975.
- (20) Schneider, T.; Kruse, T.; Wimmer, R.; Wiedemann, I.; Sass, V.; Pag, U.; Jansen, A.; Nielsen, A. K.; Mygind, P. H.; Raventos, D. S.; Neve, S.; Ravn, B.; Bonvin, A. M. J. J.; De Maria, L.; Andersen, A. S.; Gammelgaard, L. K.; Sahl, H.-G.; Kristensen, H.-H. *Science* **2010**, 328 (5982), 1168.
- (21) Levitt, M. *Spin dynamics: basics of nuclear magnetic resonance*, 2nd ed.; Wiley, 2008.
- (22) Keeler, J. *Understanding NMR Spectroscopy*, 2nd ed.; Wiley, 2002.
- (23) Duer, M. J. *Introduction to Solid-State NMR Spectroscopy*; Wiley-Blackwell, 2004.
- (24) Rule, G. S.; Hitchens, K. T. *Fundamentals of Protein NMR Spectroscopy*; Springer, 2006.
- (25) Lowe, I. J. *Phys. Rev. Lett.* **1959**, 2 (7), 285.
- (26) Andrew, E. R.; Bradbury, A.; Eades, R. G. *Nature* **1958**, 182 (4650), 1659.
- (27) Pines, A.; Gibby, M. G.; Waugh, J. S. *J. Chem. Phys.* **1973**, 59 (2), 569.
- (28) Wishart, D. S.; Bigam, C. G.; Yao, J.; Abildgaard, F.; Dyson, H. J.; Oldfield, E.; Markley, J. L.; Sykes, B. D. *J. Biomol. NMR* **1995**, 6 (2), 135.

- (29) Markley, J. L.; Bax, A.; Arata, Y.; Hilbers, C. W.; Kaptein, R.; Sykes, B. D.; Wright, P. E.; Wüthrich, K. *J. Biomol. NMR* **1998**, *12* (1), 1.
- (30) Gardiennet, C.; Schütz, A. K.; Hunkeler, A.; Kunert, B.; Terradot, L.; Böckmann, A.; Meier, B. H. *Angew. Chemie Int. Ed.* **2012**, *51* (31), 7855.
- (31) Loquet, A.; Sgourakis, N. G.; Gupta, R.; Giller, K.; Riedel, D.; Goosmann, C.; Griesinger, C.; Kolbe, M.; Baker, D.; Becker, S.; Lange, A. *Nature* **2012**, 486 (7402), 276.
- (32) Lu, M.; Hou, G.; Zhang, H.; Suiter, C. L.; Ahn, J.; Byeon, I.-J. L.; Perilla, J. R.; Langmead, C. J.; Hung, I.; Gor'kov, P. L.; Gan, Z.; Brey, W.; Aiken, C.; Zhang, P.; Schulten, K.; Gronenborn, A. M.; Polenova, T. *Proc. Natl. Acad. Sci.* **2015**, *112* (47), 14617.
- (33) Mainz, A.; Religa, T. L.; Sprangers, R.; Linser, R.; Kay, L. E.; Reif, B. *Angew. Chemie Int. Ed.* **2013**, *52* (33), 8746.
- (34) Barbet-Massin, E.; Huang, C.-T.; Daebel, V.; Hsu, S.-T. D.; Reif, B. *Angew. Chemie Int. Ed.* **2015**, *54* (14), 4367.
- (35) Jehle, S.; Rajagopal, P.; Bardiaux, B.; Markovic, S.; Kühne, R.; Stout, J. R.; Higman, V. A.; Klevit, R. E.; van Rossum, B.-J.; Oschkinat, H. *Nat. Struct. Mol. Biol.* **2010**, *17* (99), 1037.
- (36) Lamley, J. M.; Iuga, D.; Öster, C.; Sass, H.-J.; Rogowski, M.; Oss, A.; Past, J.; Reinhold, A.; Grzesiek, S.; Samoson, A.; Lewandowski, J. R. *J. Am. Chem. Soc.* **2014**, *136* (48), 16800.
- (37) Lamley, J. M.; Öster, C.; Stevens, R. A.; Lewandowski, J. R. *Angew. Chemie Int. Ed.* **2015**, *54* (51), 15374.
- (38) Hoop, C. L.; Lin, H.-K. H.-K.; Kar, K.; Magyarfalvi, G.; Lamley, J. M.; Boatz, J. C. J. C.; Mandal, A.; Lewandowski, J. R.; Wetzel, R.; van der Wel, P. C. A. P. C. A. *Proc. Natl. Acad. Sci.* **2016**, *113* (6), 201521933.
- (39) Good, D. B.; Wang, S.; Ward, M. E. M. E.; Struppe, J.; Brown, L. S.

- L. S.; Lewandowski, J. R.; Ladizhansky, V. *J. Am. Chem. Soc.* **2014**, *136* (7), 2833.
- (40) Ladizhansky, V. *BBA - Proteins Proteomics* **2017**, No. July.
- (41) Quinn, C. M.; Polenova, T. *Q. Rev. Biophys.* **2017**, *50* (May), e1.
- (42) Linser, R.; Dasari, M.; Hiller, M.; Higman, V.; Fink, U.; Lopez del Amo, J.-M.; Markovic, S.; Handel, L.; Kessler, B.; Schmieder, P.; Oesterhelt, D.; Oschkinat, H.; Reif, B. *Angew. Chemie Int. Ed.* **2011**, *50* (19), 4508.
- (43) Barbet-Massin, E.; Pell, A. J.; Retel, J. S.; Andreas, L. B.; Jaudzems, K.; Franks, W. T.; Nieuwkoop, A. J.; Hiller, M.; Higman, V.; Guerry, P.; Bertarello, A.; Knight, M. J.; Felletti, M.; Le Marchand, T.; Kotelovica, S.; Akopjana, I.; Tars, K.; Stoppini, M.; Bellotti, V.; Bolognesi, M.; Ricagno, S.; Chou, J. J.; Griffin, R. G.; Oschkinat, H.; Lesage, A.; Emsley, L.; Herrmann, T.; Pintacuda, G. *J. Am. Chem. Soc.* **2014**, *136* (35), 12489.
- (44) Wickramasinghe, N. P.; Kotecha, M.; Samoson, A.; Past, J.; Ishii, Y. *J. Magn. Reson.* **2007**, *184* (2), 350.
- (45) Böckmann, A.; Ernst, M.; Meier, B. H. *J. Magn. Reson.* **2015**, *253*, 71.
- (46) Kleckner, I. R.; Foster, M. P. *Biochim. Biophys. Acta - Proteins Proteomics* **2011**, *1814* (8), 942.
- (47) Lewandowski, J. R. *Acc. Chem. Res.* **2013**, *46* (9), 2018.
- (48) Krushelnitsky, A.; Bräuniger, T.; Reichert, D. *J. Magn. Reson.* **2006**, *182* (2), 339.
- (49) Chevelkov, V.; Diehl, A.; Reif, B. *J. Chem. Phys.* **2008**, *128* (5), 52316.
- (50) Giraud, N.; Blackledge, M.; Böckmann, A.; Emsley, L. *J. Magn. Reson.* **2007**, *184* (1), 51.
- (51) Ma, P.; Haller, J. D.; Zajakala, J.; Macek, P.; Sivertsen, A. C.;

- Willbold, D.; Boisbouvier, J.; Schanda, P. *Angew. Chem. Int. Ed. Engl.* **2014**, 53 (17), 4312.
- (52) Shen, Y.; Delaglio, F.; Cornilescu, G.; Bax, A. *J. Biomol. NMR* **2010**, 44 (4), 213.
- (53) Rosato, A.; Vranken, W.; Fogh, R. H.; Ragan, T. J.; Tejero, R.; Pederson, K.; Lee, H. W.; Prestegard, J. H.; Yee, A.; Wu, B.; Lemak, A.; Houliston, S.; Arrowsmith, C. H.; Kennedy, M.; Acton, T. B.; Xiao, R.; Liu, G.; Montelione, G. T.; Vuister, G. W. *J. Biomol. NMR* **2015**, 62 (4), 413.
- (54) Andreas, L. B.; Jaudzems, K.; Stanek, J.; Lalli, D.; Bertarello, A.; Le Marchand, T.; Cala-De Paepe, D.; Kotelovica, S.; Akopjana, I.; Knott, B.; Wegner, S.; Engelke, F.; Lesage, A.; Emsley, L.; Tars, K.; Herrmann, T.; Pintacuda, G. *Proc. Natl. Acad. Sci.* **2016**, 113 (33), 9187.
- (55) Agarwal, V.; Penzel, S.; Szekely, K.; Cadalbert, R.; Testori, E.; Oss, A.; Past, J.; Samoson, A.; Ernst, M.; Beckmann, A.; Meier, B. H. *Angew. Chemie - Int. Ed.* **2014**, 53 (45), 12253.
- (56) Verel, R.; Baldus, M.; Ernst, M.; Meier, B. H. *Chem. Phys. Lett.* **1998**, 287 (3–4), 421.
- (57) Bennett, A. E.; Griffin, R. G.; Ok, J. H.; Vega, S. *J. Chem. Phys.* **1992**, 96 (11), 8624.
- (58) Güntert, P.; Mumenthaler, C.; Wüthrich, K. *J. Mol. Biol.* **1997**, 273 (1), 283.
- (59) Yilmaz, E. M.; Güntert, P. *J. Biomol. NMR* **2015**, 63 (1), 21.
- (60) Pettersen, E. F.; Goddard, T. D.; Huang, C. C.; Couch, G. S.; Greenblatt, D. M.; Meng, E. C.; Ferrin, T. E. *J. Comput. Chem.* **2004**, 25 (13), 1605.
- (61) Koradi, R.; Billeter, M.; Wüthrich, K. *J. Mol. Graph.* **1996**, 14 (1), 51.

- (62) Volk, J.; Herrmann, T.; Wüthrich, K. *J. Biomol. NMR* **2008**, 41 (3), 127.
- (63) Herrmann, T.; Güntert, P.; Wüthrich, K. *J. Biomol. NMR* **2002**, 24 (3), 171.
- (64) Fiorito, F.; Herrmann, T.; Damberger, F. F.; Wüthrich, K. *J. Biomol. NMR* **2008**, 42 (1), 23.
- (65) Herrmann, T.; Güntert, P.; Wüthrich, K. *J. Mol. Biol.* **2002**, 319 (1), 209.



## **2 Characterization of protein-protein interfaces in large complexes by solid state NMR solvent paramagnetic relaxation enhancements**

This chapter was accepted for publication as:

*Characterization of protein-protein interfaces in large complexes by solid state NMR solvent paramagnetic relaxation enhancements*, Öster, C.; Kosol, S.; Hartlmüller, C.; Lamley, J. M.; Iuga, D.; Oss, A.; Org, M.-L.; Vanatalu, K.; Samoson, A.; Madl, T.; Lewandowski, J. R. *J. Am. Chem. Soc.* **2017**, 139 (35), 12165

### **2.1 Abstract**

Solid-state NMR is becoming a viable alternative for obtaining information about structures and dynamics of large biomolecular complexes including ones that are not accessible to other high resolution biophysical techniques. In this context, methods for probing protein-protein interfaces at atomic resolution are highly desirable. Solvent paramagnetic relaxation enhancements (sPREs) proved to be a powerful method for probing protein-protein interfaces in large complexes in solution but have not been employed towards this goal in the solid state. We demonstrate that  $^1\text{H}$  and  $^{15}\text{N}$  relaxation-based sPREs provide a powerful tool for characterizing intermolecular interactions in large assemblies in the solid state. We present approaches for measuring sPREs in practically the entire range of magic angle spinning frequencies used for biomolecular studies and discuss their benefits and limitations. We validate the approach on crystalline GB1 with our experimental results in good agreement with theoretical predictions. Finally, we use sPREs to characterize protein-protein interfaces in the GB1 complex with immunoglobulin (IgG). Our results suggest the potential existence of an additional binding site and provide new insights into GB1:IgG complex structure that amend and revise the current model available from studies with IgG fragments. We demonstrate sPREs as a practical, widely applicable, robust and very sensitive technique for determining

intermolecular interaction interfaces in large biomolecular complexes in the solid state.

## 2.2 Introduction

Knowledge of protein-protein interactions is essential for the understanding of many biological processes. However, atomic-resolution structural characterization of many important biomolecular complexes is impeded by their size, solubility or ability to form crystals, preventing the application of standard methods such as solution NMR and X-ray crystallography. Solid state NMR is an emerging alternative for studies of large protein assemblies,<sup>1-10</sup> with new technologies and methods leading to continuously improved sensitivity and signal resolution for atomic level structural information of large protein complexes.

Paramagnetic relaxation enhancement (PRE) occurs when an unpaired electron increases nuclear relaxation rates through dipolar interactions, which depend on the distance between the nucleus and the paramagnetic center. Strategies that make use of paramagnetic molecules help to alleviate the challenge of low sensitivity by enabling fast repetition of experiments and also provide a source of information about structures and dynamics.<sup>7,11-21</sup> PREs have been used successfully in the solid state with the PREs obtained from paramagnetic tags attached to the proteins<sup>22</sup> or by replacing non-paramagnetic ions with paramagnetic ions in metalloproteins.<sup>11,16,23,24</sup> One potential disadvantage of such approaches is that introducing a non-native moiety into the protein can influence its structural integrity and/or dynamics and such effects have to be considered carefully. In this context, employing an inert paramagnetic molecule dissolved in the solvent and which does not bind to the protein is less invasive and can provide long range structural information with less potential for influencing the structure and dynamics of the studied system.<sup>25,26</sup> If a paramagnetic compound, such as gadolinium diethylenetriaminepentaacetic acid bismethylamide (Gd(DTPA-BMA)), is added to the buffer surrounding the protein, the paramagnetic effects from such an agent, often called solvent PREs (sPREs), can be used to quantify solvent accessibility.<sup>27-30</sup> sPREs have been used in solution NMR

to gain additional restraints for structure calculation, prediction, and validation,<sup>31–33</sup> to probe domain architecture<sup>34</sup> and analyze protein-protein interactions.<sup>35</sup>

While paramagnetic agents are often used to speed up acquisition in solid state NMR,<sup>36</sup> there are few examples where sPREs have been used to study solvent accessibility in solid state NMR and, to our knowledge, they have not yet been employed for characterization of protein-protein interfaces in biomolecular complexes. However, sPREs have been used, e.g. to identify crystal contacts in a heavily deuterated crystalline sample of the  $\alpha$ -spectrin domain of SH3.<sup>17</sup> In that work, irregularly high  $^1\text{H}$  sPREs for residues in close proximity to exchangeable hydroxyl protons ( $< 3.5$  Å) were observed leading to major challenges in the interpretation of distances between nuclei and protein surface.<sup>17</sup> In another study,  $^{13}\text{C}$   $R_1$  based sPREs were used to identify regions with increased solvent accessibility in A $\beta_{1-40}$  fibrils.<sup>37</sup> Because of still active spin diffusion, which leads to the partial averaging of  $^{13}\text{C}$   $R_1$  rates over several sites,<sup>38</sup> the obtained sPREs were only qualitative in nature.<sup>37</sup> Overall, elimination of spin diffusion is a prerequisite for obtaining quantitative site-specific sPREs. Suppression of spin diffusion can be achieved through either dilution of the strong dipolar proton-proton network through deuteration<sup>17</sup> or fast magic angle spinning or a combination of the two approaches.<sup>39</sup>

Here, we explored sPREs derived from  $^1\text{H}$   $R_1$ ,  $^{15}\text{N}$   $R_1$  and  $^{15}\text{N}$   $R_{1\rho}$  measurements in order to develop a practical approach for applying sPREs to characterize protein-protein interfaces in large complexes in the solid state. We considered several factors that can influence applicability of the approach including signal to noise, site-specific nature of measurements, sensitivity and dynamic range of the employed probe and accessibility of specialized equipment.

To test the suitability of solid state sPREs to map solvent accessibility we have performed measurements on the B1 domain of immunoglobulin-binding protein G (GB1) in three different environments: isolated GB1 in solution (GB1<sub>free</sub>), GB1 in a crystal on its own (GB1<sub>cryst</sub>) and, finally, GB1 in a precipitated complex with full length IgG (GB1<sub>IgG</sub>). Protein G is part

of the bacterial defense strategy against antibodies that enables bacteria to escape detection by the host immune system. The high affinity between GB1 and IgG is commonly exploited in numerous biotechnological applications such as immunosorbent assays or affinity purification of antibodies. Insights into molecular aspects of the complex can guide and support therapeutic strategies as well as bio-engineering efforts. Differences in the solvent accessibility from sPREs revealed details of binding of GB1 to IgG and evidence for previously not observed additional interactions.

## **2.3 Results and Discussion**

### *2.3.1 Overview of the different sPRE approaches*

In solution NMR sPREs can be obtained by measuring relaxation rates in a sample with increasing concentration of a paramagnetic dopant. The slope of the line obtained from fitting the relaxation rates as a function of dopant concentration yields the sPREs. The same approach can be used in the solid state, but with an individually prepared sample for each dopant concentration. The most popular paramagnetic dopant used in solid state NMR applications is CuEDTA. However, complexes using EDTA as a chelator were shown to bind preferentially to some proteins due to their overall negative charge and thus introduce undesired bias in sPRE applications.<sup>40,41</sup> Even though CuEDTA does not bind to either GB1 or GB1:IgG complex, in order to increase general applicability of the approach, we have decided to use a neutral probe for most of our measurements. Towards this aim, we employed Gd(DTPA-BMA), which is one of the most popular stable neutral paramagnetic probe for sPRE applications in solution NMR and a popular intravenous MRI contrast agent. An additional benefit of using this dopant instead of CuEDTA is that  $\text{Gd}^{3+}$  is much more efficient in inducing PREs compared to  $\text{Cu}^{2+}$ , which means that much smaller concentrations of the dopant can be used to obtain similar effect.<sup>42</sup> In the solid state,  $\text{Gd}^{3+}$  complexes were shown to lead to improved SNR per unit time compared to CuEDTA in applications on a membrane protein.<sup>42</sup> In addition, reducing the required dopant concentration aids to minimize the rf induced heating.

We found that Gd(DTPA-BMA) can be added to hydrated protein samples in solid state NMR after they were prepared in the required solid form, e.g. crystal, sediment or precipitate, *without need for co-crystallization of the proteins with the paramagnetic agent* as it has been suggested previously.<sup>15</sup> We did not observe any significant deviations from a linear relationship between relaxation rates and dopant concentrations under the conditions and concentrations explored in this study. The advantage in measuring sPREs with this approach lies in that the sPREs do not need to be modelled explicitly (e.g. fitting correlation times etc.), consequently allowing a more straightforward comparison between sPREs derived from different types of measurements in solution and solid state. However, global scaling of the data is required to allow comparison of two data sets (see below).

<sup>1</sup>H relaxation for sPRE in the solid state is one of the most sensitive probes to paramagnetic effects. For <sup>1</sup>H relaxation measurements, to maximize sensitivity, one would like to maximize concentration of the protons in the sample.<sup>7,43,44,37,38</sup> On the other hand, to suppress the rate averaging spin diffusion one needs to minimize the concentration of protons or average out the <sup>1</sup>H-<sup>1</sup>H dipolar couplings by fast magic angle spinning. For different levels of protonation different spinning frequencies are optimal. For example, deuterated 100% back-exchanged samples at 60 kHz spinning provide the best compromise between resolution and sensitivity.<sup>43</sup> However, the <sup>1</sup>H-<sup>1</sup>H spin diffusion is not sufficiently suppressed under these conditions to enable site-specific measurements.<sup>45</sup> Due to both cost and practical considerations we decided to use deuterated GB1 with 100% back-exchanged protons and fully protonated natural abundance IgG. The presence of more protons in the system required very fast spinning to sufficiently suppress <sup>1</sup>H-<sup>1</sup>H spin diffusion for site-specific measurements of <sup>1</sup>H sPREs (Figure 2.4a). We have previously demonstrated that high quality spectra can be obtained for 100% back-exchanged [U-<sup>2</sup>H,<sup>13</sup>C,<sup>15</sup>N]GB1 in complex with natural abundance IgG using as little as 15 µg of labelled protein in a 0.81 mm rotor with ~100 kHz MAS.<sup>7</sup> Furthermore, recent studies report that at >100 kHz spinning frequencies <sup>1</sup>H-<sup>1</sup>H spin diffusion is significantly slowed

down even in fully protonated samples, especially for protons with large differences in their chemical shifts.<sup>45,46</sup> This is in accordance with the observation of large differences in site-specific  $^1\text{H}$   $R_1$  (Fig. 2.4a) in our experiments, suggesting that at 100 kHz spinning  $^1\text{H}$ - $^1\text{H}$  spin diffusion is sufficiently slowed down – if not completely suppressed – to at least allow characterization of the protein-protein interfaces from sPREs (e.g. T18H and E19H are separated by about 1 ppm and their sPREs differ by a factor of  $\sim 2$ ). The sufficient suppression of the proton spin diffusion is corroborated by the absence of the unusually high  $^1\text{H}$  sPREs for amide protons in the proximity of hydroxyl sites that were observed in the presence of residual spin diffusion<sup>17</sup> (e.g. T18H, which one might expect to be influenced in this way has a rather low sPRE).

Employing  $^1\text{H}$ s for sPRE measurements will therefore require specialized and still not widely available ultrafast MAS probes. In addition, experiments at  $> 100$  kHz spinning frequencies necessitate use of rotors with very small volumes. The decrease of signal-to-noise ratio due to the small sample volume can be, to a large extent, offset by detecting signal on protons.<sup>44</sup> However, 100% back-exchanged perdeuterated samples can be used effectively for  $^1\text{H}$  detected experiments already at 60 kHz in which case larger volume rotors can be used.<sup>43</sup> Finally, for systems with extensive slow dynamics sometimes adequate  $^1\text{H}$  resolution is difficult to achieve even at the highest spinning frequencies, requiring use of  $^{13}\text{C}$  or  $^{15}\text{N}$  detected experiments, in which case larger volume rotors are desirable. For the above reasons, it is worth to explore other probes for sPREs that can be utilized at slower spinning frequencies in larger volume rotors.

In the case of  $^{15}\text{N}$ , at spinning frequencies  $> 20$  kHz proton driven spin diffusion is sufficiently slowed down to enable site-specific measurements of  $^{15}\text{N}$   $R_1$  even in fully protonated systems.<sup>47–49,56</sup> In the solid state, protein  $^{15}\text{N}$   $T_1$ s are very long (20–40 s) so, in spite of lower sensitivity of  $^{15}\text{N}$  to paramagnetic effects compared to  $^1\text{H}$ , a high dynamic range of the relaxation rates is available and relatively small changes can be detected. Consequently, large variations in  $^{15}\text{N}$  sPREs can be observed just as in the case of  $^1\text{H}$  but the measurements can be performed even at moderate

spinning frequencies (as low as 10 kHz<sup>47-49</sup> if minimal rate averaging can be tolerated). A disadvantage of using  $^{15}\text{N}$   $R_1$  for sPREs is that the long relaxation times require long (i.e. many seconds) relaxation delays for adequate sampling of the relaxation rates resulting in long overall experimental times. Alternatively, we examined the applicability of the typically much shorter  $^{15}\text{N}$   $T_{1\rho}$  times (on the order of dozens to hundreds of milliseconds<sup>9,10,50-53</sup>) as basis for sPREs. Below we demonstrate that  $^{15}\text{N}$   $R_{1\rho}$  sPREs are sufficiently sensitive to characterize protein-protein interfaces with the emerging picture virtually identical to the one obtained from  $^{15}\text{N}$   $R_1$ . The much shorter required relaxation delays in  $^{15}\text{N}$   $R_{1\rho}$  experiments permit considerably faster performance compared to  $^{15}\text{N}$   $R_1$  sPRE, acquisition, further allowing higher signal to noise ratios in the available experimental time. For example, measurements for one concentration of paramagnetic dopant for GB1<sub>IgG</sub> took 3-4 days in the case of  $^{15}\text{N}$   $R_1$  (estimation of  $^{15}\text{N}$   $R_1$  from only two points, which took 5 days, was practically possible for the diamagnetic variant with the measurement of full curve being prohibitively long<sup>8</sup>) and 18-24 hours in the case of  $^{15}\text{N}$   $R_{1\rho}$ . As a side note,  $^1\text{H}$   $T_{1\rho}$  typically are too short to provide a reliable quantitative sPRE probe (or at least not in a range where no significant line broadening is observed).

### 2.3.2 sPREs: solution vs. crystal

First, we set out to explore the applicability of sPREs by investigating reduced solvent accessibility in GB1 crystals. To that end, we used experimental  $^{15}\text{N}$   $R_1$ -based sPREs of free GB1 in solution (GB1<sub>free</sub>) to provide a baseline for observing changes in solvent accessibility due to protein-protein interactions and crystal contacts. The  $^{15}\text{N}$   $R_1$ -based sPREs shown in Fig. 2.1a inform on the solvent accessibility of the protein in the absence of intermolecular interactions and regions that are well protected from solvent access in isolated GB1 can be identified as most of  $\beta 1$ , parts of the  $\alpha$ -helix and parts of  $\beta 4$ . In contrast, the most accessible regions are the outer beta strands  $\beta 2$  and  $\beta 3$ . This is in good agreement with scaled theoretical sPREs calculated from an available structure of isolated GB1 using a previously described grid-based approach<sup>30,33,54</sup> (see

experimental section). The predicted values reproduce the experimental sPREs well with the exception of  $\beta 2$  and Y45, where sPREs are underestimated. The discrepancy for  $\beta 2$  could potentially be explained by the previously reported large amplitude motions of the strand involving rotations around its long axis, which render the amide nitrogens more solvent accessible.<sup>55</sup> We note that ultimately conformational dynamics should be taken into account when calculating sPREs from structures.

The  $^{15}\text{N}$   $R_1$ -based sPREs measured in GB1 crystals (GB1<sub>cryst</sub>) present a quite different picture (Figure 2.1b): in contrast to GB1<sub>free</sub>, the outer  $\beta 2$  and  $\beta 3$  strands are much more protected in the crystal compared to the most solvent accessible residues in loop 1. This is consistent with the fact that in crystals, GB1 forms extended  $\beta$ -sheets stabilized by intermolecular hydrogen bonds between  $\beta 2$  and  $\beta 3$ .<sup>56,57</sup> Moreover, the scaled theoretical  $^{15}\text{N}$  sPREs calculated for GB1 in a lattice agree reasonably well with the experimental sPREs except for T11 and T49 which are located in the loops, and L6. In contrast to the previous study on crystalline SH3<sup>15</sup> we do not observe the unexpectedly high relaxation rates for sites in close proximity to hydroxyl groups (unless these sites are solvent accessible, in which case we do observe high PREs). That this effect is not observed in our experiments suggests that the assumption of the absence of spin diffusion in a perdeuterated sample with 10% back-exchanged protons at moderate spinning frequency (24 kHz)<sup>17</sup> might not have been entirely justified. Residual spin diffusion due to locally higher density of exchangeable protons and moderate spinning frequency can easily explain the anomalously high sPREs observed by Linser *et al*.<sup>15</sup> Under conditions suggested in the present work, proton driven spin diffusion between nitrogens is extremely well suppressed, which abolishes any effect of the exchangeable hydroxyl protons on the relaxation rates of amide sites in the vicinity.



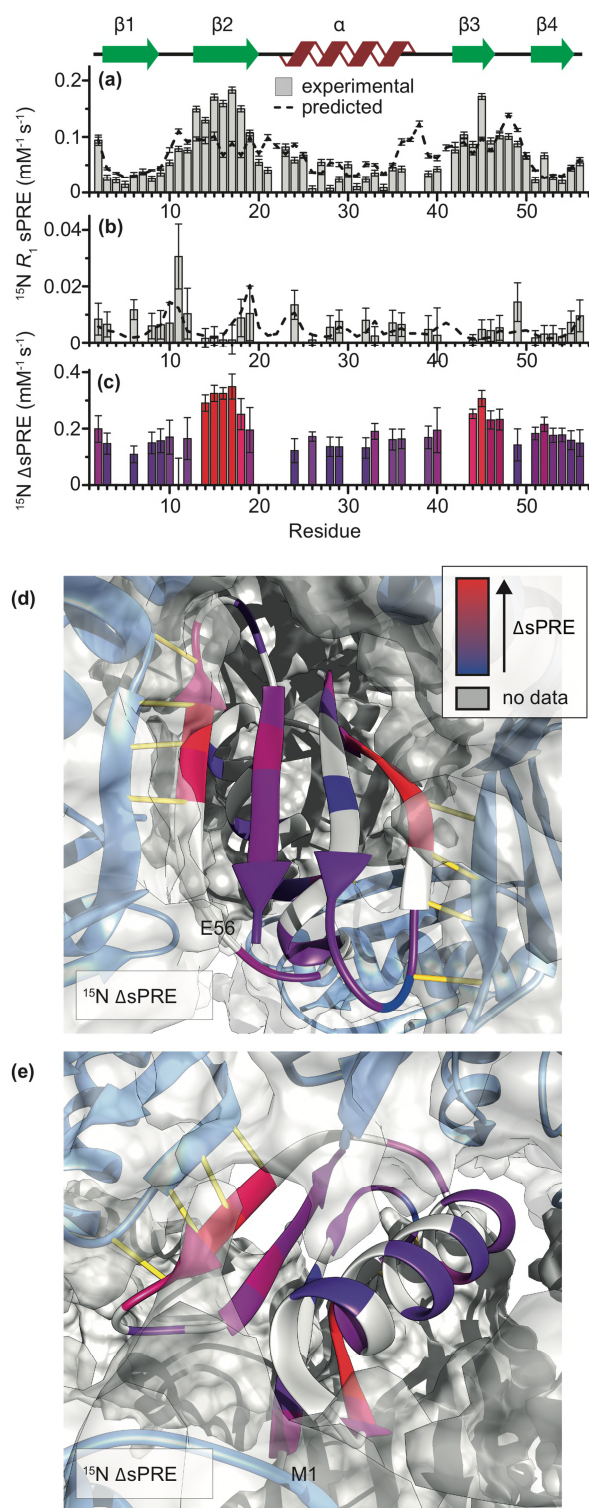


**Figure 2.1.** Experimental  $^{15}\text{N}$   $R_1$  solvent PREs for GB1 (a) in solution and (b) in a crystal. (c) Experimental  $^{15}\text{N}$   $R_1$   $\Delta$ sPREs for GB1 crystal (i.e. difference between, normalized to averages,  $^{15}\text{N}$   $R_1$  sPREs in solution and in crystal) as a function of residue, and (d-e) projected onto structure of GB1 in a lattice. Dashed lines in (a-b) indicate  $^{15}\text{N}$  sPREs calculated from structures: solution NMR structure of isolated GB1 (PDB ID: 3gb1<sup>58</sup>) in (a) and GB1 in a lattice (PDB ID: 2qmt<sup>57</sup>) in (b). Each set of predicted sPREs were scaled by a global factor equal to the ratio of the averages of the predicted sPREs and experimental sPREs. Yellow lines in (d-e) represent intermolecular hydrogen bonds. Residues for which data is not available either due to severe overlap, missing peak or insufficient signal to noise are indicated in grey.

Theoretical sPREs can be used to validate models by comparing the experimental sPREs to the ones predicted from the model. However, even in the absence of a model, intermolecular interactions can be detected by identifying sites with increased protection from the solvent due to these interactions. We propose to simply use the difference between experimental sPREs in the absence and presence of intermolecular interactions, i.e. for GB1 free in solution (GB1<sub>free</sub>) and GB1 in the assembly (GB1<sub>cryst</sub> or GB1<sub>IgG</sub> in the latter part of the manuscript) respectively. Remarkably, the difference PREs ( $\Delta$ sPREs) provide a powerful way to detect intermolecular interactions. In general, one will need to take into account any conformational changes upon binding, whose effect cannot be distinguished from reduced solvent accessibility due to binding without additional data. GB1 does not undergo any large backbone conformational changes either in crystal or GB1:IgG complex<sup>7,8,59</sup> so no further correction is required. In cases where secondary chemical shifts indicate conformational change upon binding, solving structure of the considered protein in a complex will be prerequisite for quantification of protein interface using sPREs (though qualitative information about the interactions still can be obtained in the absence of such structure). Because of the “built-in” compensation for solvent accessibility pattern due to conformation of the molecule, the effect of intermolecular interactions is effectively “amplified” in  $\Delta$ sPREs.

The potential of  $\Delta$ sPREs is illustrated by the experimental <sup>15</sup>N  $R_1$   $\Delta$ sPREs for GB1<sub>cryst</sub> shown in Fig. 2.1c-e, which highlight the increased protection of  $\beta$ 2 and  $\beta$ 3 due to the presence of intermolecular hydrogen bonds in the crystal. At the same time, other subtler features become apparent such as better protection of the N-terminus compared to the C-terminus or slightly higher protection of the C-terminal end of the helix compared to the N-terminal end. Note that to minimize the bias and to account for the different dynamic ranges of the data sets that are subtracted to yield  $\Delta$ sPREs they were scaled by a global factor equal to the ratio of the rate averages of the two data sets (see the experimental section). For visualization purposes a constant (equal to absolute value of the

minimum  $\Delta$ sPREs) is added so that all experimental  $\Delta$ sPREs have the same sign.

### 2.3.3 sPREs in GB1:IgG complex

Currently only structures of protein G domains with immunoglobulin fragments are available. Interactions between the Fab fragment of IgG and protein G domains have been investigated by X-ray crystallography<sup>60</sup> and solution NMR<sup>61</sup>. The crystal structure showed that the main interactions between the Fab fragment and GB3 correspond to residues 10-18 of GB1, and a minor contact between the Fab fragment and residues 33 and 37 of GB1 (for clarity we use GB1 residue numbering throughout this paragraph). The solution NMR analysis identified chemical shift perturbations (CSPs) in residues 9-17 (also 7, 19, 36, 37, 38, 40, 43 and 53).<sup>61</sup> In solution NMR studies of GB2 and the Fc fragment of IgG, residues in regions 23-36 and 40-46 which are located in  $\beta$ 3 and the  $\alpha$ -helix of GB1 were found to be involved in the interaction.<sup>62</sup> This is in agreement with a crystal structure of GB2 in complex with the Fc fragment of IgG where the residues involved in binding correspond to residues 27, 28, 31, 32, 35, 40, 42 and 43 of GB1.<sup>63</sup> It is worth noting that residues involved in binding to the Fab fragment (residues 9-18) were not affected by the interaction with the Fc fragment.<sup>63</sup> In our previous solid-state NMR study of the complex of GB1 bound to full length human IgG, we established that GB1 binds to both Fab and Fc fragments of IgG simultaneously.<sup>7</sup> Here we use the sPRE methodology validated above on the GB1 crystal to obtain further insights into the GB1-IgG interactions. In the range explored by us,  $^{15}\text{N}$   $R_1$  or  $R_{1\rho}$  relaxation rates vs. Gd(DTPA-BMA) concentration in a precipitated GB1:IgG complex show a good linear relationship (see Fig. 2.2a-b and Fig. SI 2.3). The sPREs obtained from slopes of such trends are shown in Fig. 2.2c ( $^{15}\text{N}$   $R_1$  sPREs) and 2.2d ( $^{15}\text{N}$   $R_{1\rho}$  sPREs). A direct comparison of predicted and experimental sPREs (Fig. SI 2.1) shows that interactions with both Fc and Fab fragments must be present.

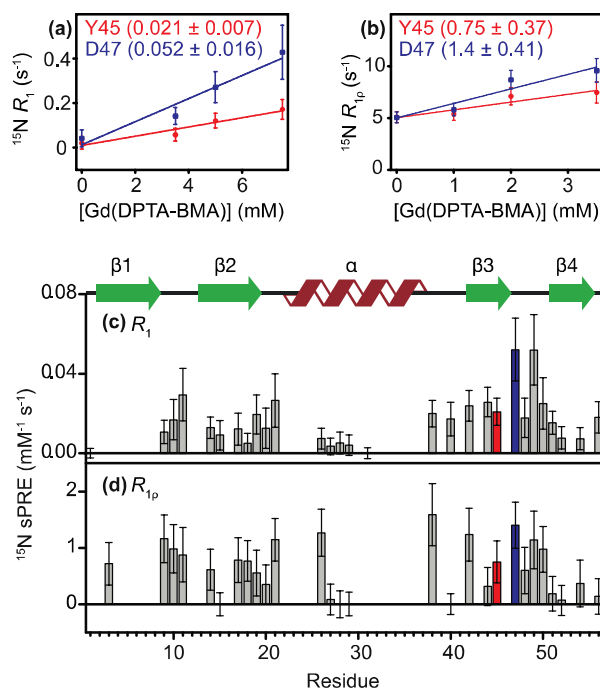


**Figure 2.2.** Examples of linear fits for sPREs for GB1 in a complex with IgG (GB1<sub>IgG</sub>) based on (a)  $^{15}\text{N}$   $R_1$  and (b)  $^{15}\text{N}$   $R_{1p}$  relaxation rates. (c)  $^{15}\text{N}$   $R_1$  sPREs and (d)  $^{15}\text{N}$   $R_{1p}$  sPREs for GB1 in a precipitated complex with IgG.

To further analyze the increased protection due to protein – protein interactions we focus the discussion on  $\Delta$ sPREs. As we mentioned above, this is preferred to direct analysis of sPREs because  $\Delta$ sPREs mostly suppress pattern of protection from solvent due to conformation of the studied protein, leaving one with a pattern mostly based on intermolecular interactions (unless the protein undergoes significant conformational change upon binding where the analysis becomes much more involved). Figure 2.3a-b shows experimental  $^{15}\text{N}$   $R_1$  and  $R_{1p}$   $\Delta$ sPREs for GB1<sub>IgG</sub>. Both data sets reveal a rather similar pattern, which differs somewhat from  $\Delta$ sPREs for GB1<sub>cryst</sub>. Overall, as expected due to the shorter  $T_{1p}$  times compared to  $T_1$  times, the dynamic range of  $R_{1p}$   $\Delta$ sPREs is smaller but still sufficient to identify changes in the solvent accessibility caused by complex formation. The fact that  $^{15}\text{N}$   $R_{1p}$   $\Delta$ sPREs appear to be sufficiently sensitive to characterize intermolecular contacts in the GB1:IgG complex is fortunate because the acquisition of high quality  $R_{1p}$  sPREs requires much shorter experimental times compared to  $^{15}\text{N}$   $R_1$  sPREs. (from several days to sometimes less than 24 h; see Table SI 2.11).

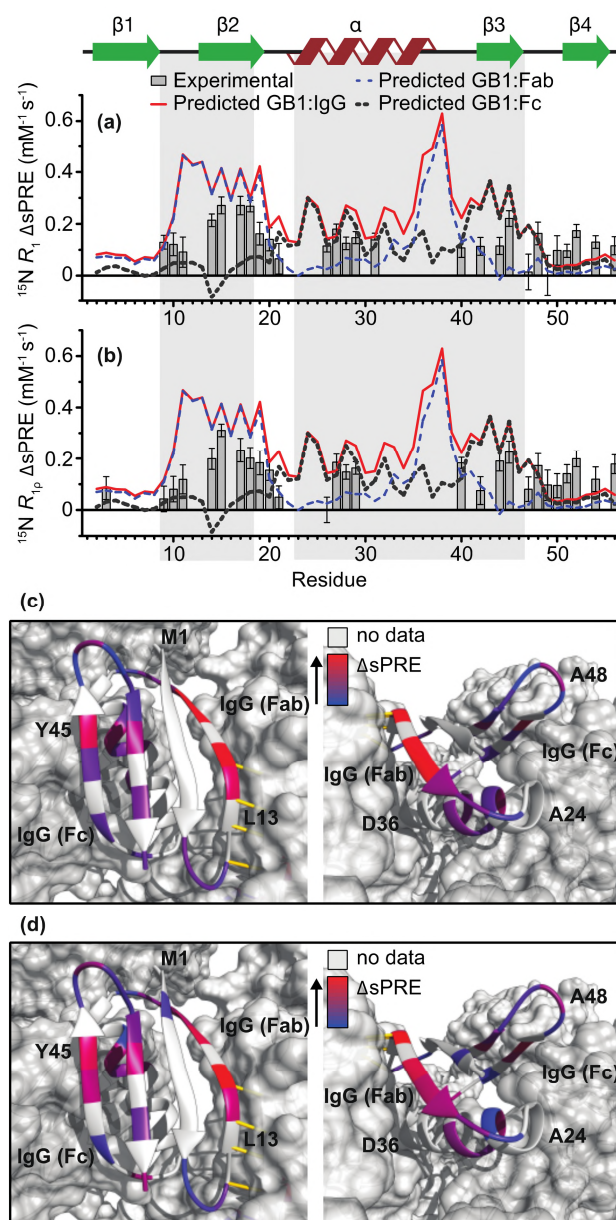


**Figure 2.3.**  $^{15}\text{N}$   $\Delta\text{sPRE}$ s for GB1<sub>IgG</sub> based on (a)  $R_1$  and (b)  $R_{1\rho}$  relaxation rates (grey bars). Lines indicate scaled  $\Delta\text{sPRE}$ s calculated from back-predicted sPREs: GB1:IgG complex model (red continuous), GB1:Fab complex model (dashed blue) and GB1:Fc complex model (dotted grey). For the comparison, all back-predicted data sets are scaled so that the average of the set is equal to the average of the experimental data. The expected binding sites are highlighted: Fab interface (residues 9-18) and Fc interface (residues 23-46). Experimental  $^{15}\text{N}$   $R_1$  (c) and  $R_{1\rho}$  (d)  $\Delta\text{sPRE}$ s projected onto the structural model of GB1 in a complex with IgG. Red indicates residues with the largest changes in solvent accessibility upon binding and blue the residues with the smallest changes upon binding. Residues for which data is not available either due to severe overlap, missing peak or insufficient signal to noise are indicated in grey.

The most prominent feature arising from a comparison of  $^{15}\text{N}$   $R_1$  and  $R_{1\rho}$   $\Delta\text{sPRE}$ s in GB1<sub>IgG</sub> and  $^{15}\text{N}$   $R_1$   $\Delta\text{sPRE}$ s in GB1<sub>cryst</sub> is that  $\beta 2$  is most protected in both assemblies. This is consistent with the intermolecular

hydrogen bonds between GB1 molecules in the crystal and intermolecular hydrogen bonds to the Fab fragment in the GB1:IgG complex. On the other hand,  $\beta 3$  which interacts but does not form hydrogen bonds with the Fc fragment in GB1<sub>IgG</sub> is somewhat less protected than in the crystals where it forms intermolecular hydrogen bonds.

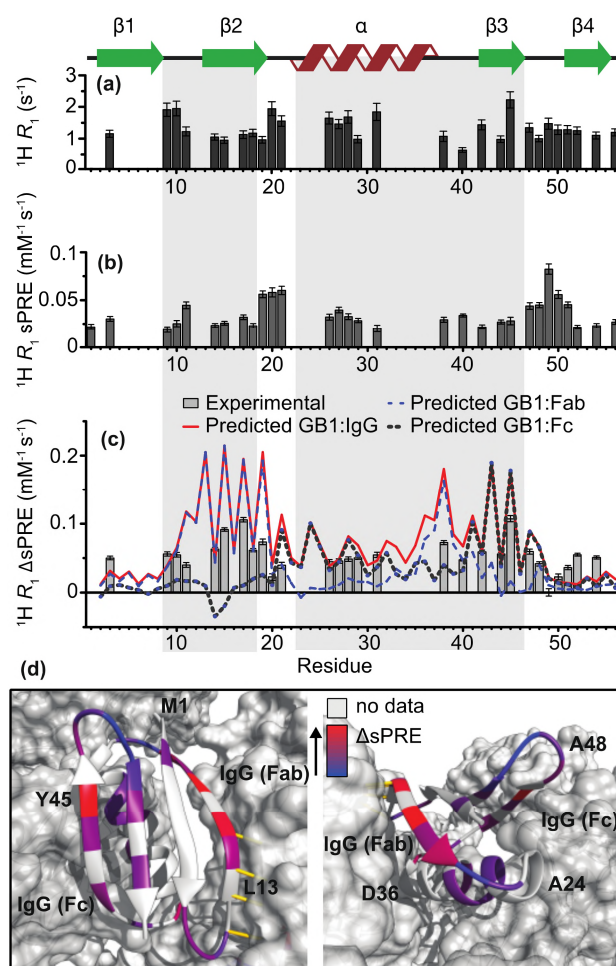


**Figure 2.4.**  $^1\text{H}$   $R_1$  relaxation rates (a),  $^1\text{H}$   $R_1$  sPREs (b) and  $^1\text{H}$   $R_1$   $\Delta$ sPREs (c) for GB1<sub>IgG</sub>. Lines indicate scaled  $\Delta$ sPREs calculated from back-predicted sPREs: GB1:IgG complex model (red continuous), GB1:Fab complex model (dashed blue) and GB1:Fc complex model (dotted grey). The scaling procedure is the same as in Fig. 2.. 3. The expected binding sites are highlighted as in Fig. 2.. 3. (d)  $^1\text{H}$   $R_1$   $\Delta$ sPREs plotted onto the structure of GB1 in complex with full length IgG. Residues for which data is not available either due to severe overlap, missing peak or insufficient signal to noise are indicated in grey.

Even more interestingly the N-terminal residues in the helix seem similarly or better protected than  $\beta 2$  as a result of complex formation. The above observations seem to be consistent with creation of the interface between the helix and  $\beta 3$  of GB1 with the Fc part of IgG.

To further investigate the protein-protein interfaces we also measured amide  $^1\text{H}$  solvent PREs.  $^1\text{H}$  sPREs of the GB1:IgG complex were obtained from  $^1\text{H}$   $R_1$  measurements (for historical reasons using CuEDTA<sup>37</sup> rather than Gd(DTPA-BMA), and are presented in Figure 2.4b (data in Tables SI 2.6-2.7, comparison between predicted and experimental sPREs in Fig. SI 2.2). Reference experimental  $^1\text{H}$  sPREs for isolated GB1 in solution were taken from ref. <sup>64</sup>.

The overall trend in  $^1\text{H}$   $\Delta$ sPREs for the GB1:IgG complex is similar to  $^{15}\text{N}$   $\Delta$ sPREs: again, as a result of the complex formation  $\beta 2$  is the most strongly protected,  $\beta 3$  is also protected but to a lesser extent with Y45 exhibiting the strongest level of protection. However, relative to the level of protection in  $\beta 2$ , the residues in the helix seem to be very slightly less protected than in  $^{15}\text{N}$   $\Delta$ sPREs.

The  $\Delta$ sPREs back-calculated from models of GB1:IgG, GB1:Fab and GB1:Fc complexes are plotted as lines in Fig. 2.3a-b and 2.4c. A simple visual inspection suffices to see that all three experimental  $\Delta$ sPRE sets are more compatible with the  $\Delta$ sPREs back-calculated from a model of the GB1:IgG complex where both of the binding interfaces are occupied at the same time. In all the cases,  $\Delta$ sPREs calculated for GB1:Fab grossly underestimate the level of protection for  $\beta 3$  and helix while  $\Delta$ sPREs calculated for GB1:Fc grossly underestimate the level of protection for  $\beta 2$  and overestimate the level of protection for  $\beta 3$  acquired upon complex formation.

In order to obtain a more quantitative handle on how well the different structural models reproduce experimental data we have also performed a series of fits of the experimental  $\Delta$ sPREs to  $\Delta$ sPREs back-calculated from the different models (note that scaling of individual back-calculated sPREs is not required before calculation of theoretical  $\Delta$ sPREs), with a global scaling factor as the only fit parameter. Again, in such data the trends are “cleaned up” from the effects of GB1 conformation simplifying quantification of the contribution from intermolecular interactions. In all the cases, data back-predicted from the GB1:IgG complex where both Fab and Fc interfaces are occupied gives the lowest  $\chi^2$  thus identifying it



as the best from the considered models of the interaction (see Table SI 2.12).

Upon closer inspection of the best fitting theoretical  $\Delta$ sPRE trends against the experimental ones we identify one particularly interesting feature where the two types of data differ. According to the experimental data the protection due to interactions between GB1 and IgG are similar for some residues in  $\beta$ 4 as for  $\beta$ 3 suggesting that either the first residues in  $\beta$ 3 are less protected than expected or  $\beta$ 4 is more protected than expected. Different levels of protection can be explained by either a change of backbone conformation between GB1<sub>free</sub> and GB1<sub>IgG</sub>, internal molecular motion, or an additional interaction with IgG.

The  $C_\alpha$  secondary chemical shifts for GB1 in complex with IgG are very similar to the ones calculated for GB1 in solution (see Fig. SI 2.5, based on data from ref. 7), with exception of L6, T11, L12 and K50 (Fig. 2.5a). Consequently, subtle changes in the backbone conformation are unlikely to explain the changes in the solvent accessibility of  $\beta$ 4. Internal molecular motions could explain the differences in the  $\Delta$ sPREs for residues which exhibit large amplitude backbone motions, but can be safely neglected for the rest of the residues including those in  $\beta$ 4.<sup>8,59</sup> This means that the observed deviations, if real and not just experimental errors, must arise from changes in the intermolecular interactions: additional interactions for the increased protection and abolished interactions for the decreased protection. Some changes in the solvent accessibility might be expected if GB1 undergoes a small amplitude anisotropic overall motion in the complex, as we have suggested based on the analysis of relaxation rates measured in the complex.<sup>8</sup> To investigate what effect such motion would have on the pattern of solvent accessibility we generated a series of conformers where the molecule of GB1 was rotated around the axes of the motion by 7°, which corresponds to the approximate amplitude of motion determined in our rather simple analysis<sup>8</sup> (the actual amplitude of motion may differ because in the absence of dipolar order parameter relaxation analysis is not very reliable<sup>51,59</sup>) followed by translating the molecules assuming that  $\beta$ 2 hydrogen bonded to Fab is the anchoring the point.



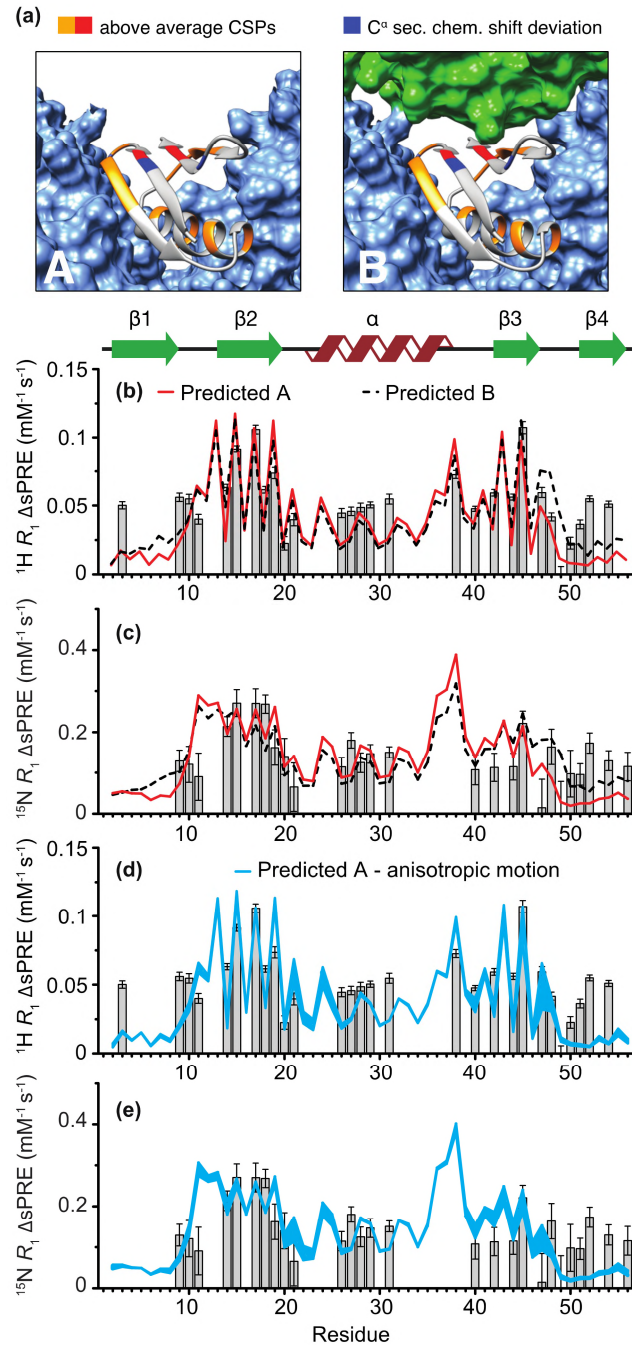


**Figure 2.5.** (a) Models of GB1:IgG complex with: A - only Fab and Fc interface (cornflower blue) and B - Fab, Fc and additional contact with  $\beta 4$  (green). Residues with higher than average chemical shift perturbations (CSPs) are indicated in orange.<sup>7</sup> Previously unexplained above average CSPs for res 7, 53, 54 are shown in red.<sup>7</sup> Sites with deviations of  $C^\alpha$  secondary chemical shift compared to solution are indicated in blue.<sup>7</sup> (b-c) Experimental  $\Delta$ SPREs vs.  $\Delta$ SPREs predicted from GB1:IgG models in (a): model A (red line) and model B (black dashed line). (d-e) Back-predicted  $\Delta$ SPREs for GB1 in complex with IgG assuming small amplitude overall anisotropic motion of GB1 as suggested in ref. 8. The lines in (d-e) represent a range of  $\Delta$ SPREs based on 5 generated conformers.

The distribution of  $\Delta$ SPREs calculated for 5 generated conformers is illustrated in Fig. 2.5d-e. In the case of a proposed overall motion the residues most immune to changes in solvent accessibility as a result of

this motion would be  $\beta 1$ ,  $\beta 4$  and the C-terminal half of the helix. Such a motion could, however, contribute to the discrepancies observed for  $\beta 3$ , V21 and loop 4 (D47 is the most influenced of all residues).

Interestingly, we previously observed large chemical shift perturbations (CSPs) for T53, V54 and L7 upon GB1:IgG complex formation but were unable to completely explain their origin (Fig. 2.5a; L7 could potentially be explained by a small backbone conformation change indicated by change in  $C^\alpha$  secondary chemical shift of L6 $C^\alpha$  compared to solution). The presence of these CSPs and the elevated  $\Delta$ sPREs suggest that there might be an additional interaction between GB1 and IgG, which involves  $\beta 4$  and that is not observed in the complexes of protein G domains with IgG fragments. Obviously, with the available data it is not possible for us to identify the region of IgG responsible for this potential additional interaction. However, we can simulate the effects of proximity of molecular fragments to  $\beta 4$  on the  $\Delta$ sPRE pattern in GB1<sub>IgG</sub>. We have generated a model by translating one of the extended IgG loops to make an intermolecular contact with  $\beta 4$  (Fig. 2.5a). This additional contact indeed reduces the anomalous  $\Delta$ sPRE trend for  $\beta 4$ . In spite of complete arbitrariness of this model (the exact structure of the fragment and its position is likely different), it is clear that the presence of a similar additional interaction is consistent with the observed elevated  $\Delta$ sPREs for  $\beta 4$  and the large CSPs for residues 53 and 54. Interestingly, the existence of such a contact would also help to explain why the complex of GB1 with IgG gives such high-quality NMR spectra that are atypical for a precipitate. With three interfaces the local environment of GB1 in the complex would be defined almost entirely by the specific interactions with IgG leaving GB1 largely unaffected by any heterogeneity of the sample.

## 2.3 Conclusions

We introduced  $^1\text{H}$  and  $^{15}\text{N}$  solvent PREs as a general and powerful tool for characterizing intermolecular interfaces in large biomolecular complexes in the solid state. The proposed methods can be applied over the majority of range of spinning frequencies employed in biomolecular solid-state NMR: moderate spinning frequencies ( $^{15}\text{N}$   $R_1$ ), intermediate

spinning frequencies ( $^{15}\text{N } R_1$ ,  $^{15}\text{N } R_{1\rho}$ ) and fast spinning frequencies ( $^{15}\text{N } R_1$ ,  $^{15}\text{N } R_{1\rho}$ ,  $^1\text{H } R_1$ ), which allows to fine tune this methodology to the specific requirements of different systems and available instrumentation. We demonstrate for 100% back-exchanged protein in the presence of a fully protonated binding partner that  $^1\text{H}$ - $^1\text{H}$  spin diffusion is sufficiently slowed down at 100 kHz to allow the use of  $^1\text{H } R_1$  as a site-specific probe of solvent accessibility.  $^1\text{H } R_1$  and  $^{15}\text{N } R_1$  are the most sensitive probes enabling accurate measurement of even small PREs. At the same time  $^{15}\text{N } R_{1\rho}$ , even though less sensitive than  $^1\text{H } R_1$  and  $^{15}\text{N } R_1$  as sPRE probes, yields essentially the same picture with the added benefit of overall shorter experiments where satisfactory signal to noise ratio can be achieved in a reasonable amount of time, even for large biomolecular complexes characterized by low sensitivity. We establish the benefits of comparing sPREs of isolated protein in solution to sPREs of the protein in a complex in the solid state to identify reduced solvent accessibility of regions involved in protein-protein interactions.

Moreover, we demonstrate the utility of solid-state sPREs for determining intermolecular interactions by applying it to characterize intermolecular contacts in GB1 crystal and protein-protein interfaces in GB1 in a complex with full length IgG. The experimental sPREs are in a very good agreement with predicted sPREs based on crystal structures. All three sPRE probes:  $^{15}\text{N } R_1$ ,  $^{15}\text{N } R_{1\rho}$ ,  $^1\text{H } R_1$  yield a highly consistent view of the GB1 interactions with IgG. Based on the local deviations of  $\Delta\text{sPRE}$  trends and CSPs we suggest that the extraordinary GB1:IgG binding interface might involve three different regions, painting a more complex picture than what can be deduced from the structures of protein G with IgG fragments, emphasizing the importance of using full length proteins in interaction studies if at all possible.

We envision the proposed approach to be widely applicable for characterization of intermolecular interfaces in large protein complexes and especially the ones that are not accessible to other high resolution techniques as is the case for the precipitated complex of GB1:IgG.

## 2.4 Experimental Section.

Sample preparation. Isotope labelled GB1 2Q6I was expressed using pGEV2 in BL21(DE3)<sup>65</sup>. [U-<sup>13</sup>C, <sup>15</sup>N]GB1 was purified from cultures grown in M9 supplemented with [U-<sup>13</sup>C]glucose and <sup>15</sup>NH<sub>4</sub>Cl. [U-<sup>2</sup>H, <sup>13</sup>C, <sup>15</sup>N]GB1 was expressed in M9 prepared in D<sub>2</sub>O with deuterated [U-<sup>13</sup>C]glucose and <sup>15</sup>NH<sub>4</sub>Cl. Cells were grown to an OD<sub>600</sub> >1.0 in two liters LB for each liter of M9 and washed once with PBS before resuspension in M9. Expression was induced with 0.5 mM IPTG after 1 h incubation at 37 °C. After expression for 4 h at 37 °C, the cells were pelleted (4000 × G for 20 min at 16 °C), and lysed by sonication in buffer (50 mM potassium phosphate; 200 mM NaCl; 1 mg/ml lysozyme; pH 7.0). The lysate was then incubated at 75 °C for 10 min and cleared by centrifugation (12000 × G for 50 min). After precipitation over night with 80% ammonium sulfate, GB1 was pelleted (15000 × G for 50 min), resuspended in buffer (50 mM potassium phosphate; 200 mM NaCl; pH 7.0), and purified on a 16/600 Sephadex pg75 (GE Healthcare) gel filtration column. Fractions containing GB1 were collected, desalted, freeze-dried and stored at -20 °C.

Freeze-dried [U-<sup>2</sup>H, <sup>13</sup>C, <sup>15</sup>N]GB1 was dissolved in buffer (50 mM sodium phosphate buffer pH 5.5) to obtain a protein concentration of 10 mg/ml and crystallized with the aid of 2:1 2-methyl-2,4-pentanediol (MPD):Isopropanol<sup>66</sup>. Lyophilized IgG from human serum was purchased from Sigma-Aldrich. GB1:IgG complex was formed by mixing GB1 and IgG solutions in 2:1 molar ratio<sup>7</sup>. Crystalline GB1 and precipitated GB1:IgG complex were packed into NMR rotors using the following procedure: The crystals/precipitate were spun down by centrifugation (1 min at 20 000 × G using a bench top centrifuge), and resuspended in a small volume of the supernatant containing 2% DSS and Gd(DTPA-BMA) at the desired concentration. The 1.3 mm rotors were packed by centrifugation (20 000 × G) and the rotor caps sealed with a silicone-based glue to prevent leakage. The smaller 0.81 mm rotors were filled manually using microspatulas.

The solution NMR sample was prepared in a 3 mm tube containing 200  $\mu$ l of 1 mM [ $U\text{-}^{13}\text{C},^{15}\text{N}$ ]GB1 in 50 mM sodium phosphate, pH 5.5, 10%  $\text{D}_2\text{O}$ , and 30  $\mu$ M DSS.

**Solution NMR.** All solution NMR data was recorded at 298 K on a 700 MHz Bruker Avance spectrometer equipped with a cryogenically cooled probehead.  $^{15}\text{N}$  longitudinal relaxation rates ( $R_1$ ) were measured with a  $^{15}\text{N}$ -HSQC based standard Bruker pseudo 3D (hsqct1etf3gpsi3d.2) with 8-10 points using delays between 0.05 and 2.0 s (details are listed in SI Table 11). Spectral widths were 8400 Hz for  $^1\text{H}$  and 2700 Hz for  $^{15}\text{N}$ , and FIDs had 2048 and 256 points, respectively. The recycle delay was 3.5 s. To obtain the sPREs, the sample was titrated with Gd(DTPA-BMA) (Omniscan; stock 20 mM) up to 2.5 mM (details in SI Table 11). All spectra were processed in TopSpin 3.2 and CCPNMR<sup>67</sup> and MatLab R2014a was used to analyze the relaxation data.

**Solid state NMR.** Solid state NMR spectra were recorded at 600 MHz Bruker Avance II+, 700 MHz Bruker Avance III HD and 850 MHz Bruker Avance III spectrometers, using Bruker 1.3 mm triple resonance probes (at MAS frequencies of 50-60 kHz) or a volume optimized 0.81 mm double resonance probe from Samoson laboratory (for experiments at  $\sim$ 100 kHz MAS). A Bruker BCU-X cooling unit was used to regulate the internal sample temperature to  $27 \pm 1$   $^\circ\text{C}$  (measured from the chemical shift of water with respect to DSS. For experiments recorded at 700 MHz  $^1\text{H}$  Larmor frequency 10 %  $\text{D}_2\text{O}$  was added to the sample buffer before packing the rotors and deuterium locking was used in the same way as in solution NMR.  $^{15}\text{N}$ - $^1\text{H}$  2D correlation spectra were recorded using a proton-detected heteronuclear correlation sequence. Double quantum cross-polarization (CP) contact times were between 0.5 – 1.5 ms and individually optimized for each sample. Recycle delays between 0.2 – 2.5 s were used depending on the amount of paramagnetic agent and magnetic field.

The maximum employed concentrations were chosen so that the paramagnetic effect does not lead to significant line broadening and are

thus are different for different samples, e.g. larger concentrations could be used in GB1:IgG complex than in GB1 crystal to obtain similar line widths.

In all solid-state experiments, hard pulses were applied at nutation frequencies of 100 kHz (1.3 mm probe) or 125 kHz (0.81 mm probe) for  $^1\text{H}$  and 83.3 kHz for  $^{15}\text{N}$ . 10 kHz WALTZ-16 decoupling was applied on protons during  $^{15}\text{N}$  evolution, and on  $^{15}\text{N}$  channel during direct  $^1\text{H}$  acquisition, while quadrature detection was achieved using the States-TPPI method. Suppression of the water signal was achieved by saturation with 50 - 200 ms of slpTPPM  $^1\text{H}$  decoupling applied at an amplitude of  $\frac{1}{4}$  of the MAS frequency<sup>38</sup> or 100-140 ms MISSISSIPPI<sup>68</sup> at an amplitude of  $\frac{1}{2}$  the MAS frequency on resonance with the water signal.

$R_1$  and  $R_{1\rho}$  relaxation curves were sampled using 8-11 points for all experiments except the diamagnetic  $^{15}\text{N}$   $R_1$  in the complex where only 2 points were used (SI Tables 10-11). Error estimates for the integrals were achieved by duplicating one of the relaxation delays ( $R_1$ ) or spin-lock lengths ( $R_{1\rho}$ ). 10 kHz nutation frequency, measured by a nutation experiment, was used for the spin-lock field in the  $R_{1\rho}$  experiments.

All spectra were processed using TopSpin 3.2. GB1 resonances in the complex with IgG were previously assigned on the basis of 3D H(H)NH, CONH, CO(CA)NH and CANH experiments.<sup>7</sup> Peak integrals were calculated in TopSpin 3.2. OriginPro 2016 and MatLab R2014a was used to analyze the relaxation data.

Error estimates. Peak integrals from TopSpin or peak volumes from CCPNMR were exported to MatLab where an exponential function was used with the `fminsearchbnd` function to fit the relaxation data. Errors were calculated by a Monte Carlo error estimations for  $R_1$  and  $R_{1\rho}$  exponential fits. A random number between 0 and 1 was multiplied with the integral error and added to the recalculated integrals or volumes. The fitting was then repeated 2000 times with a new random number between 0 and 1 generated each time. Two times the standard deviations of the  $R_1$  or  $R_{1\rho}$  values received from the fits for each residue were used as errors. Errors for sPREs were obtained in the same way but with linear

fits instead of exponential. Error propagations for  $\Delta$ sPREs were calculated using standard formulas for error propagation.

PRE predictions. Predicted sPRE data was computed using a previously published grid-based approach<sup>30,33,54</sup> To this end, the structural model was placed in a grid with equally-spaced grid points. The grid point-to-grid point distance was set to 0.2 Å and the distance between the outer atoms of the protein and the edges of the grid box was set to 20 Å. Next, all grid points that are positioned within a radius  $r_{\text{clash}}$  around an atom of the protein were removed. The radius  $r_{\text{clash}}$  was set to  $r_{\text{clash}} = r_{\text{vdW}, i} + r_{\text{Gd}}$  where  $r_{\text{vdW}, i}$  is the van-der-Waals radius of atom  $i$  and  $r_{\text{Gd}}$  is the radius of the paramagnetic compound and was set to 3.5 Å. Next, the sPRE value ( $\text{sPRE}_i$ ) of atom  $i$  of the protein was computed by summing up the contributions of all remaining grid points according to

$$\text{sPRE}_i = \sum_{d_{ij} < 20 \text{ Å}} \frac{1}{d_{ij}^6} \quad (2.1)$$

where  $i$  is the index of the protein atom, the index  $j$  iterates over all remaining grid points and  $d_{ij}$  is the distance between the atom  $i$  and grid point  $j$ .

Whenever two sPREs data sets of different origin (e.g. theoretical and experimental sPREs or experimental sPREs derived from different relaxation measurements) are compared directly, one of the data sets is scaled by the ratio of the averages of the sPREs in each data set. Only data points for residues present in both data sets were used to calculate the average.

C++ code for calculating sPREs is available from the authors upon request. For published structures that contained several models (like solution NMR structure of GB1), the error of the sPRE prediction was estimated using the standard deviation of the sPRE values of the different models. For calculation of sPREs for GB1<sub>free</sub> solution structure (PDB ID: 3gb1<sup>58</sup>; our construct is a T2Q mutant but comparison of sPREs calculated from isolated GB1 from several different solution and x-ray structures suggested that in the case of amide sPREs differences are very small) was used with the sPRE reported as an average of the sPREs

calculated for each conformer in the bundle. For calculation of sPREs for GB1<sub>cryst</sub> X-ray structure (PDB ID: 2qmt<sup>57</sup>) was used with a molecule in the middle of a 3x3 unit cell crystal lattice generated in Chimera<sup>69</sup> using Multiscale Models tool. For sPREs for GB1:Fab complex model obtained by structural alignment of X-ray structure of GB1 (PDB ID: 2qmt<sup>57</sup>) with GB3 in X-ray structure of GB3:Fab (PDB ID 1igc<sup>70</sup>) was used. For sPREs for GB1:Fc complex model obtained by structural alignment of X-ray structure of GB1 (PDB ID: 2qmt<sup>57</sup>) with GB3 in X-ray structure of GB2:Fc (PDB ID 1fcc<sup>63</sup>) was used. For sPREs for GB1:IgG complex, model obtained by the alignment of the above two complexes on GB1 (PDB ID 1igc<sup>70</sup> and 1fcc<sup>63</sup>). Before sPRE calculation protons were added to the models using the default tool in Chimera.<sup>69</sup>

$\Delta$ sPREs were calculated as a difference between sPREs for isolated molecule in solution and sPREs in the assembly. Both experimental and theoretical  $\Delta$ sPREs were calculated. sPREs were scaled by ratio of averages before calculating  $\Delta$ sPREs to minimize bias from any particular data set. Here we typically scaled up the sPREs from the assembly to solution sPREs. Note that comparison of the two different theoretical sPRE data sets does not require scaling.

Fitting of the experimental  $\Delta$ sPREs to  $\Delta$ sPREs back-predicted from various models was performed in Matlab. The best fit was determined by minimizing the  $\chi^2$  target function:

$$\chi^2 = \sum_i \frac{(\Delta sPRE_{exp,i} - A \Delta sPRE_{calc,i})^2}{\sigma_{\Delta sPRE,exp,i}^2} \quad (2.2)$$

where  $\Delta sPRE_{exp,i}$  is experimental  $\Delta$ sPRE for residue  $i$ ,  $\Delta sPRE_{calc,i}$  is  $\Delta$ sPRE for residue  $i$  calculated from a given model,  $\sigma_{\Delta sPRE,exp,i}^2$  is error for experimental  $\Delta$ sPRE for residue  $i$  and  $A$  is a constant and the only fit parameter.

## 2.5 Acknowledgements

The research leading to these results has received funding from the European Research Council under the European Union's Seventh Framework Programme (FP/2007-2013) / ERC Grant Agreement 639907. J.R.L. also acknowledges funding from Royal Society Grant RG130022,



EPSRC Grant EP/L025906/1, BBSRC Grant BB/L022761/1 and Gates Foundation. C.O. acknowledges funding from the European Union under a Marie Curie Initial Training Network FP7-PEOPLE-2012-ITN Grant Agreement Number 316630 CAS-IDP. S.K. acknowledges support from BBSRC Grant BB/L022761/1. J.M.L. acknowledges support from EPSRC DTG. T.M. is supported by the OmicsCenter Graz, the Bavarian Ministry of Sciences, Research and the Arts (Bavarian Molecular Biosystems Research Network, to T.M.), the President's International Fellowship Initiative of CAS (No. 2015VBB045, to T.M.), the National Natural Science Foundation of China (No. 31450110423, to T.M.), the Austrian Science Fund (FWF: P28854, W1226-B18) as well as the Deutsche Forschungsgemeinschaft (DFG, MA5703/1-1). The UK 850 MHz solid-state NMR Facility used in this research was funded by EPSRC and BBSRC (contract reference PR140003), as well as the University of Warwick including via part funding through Birmingham Science City Advanced Materials Projects 1 and 2 supported by Advantage West Midlands (AWM) and the European Regional Development Fund (ERDF). Tallinn group was supported by PUT 1534 grant of ETAG. Fig. 2.1, 2.3, 2.4, 2.5, and SI fig. 2.4 were produced using the UCSF Chimera package, which was developed by the RBVI at the U. of California, San Francisco (supported by NIGMS P41-GM103311).

## 2.6 References

- (1) Gardiennet, C.; Schütz, A. K.; Hunkeler, A.; Kunert, B.; Terradot, L.; Böckmann, A.; Meier, B. H. *Angew. Chemie Int. Ed.* **2012**, *51* (31), 7855.
- (2) Loquet, A.; Sgourakis, N. G.; Gupta, R.; Giller, K.; Riedel, D.; Goosmann, C.; Griesinger, C.; Kolbe, M.; Baker, D.; Becker, S.; Lange, A. *Nature* **2012**, *486* (7402), 276.
- (3) Lu, M.; Hou, G.; Zhang, H.; Suiter, C. L.; Ahn, J.; Byeon, I.-J. L.; Perilla, J. R.; Langmead, C. J.; Hung, I.; Gor'kov, P. L.; Gan, Z.; Brey, W.; Aiken, C.; Zhang, P.; Schulten, K.; Gronenborn, A. M.; Polenova, T. *Proc. Natl. Acad. Sci.* **2015**, *112* (47), 14617.

- (4) Mainz, A.; Religa, T. L.; Sprangers, R.; Linser, R.; Kay, L. E.; Reif, B. *Angew. Chemie Int. Ed.* **2013**, 52 (33), 8746.
- (5) Barbet-Massin, E.; Huang, C.-T.; Daebel, V.; Hsu, S.-T. D.; Reif, B. *Angew. Chemie Int. Ed.* **2015**, 54 (14), 4367.
- (6) Jehle, S.; Rajagopal, P.; Bardiaux, B.; Markovic, S.; Kühne, R.; Stout, J. R.; Higman, V. A.; Klevit, R. E.; van Rossum, B.-J.; Oschkinat, H. *Nat. Struct. Mol. Biol.* **2010**, 17 (99), 1037.
- (7) Lamley, J. M.; Iuga, D.; Öster, C.; Sass, H.-J.; Rogowski, M.; Oss, A.; Past, J.; Reinhold, A.; Grzesiek, S.; Samoson, A.; Lewandowski, J. R. *J. Am. Chem. Soc.* **2014**, 136 (48), 16800.
- (8) Lamley, J. M.; Öster, C.; Stevens, R. A.; Lewandowski, J. R. *Angew. Chemie Int. Ed.* **2015**, 54 (51), 15374.
- (9) Hoop, C. L.; Lin, H.-K.; Kar, K.; Magyarfalvi, G.; Lamley, J. M.; Boatz, J. C.; Mandal, A.; Lewandowski, J. R.; Wetzel, R.; van der Wel, P. C. A. *Proc. Natl. Acad. Sci.* **2016**, 113 (6), 1546.
- (10) Good, D. B.; Wang, S.; Ward, M. E. M. E.; Struppe, J.; Brown, L. S. L. S.; Lewandowski, J. R.; Ladizhansky, V. *J. Am. Chem. Soc.* **2014**, 136 (7), 2833.
- (11) Jaroniec, C. P. *J. Magn. Reson.* **2015**, 253, 50.
- (12) Knight, M. J.; Pell, A. J.; Bertini, I.; Felli, I. C.; Gonnelli, L.; Pierattelli, R.; Herrmann, T.; Emsley, L.; Pintacuda, G. *Proc. Natl. Acad. Sci.* **2012**, 109 (28), 11095.
- (13) Wickramasinghe, N. P.; Kotecha, M.; Samoson, A.; Past, J.; Ishii, Y. *J. Magn. Reson.* **2007**, 184 (2), 350.
- (14) Nadaud, P. S.; Helmus, J. J.; Sengupta, I.; Jaroniec, C. P. *J. Am. Chem. Soc.* **2010**, 132 (28), 9561.
- (15) Ward, M. E.; Wang, S.; Krishnamurthy, S.; Hutchins, H.; Fey, M.; Brown, L. S.; Ladizhansky, V. *J. Biomol. NMR* **2014**, 58 (1), 37.
- (16) Balayssac, S.; Bertini, I.; Bhaumik, A.; Lelli, M.; Luchinat, C. *Proc.*

*Natl. Acad. Sci.* **2008**, 105 (45), 17284.

- (17) Linser, R.; Fink, U.; Reif, B. *J. Am. Chem. Soc.* **2009**, 131 (38), 13703.
- (18) Sengupta, I.; Nadaud, P. S.; Jaroniec, C. P. *Acc. Chem. Res.* **2013**, 46 (9), 2117.
- (19) Ullrich, S. J.; Hölper, S.; Glaubitz, C. *J. Biomol. NMR* **2014**, 58 (1), 27.
- (20) Nadaud, P. S.; Helmus, J. J.; Kall, S. L.; Jaroniec, C. P. *J. Am. Chem. Soc.* **2009**, 131 (23), 8108.
- (21) Wang, S.; Parthasarathy, S.; Xiao, Y.; Nishiyama, Y.; Long, F.; Matsuda, I.; Endo, Y.; Nemoto, T.; Yamauchi, K.; Asakura, T.; Takeda, M.; Terauchi, T.; Kainosho, M.; Ishii, Y. *Chem. Commun.* **2015**, 51 (81), 15055.
- (22) Nadaud, P. S.; Helmus, J. J.; Höfer, N.; Jaroniec, C. P. *J. Am. Chem. Soc.* **2007**, 129 (24), 7502.
- (23) Pintacuda, G.; Giraud, N.; Pierattelli, R.; Böckmann, A.; Bertini, I.; Emsley, L. *Angew. Chemie Int. Ed.* **2007**, 46 (7), 1079.
- (24) Jaroniec, C. P. *Solid State Nucl. Magn. Reson.* **2012**, 43–44, 1.
- (25) Wang, Y.; Spiller, M.; Caravan, P. *Magn. Reson. Med.* **2010**, 63 (3), 609.
- (26) Hocking, H. G.; Zangger, K.; Madl, T. *ChemPhysChem* **2013**, 14 (13), 3082.
- (27) Petros, A. M.; Mueller, L.; Kopple, K. D. *Biochemistry* **1990**, 29 (43), 10041.
- (28) Sakakura, M.; Noba, S.; Luchette, P. A.; Shimada, I.; Prosser, R. *S. J. Am. Chem. Soc.* **2005**, 127 (16), 5826.
- (29) Bernini, A.; Venditti, V.; Spiga, O.; Niccolai, N. *Progress in Nuclear Magnetic Resonance Spectroscopy*. Elsevier B.V. 2009, pp 278–

289.

- (30) Pintacuda, G.; Otting, G. *J. Am. Chem. Soc.* **2002**, 124 (3), 372.
- (31) Madl, T.; Bermel, W.; Zangger, K. *Angew. Chemie Int. Ed.* **2009**, 48 (44), 8259.
- (32) Wang, Y.; Schwieters, C. D.; Tjandra, N. *J. Magn. Reson.* **2012**, 221, 76.
- (33) Hartlmüller, C.; Göbl, C.; Madl, T. *Angew. Chemie Int. Ed.* **2016**, 55 (39), 11970.
- (34) Tomlinson, J. H.; Thompson, G. S.; Kalverda, A. P.; Zhuravleva, A.; O'Neill, A. J. *Sci. Rep.* **2016**, 6 (January), 19524.
- (35) Madl, T.; Güttler, T.; Görlich, D.; Sattler, M. *Angew. Chemie Int. Ed.* **2011**, 50 (17), 3993.
- (36) Parthasarathy, S.; Nishiyama, Y.; Ishii, Y. *Acc. Chem. Res.* **2013**, 46 (9), 2127.
- (37) Wickramasinghe, N. P.; Parthasarathy, S.; Jones, C. R.; Bhardwaj, C.; Long, F.; Kotecha, M.; Mehboob, S.; Fung, L. W.-M.; Past, J.; Samoson, A.; Ishii, Y. *Nat. Methods* **2009**, 6 (3), 215.
- (38) Lewandowski, J. R.; Sein, J.; Sass, H. J.; Grzesiek, S.; Blackledge, M.; Emsley, L. *J. Am. Chem. Soc.* **2010**, 132 (24), 8252.
- (39) Lewandowski, J. R. *Acc. Chem. Res.* **2013**, 46 (9), 2018.
- (40) Cai, S.; Seu, C.; Kovacs, Z.; Sherry, A. D.; Chen, Y. *J. Am. Chem. Soc.* **2006**, 128 (41), 13474.
- (41) Hocking, H. G.; Zangger, K.; Madl, T. *Chemphyschem* **2013**, 14 (13), 3082.
- (42) Ullrich, S. J.; Hölper, S.; Glaubitz, C. *J. Biomol. NMR* **2014**, 58 (1), 27.
- (43) Lewandowski, J. R.; Dumez, J.-N.; Akbey, Ü.; Lange, S.; Emsley, L.; Oschkinat, H. *J. Phys. Chem. Lett.* **2011**, 2 (17), 2205.

- (44) Andreas, L. B.; Jaudzems, K.; Stanek, J.; Lalli, D.; Bertarello, A.; Le Marchand, T.; Cala-De Paepe, D.; Kotelovica, S.; Akopjana, I.; Knott, B.; Wegner, S.; Engelke, F.; Lesage, A.; Emsley, L.; Tars, K.; Herrmann, T.; Pintacuda, G. *Proc. Natl. Acad. Sci.* **2016**, *113* (33), 9187.
- (45) Wittmann, J. J.; Agarwal, V.; Hellwagner, J.; Lends, A.; Cadalbert, R.; Meier, B. H.; Ernst, M. *J. Biomol. NMR* **2016**, *66* (4), 1.
- (46) Ye, Y. Q.; Malon, M.; Martineau, C.; Taulelle, F.; Nishiyama, Y. *J. Magn. Reson.* **2014**, *239*, 75.
- (47) Chevelkov, V.; Diehl, A.; Reif, B. *J. Chem. Phys.* **2008**, *128* (5), 52316.
- (48) Giraud, N.; Blackledge, M.; Goldman, M.; Böckmann, A.; Lesage, A.; Penin, F.; Emsley, L. *J. Am. Chem. Soc.* **2005**, *127* (51), 18190.
- (49) Krushelnitsky, A.; Bräuniger, T.; Reichert, D. *J. Magn. Reson.* **2006**, *182* (2), 339.
- (50) Smith, A. A.; Testori, E.; Cadalbert, R.; Meier, B. H.; Ernst, M. *J. Biomol. NMR* **2016**, *65* (3), 171.
- (51) Haller, J. D.; Schanda, P. *J. Biomol. NMR* **2013**, *57* (3), 263.
- (52) Krushelnitsky, A.; Zinkevich, T.; Reichert, D.; Chevelkov, V.; Reif, B. *J. Am. Chem. Soc.* **2010**, *132* (34), 11850.
- (53) Lewandowski, J. R.; Sass, H. J. J.; Grzesiek, S.; Blackledge, M.; Emsley, L. *J. Am. Chem. Soc.* **2011**, *133* (42), 16762.
- (54) Hartlmüller, C.; Günther, J. C.; Wolter, A. C.; Wöhnert, J.; Sattler, M.; Madl, T. *Sci. Rep.* **2017**, *7* (1), 5393.
- (55) Bouvignies, G.; Bernadó, P.; Meier, S.; Cho, K.; Grzesiek, S.; Brüschweiler, R.; Blackledge, M. *Proc. Natl. Acad. Sci. U. S. A.* **2005**, *102* (39), 13885.
- (56) Gallagher, T.; Alexander, P.; Bryan, P.; Gilliland, G. L. *Biochemistry*

**1994**, 33, 4721.

- (57) Frericks Schmidt, H. L.; Sperling, L. J.; Gao, Y. G.; Wylie, B. J.; Boettcher, J. M.; Wilson, S. R.; Rienstra, C. M. *J. Phys. Chem. B* **2007**, 111 (51), 14362.
- (58) Kuszewski, J.; Gronenborn, A. M.; Clore, G. M. *J. Am. Chem. Soc.* **1999**, 121 (10), 2337.
- (59) Lamley, J. M.; Lougher, M. J.; Sass, H. J.; Rogowski, M.; Grzesiek, S.; Lewandowski, J. R. *Phys. Chem. Chem. Phys.* **2015**, 17 (34), 21997.
- (60) Derrick, J. P.; Wigley, D. B. *Nature* **1992**, 359, 752.
- (61) Lian, L.-Y.; Barsukov, I. L. L.; Derrick, J. P. P.; Roberts, G. C. K. C. *Nat. Struct. Biol.* **1994**, 1 (6), 355.
- (62) Gronenborn, A. M.; Clore, G. M. *J. Mol. Biol.* **1993**, 233, 331.
- (63) Sauer-Eriksson, A. E.; Kleywegt, G. J.; Uhlén, M.; Jones, T. A. *Structure* **1995**, 3 (3), 265.
- (64) Gu, X.-H.; Gong, Z.; Guo, D.-C.; Zhang, W.-P.; Tang, C. *J. Biomol. NMR* **2014**, 58 (3), 149.
- (65) Vajpai, N.; Gentner, M.; Huang, J.-R.; Blackledge, M.; Grzesiek, S. *J. Am. Chem. Soc.* **2010**, 132 (9), 3196.
- (66) Franks, W. T.; Zhou, D. H.; Wylie, B. J.; Money, B. G.; Graesser, D. T.; Frericks, H. L.; Sahota, G.; Rienstra, C. M. *J. Am. Chem. Soc.* **2005**, 127 (35), 12291.
- (67) Fogh, R. H.; Ionides, J.; Ulrich, E. L.; Boucher, W.; Vranken, W. F.; Linge, J. P.; Habeck, M.; Rieping, W.; Bhat, T. N.; Westbrook, J.; Henrick, K.; Gilliland, G.; Berman, H.; Thornton, J.; Nilges, M.; Markley, J.; Laue, E. *Nat. Struct. Biol.* **2002**, 9 (6), 416.
- (68) Zhou, D. H.; Rienstra, C. M. *J. Magn. Reson.* **2008**, 192 (1), 167.
- (69) Pettersen, E. F.; Goddard, T. D.; Huang, C. C.; Couch, G. S.;

Greenblatt, D. M.; Meng, E. C.; Ferrin, T. E. *J. Comput. Chem.* **2004**, 25 (13), 1605.

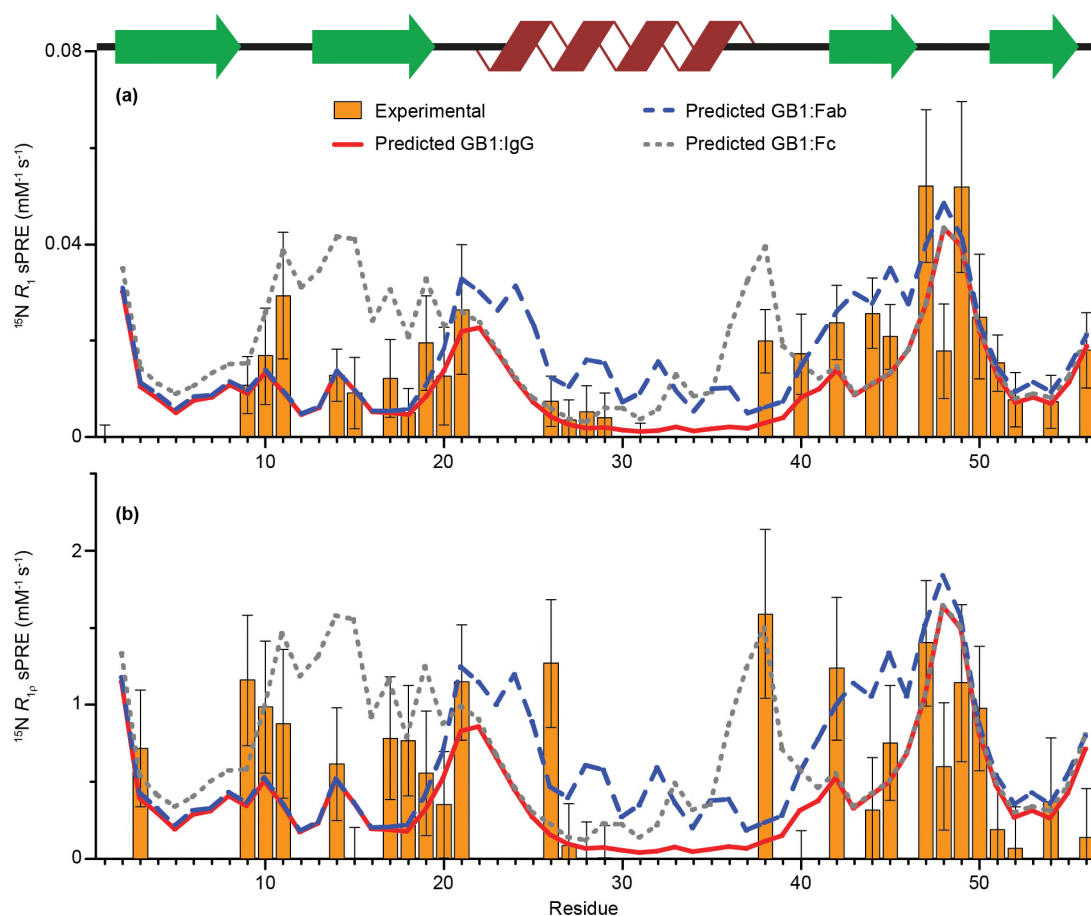
(70) Derrick, J. P.; Wigley, D. B. *J. Mol. Biol.* **1994**, 243 (5), 906.

## 2.7 Supporting Information

### 2.7.1 Results and Discussion

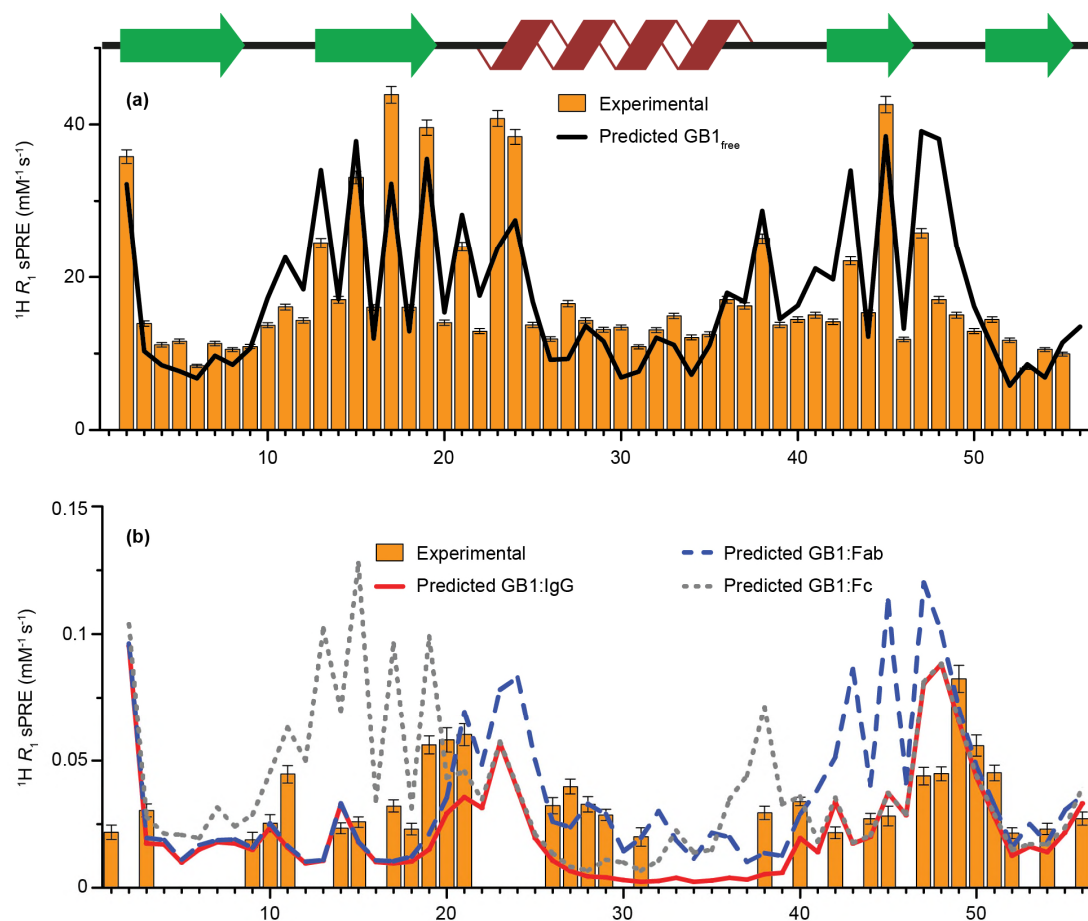
Direct comparisons between experimental and predicted sPREs of GB1<sub>IgG</sub> are presented in SI figure 2.1 for <sup>15</sup>N data, SI figure 2.2 for <sup>1</sup>H data including a comparison of predicted <sup>1</sup>H sPREs for GB1<sub>free</sub> with published experimental sPRE data<sup>1</sup>.

Examples of linear fits used to calculate sPREs from relaxation rates measured at different concentrations of Gd(DTPA-BMA) in GB1<sub>IgG</sub> samples are compared to linear fits obtained for GB1<sub>free</sub> in SI figure 2.3. The model of GB1 in complex with full length IgG that was used for the calculation of theoretical sPREs is presented in SI figure 2.4. Ca secondary chemical shifts for GB1<sub>free</sub> and GB1<sub>IgG</sub>, based on data from ref <sup>2</sup> are shown in SI figure 2.5. All data used in SI figures 2.1-2.3 are detailed in SI tables 2.1-2.9. SI tables 2.10 and 2.11 contain relaxation delays and spin-lock lengths used for all relaxation measurements. SI table 2.12 contains results from a  $\chi^2$  – based best fitting comparison between experimental and predicted  $\Delta$ sPRE data sets.

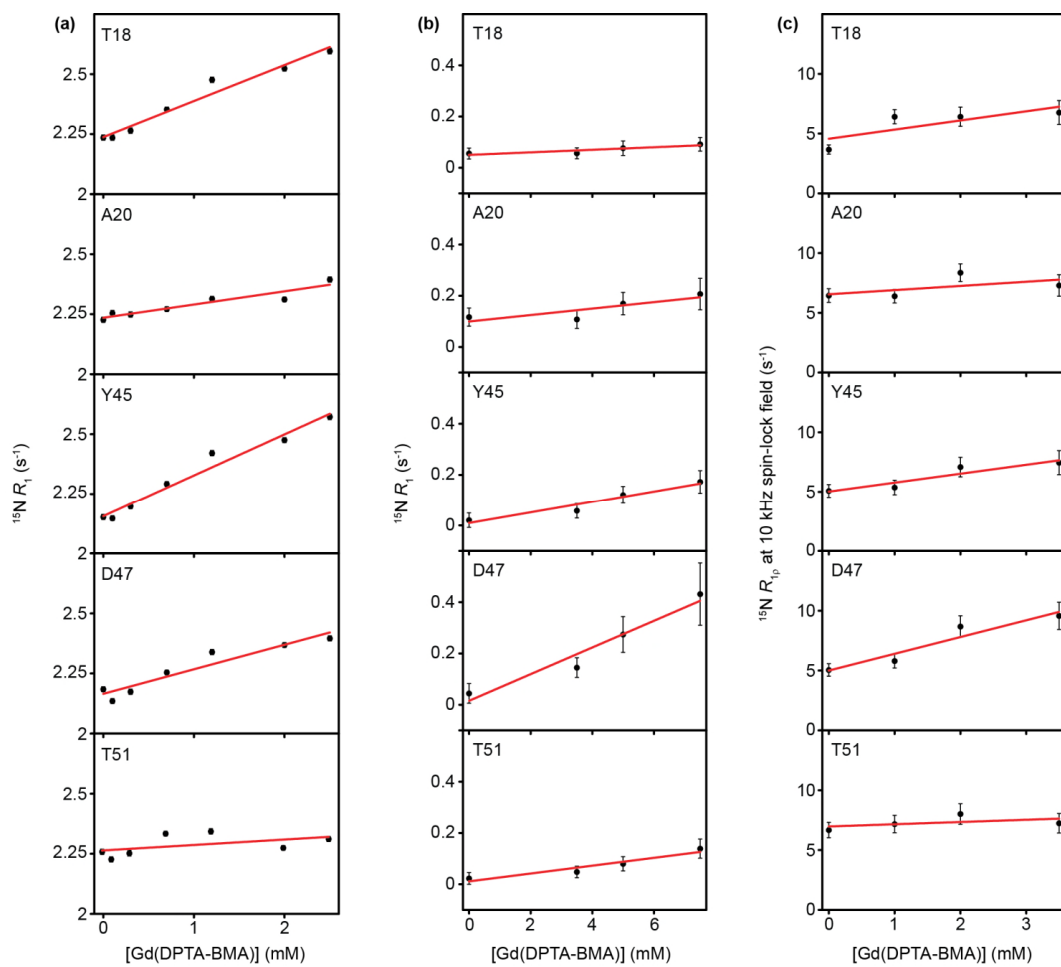


**SI figure 2.1.** Comparison between experimental and predicted  $^{15}\text{N}$  sPREs for GB1 in complex with IgG. For visualization purposes the predicted sPREs were scaled so that the average values are the same in the data sets that are compared. (a) GB1<sub>IgG</sub> based on  $^{15}\text{N}$   $R_1$ , (b) GB1<sub>IgG</sub> based on  $^{15}\text{N}$   $R_{1\rho}$ . The lines represent predicted sPREs; red line for GB1 in complex with both fragments of IgG, dashed blue line for GB1 in complex with the Fab fragment of IgG and dotted grey line for GB1 in complex with the Fc fragment of IgG.

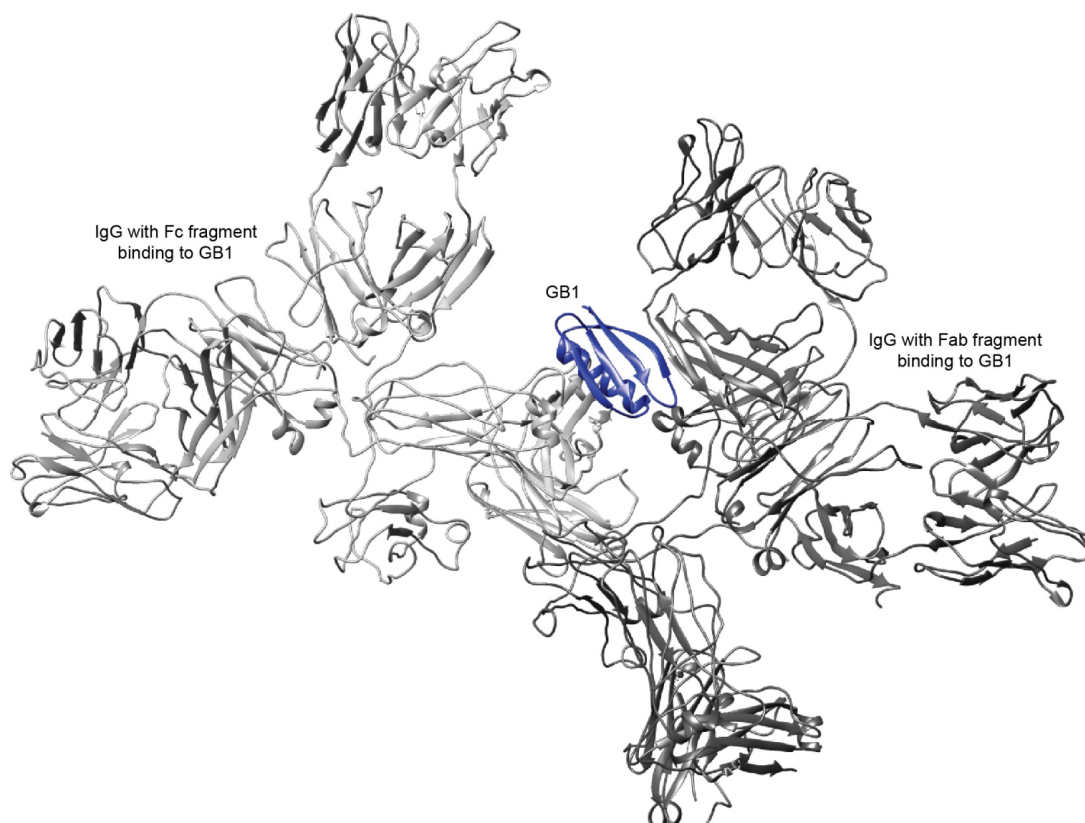




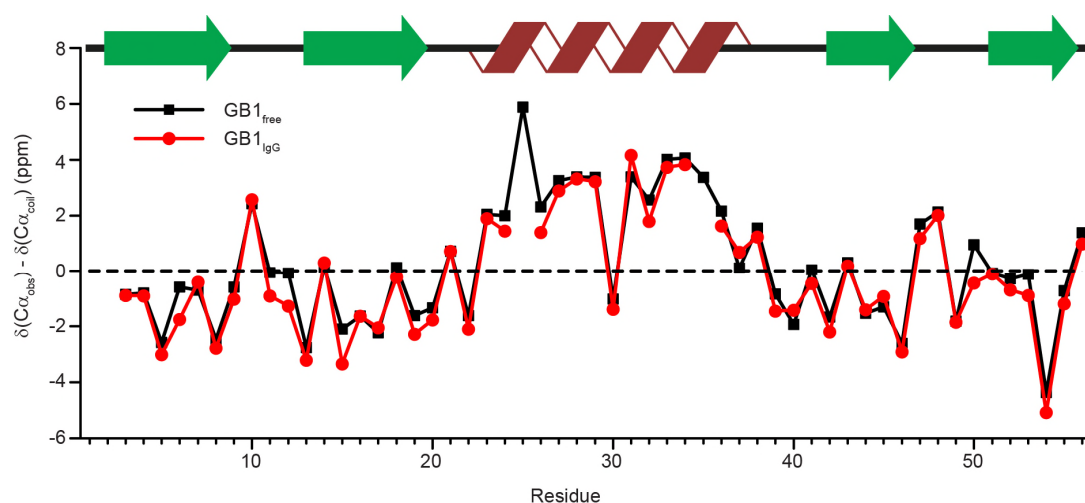
**SI figure 2.2.** Comparison between experimental and predicted  $^1\text{H}$  sPREs for GB1 free in solution (a) (experimental data from ref<sup>1</sup>) and GB1 in complex with IgG (b). For visualization purposes the predicted sPREs were scaled so that the average values are the same in the data sets that are compared. The lines represent predicted sPREs; black line for GB1 free in solution, red line for GB1 in complex with both fragments of IgG, dashed blue line for GB1 in complex with the Fab fragment of IgG and dotted grey line for GB1 in complex with the Fc fragment of IgG.



**SI figure 2.3.** Examples of linear fits used to extract  $^{15}\text{N}$  sPREs for (a) GB1<sub>free</sub>, (b) GB1<sub>IgG</sub> based on  $R_1$  and (c) GB1<sub>IgG</sub> based on  $R_{1p}$ .



**SI figure 2.4.** Model of GB1 in complex with IgG used for calculations of theoretical sPREs. The model is based on crystal structures, solution NMR and solid state NMR: Crystal structures of the Fab fragment of IgG in complex with GB3<sup>3</sup> and the Fc fragment of IgG in complex with GB2<sup>4</sup>; Solution NMR of GB2 in complex the Fab fragment<sup>5</sup>, GB2 in complex with the Fc fragment<sup>6</sup> and GB1 in complex with the Fc fragment<sup>7</sup>; and solid state NMR of GB1 in complex with full length IgG<sup>2</sup>.



**SI figure 2.5.**  $C^\alpha$  secondary chemical shifts for GB1 free in solution (black squares) and GB1 in complex with IgG (red circles), based on published data<sup>2</sup>.

**SI table 2.1.**  $^{15}\text{N}$   $R_1$  rates ( $\text{s}^{-1}$ ) for GB1<sub>free</sub> with varying concentration of Gd(DTPA-BMA)

Residue	0 mM		0.1 mM		0.3 mM		0.7 mM	
	$R_1$	Error	$R_1$	Error	$R_1$	Error	$R_1$	Error
2	2.2326	0.0109	2.2001	0.0110	2.2237	0.0113	2.3445	0.0104
3	2.2463	0.0111	2.2032	0.0110	2.2397	0.0111	2.3218	0.0103
4	2.2599	0.0115	2.3086	0.0117	2.3171	0.0119	2.3321	0.0103
5	2.3500	0.0118	2.3674	0.0124	2.3522	0.0121	2.3909	0.0103
6	2.2624	0.0110	2.2501	0.0116	2.2608	0.0116	2.3240	0.0099
7	2.2469	0.0111	2.2131	0.0112	2.2011	0.0110	2.2641	0.0098
8	2.1480	0.0108	2.1297	0.0110	2.1450	0.0108	2.1735	0.0095
9	2.2315	0.0111	2.2020	0.0109	2.2193	0.0111	2.2531	0.0097
10	2.1400	0.0106	2.1291	0.0107	2.1306	0.0110	2.1557	0.0091
11	2.0404	0.0096	2.0031	0.0101	2.0173	0.0102	2.0595	0.0088
12	1.8230	0.0087	1.8143	0.0089	1.8224	0.0090	1.9066	0.0083
13	2.0546	0.0103	2.0336	0.0101	2.0411	0.0103	2.1427	0.0093
14	2.0068	0.0098	2.0026	0.0099	2.0255	0.0099	2.0932	0.0090
15	2.0886	0.0103	2.0634	0.0104	2.1244	0.0107	2.1948	0.0096
16	2.2233	0.0111	2.2152	0.0113	2.2348	0.0113	2.2870	0.0101
17	2.1667	0.0104	2.1296	0.0103	2.1982	0.0109	2.3272	0.0100
18	2.2355	0.0112	2.2350	0.0112	2.2646	0.0113	2.3528	0.0101
19	2.0743	0.0101	2.0720	0.0102	2.1024	0.0107	2.1472	0.0088
20	2.2268	0.0109	2.2541	0.0114	2.2486	0.0113	2.2709	0.0099
21	2.2359	0.0112	2.2269	0.0112	2.2485	0.0115	2.3144	0.0100
23	2.2456	0.0112	2.2371	0.0113	2.2659	0.0113	2.3357	0.0103
24	2.1352	0.0105	2.1307	0.0108	2.1566	0.0108	2.2235	0.0096
25	2.2187	0.0107	2.1634	0.0105	2.1800	0.0109	2.2584	0.0098
26	2.3589	0.0117	2.3282	0.0117	2.3465	0.0122	2.4935	0.0107
27	2.2470	0.0110	2.2287	0.0111	2.2247	0.0112	2.2986	0.0101
28	2.2584	0.0112	2.2122	0.0111	2.2250	0.0113	2.3432	0.0101
29	2.2448	0.0112	2.2419	0.0116	2.2698	0.0112	2.3653	0.0102
30	2.2877	0.0114	2.2647	0.0116	2.2797	0.0116	2.3507	0.0103
31	2.2924	0.0114	2.3002	0.0117	2.2807	0.0115	2.3041	0.0098
32	2.2207	0.0112	2.2073	0.0114	2.2151	0.0116	2.2687	0.0098
33	2.2454	0.0114	2.2710	0.0115	2.2798	0.0115	2.2853	0.0099
34	2.3471	0.0118	2.3515	0.0117	2.3744	0.0126	2.4396	0.0104
35	2.1855	0.0111	2.1431	0.0105	2.1576	0.0109	2.2884	0.0100
36	2.2268	0.0116	2.2242	0.0113	2.2342	0.0116	2.2964	0.0102
39	2.1725	0.0109	2.1820	0.0114	2.1982	0.0110	2.2718	0.0096
40	1.9386	0.0097	1.9496	0.0099	1.9333	0.0098	1.9150	0.0084
42	2.1449	0.0106	2.1689	0.0112	2.1897	0.0110	2.2368	0.0098
43	2.1709	0.0109	2.1990	0.0113	2.2064	0.0108	2.2368	0.0098
44	2.2814	0.0110	2.2893	0.0117	2.3434	0.0120	2.4124	0.0105
45	2.1529	0.0108	2.1477	0.0103	2.1984	0.0109	2.2936	0.0101
46	2.2105	0.0107	2.2404	0.0113	2.2648	0.0110	2.2829	0.0096
47	2.1837	0.0105	2.1346	0.0102	2.1733	0.0109	2.2536	0.0097
48	2.0891	0.0103	2.0544	0.0104	2.0930	0.0105	2.1823	0.0095

49	2.1031	0.0101	2.0504	0.0099	2.0625	0.0103	2.1770	0.0095
50	2.3415	0.0115	2.2964	0.0113	2.3074	0.0119	2.3909	0.0105
51	2.2567	0.0109	2.2252	0.0108	2.2506	0.0113	2.3320	0.0100
52	2.2550	0.0110	2.2045	0.0110	2.2195	0.0110	2.2853	0.0103
53	2.2307	0.0106	2.1749	0.0105	2.1867	0.0106	2.2419	0.0097
54	2.4056	0.0122	2.3584	0.0117	2.3854	0.0120	2.4970	0.0111
55	2.2265	0.0108	2.2040	0.0112	2.2162	0.0112	2.2248	0.0095
56	2.2278	0.0112	2.2380	0.0112	2.2400	0.0113	2.2976	0.0098

**SI table 2.2.**  $^{15}\text{N}$   $R_1$  rates ( $\text{s}^{-1}$ ) for GB1<sub>free</sub> with varying concentration of Gd(DTPA-BMA)

Residue	1.2 mM		2 mM		2.5 mM	
	$R_1$	Error	$R_1$	Error	$R_1$	Error
2	2.3745	0.0110	2.3765	0.0102	2.4624	0.0114
3	2.3449	0.0110	2.2817	0.0097	2.2944	0.0102
4	2.3566	0.0109	2.3138	0.0098	2.3593	0.0104
5	2.4162	0.0112	2.3725	0.0099	2.3969	0.0114
6	2.3466	0.0104	2.2964	0.0099	2.3474	0.0106
7	2.3069	0.0107	2.2922	0.0100	2.3115	0.0104
8	2.1914	0.0101	2.1964	0.0095	2.1935	0.0099
9	2.2947	0.0104	2.2868	0.0099	2.2989	0.0106
10	2.2125	0.0101	2.2257	0.0096	2.2647	0.0101
11	2.1274	0.0095	2.1581	0.0093	2.2132	0.0099
12	1.9534	0.0087	1.9788	0.0085	1.9910	0.0092
13	2.2675	0.0105	2.3586	0.0100	2.3710	0.0106
14	2.1876	0.0099	2.2328	0.0097	2.3300	0.0104
15	2.3092	0.0105	2.4385	0.0104	2.4739	0.0111
16	2.4347	0.0111	2.5293	0.0109	2.5890	0.0118
17	2.4779	0.0117	2.5131	0.0106	2.5884	0.0117
18	2.4764	0.0113	2.5235	0.0109	2.5959	0.0117
19	2.2528	0.0100	2.2856	0.0100	2.3276	0.0107
20	2.3137	0.0103	2.3113	0.0101	2.3941	0.0110
21	2.3260	0.0106	2.3189	0.0097	2.3325	0.0107
23	2.4389	0.0112	2.3803	0.0104	2.4513	0.0109
24	2.2774	0.0104	2.2337	0.0095	2.2892	0.0102
25	2.2907	0.0105	2.2897	0.0101	2.3690	0.0106
26	2.4992	0.0112	2.3722	0.0105	2.3540	0.0108
27	2.3379	0.0104	2.3243	0.0101	2.3736	0.0107
28	2.3463	0.0108	2.2651	0.0095	2.2421	0.0097
29	2.3480	0.0108	2.3023	0.0099	2.3096	0.0105
30	2.3671	0.0110	2.3621	0.0097	2.4090	0.0109
31	2.3353	0.0108	2.3103	0.0101	2.3137	0.0105
32	2.3000	0.0104	2.2500	0.0096	2.2757	0.0103
33	2.3335	0.0110	2.3394	0.0099	2.3386	0.0105
34	2.4259	0.0112	2.3442	0.0101	2.4010	0.0110
35	2.3018	0.0108	2.2492	0.0097	2.2746	0.0104

36	2.3313	0.0108	2.2946	0.0096	2.3394	0.0107
39	2.2842	0.0106	2.2449	0.0096	2.2691	0.0101
40	1.9780	0.0089	2.0013	0.0087	2.0483	0.0095
42	2.2913	0.0103	2.3274	0.0102	2.3359	0.0105
43	2.3219	0.0105	2.3774	0.0101	2.4369	0.0107
44	2.4561	0.0111	2.4673	0.0110	2.5077	0.0112
45	2.4224	0.0111	2.4768	0.0105	2.5738	0.0113
46	2.3895	0.0110	2.4126	0.0102	2.4464	0.0110
47	2.3385	0.0107	2.3676	0.0100	2.3951	0.0107
48	2.2256	0.0099	2.2382	0.0094	2.3414	0.0107
49	2.2145	0.0100	2.2701	0.0096	2.2642	0.0100
50	2.4307	0.0111	2.4533	0.0105	2.4683	0.0112
51	2.3415	0.0110	2.2728	0.0097	2.3099	0.0104
52	2.3211	0.0105	2.3414	0.0099	2.3961	0.0107
53	2.2821	0.0104	2.2498	0.0099	2.2661	0.0102
54	2.4939	0.0115	2.4206	0.0104	2.4426	0.0112
55	2.3001	0.0103	2.3009	0.0098	2.3139	0.0105
56	2.3409	0.0107	2.3299	0.0100	2.3663	0.0106

**SI table 2.3.**  $^{15}\text{N}$   $R_1$  rates ( $\text{s}^{-1}$ ) for GB1<sub>cryst</sub> with 0 and 2 mM Gd(DTPA-BMA)

Residue	0 mM		2 mM	
	$R_1$	Error	$R_1$	Error
2	0.0616	0.0060	0.0783	0.0080
3	0.0343	0.0041	0.0474	0.0065
6	0.0157	0.0025	0.0392	0.0056
8	0.0343	0.0043	0.0461	0.0065
9	0.0466	0.0052	0.0594	0.0070
10	0.0814	0.0090	0.0954	0.0098
11	0.0993	0.0104	0.1605	0.0171
12	0.0986	0.0102	0.1193	0.0115
14	0.0542	0.0062	0.0573	0.0067
15	0.0330	0.0047	0.0377	0.0060
16	0.0416	0.0046	0.0358	0.0056
17	0.1044	0.0118	0.1063	0.0110
18	0.0650	0.0069	0.0826	0.0088
19	0.1047	0.0106	0.1255	0.0133
24	0.0358	0.0047	0.0627	0.0075
26	0.0223	0.0033	0.0238	0.0045
28	0.0252	0.0041	0.0362	0.0058
29	0.0271	0.0041	0.0422	0.0058
32	0.0259	0.0042	0.0419	0.0064
33	0.0279	0.0043	0.0327	0.0058
35	0.0316	0.0044	0.0457	0.0066
36	0.0264	0.0043	0.0393	0.0059
39	0.0514	0.0056	0.0610	0.0069

40	0.1590	0.0185	0.1644	0.0175
44	0.0217	0.0034	0.0211	0.0047
45	0.0163	0.0034	0.0258	0.0050
46	0.0246	0.0037	0.0333	0.0056
49	0.0614	0.0068	0.0902	0.0096
51	0.0205	0.0035	0.0239	0.0054
52	0.0112	0.0030	0.0174	0.0047
53	0.0110	0.0029	0.0173	0.0047
54	0.0149	0.0034	0.0192	0.0051
55	0.0225	0.0040	0.0370	0.0058
56	0.0531	0.0056	0.0722	0.0078

**SI table 2.4.**  $^{15}\text{N}$   $R_1$  rates ( $\text{s}^{-1}$ ) for GB1<sub>IG</sub> with varying concentrations of Gd(DTPA-BMA)

Residue	0 mM		3.5 mM		5 mM		7.5 mM	
	$R_1$	Error	$R_1$	Error	$R_1$	Error	$R_1$	Error
1	0.0334	-	0.0526	0.0269	0.0610	0.0248	-	-
9	0.0373	-	0.0819	0.0272	0.0877	0.0260	0.1194	0.0282
10	0.0547	-	0.1512	0.0445	0.1100	0.0367	0.1943	0.0502
11	-	-	0.1066	0.0296	0.0828	0.0300	0.2619	0.0594
14	0.0126	-	0.0858	0.0243	0.1057	0.0308	0.1039	0.0255
15	0.0620	-	0.0841	0.0324	0.0672	0.0257	0.1401	0.0377
17	0.0449	-	0.0595	0.0290	0.0623	0.0231	0.1436	0.0462
18	0.0556	-	0.0563	0.0214	0.0763	0.0284	0.0917	0.0266
19	0.0487	-	0.1452	0.0362	0.1540	0.0396	0.1971	0.0542
20	0.1158	-	0.1068	0.0352	0.1686	0.0436	0.2058	0.0614
21	0.0781	-	0.2517	0.0553	0.2270	0.0584	0.2838	0.0758
26	0.0309	-	0.0909	0.0237	0.0614	0.0224	0.0927	0.0267
27	0.0044	-	0.0270	0.0236	0.0555	0.0213	0.0225	0.0185
28	0.0296	-	0.0746	0.0236	0.0299	0.0244	0.0795	0.0278
29	0.0110	-	0.0432	0.0276	0.0540	0.0258	0.0370	0.0174
31	0.0305	-	0.0374	0.0249	0.0330	0.0212	0.0212	0.0201
38	0.0264	-	0.0557	0.0278	0.1207	0.0364	0.1716	0.0417
40	0.0644	-	0.0763	0.0311	0.0540	0.0245	0.2138	0.0484
42	0.0322	-	0.0854	0.0297	0.1276	0.0290	0.2133	0.0483
44	0.0005	-	0.0073	0.0174	0.0706	0.0260	0.2697	0.0644
45	0.0204	-	0.0573	0.0285	0.1210	0.0333	0.1722	0.0445
47	0.0422	-	0.1429	0.0384	0.2719	0.0697	0.4298	0.1216
48	0.0530	-	0.1578	0.0416	0.1331	0.0344	0.1951	0.0518
49	0.0277	-	0.3069	0.0774	0.1149	0.0329	0.4797	0.1182
50	0.0344	-	0.2602	0.0512	0.2072	0.0486	0.2279	0.0735
51	0.0227	-	0.0481	0.0227	0.0798	0.0277	0.1389	0.0374
52	0.0150	-	0.0668	0.0250	0.0999	0.0300	0.0630	0.0272
54	0.0256	-	0.0495	0.0266	0.0819	0.0278	0.0748	0.0249
56	0.0372	-	0.1102	0.0318	0.1166	0.0353	0.1765	0.0437

**SI table 2.5.**  $^{15}\text{N}$   $R_{1\rho}$  rates ( $\text{s}^{-1}$ ) at 10 kHz nutation frequency for GB1<sub>IgG</sub> with varying concentrations of Gd(DTPA-BMA)

Residue	0 mM		1 mM		2 mM		3.5 mM	
	$R_{1\rho}$	Error	$R_{1\rho}$	Error	$R_{1\rho}$	Error	$R_{1\rho}$	Error
3	6.04	0.57	5.39	0.49	7.72	0.92	8.04	1.04
9	5.78	0.61	6.57	0.68	10.03	1.13	9.32	1.15
10	6.74	0.58	5.94	0.65	10.63	1.03	9.20	1.21
11	6.85	0.73	7.18	0.60	9.38	0.88	9.58	1.34
14	5.78	0.50	6.75	0.68	11.10	1.04	7.23	0.99
15	6.09	0.60	7.80	0.67	7.70	0.86	6.11	0.90
17	3.27	0.36	7.18	0.61	6.17	0.85	6.78	1.18
18	3.66	0.39	6.41	0.59	6.41	0.80	6.76	1.00
19	4.89	0.54	7.62	0.75	6.49	0.86	7.45	1.09
20	6.44	0.57	6.39	0.57	8.36	0.74	7.29	0.90
21	5.76	0.57	7.59	0.68	8.74	1.05	9.86	1.04
26	4.89	0.63	5.80	0.60	7.17	0.89	9.26	1.20
27	8.47	0.71	6.27	0.65	7.55	0.72	8.23	0.93
28	9.14	0.81	7.21	0.69	5.93	0.73	7.25	1.06
29	6.73	0.70	7.48	0.70	6.25	0.66	7.09	0.85
38	5.76	0.57	9.97	0.92	8.75	1.00	12.23	1.59
40	7.84	0.67	5.48	0.56	7.55	0.60	6.37	0.79
42	6.97	0.66	6.19	0.61	9.99	1.02	10.50	1.28
44	6.58	0.74	5.28	0.55	6.24	0.64	7.34	0.85
45	5.08	0.54	5.37	0.61	7.09	0.82	7.46	1.01
47	5.05	0.52	5.80	0.59	8.68	0.90	9.57	1.14
48	6.19	0.57	6.69	0.68	8.03	0.91	8.12	1.13
49	7.27	0.69	8.56	0.79	9.99	1.10	11.23	1.42
50	4.85	0.49	6.14	0.68	8.02	0.93	8.12	1.13
51	6.62	0.64	7.12	0.73	7.96	0.86	7.19	0.82
52	6.94	0.64	4.88	0.56	7.16	0.81	6.46	0.97
54	6.21	0.72	7.65	0.73	7.47	0.84	7.76	1.10
56	5.50	0.56	5.25	0.58	6.53	0.79	5.70	1.06

**SI table 2.6.**  $^1\text{H}$   $R_1$  rates ( $\text{s}^{-1}$ ) for GB1<sub>IgG</sub> with 0 and 100 mM Cu(EDTA)

Residue	0 mM		100 mM	
	$R_1$	Error	$R_1$	Error
1	1.925	0.166	4.102	0.171
3	1.151	0.109	4.188	0.179
9	1.913	0.210	3.794	0.155
10	1.952	0.229	4.492	0.183
11	1.223	0.145	5.680	0.255
14	1.046	0.098	3.387	0.165
15	0.948	0.099	3.531	0.144



17	1.124	0.118	4.336	0.174
18	1.172	0.119	3.487	0.161
19	0.958	0.104	6.577	0.289
20	1.945	0.219	7.762	0.350
21	1.556	0.166	7.580	0.338
26	1.645	0.189	4.868	0.206
27	1.457	0.146	5.439	0.208
28	1.683	0.200	4.964	0.176
29	0.977	0.116	3.841	0.155
31	1.845	0.270	3.847	0.151
38	1.071	0.166	4.008	0.173
40	0.636	0.073	4.024	0.129
42	1.433	0.159	3.603	0.136
44	0.975	0.108	3.686	0.149
45	2.227	0.256	5.043	0.225
47	1.344	0.143	5.731	0.251
48	1.000	0.102	5.482	0.218
49	1.470	0.176	9.712	0.427
50	1.275	0.151	6.866	0.328
51	1.279	0.135	5.802	0.228
52	1.250	0.116	3.394	0.142
54	1.098	0.113	3.412	0.151
56	1.194	0.114	3.911	0.185

**SI table 2.7.** Experimental  $^{15}\text{N}$  sPRE values ( $\text{mM}^{-1} \text{s}^{-1}$ ) for GB1<sub>free</sub>, GB1<sub>cryst</sub> and GB1<sub>IgG</sub> and  $^1\text{H}$  sPREs for GB1<sub>IgG</sub>

Residue	$^{15}\text{N}$ $R_1$ GB1 <sub>free</sub>		$^{15}\text{N}$ $R_1$ GB1 <sub>cryst</sub>		$^{15}\text{N}$ $R_1$ GB1 <sub>IgG</sub>		$^{15}\text{N}$ $R_{1\rho}$ GB1 <sub>IgG</sub>		$^1\text{H}$ $R_1$ GB1 <sub>IgG</sub>	
	PRE	Error	PRE	Error	PRE	Error	PRE	Error	PRE	Error
1	-	-	-	-	0	0.0025	-	-	0.0218	0.0028
2	0.0944	0.0053	0.0084	0.0056	-	-	-	-	-	-
3	0.0271	0.005	0.0065	0.0045	-	-	0.7156	0.3773	0.0304	0.0025
4	0.0228	0.0052	-	-	-	-	-	-	-	-
5	0.0145	0.0055	-	-	-	-	-	-	-	-
6	0.0317	0.0051	0.0117	0.0035	-	-	-	-	-	-
7	0.0378	0.0052	-	-	-	-	-	-	-	-
8	0.0248	0.005	0.0059	0.0046	-	-	-	-	-	-
9	0.0357	0.0051	0.0064	0.0051	0.0107	0.0059	1.1588	0.4248	0.0188	0.003
10	0.0541	0.0048	0.0070	0.0073	0.0168	0.0101	0.9828	0.4281	0.0254	0.0034
11	0.0789	0.0047	0.0306	0.0115	0.0294	0.0132	0.8748	0.483	0.0446	0.0034
12	0.0762	0.0043	0.0103	0.0090	-	-	-	-	-	-
13	0.1495	0.005	-	-	-	-	-	-	-	-
14	0.1296	0.0048	0.0016	0.0035	0.0128	0.0054	0.6142	0.3647	0.0234	0.0022
15	0.1706	0.0053	0.0024	0.0034	0.0091	0.0074	0	0.2029	0.0258	0.002
16	0.1593	0.0055	0.0010	0.0024	-	-	-	-	-	-
17	0.1832	0.0054	0.0010	0.0053	0.0121	0.008	0.7815	0.3969	0.0321	0.0024

18	0.15	0.0054	0.0088	0.0066	0.005	0.005	0.7663	0.3577	0.0231	0.0023
19	0.1072	0.0049	0.0104	0.0096	0.0195	0.0099	0.5544	0.4032	0.0562	0.0036
20	0.055	0.0053	-	-	0.0126	0.0101	0.3511	0.3448	0.0582	0.0048
21	0.0408	0.0052	-	-	0.0265	0.0135	1.1452	0.3779	0.0602	0.0043
22	-	-	-	-	-	-	-	-	-	-
23	0.0822	0.0053	-	-	-	-	-	-	-	-
24	0.059	0.0049	0.0134	0.0051	-	-	-	-	-	-
25	0.0675	0.0052	-	-	-	-	-	-	-	-
26	0.0065	0.0053	0.0010	0.0019	0.0074	0.0052	1.2675	0.4171	0.0322	0.0032
27	0.0548	0.0052	-	-	0.0035	0.0042	0.0857	0.2732	0.0398	0.003
28	0.0074	0.005	0.0055	0.0041	0.0052	0.0054	0	0.2381	0.0328	0.0031
29	0.0238	0.0052	0.0076	0.0041	0.004	0.0051	0.0054	0.2093	0.0286	0.0022
30	0.0508	0.0054	-	-	-	-	-	-	-	-
31	0.0103	0.0053	-	-	0	0.0028	-	-	0.02	0.0036
32	0.0238	0.0053	0.0080	0.0043	-	-	-	-	-	-
33	0.0358	0.0052	0.0024	0.0033	-	-	-	-	-	-
34	0.0089	0.0055	-	-	-	-	-	-	-	-
35	0.0451	0.0051	0.0070	0.0045	-	-	-	-	-	-
36	0.043	0.0053	0.0065	0.0042	-	-	-	-	-	-
37	-	-	-	-	-	-	-	-	-	-
38	-	-	-	-	0.0199	0.0067	1.5898	0.5496	0.0294	0.0027
39	0.0344	0.0049	0.0048	0.0048	-	-	-	-	-	-
40	0.0426	0.0046	0.0027	0.0097	0.0172	0.0084	0	0.1836	0.0339	0.0017
41	-	-	-	-	-	-	-	-	-	-
42	0.077	0.0051	-	-	0.0238	0.0078	1.2338	0.465	0.0217	0.0023
43	0.1036	0.0052	-	-	-	-	-	-	-	-
44	0.0869	0.0054	0.0010	0.0019	0.0257	0.0074	0.3167	0.3382	0.0271	0.0021
45	0.1717	0.0053	0.0047	0.0034	0.0208	0.0068	0.7502	0.3728	0.0282	0.0039
46	0.0929	0.0053	0.0043	0.0038	-	-	-	-	-	-
47	0.102	0.0051	0.0053	0.0044	0.0521	0.0158	1.4001	0.4093	0.0439	0.0034
48	0.1009	0.005	-	-	0.0178	0.0099	0.5972	0.4123	0.0448	0.0028
49	0.0875	0.0048	0.0144	0.0068	0.0519	0.0177	1.1401	0.5106	0.0824	0.0053
50	0.0667	0.0054	-	-	0.025	0.013	0.974	0.4039	0.0559	0.0042
51	0.0226	0.0051	0.0017	0.0026	0.0153	0.0058	0.1878	0.3055	0.0452	0.0031
52	0.0668	0.0052	0.0031	0.0031	0.0077	0.0056	0.0688	0.2669	0.0214	0.0021
53	0.0283	0.0049	0.0031	0.0030	-	-	-	-	-	-
54	0.0215	0.0055	0.0022	0.0028	0.0073	0.0055	0.3692	0.4143	0.0231	0.0022
55	0.0447	0.0051	0.0073	0.0040	-	-	-	-	-	-
56	0.054	0.0051	0.0096	0.0056	0.018	0.0079	0.1379	0.3161	0.0272	0.0025

**SI table 2.8.** Predicted  $^{15}\text{N}$  sPRE values ( $\text{mM}^{-1} \text{s}^{-1}$ ) for GB1<sub>free</sub>, GB1<sub>cryst</sub>, GB1<sub>IgG</sub> and GB1 in complex with IgG fragments

Residue	GB1 <sub>free</sub>		GB1 <sub>cryst</sub>		GB1 <sub>IgG</sub>		GB1 <sub>IgG</sub> (Fab)		GB1 <sub>IgG</sub> (Fc)	
	PRE	Error	PRE	Error	PRE	Error	PRE	Error	PRE	Error
1	-	-	-	-	-	-	-	-	-	-

2	4.234	0.275	0.241	-	3.564	-	3.652	-	4.128	-
3	1.944	0.134	0.179	-	1.219	-	1.328	-	1.685	-
4	1.593	0.07	0.159	-	0.929	-	1.021	-	1.288	-
5	1.245	0.028	0.092	-	0.594	-	0.677	-	1.054	-
6	1.344	0.023	0.081	-	0.892	-	0.974	-	1.251	-
7	1.554	0.093	0.097	-	0.964	-	1.021	-	1.561	-
8	1.826	0.11	0.203	-	1.267	-	1.343	-	1.782	-
9	2.030	0.111	0.262	-	1.060	-	1.134	-	1.795	-
10	3.447	0.098	0.603	-	1.570	-	1.640	-	3.046	-
11	4.965	0.062	0.516	-	1.106	-	1.139	-	4.556	-
12	4.079	0.078	0.175	-	0.541	-	0.569	-	3.666	-
13	4.337	0.188	0.132	-	0.715	-	0.733	-	4.072	-
14	4.217	0.161	0.100	-	1.601	-	1.617	-	4.906	-
15	4.557	0.192	0.074	-	1.134	-	1.146	-	4.838	-
16	3.029	0.043	0.116	-	0.607	-	0.636	-	2.854	-
17	3.990	0.112	0.290	-	0.588	-	0.639	-	3.616	-
18	3.016	0.103	0.454	-	0.547	-	0.676	-	2.440	-
19	4.470	0.084	0.853	-	0.986	-	1.285	-	3.871	-
20	3.142	0.06	0.234	-	1.613	-	2.158	-	2.717	-
21	4.445	0.108	0.109	-	2.565	-	3.866	-	3.072	-
22	3.773	0.037	0.133	-	2.664	-	3.563	-	2.818	-
23	3.106	0.058	0.374	-	2.047	-	3.105	-	2.103	-
24	3.899	0.032	0.444	-	1.396	-	3.705	-	1.442	-
25	3.046	0.026	0.187	-	0.844	-	2.764	-	0.946	-
26	1.666	0.032	0.118	-	0.488	-	1.452	-	0.705	-
27	1.557	0.015	0.087	-	0.304	-	1.229	-	0.443	-
28	2.441	0.035	0.097	-	0.210	-	1.881	-	0.372	-
29	2.297	0.067	0.236	-	0.230	-	1.789	-	0.714	-
30	1.357	0.023	0.191	-	0.172	-	0.845	-	0.699	-
31	1.373	0.029	0.095	-	0.133	-	1.083	-	0.435	-
32	2.322	0.094	0.153	-	0.158	-	1.837	-	0.678	-
33	2.259	0.062	0.321	-	0.240	-	1.127	-	1.523	-
34	1.483	0.023	0.129	-	0.147	-	0.626	-	0.994	-
35	2.225	0.079	0.170	-	0.195	-	1.177	-	1.094	-
36	4.091	0.162	0.214	-	0.247	-	1.198	-	2.686	-
37	4.257	0.07	0.138	-	0.207	-	0.582	-	3.836	-
38	5.536	0.136	0.138	-	0.349	-	0.721	-	4.667	-
39	2.980	0.068	0.124	-	0.472	-	0.868	-	2.211	-
40	2.808	0.09	0.221	-	0.971	-	1.740	-	1.795	-
41	3.629	0.128	0.295	-	1.166	-	2.405	-	1.429	-
42	3.854	0.071	0.219	-	1.637	-	3.084	-	1.725	-
43	4.062	0.104	0.087	-	1.023	-	3.530	-	1.059	-
44	3.141	0.046	0.063	-	1.289	-	3.267	-	1.313	-
45	4.404	0.086	0.066	-	1.544	-	4.141	-	1.557	-
46	3.362	0.049	0.081	-	2.121	-	3.265	-	2.140	-
47	4.889	0.225	0.180	-	3.273	-	4.713	-	3.294	-

48	6.265	0.154	0.147	-	5.107	-	5.714	-	5.122	-
49	5.042	0.049	0.171	-	4.663	-	4.889	-	4.695	-
50	2.830	0.041	0.183	-	2.568	-	2.764	-	2.623	-
51	1.813	0.031	0.121	-	1.475	-	1.685	-	1.554	-
52	1.176	0.017	0.064	-	0.839	-	1.100	-	0.937	-
53	1.455	0.016	0.069	-	0.971	-	1.333	-	1.057	-
54	1.340	0.017	0.089	-	0.815	-	1.106	-	0.960	-
55	1.999	0.047	0.164	-	1.323	-	1.695	-	1.474	-
56	2.695	0.075	0.386	-	2.208	-	2.473	-	2.501	-

**SI table 2.9.** Predicted  $^1\text{H}$  PRE values ( $\text{mM}^{-1} \text{s}^{-1}$ ) for GB1<sub>free</sub>, GB1<sub>IgG</sub> and GB1 in complex with IgG fragments

Residue	$^1\text{H}$ GB1 <sub>free</sub>		$^1\text{H}$ GB1 <sub>IgG</sub>		$^1\text{H}$ GB1 <sub>IgG</sub> (Fab)		$^1\text{H}$ GB1 <sub>IgG</sub> (Fc)	
	PRE	Error	PRE	Error	PRE	Error	PRE	Error
1	-	-	-	-	-	-	-	-
2	6.05579	0.86467	5.713	-	5.771	-	6.225	-
3	1.92983	0.07241	1.043	-	1.166	-	1.674	-
4	1.58913	0.06759	1.020	-	1.125	-	1.278	-
5	1.44369	0.04194	0.592	-	0.658	-	1.247	-
6	1.26859	0.02899	0.907	-	1.015	-	1.165	-
7	1.8265	0.07138	1.075	-	1.117	-	1.890	-
8	1.59691	0.04574	1.038	-	1.142	-	1.442	-
9	2.00112	0.07334	0.889	-	0.951	-	1.727	-
10	3.23847	0.13902	1.424	-	1.518	-	2.725	-
11	4.24353	0.18799	0.946	-	0.992	-	3.780	-
12	3.45689	0.13274	0.577	-	0.617	-	2.996	-
13	6.39924	0.26087	0.641	-	0.653	-	6.128	-
14	3.20512	0.19916	1.964	-	1.986	-	4.184	-
15	7.10608	0.63004	1.078	-	1.087	-	7.666	-
16	2.24653	0.10432	0.608	-	0.645	-	2.049	-
17	6.05796	0.23198	0.576	-	0.622	-	5.773	-
18	2.42318	0.11199	0.614	-	0.731	-	1.866	-
19	6.66838	0.63787	0.908	-	1.262	-	5.941	-
20	2.88295	0.18841	1.753	-	2.123	-	2.589	-
21	5.294	0.25301	2.133	-	4.159	-	2.745	-
22	3.29529	0.11104	1.884	-	2.901	-	2.086	-
23	4.47693	0.33442	3.417	-	4.690	-	3.447	-
24	5.16172	0.15534	2.304	-	4.973	-	2.349	-
25	3.13895	0.14487	1.172	-	3.001	-	1.265	-
26	1.72057	0.05982	0.634	-	1.556	-	0.812	-
27	1.74493	0.07566	0.388	-	1.427	-	0.500	-
28	2.55056	0.27893	0.264	-	1.976	-	0.408	-
29	2.17533	0.13373	0.245	-	1.737	-	0.660	-
30	1.29119	0.04752	0.181	-	0.863	-	0.594	-
31	1.43688	0.09264	0.138	-	1.179	-	0.399	-
32	2.26622	0.18417	0.163	-	1.806	-	0.642	-

33	2.08873	0.10234	0.229	-	1.120	-	1.346	-
34	1.35966	0.0466	0.142	-	0.676	-	0.825	-
35	2.07551	0.14472	0.172	-	1.297	-	0.889	-
36	3.36134	0.17582	0.231	-	1.191	-	2.085	-
37	3.14332	0.10107	0.195	-	0.611	-	2.650	-
38	5.39785	0.25964	0.324	-	0.823	-	4.271	-
39	2.72259	0.1352	0.349	-	0.751	-	1.971	-
40	3.05651	0.28448	1.174	-	1.745	-	2.147	-
41	3.9637	0.91033	0.841	-	2.320	-	1.087	-
42	3.69336	0.14428	2.023	-	3.097	-	2.124	-
43	6.38352	0.62965	1.038	-	5.179	-	1.065	-
44	2.28854	0.06131	1.198	-	2.417	-	1.234	-
45	7.23329	0.11884	2.227	-	6.785	-	2.234	-
46	2.4899	0.04131	1.713	-	2.467	-	1.738	-
47	7.35167	0.0862	4.824	-	7.204	-	4.875	-
48	7.15681	0.10108	5.291	-	6.043	-	5.305	-
49	4.5353	0.0803	3.932	-	4.236	-	3.955	-
50	3.03221	0.09807	2.602	-	2.868	-	2.641	-
51	2.05768	0.0396	1.671	-	1.933	-	1.726	-
52	1.09254	0.01821	0.759	-	0.958	-	0.893	-
53	1.61171	0.0239	0.967	-	1.498	-	1.029	-
54	1.28433	0.02151	0.839	-	1.047	-	1.026	-
55	2.13988	0.08549	1.295	-	1.824	-	1.415	-
56	2.53396	0.17187	1.992	-	2.183	-	2.354	-

**SI table 2.10.** Relaxation delays (s) used and total experimental time for  $R_1$  measurements of GB1<sub>free</sub> and GB1<sub>cryst</sub>

15N $R_1$ , GB1 free in solution, Gd(DTPA-BMA)								15N $R_1$ , GB1 crystals, Gd(DTPA-BMA)	
	0 mM	0.1 mM	0.3 mM	0.7 mM	1.2 mM	2 mM	2.5 mM	0 mM	2 mM
	0.05	0.05	0.05	0.05	0.05	0.05	0.05	0.001	0.001
	0.1	0.1	0.1	0.075	0.075	0.075	0.075	0.2	0.1
	0.2	0.2	0.2	0.1	0.1	0.1	0.1	0.5	0.4
	0.3	0.3	0.3	0.2	0.2	0.2	0.2	0.8	0.8
	0.5	0.5	0.5	0.3	0.3	0.3	0.3	1.2	1.5
	0.75	0.75	0.75	0.4	0.4	0.4	0.4	2.2	3
	1	1	1	0.5	0.5	0.5	0.5	4	5.5
	1.5	1.5	1.5	0.75	0.75	0.6	0.75	8	9
	2			1	1.1	0.75	1	15	15
				1.2		1		22	
Total	46 h	35 h	35 h	42.5 h	42 h	46.5 h	42.5 h	12 h	12 h

**SI table 2.11.** Relaxation delays (s) and spin-lock lengths (s) and total experimental time used for  $R_1$  and  $R_{1\rho}$  measurements of GB1<sub>IgG</sub>

	<sup>15</sup> N R <sub>1</sub> , Gd(DTPA-BMA)				<sup>15</sup> N R <sub>1ρ</sub> , Gd(DTPA-BMA)				<sup>1</sup> H R <sub>1</sub> , CuEDTA	
	0 mM	3.5 mM	5 mM	7.5 mM	0 mM	1 mM	2 mM	3.5 mM	0 mM	100 mM
	0.01	0.001	0.001	0.001	0.002	0.002	0.002	0.002	0.25	0
15		0.01	0.01	0.01	0.005	0.005	0.005	0.005	0.5	0.02
		0.05	0.04	0.04	0.01	0.01	0.01	0.01	0.75	0.04
		0.2	0.1	0.1	0.02	0.02	0.02	0.02	1	0.07
		0.5	0.5	0.5	0.04	0.04	0.04	0.04	1.25	0.1
		1.5	1.5	1.5	0.07	0.06	0.06	0.06	1.5	0.14
		3.2	3	3	0.1	0.09	0.09	0.09	1.75	0.2
		6	7.5	7.5	0.15	0.13	0.13	0.13	2.2	0.3
Total	87 h	89 h	65.5 h	65.5 h	120 h	24 h	18h	23.5 h	30 h	37 h

**SI table 2.12.** Result of fitting of experimental ΔsPREs against ΔsPREs back-calculated for several different models with global scaling as the only fit parameters and weighted by experimental errors.

Experimental data set	Predicted data set	Scaling factor	χ <sup>2</sup>
<sup>15</sup> N R <sub>1</sub>	GB1:IgG (model B Fig. 5)	16.34	4.10
<sup>15</sup> N R <sub>1</sub>	GB1:IgG	13.33	4.34
<sup>15</sup> N R <sub>1</sub>	GB1:Fab	11.86	9.63
<sup>15</sup> N R <sub>1</sub>	GB1:Fc	11.26	14.09
<sup>15</sup> N R <sub>1ρ</sub>	GB1:IgG (model B Fig. 5)	16.27	3.29
<sup>15</sup> N R <sub>1ρ</sub>	GB1:IgG	13.60	4.30
<sup>15</sup> N R <sub>1ρ</sub>	GB1:Fab	12.40	8.64
<sup>15</sup> N R <sub>1ρ</sub>	GB1:Fc	11.10	12.58
<sup>1</sup> H R <sub>1</sub>	GB1:IgG (model B Fig. 5)	59.07	5.27
<sup>1</sup> H R <sub>1</sub>	GB1:IgG	51.27	6.77
<sup>1</sup> H R <sub>1</sub>	GB1:Fab	50.91	14.44
<sup>1</sup> H R <sub>1</sub>	GB1:Fc	36.18	19.23

**SI table 2.13.** Predicted <sup>1</sup>H sPREs for GB1<sub>IgG</sub> based on modified models with an additional interaction site (model B) or anisotropic motion (1-5).

Residue	Model B	Motion 1	Motion 2	Motion 3	Motion 4	Motion 5
2	5.593	5.753	5.612	5.685	5.614	5.748
3	0.956	1.087	1.030	1.052	1.013	1.095
4	0.690	1.039	1.026	1.029	1.018	1.041
5	0.308	0.593	0.612	0.598	0.594	0.600
6	0.185	0.917	0.911	0.912	0.923	0.899
7	0.187	1.049	1.137	1.087	1.125	1.033
8	0.239	1.054	1.051	1.053	1.095	0.997
9	0.275	0.885	0.931	0.902	0.978	0.814
10	0.971	1.459	1.447	1.432	1.613	1.286
11	0.616	0.974	0.994	0.955	1.166	0.799
12	0.308	0.583	0.618	0.586	0.704	0.492
13	0.178	0.583	0.763	0.653	0.778	0.532
14	0.311	1.831	2.197	1.991	2.141	1.764

15	0.420	0.965	1.276	1.089	1.166	0.999
16	0.285	0.589	0.656	0.613	0.619	0.606
17	0.458	0.563	0.632	0.577	0.544	0.621
18	0.537	0.650	0.614	0.622	0.594	0.658
19	0.894	1.114	0.781	0.912	0.797	1.082
20	1.736	1.885	1.638	1.760	1.593	1.918
21	2.134	2.358	1.979	2.139	1.710	2.650
22	1.880	1.990	1.804	1.892	1.666	2.103
23	3.343	3.323	3.447	3.390	3.141	3.536
24	2.251	2.205	2.334	2.278	1.883	2.595
25	1.157	1.232	1.097	1.168	0.946	1.417
26	0.618	0.671	0.608	0.637	0.555	0.729
27	0.357	0.407	0.375	0.388	0.343	0.440
28	0.250	0.280	0.248	0.259	0.219	0.317
29	0.238	0.255	0.241	0.243	0.222	0.275
30	0.157	0.197	0.168	0.179	0.174	0.190
31	0.110	0.144	0.125	0.131	0.132	0.136
32	0.150	0.153	0.168	0.154	0.161	0.157
33	0.217	0.265	0.195	0.223	0.247	0.214
34	0.114	0.159	0.125	0.137	0.157	0.125
35	0.155	0.192	0.153	0.166	0.209	0.142
36	0.224	0.250	0.215	0.226	0.256	0.225
37	0.183	0.236	0.161	0.191	0.233	0.179
38	0.311	0.436	0.252	0.319	0.479	0.247
39	0.315	0.439	0.293	0.348	0.483	0.268
40	1.087	1.367	1.030	1.173	1.449	0.958
41	0.736	0.964	0.742	0.842	0.977	0.725
42	1.518	2.260	1.773	2.028	2.139	1.929
43	0.567	1.447	0.769	1.039	1.147	0.956
44	0.260	1.413	1.007	1.198	1.247	1.153
45	0.578	3.006	1.677	2.218	2.283	2.144
46	0.515	1.868	1.572	1.710	1.702	1.710
47	2.902	5.642	3.927	4.840	4.597	5.052
48	2.794	5.524	5.015	5.300	5.231	5.345
49	1.890	4.024	3.861	3.946	3.932	3.951
50	1.743	2.658	2.568	2.611	2.594	2.622
51	0.762	1.722	1.638	1.677	1.670	1.682
52	0.288	0.786	0.747	0.765	0.764	0.764
53	0.183	1.050	0.892	0.967	0.985	0.949
54	0.176	0.876	0.813	0.847	0.870	0.822
55	0.615	1.417	1.153	1.300	1.359	1.245
56	1.083	2.035	1.957	2.003	2.090	1.913

**SI table 2.14.** Predicted  $^1\text{H}$  sPREs for GB1<sub>IgG</sub> based on modified models with an additional interaction site (model B) or anisotropic motion (1-5).

Residue	Model B	Motion 1	Motion 2	Motion 3	Motion 4	Motion 5
2	3.477	3.630	3.491	3.559	3.487	3.625
3	1.099	1.254	1.213	1.227	1.195	1.263
4	0.649	0.945	0.940	0.939	0.924	0.951
5	0.281	0.600	0.609	0.602	0.600	0.601
6	0.192	0.894	0.910	0.900	0.912	0.884
7	0.165	0.954	1.004	0.976	1.008	0.932
8	0.239	1.268	1.300	1.284	1.339	1.204
9	0.367	1.059	1.097	1.072	1.159	0.976
10	0.938	1.566	1.639	1.581	1.775	1.422
11	0.657	1.095	1.200	1.114	1.357	0.928
12	0.255	0.532	0.596	0.551	0.665	0.456
13	0.186	0.664	0.829	0.730	0.848	0.607
14	0.318	1.455	1.859	1.626	1.783	1.408
15	0.376	1.036	1.305	1.146	1.212	1.064
16	0.318	0.579	0.667	0.611	0.615	0.605
17	0.453	0.581	0.635	0.593	0.564	0.627
18	0.487	0.591	0.541	0.552	0.522	0.594
19	0.968	1.152	0.880	0.992	0.879	1.137
20	1.602	1.783	1.466	1.618	1.403	1.843
21	2.565	2.759	2.414	2.572	2.174	2.959
22	2.660	2.769	2.579	2.673	2.424	2.882
23	1.999	2.028	2.049	2.040	1.869	2.165
24	1.356	1.364	1.399	1.384	1.154	1.595
25	0.832	0.900	0.783	0.841	0.672	1.050
26	0.473	0.523	0.466	0.489	0.424	0.568
27	0.273	0.322	0.291	0.303	0.272	0.341
28	0.195	0.222	0.199	0.205	0.179	0.246
29	0.223	0.231	0.233	0.227	0.215	0.248
30	0.149	0.189	0.155	0.169	0.169	0.175
31	0.103	0.141	0.119	0.125	0.132	0.126
32	0.145	0.151	0.162	0.149	0.162	0.147
33	0.229	0.281	0.205	0.234	0.262	0.222
34	0.121	0.168	0.130	0.143	0.167	0.129
35	0.178	0.224	0.170	0.189	0.247	0.158
36	0.241	0.275	0.226	0.243	0.285	0.244
37	0.197	0.256	0.167	0.203	0.246	0.199
38	0.332	0.480	0.271	0.345	0.528	0.259
39	0.430	0.603	0.393	0.471	0.667	0.356
40	0.901	1.140	0.844	0.971	1.215	0.782
41	1.039	1.307	1.049	1.168	1.320	1.027
42	1.249	1.883	1.408	1.640	1.754	1.539
43	0.509	1.342	0.786	1.025	1.115	0.953
44	0.292	1.613	1.031	1.289	1.355	1.229



45	0.393	1.949	1.246	1.538	1.567	1.506
46	0.664	2.387	1.876	2.120	2.103	2.122
47	1.929	3.679	2.882	3.278	3.169	3.373
48	3.274	5.277	4.937	5.121	5.064	5.157
49	2.664	4.735	4.624	4.681	4.668	4.680
50	1.735	2.611	2.549	2.578	2.565	2.586
51	0.723	1.514	1.458	1.483	1.476	1.488
52	0.275	0.875	0.818	0.844	0.844	0.842
53	0.173	1.029	0.918	0.972	0.988	0.957
54	0.195	0.867	0.771	0.822	0.846	0.796
55	0.554	1.414	1.218	1.331	1.382	1.280
56	1.389	2.276	2.136	2.217	2.301	2.131

### 2.6.2 References

- (1) Gu, X.-H.; Gong, Z.; Guo, D.-C.; Zhang, W.-P.; Tang, C. *J. Biomol. NMR* **2014**, *58* (3), 149.
- (2) Lamley, J. M.; Iuga, D.; Öster, C.; Sass, H.-J.; Rogowski, M.; Oss, A.; Past, J.; Reinhold, A.; Grzesiek, S.; Samoson, A.; Lewandowski, J. R. *J. Am. Chem. Soc.* **2014**, *136* (48), 16800.
- (3) Derrick, J. P.; Wigley, D. B. *Nature* **1992**, *359* (6397), 752.
- (4) Sauer-Eriksson, A. E.; Kleywegt, G. J.; Uhlén, M.; Jones, T. A. *Structure* **1995**, *3* (3), 265.
- (5) Lian, L.-Y.; Barsukov, I. L. L.; Derrick, J. P. P.; Roberts, G. C. K. C. *Nat. Struct. Biol.* **1994**, *1* (6), 355.
- (6) Kato, K.; Lian, L.-Y.; Barsukov, I. L.; Derrick, J. P. *Structure* **1995**.
- (7) Gronenborn, A. M.; Clore, G. M. *J. Mol. Biol.* **1993**, *233* (3), 331.

### 3. Intermolecular interactions and protein dynamics by SSNMR

This chapter was published as:

*Intermolecular interactions and protein dynamics by SSNMR*, Lamley, J.M., Öster, C., Stevens, R.A., Lewandowski, J.R. *Angewandte Chemie* **2015** 54(51), 15374–15378.

#### 3.1 Abstract

Understanding the dynamics of interacting proteins is a crucial step toward describing many biophysical processes. Here we investigate the backbone dynamics for protein GB1 in two different assemblies: crystalline GB1 and precipitated >300 kDa GB1-antibody complex. We perform these measurements on samples containing as little as 8 nanomoles of protein. From measurements of site-specific  $^{15}\text{N}$  relaxation rates including relaxation dispersion we obtain snapshots of dynamics spanning nine orders of magnitude in terms of time scale. Comparison of measurements for GB1 in either environment reveals that while many of the dynamic features of the protein are conserved between them (in particular for the fast (ps-ns) motions), much greater differences occur for slow motions with >500 ns range motions being more prevalent in the complex. The data suggest that GB1 can potentially undergo a small-amplitude overall anisotropic motion sampling the interaction interface in the complex.

#### 3.2 Introduction and Discussion

Protein dynamics are fundamental to a wide range of biophysical processes, from enzymatic catalysis and ligand binding to molecular recognition and signaling.<sup>[1]</sup> Often, the mechanisms that underlie these processes rely on the interactions of proteins with other molecules. Thus, characterization of the dynamics of interacting proteins and the manner in which intermolecular interactions influence those dynamics is required to fully understand them. In general, the local molecular environment of

a protein potentially has significant effects upon motions relevant to its function.<sup>[2]</sup>

NMR offers access to atomic-resolution details about dynamics over a wide range of time scales.<sup>[3]</sup> Unfortunately, proteins and protein complexes above a few tens of kDa represent a severe challenge for solution NMR methods, where slow molecular tumbling leads to enhanced  $T_2$  relaxation and hence broad NMR lines. In solid-state NMR (SSNMR) experiments, however, this size-dependent broadening does not occur and so biomolecules of several hundred kDa and beyond may be studied, provided intrinsic challenges of sensitivity and resolution can be successfully addressed.<sup>[4]</sup>

We recently demonstrated that high quality spectra could be obtained for a protein in a precipitated large protein complex, by using an approach based on combination of high field, fast (60-100 kHz) magic angle spinning (MAS) and optional sample deuteration.<sup>[4d]</sup> Notably, this methodology is applicable to a general case of systems with little or no overall symmetry, and samples containing only a few nanomoles of protein can yield spectra with the sensitivity and resolution suitable for performing quantitative measurements of structure and dynamics.<sup>[4d, 4g]</sup> We take advantage of the described approach to, for the first time, use SSNMR to conduct widespread site-specific relaxation measurements that shed light on motions for a protein GB1 in a large (> 300 kDa) protein-antibody complex. We compare these data to analogous data for GB1 in a crystal, where the pattern of intermolecular interactions is different than in the complex. Since the backbone conformation of GB1 is very similar in either form<sup>[4d, 5]</sup> we expect these to be ideal systems with which to investigate the influence of different intermolecular interactions and packing on molecular dynamics. In our comparison we take advantage of the fact that relaxation rates in the solid state are sensitive to motions spanning nine orders of magnitude in terms of time scale (this enhanced range of sensitivity compared to the solution case is related to the lack of overall tumbling) Relaxation rates relate directly to the time scales and amplitudes of motions, and thus observed changes in relaxation rates measured under identical experimental conditions will necessarily reflect

changes in the underlying protein dynamics (time scales, amplitudes or both). To ensure a direct comparison, relaxation rates were measured at the same magnetic field (850 MHz  $^1\text{H}$  Larmor frequency), spinning frequency (60 kHz) and sample temperature ( $27 \pm 1$  °C) in the two different assemblies: a GB1 ( $\sim 6$  kDa) crystal and precipitated complex of GB1 and immunoglobulin G (IgG;  $\sim 150$  kDa) where GB1 binds to both the Fab and Fc fragments of the IgG antibody in a  $>300$  kDa complex.<sup>[4d, 7]</sup> Note that GB1:IgG complex precipitates instantaneously upon mixing of the GB1 and IgG solutions and without application of any centrifugal force (i.e. is not sedimented). 100% back-exchanged [ $\text{U-}^2\text{H}, ^{13}\text{C}, ^{15}\text{N}$ ]GB1 was used for preparation of both samples with proteins dissolved in pH 5.5 phosphate buffer. All samples were fully hydrated with bulk solvent being present in the rotors. The amount of GB1 was estimated to be  $\sim 8$  nanomoles and  $\sim 310$  nanomoles in the samples of the complex and crystal respectively.

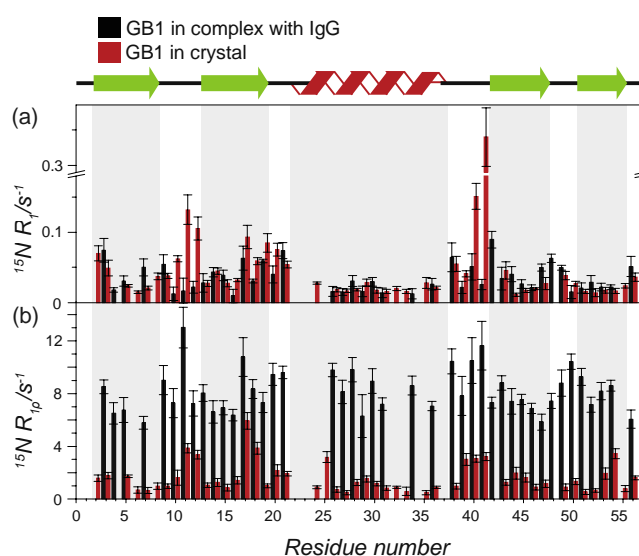


**Figure 3.1.**  $^{15}\text{N}$   $R_1$  (a) and  $R_{1\rho}$  (b) relaxation rates measurements in 100% proton back-exchanged [ $\text{U-}^2\text{H}, ^{13}\text{C}, ^{15}\text{N}$ ]GB1 in a complex with IgG (black) and in a GB1 crystal (red). For the severely overlapping peaks values were removed (see Fig. S3.2-3). Experiments were performed at 850 MHz spectrometer, 60 kHz spinning frequency and with a 17 kHz spin-lock field for measurements in (b). Sample temperature was  $27 \pm 1$  °C as calculated from the chemical shift of water protons.

In contrast to solution, in the solid state the absence of overall tumbling enables access to motions in the full range from ps to ms through NMR relaxation measurements.<sup>[3c]</sup> To obtain snapshots of dynamics at different time scales we performed three types of site-specific measurements dominated by motions on different time scales:

$^{15}\text{N}$   $R_1$ ,  $R_{1\rho}$  and  $R_{1\rho}$  relaxation dispersion. At 20 T,  $^{15}\text{N}$   $R_1$  is dominated by ns-range motions.<sup>[6]</sup>  $^{15}\text{N}$   $R_{1\rho}$  is sensitive to ps-ms motions but is dominated by the motions with longer correlation times.<sup>[6, 8]</sup> When the time scales of motions approach that associated with spinning (i.e.  $\mu\text{s}$ -ms motions), the incoherent (molecular motion) and coherent (spinning) processes interfere with one another, introducing an  $R_{1\rho}$  spinning frequency dependence.<sup>[9]</sup> Finally, exchange contributions to  $^{15}\text{N}$   $R_{1\rho}$  can be evaluated from relaxation dispersion, which reports on  $\mu\text{s}$ -range motions.<sup>[10]</sup>

Figure 3.1a shows  $^{15}\text{N}$   $R_1$  rates measured for GB1 in both environments as a function of the residue number (GB1:IgG complex in black and GB1 crystal in red). The  $R_1$  rates are similar between crystal and complex with a few notable localized differences, e.g. residues K10-K13 and D40-G41, which are elevated in the crystal compared to in the complex. These differences could be explained by different intermolecular contacts<sup>[11]</sup>: these loop residues are involved in specific interactions with IgG in the complex<sup>[4d]</sup> but have a large solvent accessible surface and some of the largest amplitude motions in the crystal.<sup>[6]</sup> Consequently, overall the fast ps-ns motions seem largely similar in GB1 in the two different molecular assemblies, which is consistent with the general observation that a crystalline environment does not induce large changes in fast ps-ns dynamics compared to a free molecule in solution (unless a strong direct contact is present)<sup>[11-12]</sup> or the interpretation that ps-ns dynamics are primarily defined by the fold of a protein.

Figure 3.1b shows  $^{15}\text{N}$   $R_{1\rho}$  rates measured for GB1 in both environments as a function of the residue number (complex rates in black, crystal rates in red). Remarkably, the rates for GB1 in the complex are, on average (at the same temperature),  $\sim 6$  times higher than those in the crystal (mean  $R_{1\rho}$  values of  $8.1 \text{ s}^{-1}$  and  $1.4 \text{ s}^{-1}$  respectively). The similarity of  $^{15}\text{N}$   $R_1$ 's in the complex and crystal suggests that these differences in  $R_{1\rho}$  rates must originate primarily from differences in motions occurring on a high-ns to ms time scale, which have a minimal effect on  $R_1$ .

Besides the general offset in the  $^{15}\text{N}$   $R_{1\rho}$  rates for GB1 in the crystals and complex, we observe changes in their relative magnitudes as a

function of the residue number.  $^{15}\text{N}$   $R_{1\rho}$  rates are generally elevated in the loops and at the ends of  $\beta$ -strands both in crystal and complex. However, in the crystal, the rates for the helix residues are generally similar or smaller compared to the rates in  $\beta$ -sheet but they are elevated in the complex.

Assuming that the basic interaction interfaces between GB1 and IgG are well represented by the interfaces observed in crystal structures of GB1 analogues in complexes with IgG fragments,<sup>[4d]</sup> one can compare the local density of packing for GB1 in the crystal and complex. For the portions of GB1 involved in interactions with IgG, the buried surface area for the solvent accessible surface is larger in the complex compared to in the crystal (see Fig. S3.7). The increased  $^{15}\text{N}$   $R_{1\rho}$  rates observed in the complex are therefore more likely to be due to generally longer correlation times rather than larger amplitudes of motions (i.e. due to denser packing in the complex, the amplitudes of motions are unlikely to be greater than in the crystal). Since in GB1 crystals the average correlation time for the slow motions at this temperature is  $\sim 450$  ns,<sup>[6]</sup> the average correlation time for the *dominant* slow motions in the complex must be  $>500$  ns.

Since the  $^{15}\text{N}$   $R_{1\rho}$  rates are elevated for all the residues in the complex compared to crystal, this means that either local slow motions are induced in most residues upon binding with IgG (these also might be motions that are present in the crystal but become slower in complex) and/or GB1 undergoes a small amplitude overall slow motion in the complex. In the first scenario, local conformational changes occurring on a slow time scale are likely to modulate isotropic chemical shift and thus be observable by chemical exchange based methods such as  $^{15}\text{N}$   $R_{1\rho}$  relaxation dispersion.<sup>[10, 13]</sup> In the second scenario, motion may not modulate isotropic chemical shift if it is not associated with a local conformational change, and thus may not be picked up by the relaxation dispersion measurements. However, such motions in the  $\mu\text{s}$ -ms range should induce a spinning frequency dependence of  $R_{1\rho}$ .<sup>[9]</sup>

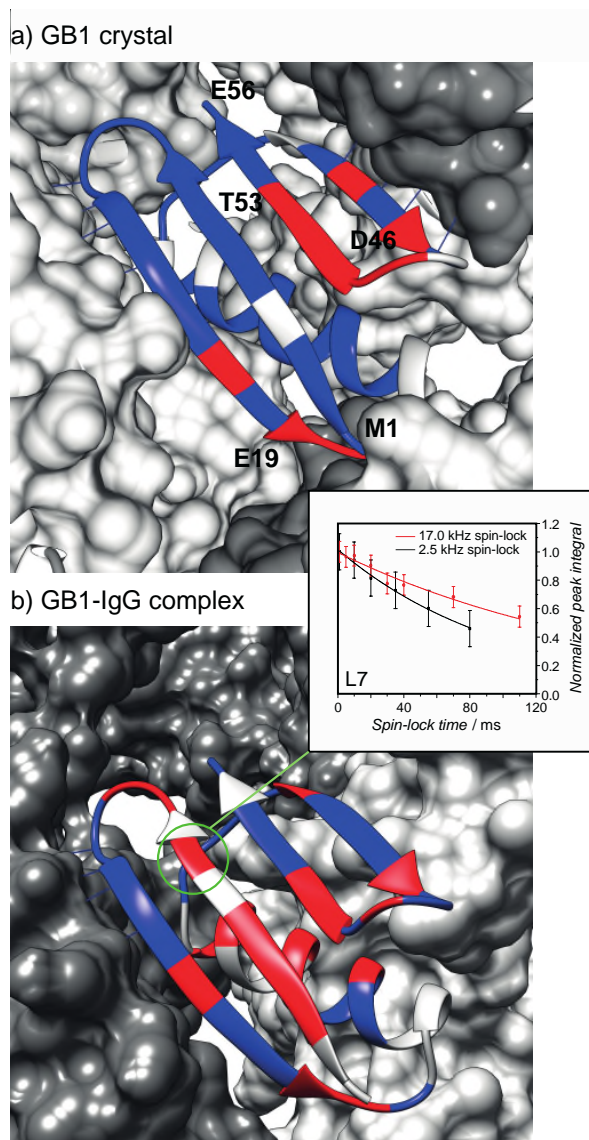


**Figure 3.2.** Residues clearly exhibiting chemical exchange on the  $\mu\text{s}$  time scale in (a) crystalline GB1 and (b) GB1 in complex with IgG. The colors of the residues indicate: red - clear  $\mu\text{s}$ -exchange contribution, blue - no clear  $\mu\text{s}$ -exchange contribution and grey - data is unavailable (see SI Figs. S5 & S6 for the selection criteria). Example decay curves from measurements on the complex are shown in the inset of panel (b).

In order to distinguish motion-induced effects from motionally independent dipolar dephasing, currently,  $^{15}\text{N}$   $R_{1\rho}$  relaxation dispersion and spinning dependent measurements need to be conducted in heavily deuterated samples preferably at spinning frequencies of  $>40$  kHz.<sup>[8b, 10]</sup>

First, we measured relaxation dispersion for 100% back-exchanged deuterated crystalline GB1 (at 50-60 kHz MAS apparently no further dilution of proton network is required, with coherent contributions being smaller than  $1\text{ s}^{-1}$  at lower spin-lock fields). Clear dispersion is observed for only a handful of residues in crystalline GB1 (see Fig. S3.5), which

must undergo local  $\mu$ s-range motions (more precisely motions on a time scale of tens to hundreds of  $\mu$ s). In general, residues with  $\mu$ s-range motions cluster in two regions: the C-terminal end of  $b_3$ , loop 4 and the N-terminal end of  $b_4$  (residues 44, 46, 48-53) and the C-terminal end of  $b_2$  and loop 2 (residues 17, 19-20) (see Fig. 3.2). In the complex, the presence of  $\mu$ s-range motions (though not the precise rate of exchange) can be evaluated by comparing  $^{15}\text{N}$   $R_{1\rho}$  measurements at two different spin-lock values. In the presence of  $\mu$ s-range motions, the contribution from chemical exchange should render the measured rate of decay larger at the lower spin-lock frequencies. For many of the GB1 residues, rates measured using a 2.5 kHz spin-lock field are considerably elevated compared to those measured using a 17 kHz spin-lock field, which indicates that local  $\mu$ s-range motions are much more common in the complex compared to in the crystal. Generally, the regions displaying conformational exchange on the  $\mu$ s-time scale in the crystal show similar behavior in the complex (though with a few differences). Other residues, e.g. the C-terminal end of the helix and  $b_1$  strand (see Fig. 3.2) exhibit the presence of  $\mu$ s-range motions only in the complex. However, many residues that have elevated  $^{15}\text{N}$   $R_{1\rho}$  rates in the complex compared to crystal do not contain significant contributions from chemical exchange in the  $\mu$ s range (at least not above the current experimental errors). Such residues either undergo motions that are outside of the sensitivity range for the  $^{15}\text{N}$   $R_{1\rho}$  relaxation dispersion (e.g. in ms or  $< 10$   $\mu$ s range) or undergo motions that do not modulate isotropic chemical shift and thus do not contribute to the rates through chemical exchange. In either case, such motions with correlation times  $> 1$   $\mu$ s should display spinning frequency-dependent  $^{15}\text{N}$   $R_{1\rho}$  rates.<sup>[9]</sup>

Fig. 3.3a shows a comparison of  $^{15}\text{N}$   $R_{1\rho}$  rates measured at 60 kHz, 52 kHz and 45 kHz spinning frequencies. Overall, the rates at 45 kHz spinning are on average about  $8\text{ s}^{-1}$  larger than at 60 kHz spinning, indicating the presence of slow ( $\mu$ s-ms) motions for essentially all the residues (in contrast, in the crystal most rates are either the same within the experimental error or different by less than  $0.5\text{ s}^{-1}$  under similar conditions, see Fig. S3.8). A pertinent question is whether the



omnipresence of slow motions may be a manifestation of an overall small amplitude motion.<sup>[14]</sup> Cases in which a protein samples different orientations in a transient complex were reported previously.<sup>[15]</sup> Depending on the nature of the overall motion it would contribute differently to the observed rates: isotropic motion would result in an equal contribution to all the rates; anisotropic motion would induce contributions to the rates that depend on the orientation of the NH bond vector with respect to the axis of motion.<sup>[3c, 14, 16]</sup> Figure S3.4 in the supporting information illustrates this idea by showing the simulated effect on the  $^{15}\text{N}$   $R_{1\rho}$  rates in GB1 in different cases of overall 3D Gaussian Axial Fluctuations (GAF)<sup>[3c, 14, 16]</sup> of the molecule. We use the same model (see S.I.) to fit the experimental  $^{15}\text{N}$   $R_{1\rho}$ 's obtained at three spinning frequencies to get an idea of the type of overall motion that would be compatible with them. In such a procedure one can safely neglect any contribution from fast ps-ns motions because they contribute only to a small fraction of the observed rates and are spinning frequency independent.<sup>[6]</sup> Because of the limitations of the available data we also have been forced to neglect at this stage contributions of slow local motions (e.g. some of the motions picked up by the relaxation dispersion). The model involves 6 fit parameters: three amplitudes of fluctuations against three orthogonal axes, a single time scale for the overall motion and the two parameters describing the orientation of the motional reference frame in which the coordinates for all NH vectors are expressed. The overall motion that leads to the best reproduction of data (see Fig 3.3c) is essentially axially symmetric, with the largest fluctuation of  $\sim 7^\circ$  against the blue and green axes in Fig. 3.3b and  $\sim 4^\circ$  against the red axis and a correlation time of  $\sim 80$   $\mu\text{s}$ . Note that for such slow motions, contributions to the rates from non-directly bonded to nitrogen protons (including IgG protons) may be non-negligible. In the SI we consider how including such contributions would affect the above analysis.

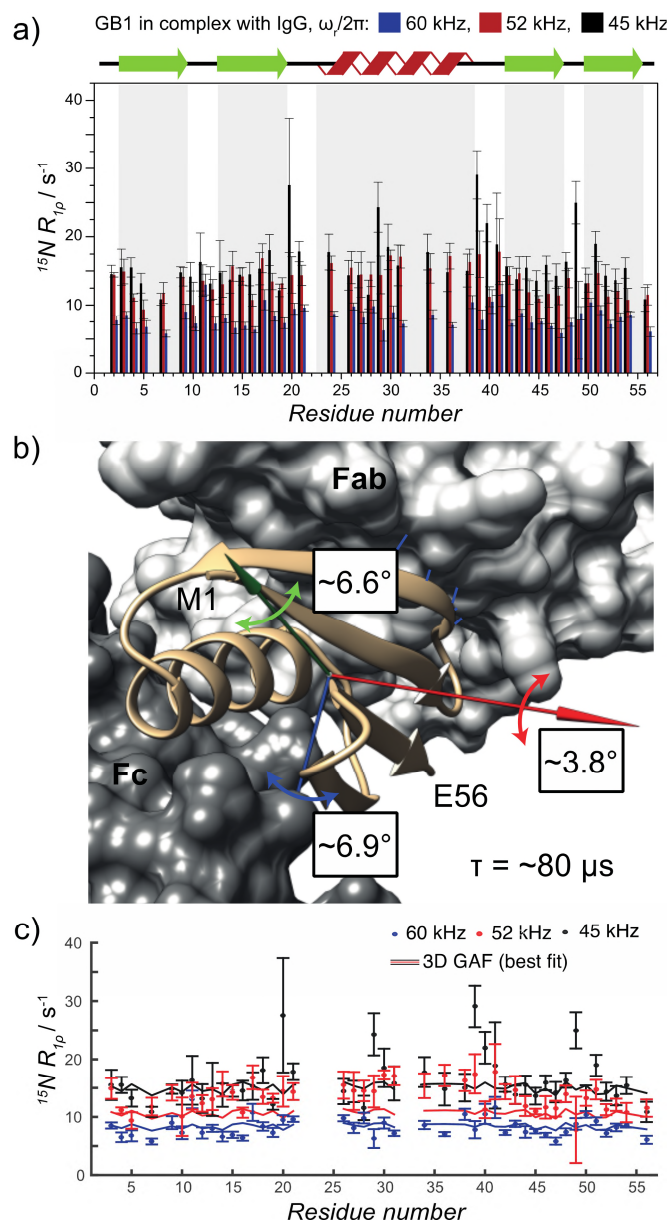


**Figure 3.3.** (a)  $^{15}\text{N } R_{1\rho}$  rates for GB1 in complex with IgG measured at 60 kHz (blue bars;  $\omega_{1\text{N}}/2\pi = 17$  kHz), 52 kHz (red bars;  $\omega_{1\text{N}}/2\pi = 13.1$  kHz) and 45 kHz (black bars;  $\omega_{1\text{N}}/2\pi = 13$  kHz) spinning frequency at 850 MHz  $^1\text{H}$  Larmor frequency and a sample temperature of  $27 \pm 1$  °C. (b) Visualization of the overall 3D GAF motion of GB1 in the complex with IgG consistent with the data in (a). The amplitudes of fluctuations are listed next to the axes of motion. The approximate correlation time for the motion is 80  $\mu\text{s}$ . (c) Comparison of  $^{15}\text{N } R_{1\rho}$  rates back-calculated from the best-fit to the 3D GAF model in (b) to experimental rates.

Proper quantification of the amplitudes and time scales of motions for GB1 in the complex will require further extensive measurements and a far more involved analysis (our results suggest that motions occurring at even four distinct timescales may need to be considered to model adequately the dynamics for some residues). However, even without this information it is clear that changes to protein dynamics associated with

differences in intermolecular interactions are potentially very complex, that studies of protein dynamics in actual assemblies provide additional insights not available from studies on isolated systems and that information about the dynamics of proteins in large complexes may be now accessed directly through approaches similar to the one proposed here.

In summary, we have presented a comparison of site-specific backbone dynamics spanning over nine orders of magnitude in time scale for the protein GB1 in two different environments: a crystalline form and the > 300 kDa precipitated GB1:IgG complex. Comparison of site-specific  $^{15}\text{N}$   $R_1$  measurements under the same experimental conditions highlighted general similarities of fast ps-ns dynamics in both environments only minimally perturbed by strong intermolecular contacts. Comparison of site-specific  $^{15}\text{N}$   $R_{1\rho}$  measurements including relaxation dispersion and spinning frequency-dependent measurements suggested that different intermolecular interactions modify the pattern of slow motions, with slow  $\mu\text{s}$ -ms motions being more prevalent in the complex. The generally elevated  $^{15}\text{N}$   $R_{1\rho}$  rates throughout GB1 in the complex compared to crystal are consistent with an overall small amplitude anisotropic orientation sampling of the interaction interface of the protein. This study paves the way for direct characterization of dynamics in biologically important but sensitivity-limited samples of proteins within large complexes that will supplement the picture from studies of isolated proteins.

### 3.3 Acknowledgements

The research leading to these results has received funding from the European Research Council under the European Union's Seventh Framework Programme (FP/2007-2013) / ERC Grant Agreement 639907. J.R.L. also acknowledges funding from Royal Society Grant RG130022, EPSRC Grant EP/L025906/1, BBSRC Grant BB/L022761/1. C.O. acknowledges funding from the European Union under a Marie Curie Initial Training Network FP7-PEOPLE-2012-ITN Grant Agreement Number 316630 CAS-IDP. We thank Stephan Grzesiek, Hans Juergen Sass and Marco Rogowski for the generous gift of deuterated GB1. The UK 850

MHz solid-state NMR Facility used in this research was funded by EPSRC and BBSRC (contract reference PR140003), as well as the University of Warwick including via part funding through Birmingham Science City Advanced Materials Projects 1 and 2 supported by Advantage West Midlands (AWM) and the European Regional Development Fund (ERDF). Fig. 3.2,3.3b were produced using the UCSF Chimera package, which was developed by the RBVI at the U. of California, San Francisco (supported by NIGMS P41-GM103311). Raw NMR data and Matlab scripts used for the analysis can be obtained from the authors upon request.

### 3.4 References

- [1] <sup>a</sup>M. Karplus, J. A. McCammon, *Annu. Rev. Biochem.* **1983**, 52, 263-300; <sup>b</sup>K. Henzler-Wildman, D. Kern, *Nature* **2007**, 450, 964-972.
- [2] C. S. Goh, D. Milburn, M. Gerstein, *Curr. Opin. Struct. Biol.* **2004**, 14, 104-109.
- [3] <sup>a</sup>A. K. Mittermaier, L. E. Kay, *Trends Biochem. Sci.* **2009**, 34, 601-611; <sup>b</sup>J. Yang, M. L. Tasayco, T. Polenova, *J. Am. Chem. Soc.* **2009**, 131, 13690-13702; <sup>c</sup>J. z. R. Lewandowski, *Acc. Chem. Res.* **2013**, 46, 2018-2027.
- [4] <sup>a</sup>A. Mainz, T. L. Religa, R. Sprangers, R. Linser, L. E. Kay, B. Reif, *Angew. Chem. Int. Ed.* **2013**, 52, 8746-8751; <sup>b</sup>A. Mainz, S. Jehle, B. J. van Rossum, H. Oschkinat, B. Reif, *J. Am. Chem. Soc.* **2009**, 131, 15968-15969; <sup>c</sup>A. Mainz, B. Bardiaux, F. Kuppler, G. Multhaup, I. C. Felli, R. Pierattelli, B. Reif, *J. Biol. Chem.* **2012**, 287, 1128-1138; <sup>d</sup>J. M. Lamley, D. Iuga, C. Oster, H. J. Sass, M. Rogowski, A. Oss, J. Past, A. Reinhold, S. Grzesiek, A. Samoson, J. R. Lewandowski, *J. Am. Chem. Soc.* **2014**, 136, 16800-16806; <sup>e</sup>I. Gelis, V. Vitzthum, N. Dhimole, M. A. Caporini, A. Schedlbauer, D. Carnevale, S. R. Connell, P. Fucini, G. Bodenhausen, *J. Biomol. NMR* **2013**, 56, 85-93; <sup>f</sup>C. Gardiennet, A. K. Schütz, A. Hunkeler, B. Kunert, L. Terradot, A. Böckmann, B. H. Meier, *Angew. Chem. Int. Ed.* **2012**, 51, 7855-7858; <sup>g</sup>E. Barbet-Massin, C.-T. Huang, V. Daebel, S.-T. D. Hsu, B. Reif, *Angew. Chem. Int. Ed.* **2015**, 4367-4369.; <sup>h</sup>A. J. Baldwin, P. Walsh, D. F. Hansen, G. R. Hilton, J. L. Benesch, S. Sharpe, L. E. Kay, *J. Am. Chem. Soc.* **2012**, 134, 15343-15350.

- [5] W. T. Franks, D. H. Zhou, B. J. Wylie, B. G. Money, D. T. Graesser, H. L. Frericks, G. Sahota, C. M. Rienstra, *J. Am. Chem. Soc.* **2005**, *127*, 12291-12305.
- [6] J. M. Lamley, M. J. Lougher, H. J. Sass, S. Grzesiek, J. R. Lewandowski, *Phys. Chem. Chem. Phys.* **2015**, *17*, 21997-22008.
- [7] G. C. Stone, U. Sjöbring, L. Björck, J. Sjöquist, C. Barber, F. Nardella, *J. Immunol.* **1989**, *143*, 565-570.
- [8] <sup>a</sup>A. Krushelnitsky, T. Zinkevich, D. Reichert, V. Chevelkov, B. Reif, *J. Am. Chem. Soc.* **2010**, *132*, 11850-11853; <sup>b</sup>J. R. Lewandowski, H. J. Sass, S. Grzesiek, M. Blackledge, L. Emsley, *J. Am. Chem. Soc.* **2011**, *133*, 16762-16765.
- [9] <sup>a</sup>M. Yamaguchi, A. Tsutsumi, *Polym. J.* **1993**, *25*, 131-139; <sup>b</sup>R. Kurbanov, T. Zinkevich, A. Krushelnitsky, *J. Chem. Phys.* **2011**, *135*, 184104; <sup>c</sup>A. Krushelnitsky, R. Kurbanov, D. Reichert, G. Hempel, H. Schneider, V. Fedotov, *Solid State Nucl. Mag.* **2002**, *22*, 423-438; <sup>d</sup>C. Farès, J. Qian, J. H. Davis, *J. Chem. Phys.* **2005**, *122*, 194908.
- [10] P. Ma, J. D. Haller, J. Zajakala, P. Macek, A. C. Sivertsen, D. Willbold, J. Boisbouvier, P. Schanda, *Angew. Chem. Int. Ed.* **2014**, *53*, 4312-4317.
- [11] R. B. Fenwick, H. van den Bedem, J. S. Fraser, P. E. Wright, *Proc. Natl. Acad. Sci. U.S.A.* **2014**, *111*, E445-E454.
- [12] <sup>a</sup>H. B. Cole, D. A. Torchia, *Chem. Phys.* **1991**, *158*, 271-281; <sup>b</sup>V. Chevelkov, A. V. Zhuravleva, Y. Xue, B. Reif, N. R. Skrynnikov, *J. Am. Chem. Soc.* **2007**, *129*, 12594-12595; <sup>c</sup>V. Agarwal, Y. Xue, B. Reif, N. R. Skrynnikov, *J. Am. Chem. Soc.* **2008**, *130*, 16611-16621.
- [13] A. G. Palmer, F. Massi, *Chem. Rev.* **2006**, *106*, 1700-1719.
- [14] J. R. Lewandowski, J. Sein, M. Blackledge, L. Emsley, *J. Am. Chem. Soc.* **2009**, *132*, 1246-1248.
- [15] A. N. Volkov, J. A. Worrall, E. Holtzmann, M. Ubbink, *Proc. Natl. Acad. Sci. U.S.A.* **2006**, *103*, 18945-18950.
- [16] D. B. Good, S. Wang, M. E. Ward, J. Struppe, L. S. Brown, J. R. Lewandowski, V. Ladizhansky, *J. Am. Chem. Soc.* **2014**, *136*, 2833-2842.

### 3.5 Supplementary Information

#### 3.5.1 Experimental Section

Deuterated [ $^{13}\text{C}$ ,  $^{15}\text{N}$ ]-labeled GB1 (T2Q) was expressed in *E.coli* BL21(DE3) after one cycle of adaptation to  $\text{D}_2\text{O}$  in a 50 mL pre-culture. The production was carried out in a 3.6 L fermenter using 1 L  $\text{D}_2\text{O}$  M9 minimal media with 6 g  $^{13}\text{C}$ -glucose and 1.5 g  $^{15}\text{NH}_4\text{Cl}$ . The final yield after cell rupture by heating to 75 °C and HPLC purification (RP HPLC column, Jupiter 10 mm  $\text{C}_4$  300 Å) was 152 mg. The level of deuteration was approximately 87%, estimated from solution-state 1D NMR spectra. After lyophilization, the final buffer (10 mL) was adjusted by dialysis against 4 x 1 L 50 mM sodium phosphate, pH 5.5. Lyophilized IgG from human serum was purchased from Sigma-Aldrich. The complex sample was prepared for solid-state NMR by mixing 0.3 mM GB1 and 0.15 mM IgG solutions (2:1 molar ratio; note that in later experiments we used 1:1 molar ratio to the same effect), which resulted in instantaneous precipitation of the complex. The resulting precipitate was centrifuged into a Bruker 1.3 mm NMR rotor. Note that in contrast to several studies that rely on sedimentation by ultracentrifugation for preparing sample of a complex in the case of GB1:IgG complex precipitation occurs spontaneously without any application of centrifugal force. Thus as studied here the complex *is not a sediment but a precipitate*, which is a direct consequence of bivalent nature of interaction of GB1 with IgG. Here centrifugation is a means for mechanical transfer of already formed solid-state sample and not as a way of preparing the sample. The amount of GB1 in the final sample was estimated to be on the order of 8 nanomoles (or ~50  $\mu\text{g}$  of protein).

GB1 was also crystallized from a 10 mg/mL solution with the aid of a precipitant of 2:1 2-methylpentane-2,4-diol:propan-2-ol.<sup>[1]</sup> The resulting nanocrystals were then centrifuged into a Bruker 1.3 mm rotor. The amount of GB1 in the final sample was estimated to be on the order of 310 nanomoles (or ~2 mg of protein).

All solid-state NMR spectra shown, except for  $^{15}\text{N}$   $R_{1\rho}$  relaxation dispersion on crystalline GB1, were recorded at 850 MHz  $^1\text{H}$  Larmor frequency with a Bruker Avance III spectrometer, with a Bruker 1.3 mm

triple resonance probe operating at a magic-angle spinning (MAS) frequency of 60 kHz.  $^{15}\text{N}$   $R_{1\rho}$  relaxation dispersion experiments on crystalline GB1 were recorded at 600 MHz  $^1\text{H}$  Larmor frequency with a Bruker Avance II+ spectrometer, with a Bruker 1.3 mm triple resonance probe operating at an MAS frequency of 50 kHz. The rotor caps were sealed with a silicone-based glue to eliminate water leakage, while a Bruker BCU-X cooling unit was used to regulate the internal sample temperature to  $27 \pm 1$  °C (measured from the chemical shift of water with respect to DSS; Bruker macro for calibrating the sample temperature can be downloaded from the authors' website).  $^{15}\text{N}$   $R_{1\rho}$  rates in the complex were measured by recording a series of  $^{15}\text{N}$  - $^1\text{H}$  correlation spectra using the proton-detected pulse sequence shown in SI Fig.1, where the spin-lock duration,  $\tau$ , is incremented between full experiments.

The nutation frequencies for all the spin lock fields used for  $^{15}\text{N}$   $R_{1\rho}$  measurements were determined using nutation experiments.

For  $^{15}\text{N}$   $R_{1\rho}$  measurements on the complex at 60 kHz spinning, double quantum cross-polarization (CP) contact times were 1 ms ( $^1\text{H}$ - $^{15}\text{N}$ ) and 0.4 ms ( $^{15}\text{N}$ - $^1\text{H}$ ), with nutation frequencies of 10 kHz and  $\sim 50$  kHz for  $^{15}\text{N}$  and  $^1\text{H}$  (with 5% tangential sweep) respectively. Relaxation series were collected with spin-lock nutation frequencies of both 17 kHz and 2.5 kHz. For each experiment within the 17 kHz series, 224 scans of 74  $t_1$  increments were taken (experimental time  $\sim 85$  h), while for the 2.5 kHz series 96 scans of 64  $t_1$  increments were taken per experiment (experimental time  $\sim 10$  h). Recycle delays were 2 s.

For  $^{15}\text{N}$   $R_{1\rho}$  measurements on the complex at 52 kHz spinning, double quantum cross-polarization (CP) contact times were 1.3 ms ( $^1\text{H}$ - $^{15}\text{N}$ ) and 0.75 ms ( $^{15}\text{N}$ - $^1\text{H}$ ), with nutation frequencies of 10 kHz and  $\sim 42$  kHz for  $^{15}\text{N}$  and  $^1\text{H}$  (with 5% tangential sweep) respectively. Relaxation series were collected with spin-lock nutation frequencies of 13.1 kHz. 168 scans of 46  $t_1$  increments were taken (experimental time  $\sim 45$  h). Recycle delays were 2 s. Data was acquired in an interleaved fashion.

For  $^{15}\text{N}$   $R_{1\rho}$  measurements on the complex at 45 kHz spinning, double quantum cross-polarization (CP) contact times were 1.2 ms ( $^1\text{H}$ - $^{15}\text{N}$ ) and

0.5 ms ( $^{15}\text{N}$ - $^1\text{H}$ ), with nutation frequencies of 8 kHz and  $\sim 37$  and  $\sim 53$  kHz for  $^{15}\text{N}$  and  $^1\text{H}$  (with 5% tangential sweep) respectively. Relaxation series were collected with spin-lock nutation frequencies of 13 kHz. 160 scans of 68  $t_1$  increments were taken (experimental time  $\sim 63$  h). Recycle delays were 2 s. Data was acquired in an interleaved fashion.

For  $^{15}\text{N}$   $R_1$  measurements on the complex at 60 kHz spinning, double quantum cross-polarization (CP) contact times were 1.2 ms ( $^1\text{H}$ - $^{15}\text{N}$ ) and 0.85 ms ( $^{15}\text{N}$ - $^1\text{H}$ ), with nutation frequencies of 10 kHz and  $\sim 50$  kHz for  $^{15}\text{N}$  and  $^1\text{H}$  respectively. The relaxation curve was sampled with five points with relaxation delays between 2 ms and 24 s. 128 scans of 56  $t_1$  increments were taken (experimental time 118.5 h). Recycle delays were 2 s.

For  $^{15}\text{N}$   $R_{1\rho}$  relaxation dispersion on crystalline GB1, a series of interleaved  $^{15}\text{N}$   $R_{1\rho}$  measurements were performed at spin-lock frequencies 1.95, 2.44, 3, 4, 5, 6 and 8 kHz. Each  $R_{1\rho}$  curve was sampled using 10-12 points with spin-locks up to 0.5 s. 4 scans of 70  $t_1$  increments were collected, with a recycle delay of 2 s (total experimental time X).  $^1\text{H}$ - $^{15}\text{N}$  and  $^{15}\text{N}$ - $^1\text{H}$  CP contact times were 1.5 and 1.0 ms, respectively, with nutation frequencies of 10 kHz ( $^{15}\text{N}$ ) and  $\sim 40$  kHz ( $^1\text{H}$ ).

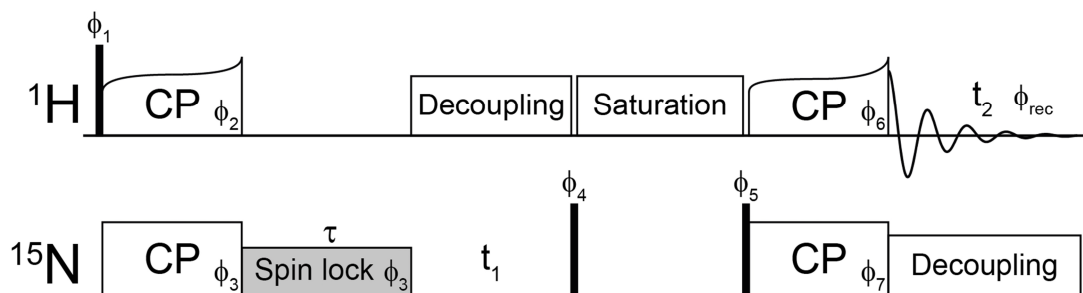
For  $^{15}\text{N}$   $R_1$  measurements on crystalline GB1 at 60 kHz spinning, double quantum cross-polarization (CP) contact times were 0.6 ms ( $^1\text{H}$ - $^{15}\text{N}$ ) and 0.7 ms ( $^{15}\text{N}$ - $^1\text{H}$ ), with nutation frequencies of 10 kHz and  $\sim 50$  kHz for  $^{15}\text{N}$  and  $^1\text{H}$  respectively. The relaxation curve was sampled with ten points with relaxation delays between 2 ms and 27 s. 16 scans of 98  $t_1$  increments were taken (experimental time 42 h). Recycle delays were 2 s.

For all experiments, 10 kHz WALTZ-16 heteronuclear decoupling was applied to  $^1\text{H}$  during  $^{15}\text{N}$  evolution, and to  $^{15}\text{N}$  during direct  $^1\text{H}$  acquisition, while suppression of the  $^1\text{H}$  signal of water was achieved by saturation with 200 ms (for the complex) or 50 ms (for the crystals) of slpTPPM  $^1\text{H}$  decoupling<sup>[2]</sup> applied at an amplitude of  $\frac{1}{4}$  of the MAS frequency. In all experiments, hard pulses were applied at nutation frequencies of 100 kHz ( $^1\text{H}$  and  $^{13}\text{C}$ ) and 50 or 83.3 kHz ( $^{15}\text{N}$ ). Quadrature detection was

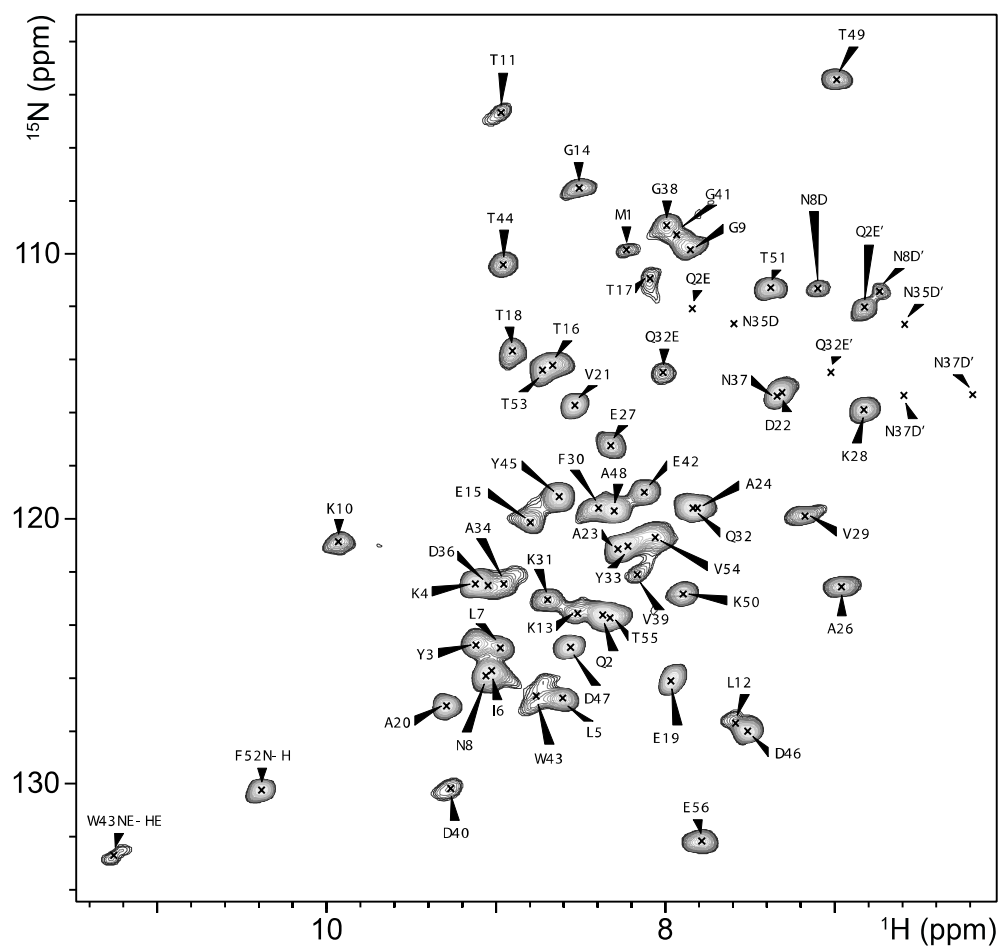


achieved using the States-TPPI method. Each of the spin-lock frequencies were determined using nutation experiments.

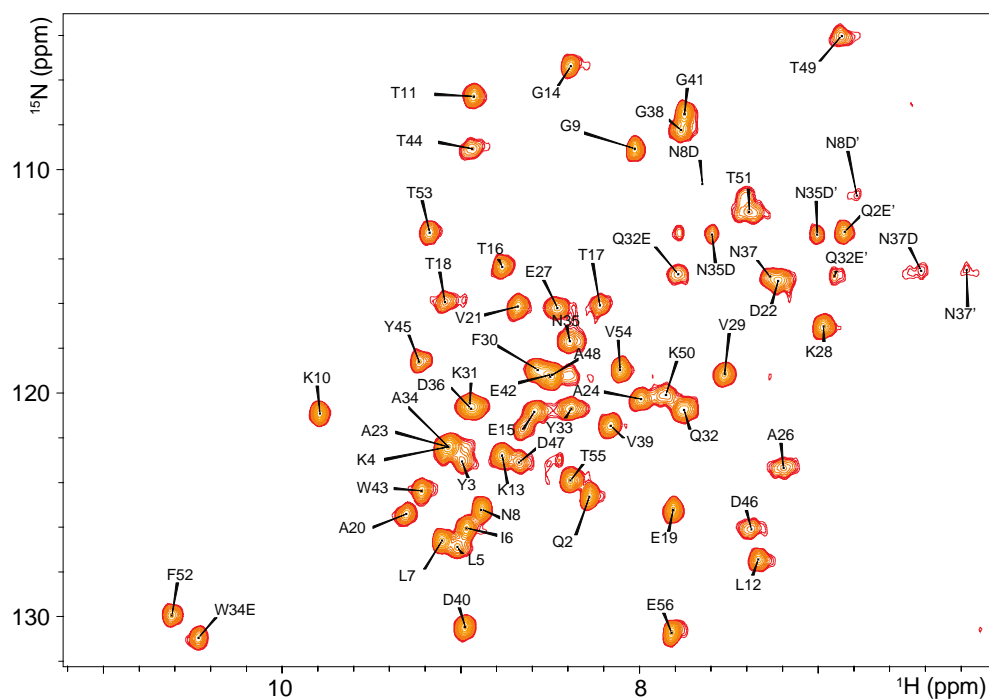
TopSpin 3.2 and CcpNmr Analysis 2.2.2 were used to process spectra and analyze the relaxation data, which was subsequently fitted using Origin 9.1. Fig.3.2-3.3 were produced using the UCSF Chimera package<sup>[3]</sup>.



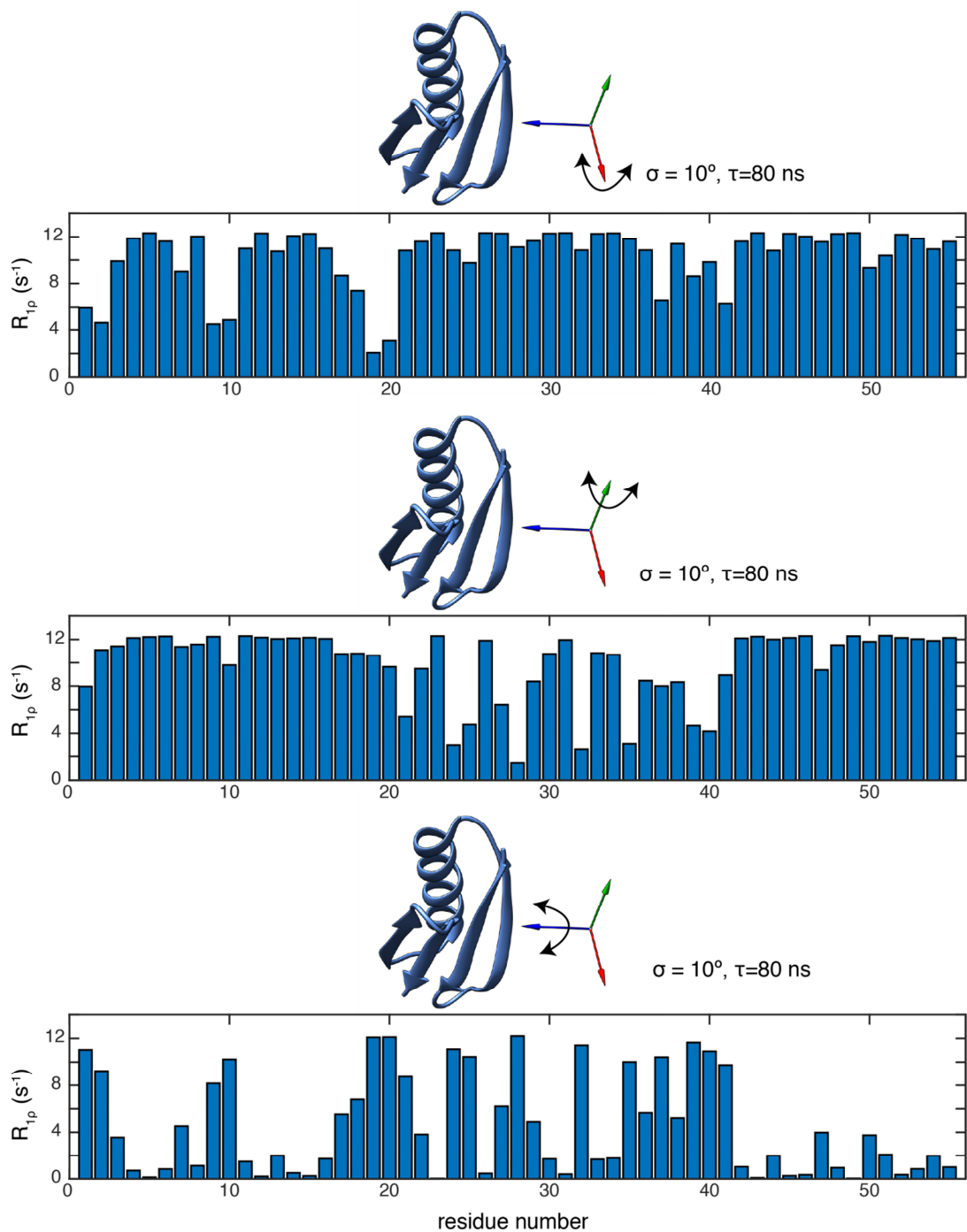
**Figure S3.1.** Pulse sequence used for measuring  $^{15}\text{N}$   $R_{1\rho}$  rates in the GB1:IgG complex, where direct proton detection offers a crucial enhancement in sensitivity compared to nitrogen or carbon detection. Hard  $\pi/2$  pulses are shown as black rectangles. The spin-lock pulse, colored in gray, is incremented (length  $\tau$ ) between experiments to follow the  $R_{1\rho}$  relaxation of the  $^{15}\text{N}$  nuclei. Phase cycling:  $\phi_1=(+y)$ ,  $\phi_2=(+y +y +y +y -y -y -y -y)$ ,  $\phi_3=(+x)$ ,  $\phi_4=-\phi_5=(+x +x -x -x)$ ,  $\phi_6=(+y +y -y -y)$ ,  $\phi_7=(+y -y +y -y)$ ,  $\phi_{\text{rec}}=(+y -y -y +y -y +y -y)$



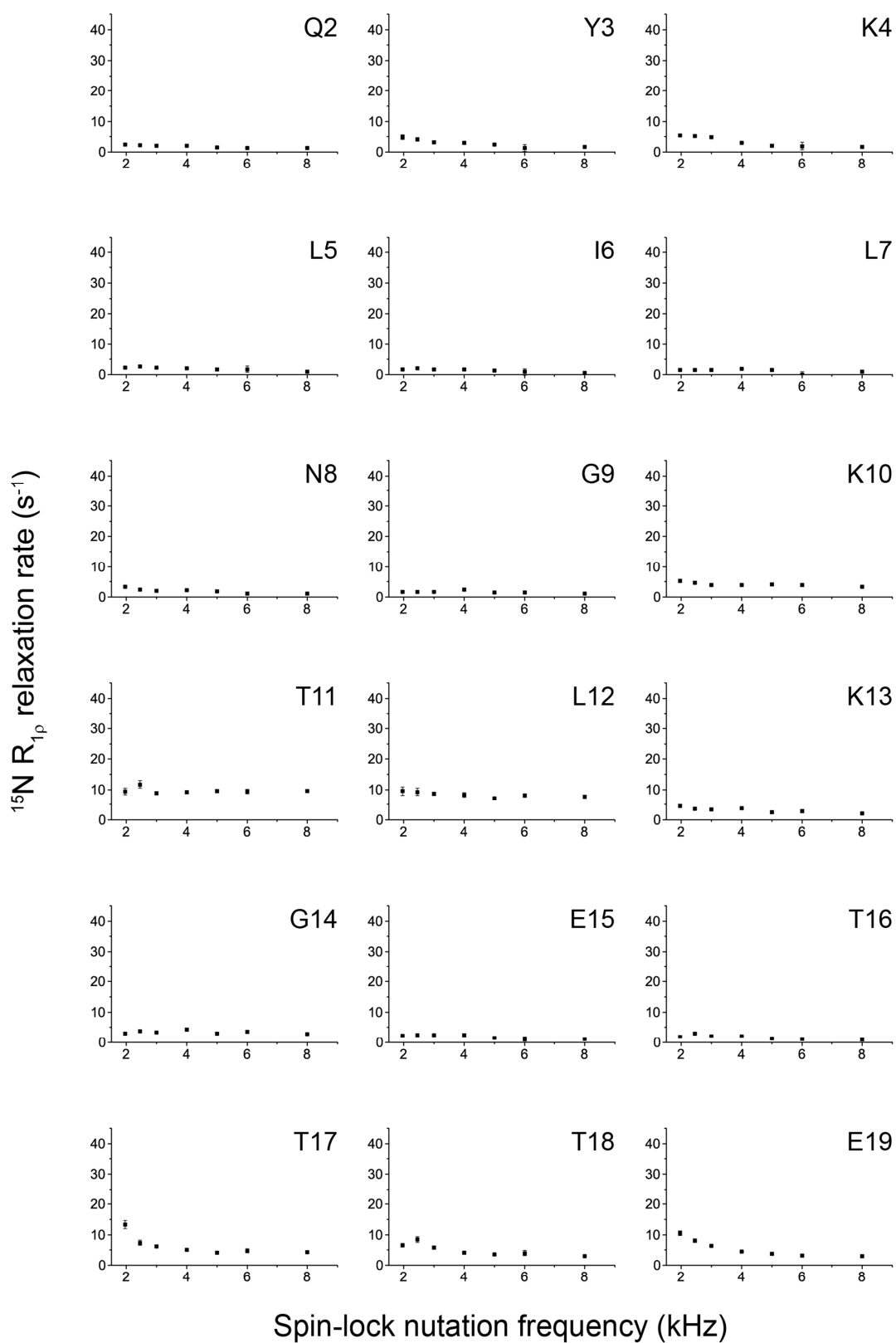
**Figure S3.2.** Assigned 2D  $^{15}\text{N}$ - $^1\text{H}$  spectrum of deuterated (full-protonated at exchangeable sites) [U- $^{13}\text{C}$ ,  $^{15}\text{N}$ ]GB1 in complex with natural abundance full-length human IgG, recorded at a  $^1\text{H}$  Larmor frequency of 850 MHz and at an MAS frequency of 60 kHz.

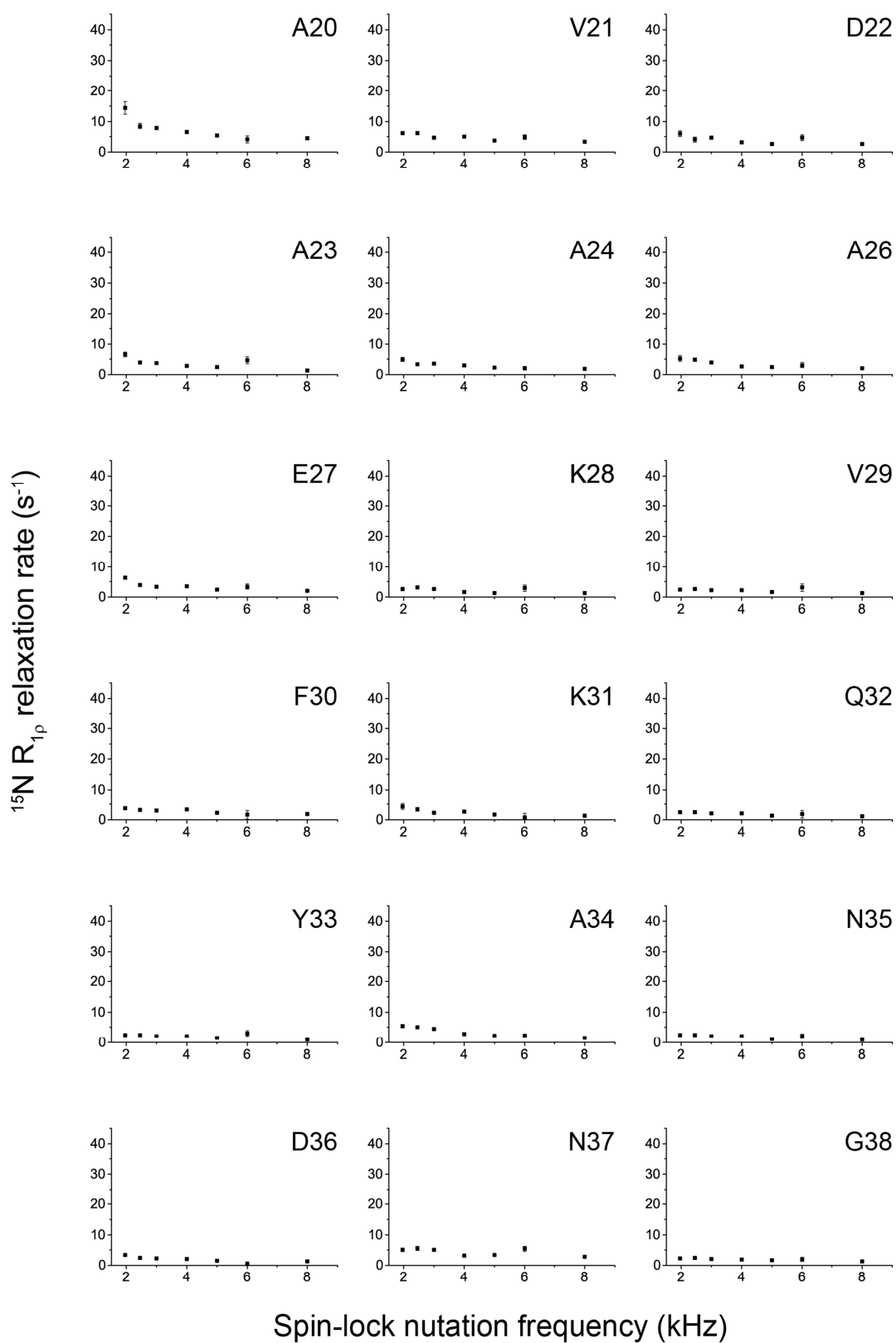


**Figure S3.3.** Assigned 2D  $^{15}\text{N}$ - $^1\text{H}$  spectrum of deuterated (full-protonated at exchangeable sites) crystalline  $[\text{U-}^{13}\text{C}, ^{15}\text{N}]\text{GB1}$ , recorded at a  $^1\text{H}$  Larmor frequency of 850 MHz and at an MAS frequency of 60 kHz.



**Figure S3.4.** Simulated  $^{15}\text{N}$   $R_{1\rho}$  rates for overall anisotropic motion of GB1 about three different motional axes (inertia axes for GB1 structure PDB ID: 2qmt<sup>[4]</sup>). The rates were simulated using 3D GAF<sup>[5]</sup> for a 10 degree fluctuation against the indicated axes, with a correlation time of 80 ns at 850  $^1\text{H}$  Larmor frequency. Both  $^{15}\text{N}$ - $^1\text{H}$  dipolar and  $^{15}\text{N}$  CSA contributions were considered. For  $^{15}\text{N}$  CSA the following parameters were assumed:  $\sigma_{11}=231.4$  ppm,  $\sigma_{22}=80.6$  ppm and  $\sigma_{33}=54.0$  ppm.





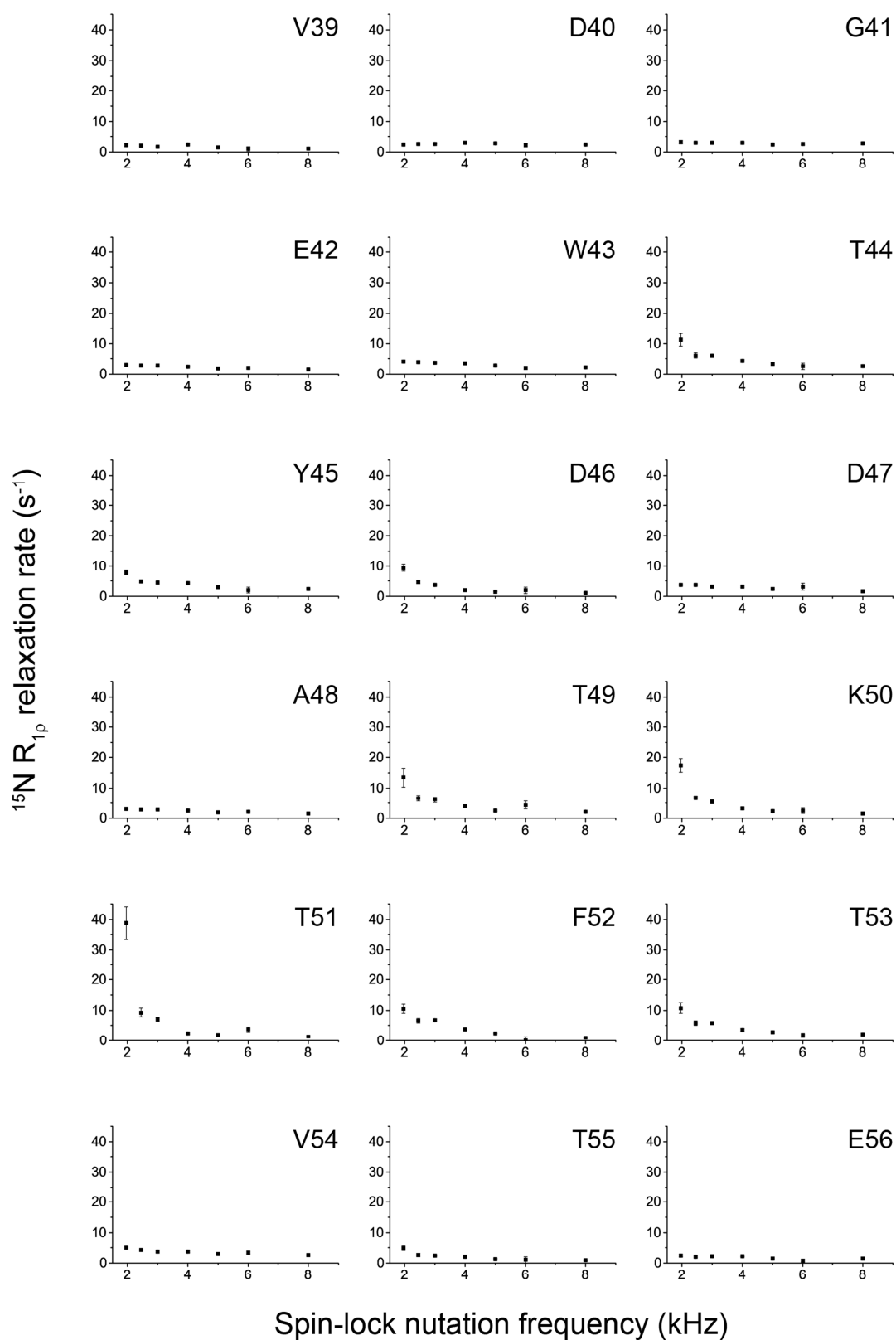


**Figure S3.5.**  $^{15}\text{N}$   $R_{1\rho}$  relaxation dispersion curves measured on crystalline 100% back-exchanged  $[\text{U-}^2\text{H}, ^{13}\text{C}, ^{15}\text{N}]\text{GB1}$  at a  $^1\text{H}$  Larmor frequency of 600 MHz, 50 kHz MAS and at a sample temperature of 27 °C. Spin-lock frequencies were determined by recording nutation experiments. While the majority of residues display little in the way of dispersion (i.e. most are flat), residues 17, 19, 20, 44, 46, 49, 50, 51, 52 and 53 show clear dispersion (displayed in Fig. 3b in the main manuscript). For those that are “flat”, the  $R_{1\rho}$  rate at a spin-lock field of 1.95 kHz is actually on average  $1.7\text{ s}^{-1}$  higher than the plateau

value at 8 kHz spin-lock, an increase we attribute to the presence of coherent contributions to the measured rates at the lower spin-lock field.

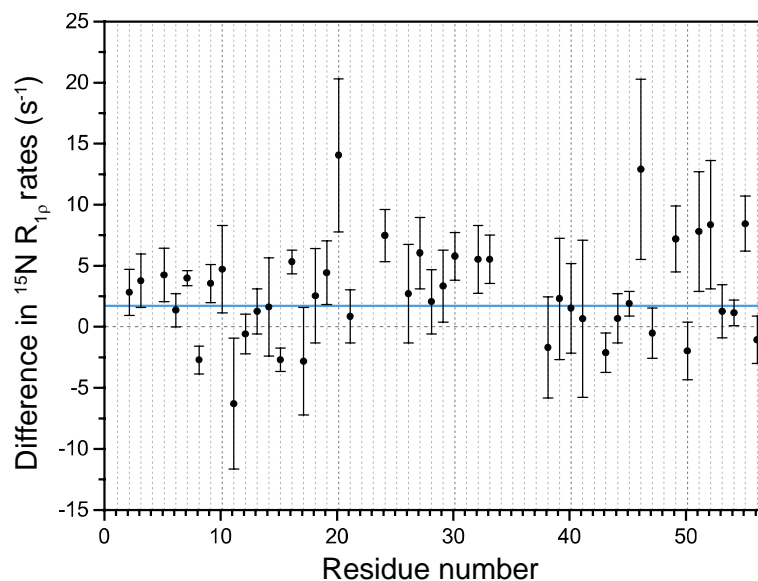


**Figure S3.6.** Differences between the  $^{15}\text{N}$   $R_{1\rho}$  relaxation rates measured at 2.5 kHz and 17 kHz spin-lock fields (i.e.  $R_{1\rho}[2.5 \text{ kHz}] - R_{1\rho}[17 \text{ kHz}]$ ) in 100% back-exchanged deuterated GB1 in complex with IgG, at a sample temperature of  $27 \pm 1$  °C. Exchange contributions are decoupled at 17 kHz, but at 2.5 kHz have observable effects on the decay rates. The horizontal blue line at  $1.7 \text{ s}^{-1}$  represents the average coherent contribution to measured rates as found in crystalline deuterated GB1 at 50 kHz MAS and a spin-lock field amplitude of 1.95 kHz. While the latter conditions differ slightly from those used here (60 kHz MAS and 2.5 kHz spin-lock), this fact only ensures that  $1.7 \text{ s}^{-1}$  is a safe overestimate of the coherent contribution in this case. All residues for which  $R_{1\rho}[2.5 \text{ kHz}] - R_{1\rho}[17 \text{ kHz}]$  is greater than this threshold by about one error bar or more (calculated from fit errors) were taken to be undergoing exchange processes on the  $\mu\text{s}$ -time scale (displayed in Fig. 3a in the main manuscript). These are residues 3-5, 7, 9, 10, 16, 19, 20, 24, 27, 30-31, 34, 36, 42, 46, 49, 51 and 52.



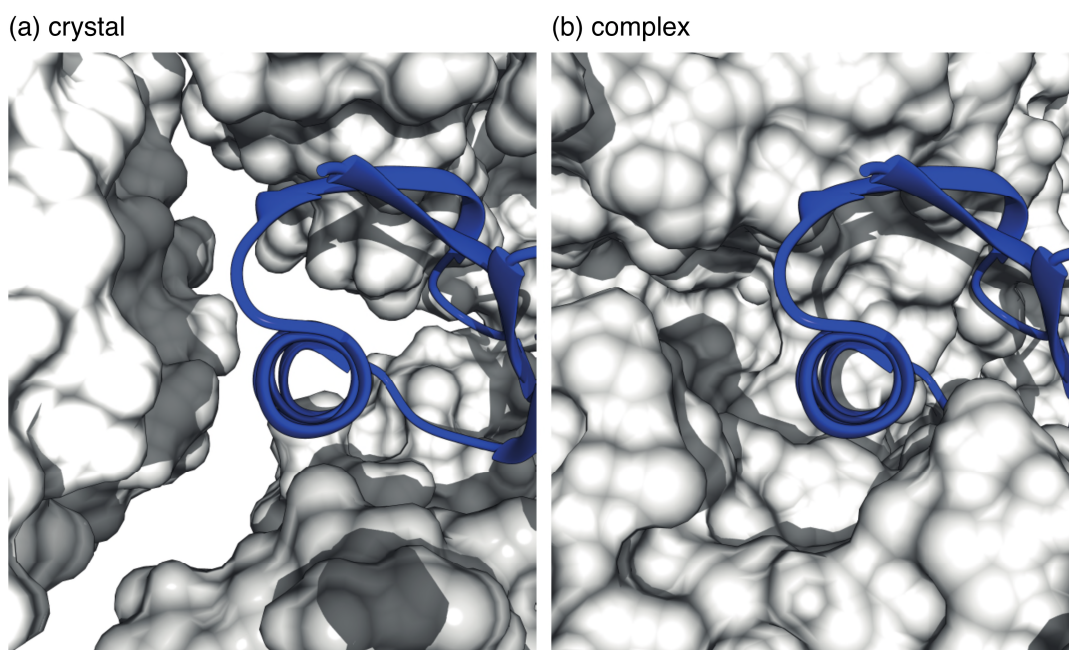


**Figure S3.7.** Comparison of helix packing in GB1 crystal (modeled using structure with PDB ID 2qmt<sup>[4]</sup>) and complex with IgG (modeled using structure of GB1 in complex with Fc fragment of IgG with PDB ID 1fcc<sup>[6]</sup> our previous studies show that the interaction interface identified for a complex with a fragment is consistent with the interface in the complex with full length IgG). The buried surface area for the solvent accessible surface, calculated for the interface between the loop2-helix-loop3 fragment of GB1 and other molecules, is  $\sim 440 \text{ \AA}^2$  for the GB1 in the crystal and  $\sim 571 \text{ \AA}^2$  for GB1 in the complex. This indicates denser packing of the helix in the complex compared to in the crystal. Similarly, the buried surface area for the solvent accessible surface, calculated for the interface between the loop1-strand2-loop2 fragment of GB1 and other molecules,  $\sim 334 \text{ \AA}^2$  for the GB1 in the crystal and  $\sim 457 \text{ \AA}^2$  for GB1 in the complex (PDB ID 1igc<sup>[7]</sup> used as reference). The buried surface area was calculated in Chimera<sup>[3, 8]</sup> using models with added protons and deleted solvent molecules, ligands and ions.

### 3.5.2 3D GAF model including spinning frequency dependent expressions for $R_{1\rho}$

Single rigid-body motion is assumed and parameterized using a 3D GAF (Gaussian axial fluctuations) model where the coordinates of all NH vectors are expressed in a common molecular frame. As a starting point we expressed the NH vectors using polar coordinates in the inertia frame of GB1 (computed for the x-ray structure (PDB ID: 2qmt<sup>[4]</sup>)) and then used two angles to define the orientation of the reference frame as fit parameters. Thus the fit parameters included amplitudes of fluctuations against three orthogonal axes ( $\sigma_\alpha$ ,  $\sigma_\beta$ ,  $\sigma_\gamma$ ), a correlation time for the overall motion,  $\tau$ , and two angles  $\Delta\theta$  and  $\Delta\phi$  defining the orientation of the reference frame for the motion (see below).

Fitting of the relaxation data (see Fig. 3a) to the model was performed in Matlab. The minimization was performed using code based on the *fminsearch* function with several random starting points to ensure a global minimum was found. The best-fit amplitude and time scale parameters for all the models were determined by minimizing the  $\chi^2$  target function:

$$\chi^2 = \sum_i \frac{(X_{i,calc} - X_{i,exp})^2}{\sigma_{i,exp}^2}$$

where  $X_i$  are relaxation rates,  $\sigma_i$  appropriate experimental errors.

Both dipolar NH ( $r_{NH} = 1.02 \text{ \AA}$ ) and  $^{15}\text{N}$  CSA (assuming axially symmetric CSA tensor collinear with NH vector;  $\Delta\sigma = -170 \text{ ppm}$ ,  $\eta = 0$ ) contributions to the relaxation were considered. The following expressions for relaxation rates were used:

$$R_{1\rho,N} = R_{1\rho,NH} + R_{1\rho,NCSA}$$

$$R_{1\rho,NH} = \frac{1}{20} \left( \frac{\mu_0}{4\pi} \frac{\hbar \gamma_H \gamma_N}{r_{NH}^3} \right)^2 \left( \frac{2}{3} J_0(\omega_1 + 2\omega_r) + \frac{2}{3} J_0(\omega_1 - 2\omega_r) + \frac{4}{3} J_0(\omega_1 + \omega_r) + \frac{4}{3} J_0(\omega_1 - \omega_r) + 3J_1(\omega_N) + J_0(\omega_H - \omega_N) + 6J_1(\omega_H) + 6J_2(\omega_H + \omega_N) \right)$$

$$R_{1\rho,NCSA} = \frac{1}{45} (\sigma_{\parallel} - \sigma_{\perp})^2 \left( \frac{2}{3} J_0(\omega_1 + 2\omega_r) + \frac{2}{3} J_0(\omega_1 - 2\omega_r) + \frac{4}{3} J_0(\omega_1 + \omega_r) + \frac{4}{3} J_0(\omega_1 - \omega_r) + 3J_1(\omega_N) \right)$$

The above expressions for  $R_{1\rho}$  are based on the expressions from ref. [9] considering an on-resonance  $R_{1\rho}$  measurement .

The spectral density was defined as:

$$J(\omega) = (1 - S_{\mu\nu}^2) \frac{\tau}{1 + (\omega\tau)^2}$$

with the 3D GAF order parameter  $S_{\mu\nu}^2$  being defined as:

$$S_{\mu\nu}^2 = \frac{4\pi}{5} \sum_{l,k,k',m,m'=-2}^2 (-i)^{k-k'} e^{-\frac{\sigma_\alpha^2}{l^2} - \frac{\sigma_\beta^2(k^2+k'^2)}{2} - \frac{\sigma_\gamma^2(m^2+m'^2)}{2}} d_{kl}^{(2)}\left(\frac{\pi}{2}\right) d_{k'l}^{(2)}\left(\frac{\pi}{2}\right) d_{m'k'}^{(2)}\left(\frac{\pi}{2}\right) Y_{2m}(\mathbf{e}_\mu^{pp}) Y_{2m'}^*(\mathbf{e}_\nu^{pp})$$

where  $Y_{2m}$  are the second spherical harmonics and  $\mathbf{e}_\mu^{pp} = (\theta_\mu, \varphi_\mu)$  defines the principal axis for the interaction  $\mu$  in the 3D GAF reference frame for the motions.<sup>[10]</sup>  $d_{kl}^{(2)}(\frac{\pi}{2})$  are the reduced Wigner matrix elements with the rotation angle in the parenthesis.  $\sigma_\alpha$ ,  $\sigma_\beta$ ,  $\sigma_\gamma$  are the fluctuations (in rad) against three orthogonal axes  $\alpha$ ,  $\beta$ ,  $\gamma$ .

For very slow motions the contributions to  $^{15}\text{N}$   $R_{1\rho}$  from fluctuations of dipolar couplings between nitrogens and protons that are not directly bonded to them (including protons on IgG) may be non-negligible. By considering x-ray structures of GB1 analogues with IgG fragments we estimated that typically the cumulative effect of such couplings should not exceed the effective coupling corresponding to a distance of  $\sim 2.5$  Å. In order to evaluate how such contributions would influence the above 3D GAF analysis we refitted the data including an additional term for all the residues corresponding to relaxation induced by 2.5 Å NH dipolar relaxation. The isotropic  $S^2$  for this contribution was treated as an additional fit parameter. In order to avoid solutions that may violate assumptions of Redfield theory we have also imposed an additional penalty for correlation times that approach the largest relaxation rates. The best fit yielded fluctuations of  $3.1^\circ$ ,  $5.3^\circ$ ,  $5.6^\circ$  with  $\Delta\theta = 11.8^\circ$ ,  $\Delta\varphi = 14.7^\circ$  (i.e. axes similar to the ones presented in Fig. 3.3), with a correlation time of  $\tau = \sim 54$   $\mu\text{s}$  and  $S^2 = 0.999$ .

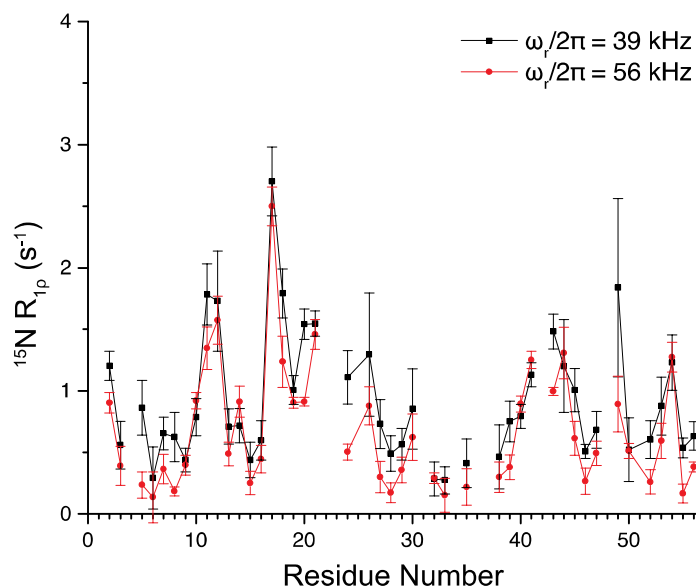


**Figure S3.8.** Comparison of  $^{15}\text{N}$   $R_{1\rho}$  rates measured at 56 and 39 kHz spinning frequencies measured for crystalline 100%  $\text{H}_2\text{O}$  [ $\text{U-}^2\text{H}$ ,  $^{13}\text{C}$ ,  $^{15}\text{N}$ ]GB1 at  $\omega_{1\text{N}}/2\pi = 10$  kHz, 600 MHz  $^1\text{H}$  Larmor frequency with a sample temperature of  $27 \pm 1$  °C.

### 3.5.2 References

- [1] W. T. Franks, D. H. Zhou, B. J. Wylie, B. G. Money, D. T. Graesser, H. L. Frericks, G. Sahota, C. M. Rienstra, *J. Am. Chem. Soc.* **2005**, *127*, 12291-12305.
- [2] J. R. Lewandowski, J. Sein, H. J. Sass, S. Grzesiek, M. Blackledge, L. Emsley, *J. Am. Chem. Soc.* **2010**, *132*, 8252-8254.
- [3] E. F. Pettersen, T. D. Goddard, C. C. Huang, G. S. Couch, D. M. Greenblatt, E. C. Meng, T. E. Ferrin, *J. Comp. Chem.* **2004**, *25*, 1605-1612.
- [4] H. L. Frericks Schmidt, L. J. Sperling, Y. G. Gao, B. J. Wylie, J. M. Boettcher, S. R. Wilson, C. M. Rienstra, *J. Phys. Chem. B* **2007**, *111*, 14362-14369.
- [5] D. B. Good, S. Wang, M. E. Ward, J. Struppe, L. S. Brown, J. R. Lewandowski, V. Ladizhansky, *J. Am. Chem. Soc.* **2014**, *136*, 2833-2842.
- [6] A. E. Sauer-Eriksson, G. J. Kleywegt, M. Uhlen, T. A. Jones, *Structure* **1995**, *3*, 265-278.
- [7] J. P. Derrick, D. B. Wigley, *J. Mol. Biol.* **1994**, *243*, 906-918.

- [8] M. F. Sanner, A. J. Olson, J. C. Spehner, *Biopolymers* **1996**, 38, 305-320.
- [9] R. Kurbanov, T. Zinkevich, A. Krushelnitsky, *J. Chem. Phys.* **2011**, 135, 184104.
- [10] S. F. Lienin, T. Bremi, B. Brutscher, R. Bruschweiler, R. R. Ernst, *J. Am. Chem. Soc.* **1998**, 120, 9870-9879.

## **4. Accelerated Experiments for Probing Microsecond Exchange in Large Protein Complexes in the Solid State**

### **4.1 Abstract**

Solid state NMR is a powerful method to obtain information on structure and dynamics of protein complexes, that due to solubility and size limitations cannot be achieved by other methods. Here we present an approach that uses a paramagnetic agent to accelerate  $^{15}\text{N}$   $R_{1\rho}$  relaxation dispersion measurements thus enabling quantification of microsecond conformational exchange in large protein complexes in reasonable amounts of time. The method is validated on crystalline GB1 and then applied to a  $> 300$  kDa precipitated complex of GB1 with full length human immunoglobulin G (IgG). We discover an exchange process spanning the  $\beta$  sheet that is similar for GB1 in crystals and in complex with IgG. Our results suggest that the intermolecular hydrogen bonds to the  $\beta_2$  strand in GB1 involved in the molecular recognition might be the main factor responsible for inducing this exchange process that does not occur for the isolated GB1 in solution.

### **4.2 Introduction and Discussion**

Protein dynamics play an important role in many biological processes such as enzymatic catalysis, ligand binding, or molecular recognition. Many motions implicated in these processes occur on a microsecond or slower time scale and can be probed using chemical exchange based methods, e.g. relaxation dispersion (RD).<sup>[1,2]</sup> Application of such or any other methods in solution becomes increasingly difficult for slowly tumbling proteins and protein complexes above a few tens of kDa due to the enhanced  $T_2$  relaxation resulting in size dependent broadening of NMR lines. In solid-state NMR, however, line broadening is independent of size of the system so biomolecules in assemblies of several hundred kDa and beyond may be studied, provided its intrinsic challenges of sensitivity and resolution can be successfully addressed.<sup>[3-11]</sup> Previously, we have shown that we can access information on protein backbone

dynamics of a protein G domain (GB1) in a > 300 kDa asymmetric complex with full length immunoglobulin G (IgG) by measuring  $^{15}\text{N}$   $R_1$  and  $R_{1\rho}$  relaxation rates.<sup>[3]</sup> The sensitivity enhancement from the proton detection at > 50 kHz magic angle spinning (MAS) frequencies enabled obtaining measurements in a reasonable amount of time for samples where the observed protein (GB1) is present in very small quantities (~50  $\mu\text{g}$  in a 1.3 mm rotor).<sup>[4]</sup> However, since methods such as  $R_{1\rho}$  relaxation dispersion<sup>[12]</sup> rely on recording of numerous 2D spectra to measure  $R_{1\rho}$  relaxation rates at several different spin lock fields, they require unpractically long experimental time for such a large complex forcing us to resort in a previous study to more approximate methods to detect presence of microsecond exchange.<sup>[3]</sup> By extrapolating from a single  $^{15}\text{N}$   $R_{1\rho}$  measurement on GB1:IgG complex, recording of a full relaxation dispersion curve with sensitivity sufficient for quantification would require experimental times on the order of one-two months. In order to circumvent this problem, here we propose to use paramagnetic agents such as (Gd(DTPA-BMA)) as additives to the samples to accelerate  $^{15}\text{N}$   $R_{1\rho}$  relaxation dispersion and thus enable us to perform this type of experiment on large protein complexes in more realistic time frames. The shortening of  $^1\text{H}$   $T_1$ 's due to addition of a paramagnetic agent into the sample enables fast recycling of the experiments, and is frequently used in solid state NMR to speed up acquisition for chemical shift assignments and structure calculation.<sup>[4,13-27]</sup> Since the paramagnetic agent also affects  $^1\text{H}$  and  $^{15}\text{N}$   $R_2$ 's ( $R_2=1/T_2$ ), its concentration needs to be adjusted so that it does not induce excessive line broadening. However, the exchange contribution to  $R_2$  or  $R_{1\rho}$  originating from modulation of isotropic chemical shift (or anisotropic interactions near rotary resonance conditions),<sup>[2,12]</sup> which is the source of relaxation dispersion, is not affected by the paramagnetic relaxation enhancement (provided it does not induce paramagnetic shifts). Thus quantitative relaxation dispersion can still be measured in the presence of paramagnetic agents. The main difference in such

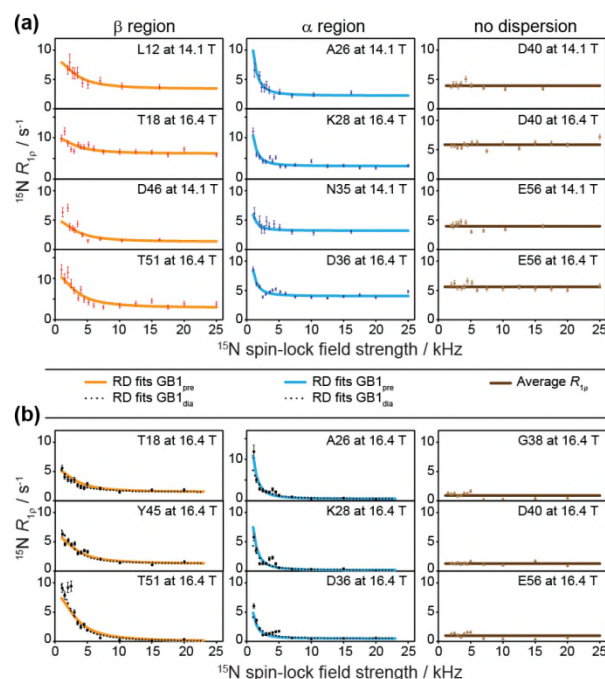


**Figure 4.1.**  $^{15}\text{N}$   $R_{1\rho}$  relaxation dispersion for crystalline GB1. (a) Example fits based on the data from crystalline GB1 in a presence of paramagnetic agent ( $\text{GB1}_{\text{pre}}$ ). From left to right;  $\beta$  and  $\alpha$  regions showing dispersion and the region with no dispersion. Solid lines represent the results of Bloch-McConnell fits of a two-state exchange model using data obtained at 14.1 and 16.4 T and a sample temperature of  $300 \pm 2$  K. (b) Example fits based on data from crystalline GB1 without paramagnetic dopant ( $\text{GB1}_{\text{dia}}$ ). From left to right;  $\beta$  region,  $\alpha$  region and the region with no dispersion. Dotted black lines represent the results of Bloch-McConnell fits of a two-state exchange model using data obtained at 14.1 and 16.4 T, solid lines represent the curves back-calculated from the best fit parameters for  $\text{GB1}_{\text{pre}}$  with  $R_{1\rho,0}$  from  $\text{GB1}_{\text{dia}}$ .

an ACCELErated RELaxation Dispersion (ACCELERED) experiment compared to one obtained in the absence of paramagnetic dopants should be only a different base/plateau relaxation rate ( $R_{1\rho,0}$ ). To validate the ACCELERED method we compared  $^{15}\text{N}$   $R_{1\rho}$  relaxation dispersion experiments on crystalline GB1 where such measurements are practical with ( $\text{GB1}_{\text{pre}}$ ) and without ( $\text{GB1}_{\text{dia}}$ ) the presence of a paramagnetic agent. Subsequently, we applied this validated technique to obtain site specific information on microsecond conformational exchange of GB1 in the  $> 300$  kDa complex with IgG.

In the solid state in order to obtain quantitative relaxation dispersion measurements the experiments need to be performed under conditions where coherent effects, which originate from dipolar couplings that are not completely averaged by magic angle spinning, are suppressed.<sup>[28,29]</sup> For  $^{15}\text{N}$  measurements this is typically achieved by deuteration and partial re-protonation at exchangeable sites of the studied protein and



application of fast, >40 kHz, spinning.<sup>[12]</sup> The larger the concentration of the remaining protons in the sample the faster spinning frequencies need to be employed. Here we employ 60 kHz spinning in a 100 % back-exchanged perdeuterated [U-<sup>13</sup>C, <sup>15</sup>N]GB1 sample. As can be seen by the flat dispersion curves for residues not undergoing conformational exchange the dipolar dephasing is sufficiently suppressed under these conditions (Fig. 4.1). Generally, the same residues are showing clear dispersion in experiments with and without paramagnetic dopant (SI figure 4.7). We observe dispersion in two regions: residues in the  $\alpha$  helix (region  $\alpha$ , residues 24, 26, 28, 29, 32, 33, 35, 36 in GB1<sub>pre</sub> indicated in blue in Figure 4.1a) and residues in  $\beta$  sheet (region  $\beta$ ; strands 2-4 and loops between strand; residues 12, 17-18, 44-46, 49-53 GB1<sub>pre</sub>, indicated in orange red in Fig. 4.1a). To quantify the microsecond exchange processes in crystalline GB1 in diamagnetic and paramagnetic samples we fitted residues showing clear dispersion in measurements at two magnetic fields (14.1 and 16.4 T; SI figures 4.1-4.4, 4.7) to the two-site exchange Bloch-McConnell formalism (eq. 4.1, see SI).<sup>[30,31]</sup> All residues were initially fitted individually. Because the values of exchange rates for residues that are close in space are rather closely distributed we also fitted such groups of residues simultaneously assuming that they undergo a common motion, i.e. assuming common exchange rate,  $k_{ex}$ , and populations for the exchanging states,  $p_A$  &  $p_B$ , but residue specific chemical shift differences between the states,  $\Delta\delta$ . The fit where residues in the  $\alpha$  region were fitted simultaneously to one motion and residues in the  $\beta$  region simultaneously to another motion (see Table 1) yielded the lowest Bayesian Information Criterion suggesting that, at least statistically, this is the most justified model (see SI table 4.14).

Table 4.1. Results from RD fits for GB1<sub>dia</sub> (left) and GB1<sub>pre</sub> (right).

	Crystalline GB1 <sub>dia</sub>				Crystalline GB1 <sub>pre</sub>			
	$k_{ex}$ (s <sup>-1</sup> )	±	$p_B$ (%)	±	$k_{ex}$ (s <sup>-1</sup> )	±	$p_B$ (%)	±
All	14094	420	1.28	0.08	14988	814	1.95	0.22
α	8750	546	0.9	0.07	4176	804	1.66	0.16
β	14374	486	2.54	0.24	19945	1320	3.73	0.21

The results of all performed fits are shown in the SI (SI tables 4.1-4.8). Examples of relaxation dispersion profile fits for GB1<sub>pre</sub> are shown in Fig. 4.1a and for GB1<sub>dia</sub> in Fig. 4.1b. Overall, the parameters of the exchange processes obtained from GB1<sub>pre</sub> agree well with the data for GB1<sub>dia</sub> confirming that although a paramagnetic agent affects  $R_{1\rho}$  relaxation rates it does not affect the exchange contribution. As another way of validating that relaxation dispersion curves in GB1<sub>pre</sub> paint the same picture of microsecond exchange as relaxation dispersion curves in GB1<sub>dia</sub>, we have also plotted in Fig. 4.1b dispersion curves back-calculated from best fit parameters for GB1<sub>pre</sub> but with the plateau value for  $R_{1\rho}$ ,  $R_{1\rho,0}$ , from GB1<sub>dia</sub>. The orange and blue lines in Fig. 4.1b, which represent the  $R_{1\rho}$  rates back-calculated from GB1<sub>pre</sub> parameters follow closely the best fit curves for GB1<sub>dia</sub> indicated with the dotted black lines. Encouraged by the good correspondence of the view of microsecond exchange between crystalline GB1<sub>dia</sub> and GB1<sub>pre</sub>, we have applied the ACCELERED approach to a more challenging system, GB1 in a > 300 kDa complex with IgG, where performing <sup>15</sup>N  $R_{1\rho}$  RD on a diamagnetic sample would require unpractically long experimental times. For a diamagnetic sample of GB1:IgG complex each  $R_{1\rho}$  measurement requires ~3-5 days to obtain signal to noise sufficient for quantitative analysis, yielding experimental times on the order of 1-2 months for a full relaxation dispersion. Even if such long times could be dedicated for a single experiment, it is very challenging to maintain sufficient experimental stability over such long periods of time.

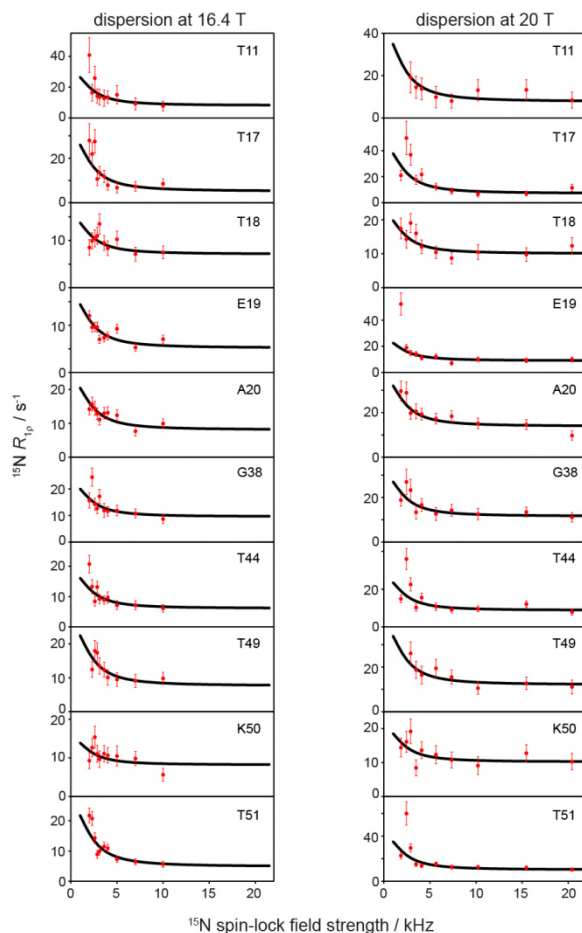


**Figure 4.2.**  $^{15}\text{N}$   $R_{1\rho}$  relaxation dispersion profiles for GB1 in complex with IgG measured at 16.4 T (left) and 20 T (right) and sample temperature  $300 \pm 2$  K for the diamagnetic sample (GB1<sub>dia</sub>) and sample with added paramagnetic agent (GB1<sub>pre</sub>). Best fit curves to a two-site exchange model assuming common motion are shown as black lines.

The addition of Gd(DTPA-BMA) allowed us to perform these experiments in 5 days on an 850 MHz spectrometer (20 T) and 10 days on a 700 MHz spectrometer (16.4 T), using 10 different spin-lock field strengths at each  $B_0$  field (RD profiles in SI figs 4.5-4.6; experimental durations in SI table 4.11). For the  $\beta$  region in the GB1:IgG complex dispersion was identified generally in the same places as in crystalline GB1, except for residue 38, which showed dispersion in the GB1:IgG complex but is in the loop region that was consistently flat in crystalline GB1 (see Fig. 4.3 and SI figures 4.5-4.6 and 4.8; note that data for some residues that show  $\mu\text{s}$  exchange in crystalline GB1 could not be obtained due to either severe overlap or insufficient signal to noise in the GB1:IgG complex).

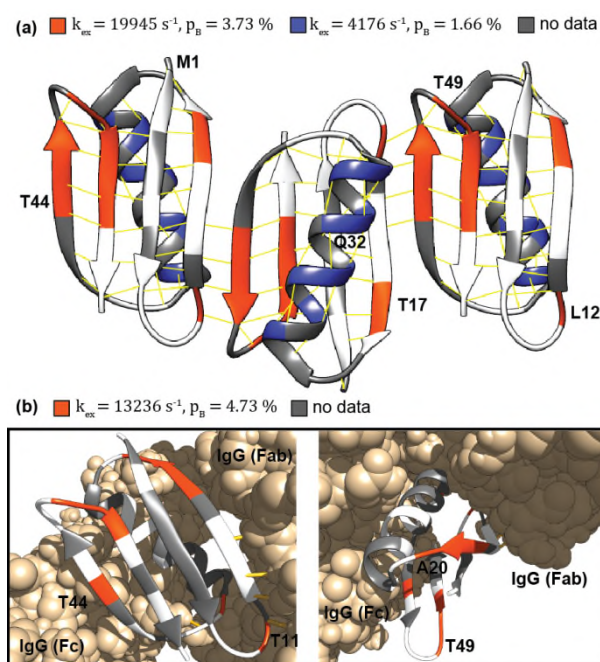


**Figure 4.3.** Microsecond exchange in crystalline GB1 (a) and GB1 in a complex with IgG (b). Residues in the  $\beta$  region are shown in orange. Residues in the  $\alpha$  region are shown in blue. Exchange rates for group fits of the regions and populations for the minor conformer are given above the figures. Grey represents missing data.

The dispersion at the C-terminal end of  $\beta 4$  is less clear, especially at lower magnetic field, which could be potentially explained by the additional intermolecular interaction in that region restricting the amplitude of the conformational change or slowing its time scale, and which we have recently proposed to be present in the complex with full length IgG based on chemical shift perturbations and solvent PREs. No residues in the  $\alpha$  region could be identified as showing clear dispersion at both  $B_0$  fields, which may indicate that this slow motion seen in the crystalline sample is not present in the complex or is slower and thus not picked up by our experiments where the lowest spin lock field employed was 2 kHz. Overall, the RD is identified in similar regions as with an approximate method we applied to GB1:IgG complex in a previous study<sup>[3]</sup> but a number of false positives from the approximate method highlights the need for measuring full relaxation dispersion curves. In the GB1:IgG complex all residues showing dispersion were considered as being involved in the same motion and fitted together to obtain single values for  $k_{ex}$  ( $13236 \pm 2812 \text{ s}^{-1}$ ; see Fig. 4.2) and minor state population,  $p_B$  ( $4.73 \pm 0.73 \%$ ). The best fit parameters for individual

residues separately and for a single motion in GB1:IgG are listed in SI Tables 4.9-4.10. To investigate if there were separate motions for the individual binding sites to the Fab and Fc fragments of IgG we fitted residues close to each binding site separately, the results from these fits are very similar to the fit of all residues combined (SI tables 4.11-4.12).

Interestingly, the results of  $^{15}\text{N}$   $R_{1\rho}$  RD on crystalline GB1 and GB1 in the complex with full length IgG indicate that the conformational exchange process occurring on microsecond time scale in the  $\beta$  region is very similar in the two different assemblies: overall the same residues seem to participate in the process which is characterized by similar exchange rate and populations for the two states. In contrast, for isolated GB3 in solution (which has virtually the same structure as GB1) no microsecond exchange was detected at room temperature.<sup>[32]</sup> Using high powered  $^1\text{H}$  RD with GB3 under supercooled conditions exchange in the low microsecond range was detected for residues in loop 1 (residues 9-13),<sup>[32]</sup> which extrapolated to 310 K occurs with time scales on the order of 400 ns. This timescale of the motion is consistent with the time scale of motions at room temperature determined from the relaxation measurements in crystalline GB1<sup>[33]</sup> though the average activation energies for this slow backbone motion is estimated to be slightly lower<sup>[34]</sup> (in the 35-45 kJ/mol range) than the value from solution measurements. Thus the microsecond exchange observed using ACCELERED both in crystalline GB1 and GB1 in complex with IgG seems to be not present for the isolated GB1 in solution under the same experimental conditions. The influence of intermolecular interactions on the slow motions was observed previously, e.g. the main slow conformational exchange process for ubiquitin observed in solution and crystal involves the same residues but appears much slower in the latter.<sup>[12,35]</sup> However, here the microsecond conformational exchange process seems to be induced by intermolecular interactions. Importantly, the similarity of the  $\beta$  region motion parameters for crystalline GB1 and GB1:IgG complex seems to suggest that formation of intermolecular hydrogen bonds for the  $\beta 2$  strand (to another molecule of GB1 in the crystal and to the Fab fragment in the GB1:IgG complex), which exhibits largest amplitude slow motions in isolated molecule in solution,<sup>[36]</sup> is the

main factor determining the pattern of microsecond motions detected in the  $\beta$  region in the solid state.

Our ACCELERED results explain a number of previous observations about dynamics in crystalline GB1 and GB1:IgG complex. For example, presence of  $\mu$ s motions should induce spinning frequency dependence of  $R_{1\rho}$  but very little of such effect was observed for crystalline GB1. However, low population for the minor state means that even though the amplitude of motion may be appreciable the effective order parameter is very high<sup>[37]</sup> and thus contribution to relaxation not very large. A similar argument confirms that the strong spinning frequency dependence of  $^{15}\text{N}$   $R_{1\rho}$  observed in GB1:IgG does not originate from  $\mu$ s exchange and is consistent with a presence of overall small amplitude motion of GB1 in the complex with IgG.<sup>[3]</sup>

In summary, we have shown that adding a paramagnetic agent to hydrated solid state samples enables relaxation dispersion measurements in large protein complexes, in which low sensitivity otherwise prevents such measurements from being performed in a realistic time frame. This method, ACCELERED, has revealed a  $\mu$ s motion in  $\beta$  strands and connecting loop regions that occurs in both crystalline GB1 and in the GB1:IgG complex but is not present in isolated protein in solution. This suggests that this motion may be induced by intermolecular interactions and, in particular, intermolecular hydrogen bonds to the  $\beta_2$  strand of GB1 that is a common feature between the two studied assemblies.

#### **4.3 Acknowledgements**

The research leading to these results has received funding from the European Research Council under the European Union's Seventh Framework Programme (FP/2007-2013) / ERC Grant Agreement 639907. J.R.L. also acknowledges funding from BBSRC Grant BB/L022761/1 and Gates Foundation. C.O. acknowledges funding from the European Union under a Marie Curie Initial Training Network FP7-PEOPLE-2012-ITN Grant Agreement Number 316630 CAS-IDP. The UK 850 MHz solid-state NMR Facility used in this research was funded by EPSRC and BBSRC (contract reference PR140003), as well as the University of Warwick including via

part funding through Birmingham Science City Advanced Materials Projects 1 and 2 supported by Advantage West Midlands (AWM) and the European Regional Development Fund (ERDF). We thank the 850 MHz Facility Manager, Dinu Iuga, for assistance in acquiring the data at the 850 MHz spectrometer.

#### 4.4 References

- [1] A. G. Palmer, F. Massi, *Chem. Rev.* **2006**, *106*, 1700–1719.
- [2] P. Schanda, M. Ernst, *Prog. Nucl. Magn. Reson. Spectrosc.* **2016**, *96*, 1–46.
- [3] J. M. Lamley, C. Öster, R. A. Stevens, J. R. Lewandowski, *Angew. Chemie Int. Ed.* **2015**, *54*, 15374–15378.
- [4] J. M. Lamley, D. Iuga, C. Öster, H.-J. Sass, M. Rogowski, A. Oss, J. Past, A. Reinhold, S. Grzesiek, A. Samoson, et al., *J. Am. Chem. Soc.* **2014**, *136*, 16800–16806.
- [5] J. Struppe, C. M. Quinn, M. Lu, M. Wang, G. Hou, X. Lu, J. Kraus, L. B. Andreas, J. Stanek, D. Lalli, et al., *Solid State Nucl. Magn. Reson.* **2017**, DOI 10.1016/j.ssnmr.2017.07.001.
- [6] E. Barbet-Massin, C.-T. Huang, V. Daebel, S.-T. D. Hsu, B. Reif, *Angew. Chemie Int. Ed.* **2015**, *54*, 4367–4369.
- [7] A. Mainz, T. L. Religa, R. Sprangers, R. Linser, L. E. Kay, B. Reif, *Angew. Chemie Int. Ed.* **2013**, *52*, 8746–8751.
- [8] C. Gardiennet, A. K. Schütz, A. Hunkeler, B. Kunert, L. Terradot, A. Böckmann, B. H. Meier, *Angew. Chemie Int. Ed.* **2012**, *51*, 7855–7858.
- [9] M. Lu, G. Hou, H. Zhang, C. L. Suiter, J. Ahn, I.-J. L. Byeon, J. R. Perilla, C. J. Langmead, I. Hung, P. L. Gor'kov, et al., *Proc. Natl. Acad. Sci.* **2015**, *112*, 14617–14622.
- [10] H. R. W. Dannatt, M. Felletti, S. Jehle, Y. Wang, L. Emsley, N. E. Dixon, A. Lesage, G. Pintacuda, *Angew. Chemie Int. Ed.* **2016**, *55*, 6638–6641.
- [11] J.-P. Demers, B. Habenstein, A. Loquet, S. Kumar Vasa, K. Giller, S. Becker, D. B. Baker, A. Lange, N. G. Sgourakis, *Nat. Commun.* **2014**, *5*, 4976.

- [12] P. Ma, J. D. Haller, J. Zajakala, P. Macek, A. C. Sivertsen, D. Willbold, J. Boisbouvier, P. Schanda, *Angew. Chemie - Int. Ed.* **2014**, *53*, 4312–4317.
- [13] S. Parthasarathy, Y. Nishiyama, Y. Ishii, *Acc. Chem. Res.* **2013**, *46*, 2127–2135.
- [14] C. P. Jaroniec, *J. Magn. Reson.* **2015**, *253*, 50–59.
- [15] M. J. Knight, A. J. Pell, I. Bertini, I. C. Felli, L. Gonnelli, R. Pierattelli, T. Herrmann, L. Emsley, G. Pintacuda, *Proc. Natl. Acad. Sci.* **2012**, *109*, 11095–11100.
- [16] N. P. Wickramasinghe, M. Kotecha, A. Samoson, J. Past, Y. Ishii, *J. Magn. Reson.* **2007**, *184*, 350–356.
- [17] P. S. Nadaud, J. J. Helmus, I. Sengupta, C. P. Jaroniec, *J. Am. Chem. Soc.* **2010**, *132*, 9561–9563.
- [18] M. E. Ward, S. Wang, S. Krishnamurthy, H. Hutchins, M. Fey, L. S. Brown, V. Ladizhansky, *J. Biomol. NMR* **2014**, *58*, 37–47.
- [19] S. Balayssac, I. Bertini, A. Bhaumik, M. Lelli, C. Luchinat, *Proc. Natl. Acad. Sci.* **2008**, *105*, 17284–17289.
- [20] R. Linser, U. Fink, B. Reif, *J. Am. Chem. Soc.* **2009**, *131*, 13703–13708.
- [21] I. Sengupta, P. S. Nadaud, C. P. Jaroniec, *Acc. Chem. Res.* **2013**, *46*, 2117–2126.
- [22] S. J. Ullrich, S. Hölper, C. Glaubitz, *J. Biomol. NMR* **2014**, *58*, 27–35.
- [23] P. S. Nadaud, J. J. Helmus, S. L. Kall, C. P. Jaroniec, *J. Am. Chem. Soc.* **2009**, *131*, 8108–8120.
- [24] P. S. Nadaud, J. J. Helmus, N. Höfer, C. P. Jaroniec, *J. Am. Chem. Soc.* **2007**, *129*, 7502–7503.
- [25] G. Pintacuda, N. Giraud, R. Pierattelli, A. Böckmann, I. Bertini, L. Emsley, *Angew. Chemie Int. Ed.* **2007**, *46*, 1079–1082.
- [26] C. P. Jaroniec, *Solid State Nucl. Magn. Reson.* **2012**, *43–44*, 1–13.
- [27] N. P. Wickramasinghe, S. Parthasarathy, C. R. Jones, C. Bhardwaj, F. Long, M. Kotecha, S. Mehboob, L. W.-M. Fung, J. Past, A. Samoson, et al., *Nat. Methods* **2009**, *6*, 215–218.
- [28] J. R. Lewandowski, H. J. J. Sass, S. Grzesiek, M. Blackledge, L. Emsley, *J. Am. Chem. Soc.* **2011**, *133*, 16762–5.



- [29] J. R. Lewandowski, *Acc. Chem. Res.* **2013**, 46, 2018–2027.
- [30] O. Trott, A. G. Palmer, *J. Magn. Reson.* **2002**, 154, 157–160.
- [31] A. J. Baldwin, L. E. Kay, *J. Biomol. NMR* **2013**, 55, 211–218.
- [32] S. Pratihaar, T. M. Sabo, D. Ban, R. B. Fenwick, S. Becker, X. Salvatella, C. Griesinger, D. Lee, *Angew. Chemie Int. Ed.* **2016**, 55, 9566–9569.
- [33] J. M. Lamley, M. J. Lougher, H. J. Sass, M. Rogowski, S. Grzesiek, J. R. Lewandowski, *Phys. Chem. Chem. Phys.* **2015**, 17, 21997–2008.
- [34] J. R. Lewandowski, M. E. Halse, M. Blackledge, L. Emsley, *Science* **2015**, 348, 578–581.
- [35] D. F. Gauto, A. Hessel, P. Rovó, V. Kurauskas, R. Linser, P. Schanda, *Solid State Nucl. Magn. Reson.* **2017**, DOI 10.1016/j.ssnmr.2017.04.002.
- [36] G. Bouvignies, P. Bernado, S. Meier, K. Cho, S. Grzesiek, R. Bruschweiler, M. Blackledge, *Proc. Natl. Acad. Sci.* **2005**, 102, 13885–13890.
- [37] T. Zinkevich, V. Chevelkov, B. Reif, K. Saalwächter, A. Krushelnitsky, *J. Biomol. NMR* **2013**, 57, 219–235.

## 4.5 Supplementary Information

### 4.5.1 Experimental Section

Sample preparation. Isotope labelled [U-<sup>2</sup>H,<sup>13</sup>C,<sup>15</sup>N]GB1 2Q6I was expressed in M9 with D<sub>2</sub>O, deuterated [U-<sup>13</sup>C]glucose and <sup>15</sup>NH<sub>4</sub>Cl using pGEV2 in BL21(DE3)<sup>[1]</sup>. Cells were grown to an OD<sub>600</sub> >1.0 in two liters LB for each liter of M9 and washed once with PBS before resuspension in M9. Expression was induced with 0.5 mM IPTG after 1 h incubation at 37 °C. After expression for 4 h at 37 °C, the cells were pelleted (4000 × G for 20 min at 16 °C), and lysed by sonication in buffer containing lysozyme (50 mM potassium phosphate; 200 mM NaCl; 1 mg/ml lysozyme; pH

7.0). The lysate was then incubated at 75 °C for 10 min and cleared by centrifugation ( $12000 \times G$  for 50 min). After precipitation over night with 80% ammonium sulfate, GB1 was pelleted ( $15000 \times G$  for 50 min), resuspended in buffer (50 mM potassium phosphate; 200 mM NaCl; pH 7.0), and purified on a 16/600 Sephadex pg75 (GE Healthcare) gel filtration column. Fractions containing GB1 were collected, desalted, freeze-dried and stored at -20 °C.

Freeze-dried [ $U\text{-}^2H, ^{13}C, ^{15}N$ ]GB1 was dissolved in buffer (50 mM sodium phosphate buffer pH 5.5) to obtain a protein concentration of 10 mg/ml and crystallized with the aid of 2:1 2-methyl-2,4-pentanediol (MPD):Isopropanol<sup>[2]</sup>. GB1:IgG complex was formed by mixing GB1 and IgG (Sigma – Aldrich, lyophilized, human serum) solutions in 2:1 molar ratio<sup>[3]</sup>. Crystalline GB1 and precipitated GB1:IgG complex were packed into NMR rotors using the following procedure: The crystals/precipitate were spun down by centrifugation (1 min at  $20\,000 \times G$  using a bench top centrifuge), and resuspended in a small volume of the supernatant containing 2% DSS and Gd(DTPA–BMA) at the desired concentration. The samples were transferred into 200  $\mu$ l pipette tips, which were then attached to the rotors, put into 1.5 ml Eppendorf tubes and centrifuged ( $20\,000 \times G$ ) in 1-4 minutes intervals until the rotors were full. The rotor caps were sealed with a silicone-based glue to prevent leakage.

Solid state NMR. Solid state NMR spectra were recorded at 600 MHz Bruker Avance II+, 700 MHz Bruker Avance III HD and 850 MHz Bruker Avance III spectrometers, using Bruker 1.3 mm triple resonance probes at 60 kHz magic angle spinning. A Bruker BCU-X cooling unit was used to regulate the internal sample temperature to  $27 \pm 2$  °C (measured from the chemical shift of water with respect to DSS. For experiments recorded at 700 MHz  $^1H$  Larmor frequency with the GB1:IgG complex 10 %  $D_2O$  was added to the sample buffer before packing the rotors and deuterium locking was used in the same way as in solution NMR.  $^{15}N\text{-}^1H$  2D correlation spectra were recorded using a proton-detected heteronuclear correlation sequence. Double quantum cross-polarization (CP) contact times were between 0.5 – 1.5 ms and individually optimized for each sample. Recycle delays between 0.2 – 2 s were used depending

on the amount of paramagnetic agent and magnetic field.  $R_{1\rho}$  relaxation dispersion experiments were recorded as pseudo 3Ds with the varying spin-lock lengths as the 3<sup>rd</sup> dimension or a pseudo 4D (GB1:IgG complex at 850 MHz  $^1\text{H}$  Larmor frequency) with the varying spin-lock power as the 4<sup>th</sup> dimension.

In all solid-state experiments, hard pulses were applied at nutation frequencies of 100 kHz for  $^1\text{H}$  and 83.3 kHz for  $^{15}\text{N}$ . 10 kHz WALTZ-16 decoupling was applied on protons during  $^{15}\text{N}$  evolution, and on the  $^{15}\text{N}$  channel during direct  $^1\text{H}$  acquisition, while quadrature detection was achieved using the States-TPPI method. Suppression of the water signal was achieved by saturation with 50 - 200 ms of slpTPPM  $^1\text{H}$  decoupling applied at an amplitude of  $\frac{1}{4}$  of the MAS frequency<sup>[4]</sup> or 100-140 ms MISSISSIPPI<sup>[5]</sup> at an amplitude of  $\frac{1}{2}$  the MAS frequency on resonance with the water signal.  $R_{1\rho}$  relaxation curves were sampled using 7-10 points for all experiments. 1-25 kHz nutation frequencies, measured by nutation experiments, were used for the spin-lock fields in the  $R_{1\rho}$  experiments (see SI table 12 for number of points used and total duration of the experiments). All spectra were processed using TopSpin 3.2. GB1 resonances in the complex with IgG were previously assigned on the basis of 3D H(H)NH, CONH, CO(CA)NH and CANH experiments<sup>[3]</sup>. Peak integrals were calculated in TopSpin 3.2. OriginPro 2016 and MatLab R2014a were used to analyze the relaxation data.

Data fitting. Peak integrals from TopSpin were exported to MatLab where a mono-exponential function was used with the `fminsearchbnd` function to fit the relaxation data. Average values calculated from integral regions containing only noise were used as input errors. Fit errors were calculated by Monte Carlo error estimations. A random number between 0 and 1 was multiplied with the integral error and added to the recalculated integrals. The fitting was then repeated 2000 times with a new random number between 0 and 1 generated each time. Two times the standard deviations of the  $R_{1\rho}$  values received from the fits for each residue were used as errors.

Exchange coefficients ( $k_{\text{ex}}$ ), population of the minor state ( $p_{\text{B}}$ ), difference in chemical shifts between the two states ( $\Delta\delta$ ) were obtained by fitting

the  $R_{1\rho}$  values obtained at two different  $B_0$  fields simultaneously to a Bloch-McConnell two-site exchange equation (1) derived as described in<sup>[6,7]</sup>:

$$R_{1\rho} = R_{1\rho,0} + \frac{p_A p_B \times \Delta\delta^2 \times k_{ex}}{\omega_1^2 + k_{ex}^2} \quad (4.1)$$

where  $R_{1\rho,0}$  is the plateau value for  $R_{1\rho}$ ,  $p_A p_B$  are the populations of the major and minor sites,  $\Delta\delta$  is the chemical shift difference between the minor and the major site (in rad s<sup>-1</sup>),  $\omega_1$  is the <sup>15</sup>N spin-lock field strength (in rad s<sup>-1</sup>) and  $k_{ex}$  is the exchange coefficient (s<sup>-1</sup>). For the higher  $B_0$  field used in the fits the ratio between the fields squared was multiplied with the fraction in the equation to account for the differences in field strengths. Errors were calculated using Monte Carlo error estimation in the same way as for  $R_{1\rho}$  exponential fits. In these fits on resonance  $R_{1\rho}$  rates were used, and were calculated from the measured rates ( $R_{1\rho,obs}$ ) by equation 2:

$$R_{1\rho} = \frac{R_{1\rho,obs} - \cos^2\theta \times R_1}{\sin^2\theta} \quad (4.2)$$

where the  $R_1$  rates used are published elsewhere<sup>[8]</sup> and the angle  $\theta$  is calculated from equation 3 with  $\Omega$  as the offset for each peak.

$$\theta = \tan^{-1} \frac{\omega_1}{\Omega} \quad (4.3)$$

The fitting of the data was done by minimization of the  $\chi^2$  target function:

$$\chi^2 = \sum \frac{(X_{i,calc} - X_{i,exp})^2}{\sigma_{i,exp}^2} \quad (4.4)$$

Where  $X_i$  are the data sets and  $\sigma_i$ , the corresponding error.

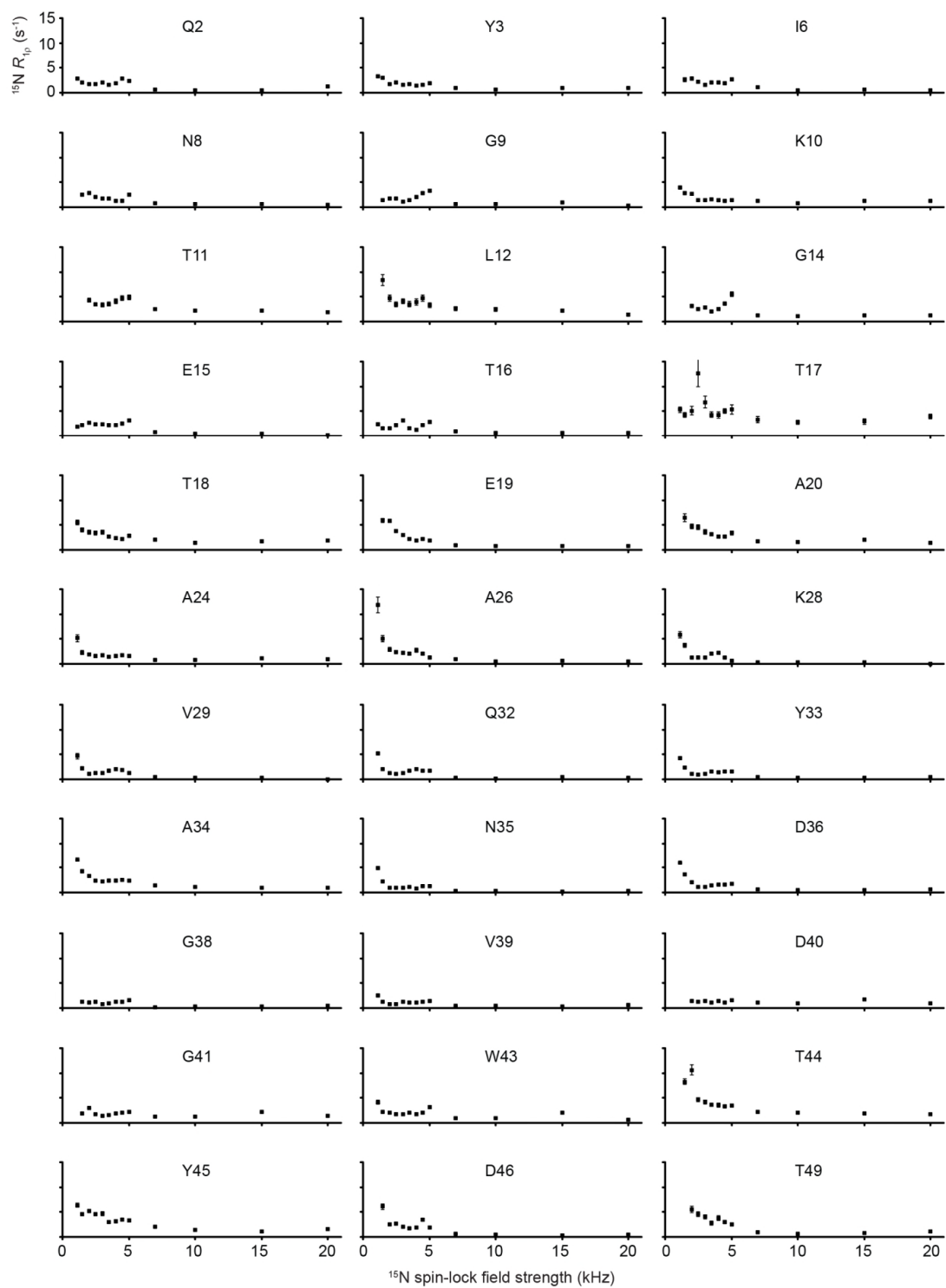
To compare how different models performed Bayesian Information Criterion (BIC) where calculated as:

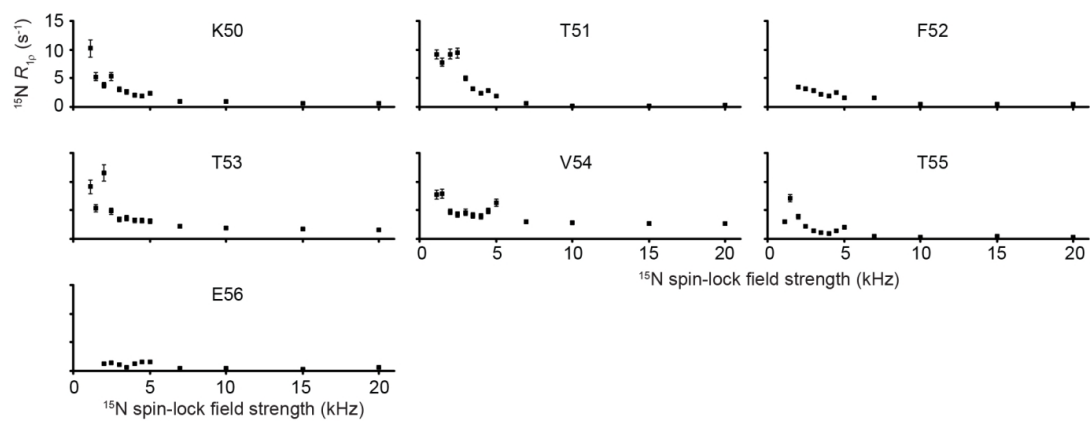
$$BIC = \chi^2 + k \times \ln(n) \quad (4.5)$$

where k is number of fit parameters and n number of data points (see SI table 13 for comparisons between single residue and combined residue fits).

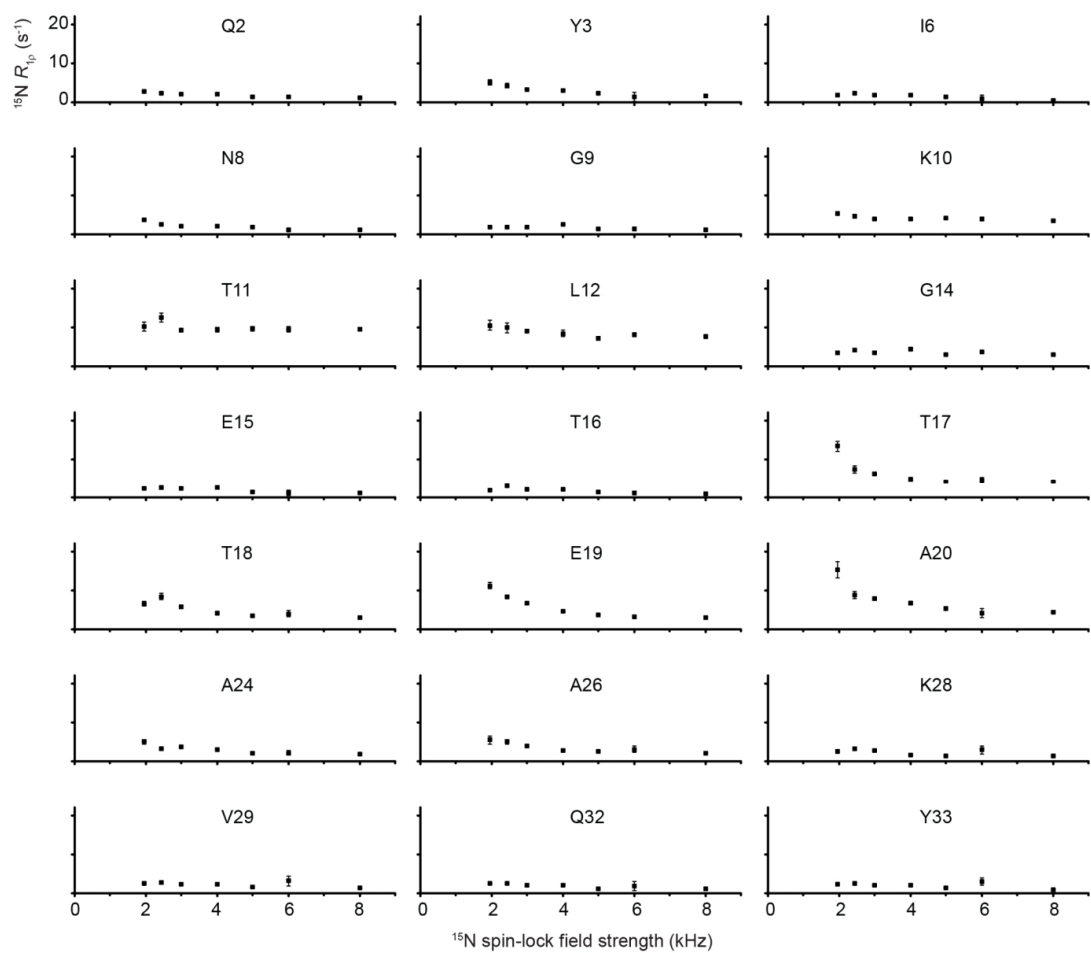
#### *4.5.2 Results and Discussion*

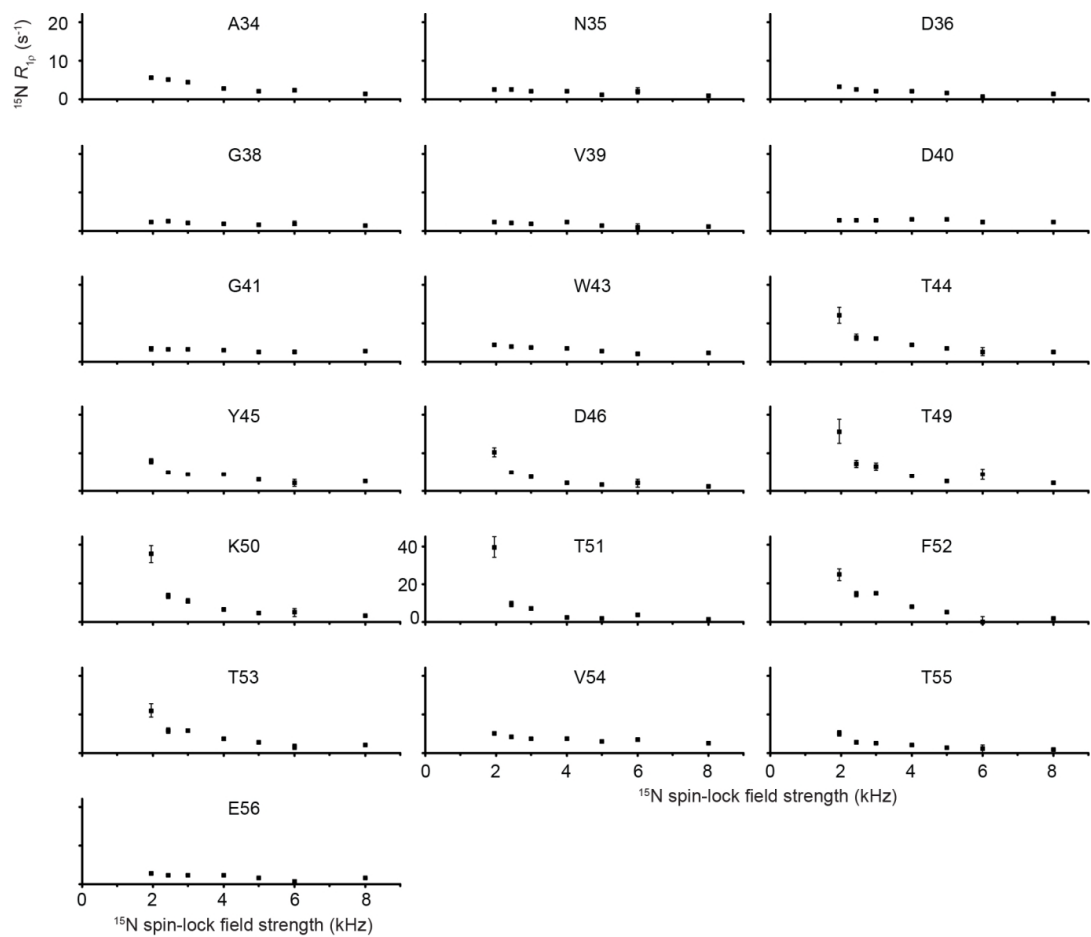
SI figures 4.1-4.6 contain relaxation dispersion profiles for crystalline GB1 and GB1 in complex with IgG. Crystalline GB1 without any addition of paramagnetic relaxation enhancement agent (GB1<sub>dia</sub>) in SI figures 4.1-4.2, crystalline GB1 with 2 mM Gd(DTPA-BMA) as solvent paramagnetic relaxation enhancement agent (GB1<sub>pre</sub>) in SI figures 4.3-4.4. GB1 in complex with IgG in SI figures 4.5-4.6. In SI figures 4.1-4.6 the values on the y-axes are the same as the first plot for all plots unless other values are given and the values on the x-axes are the same as in the last plot for all.





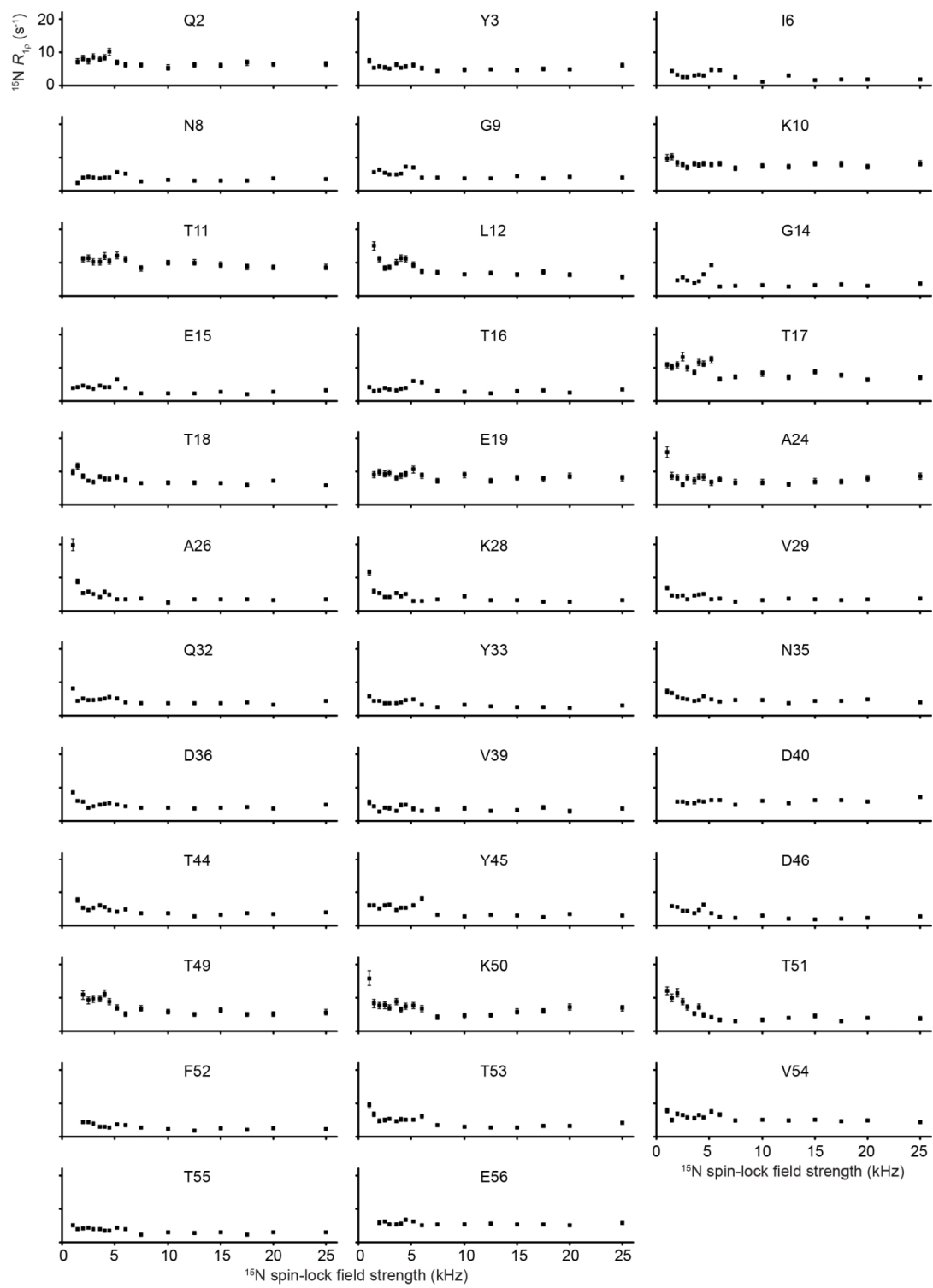
**SI figure 4.1.** Relaxation dispersion profiles for GB1<sub>dia</sub> at 16.4 T.



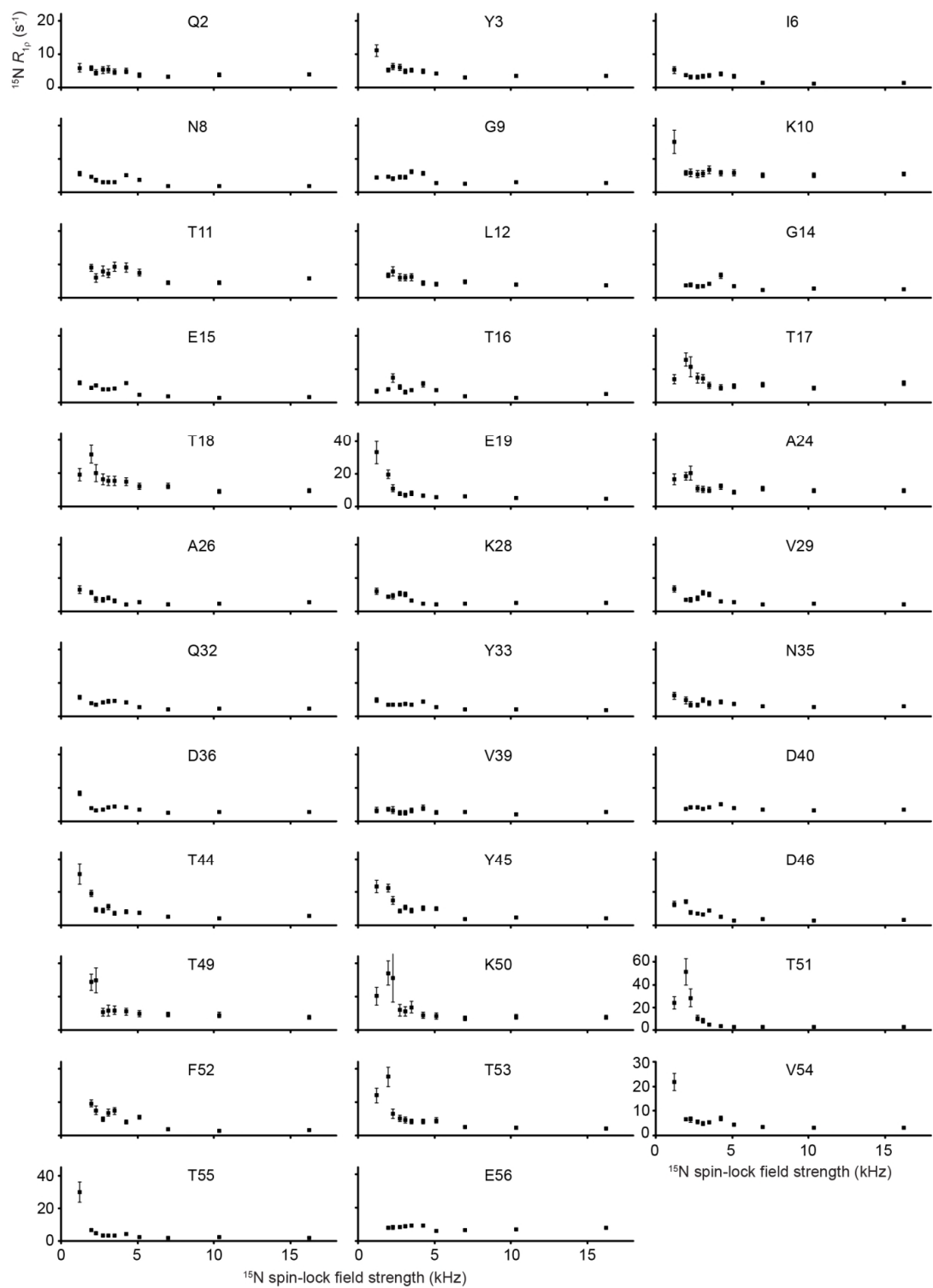


**SI figure 4.2.** Relaxation dispersion profiles for GB1<sub>dia</sub> at 14.1 T. Based on previously published data<sup>[6]</sup>.

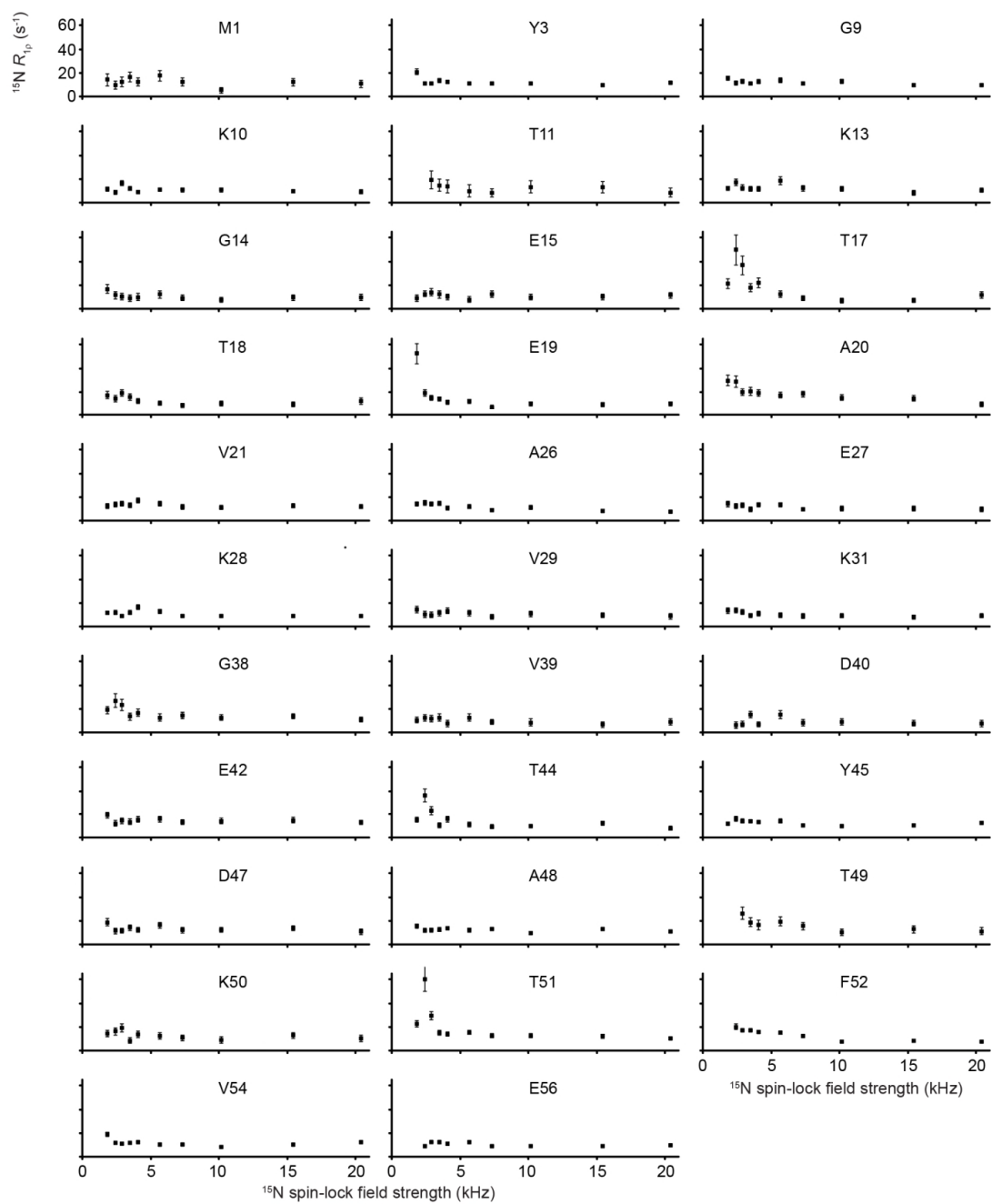




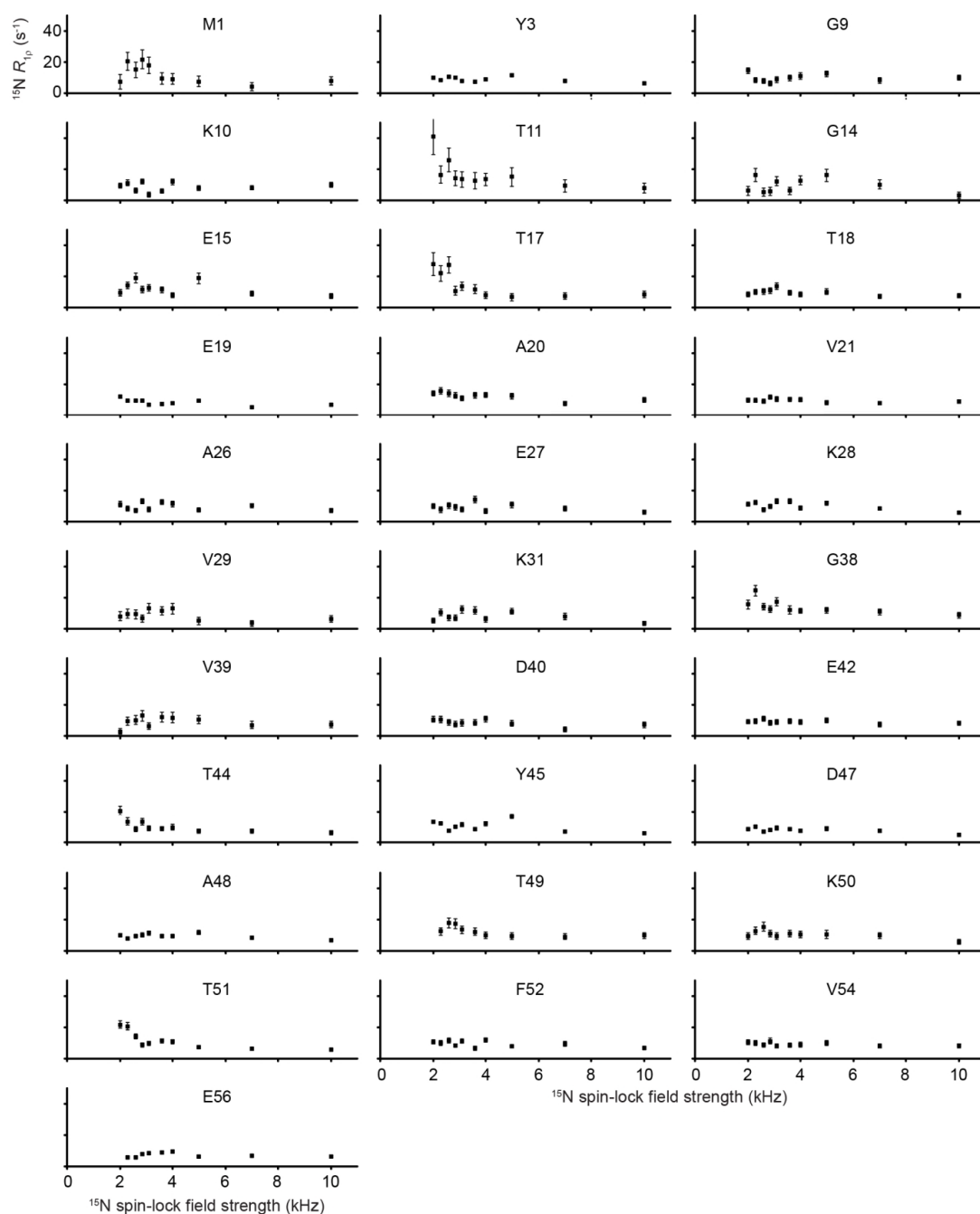
**SI figure 4.3.** Relaxation dispersion profiles for GB1<sub>pre</sub> at 16.4 T.



**SI figure 4.4.** Relaxation dispersion profiles for GB1<sub>pre</sub> at 14.1 T.

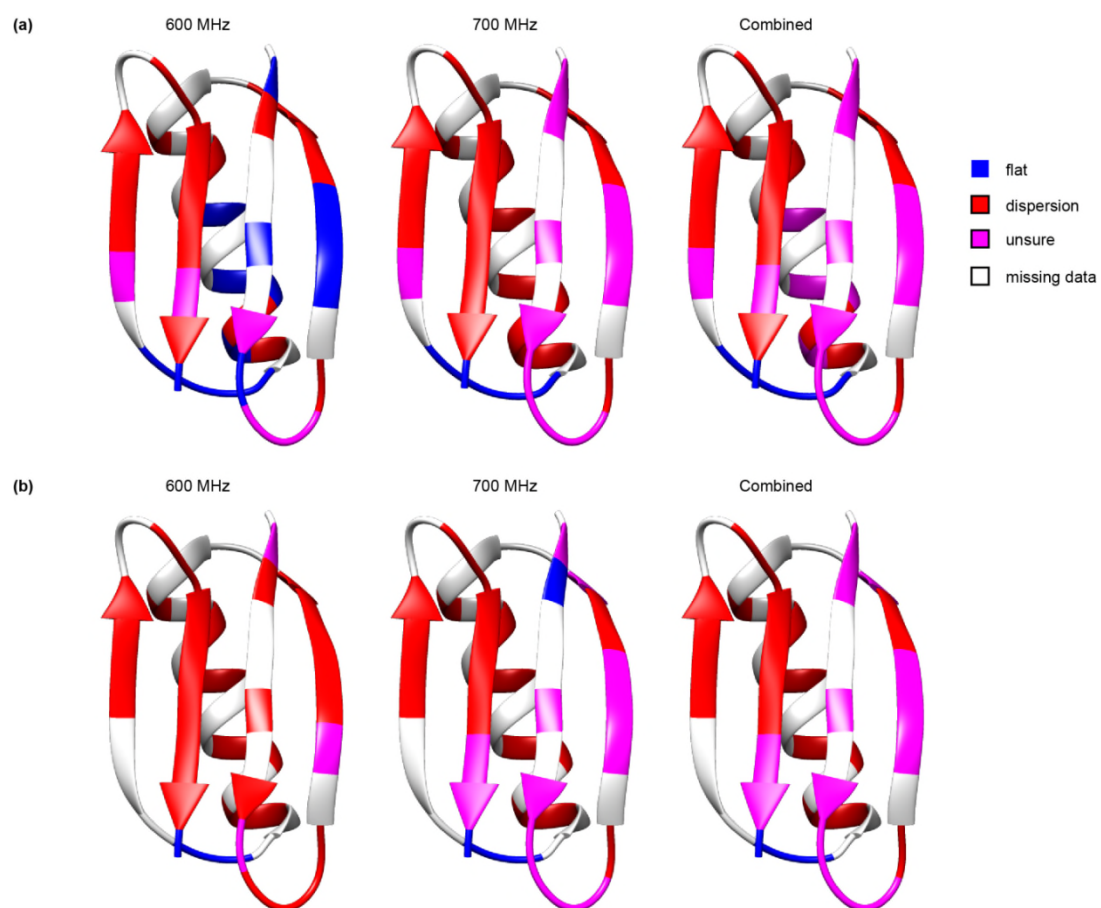


**SI figure 4.5.** Relaxation dispersion profiles for GB1 in complex with IgG, with 5 mM Gd(DTPA-BMA) as paramagnetic relaxation enhancement agent, measured at 20 T.

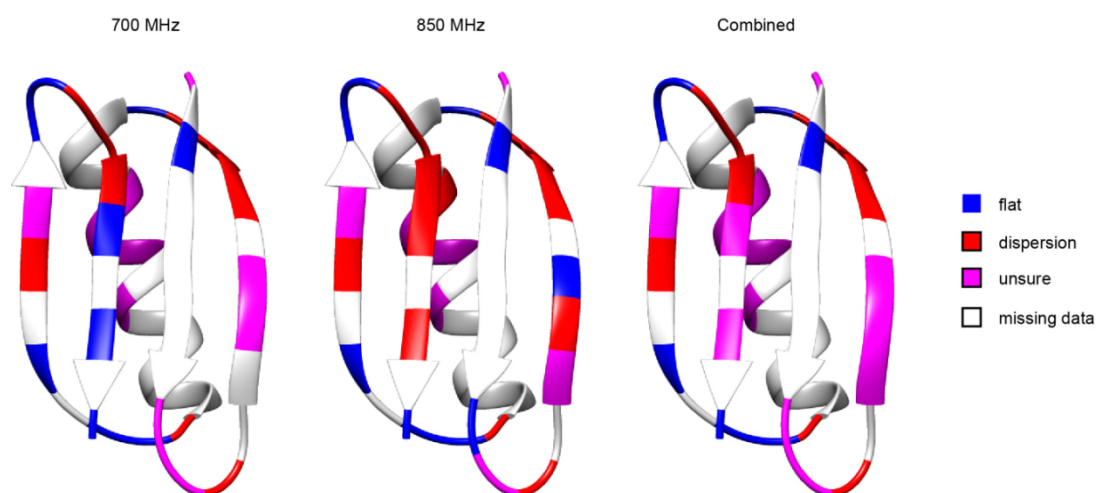


**SI figure 4.6.** Relaxation dispersion profiles for GB1 in complex with IgG, with 2 mM Gd(DTPA-BMA) as paramagnetic relaxation enhancement agent, measured at 16.4 T.

Residues were identified, based on SI figures 4.1-4.6, to either be flat (blue in SI figures 4.7-4.8) or show dispersion (red in SI figures 4.7-4.8). Residues that couldn't be clearly identified as flat or showing dispersion are colored pink in SI figures 4.7-4.8 and residues for which data are missing due to severe overlap or missing peaks in the spectra are colored grey.



**SI figure 4.7.** GB1 structures with residues colored based on relaxation dispersion profiles. (a) GB1<sub>dia</sub>. (b) GB1<sub>pre</sub>. Residues showing flat dispersion curves are blue, residues showing dispersion are red, residues that couldn't be clearly identified as being flat or showing dispersion are pink and residues for which data are missing due to severe overlap or missing peaks in the spectra are grey.



**SI figure 4.8.** GB1 structures with residues colored based on relaxation dispersion profiles of GB1 in complex with IgG. Residues showing flat curves are blue, residues showing dispersion are red, residues that couldn't be clearly identified as being flat or showing dispersion are pink and residues for which data are missing due to severe overlap or missing peaks in the spectra are grey.

SI tables 4.1-4.12 contain results from RD fits for the residues identified as showing dispersion at both fields for each sample (colored red in 'combined' in SI figures 4.7-4.8). For the GB1 samples, GB1<sub>dia</sub> and GB1<sub>pre</sub>, the different fits were; Individual residues, all residues combined (12, 17-20, 24, 26, 28, 29, 32-36, 44-46, 49-53, 55 for GB1<sub>dia</sub>, 12, 17, 18, 24, 26, 28, 29, 32, 33, 35, 36, 44-46, 49-53, for GB1<sub>pre</sub>)  $\beta$  region combined (12, 17-20, 44-46, 49-53, 55, for GB1<sub>dia</sub>, 12, 17, 18, 44-46, 49-53, for GB1<sub>pre</sub>),  $\alpha$  region combined (24, 26, 28, 29, 32-36 for GB1<sub>dia</sub>, 24, 26, 28, 29, 32, 33, 35, 36, for GB1<sub>pre</sub>). Since the residues in the  $\alpha$  helix mostly show clear dispersion at spin-lock fields below 2 kHz and the RD measurements for GB1<sub>dia</sub> at 14.1 T were only done down to 1.95 kHz all residues showing clear dispersion in the  $\alpha$  helix at 16.4 T were used in the fits. For GB1 in complex with IgG no clear dispersion was seen in the  $\alpha$ -helix. Fits were done for individual residues, residues close to the Fab binding site in IgG, residues close to the Fc binding site of IgG and all residues showing dispersion combined (11, 17-20, 38, 44, 49-51).

**SI table 4.1.** Results from RD fits of individual residues for GB1<sub>dia</sub> at 14.1 and 16.4 T.

Res	$k_{ex}$ (s <sup>-1</sup> )	Error	$p_B$ (%)	Error	$\delta\Delta$ (ppm)	Error	$R_{1\rho,0}$ (s <sup>-1</sup> ) at 16.4 T	Error	$R_{1\rho,0}$ (s <sup>-1</sup> ) at 14.1 T	Error
12	28481	9775	0.88	2.43	7.94	5.88	1.57	0.31	6.89	0.40
17	26002	10419	2.04	0.79	4.50	3.32	2.76	0.40	3.87	0.39
18	13888	2966	9.18	1.85	1.97	0.71	1.51	0.16	3.26	0.20

19	10097	1079	5.49	0.26	3.43	0.61	0.54	0.06	3.03	0.07
20	12583	3228	4.29	0.64	3.56	1.02	1.35	0.15	5.01	0.26
24	19660	4427	5.51	1.43	2.44	0.75	0.40	0.15	1.73	0.12
26	7902	2116	7.87	2.45	2.57	1.81	0.49	0.10	2.01	0.12
34	16859	1683	6.16	0.74	2.65	0.72	0.75	0.07	1.38	0.07
36	2003	1904	3.30	5.23	4.62	9.19	0.57	0.03	1.50	0.05
44	10685	1936	4.80	0.66	3.85	0.91	1.64	0.13	2.61	0.17
45	21380	2071	3.96	1.05	3.92	1.23	1.02	0.10	1.95	0.12
46	14669	1948	5.91	0.97	2.78	0.65	0.26	0.06	0.93	0.07
49	12998	3047	6.41	0.22	3.50	0.56	0.47	0.12	1.60	0.20
50	14373	2148	5.77	0.58	3.43	0.78	0.27	0.14	1.19	0.12
51	12316	909	9.92	2.04	3.12	2.01	0.00	0.05	0.63	0.08
52	20040	2117	5.38	1.42	3.74	1.61	0.00	0.05	0.66	0.09
53	15632	2719	5.88	0.64	3.30	0.84	1.34	0.16	1.79	0.16
55	15936	1716	9.24	2.02	2.09	1.05	0.08	0.07	0.77	0.08

**SI table 4.2.** Results from RD fits of all residues combined for GB1<sub>dia</sub> at 14.1 and 16.4 T.

$k_{ex}$ (s <sup>-1</sup> )	Error	p <sub>B</sub> (%)	Error			
14094	420	1.28	0.08			
Res	ΔΔ (ppm)	Error	$R_{1\rho,0}$ (s <sup>-1</sup> ) at 16.4 T	Error	$R_{1\rho,0}$ (s <sup>-1</sup> ) at 14.1 T	Error
12	5.85	1.02	1.88	0.19	7.29	0.27
17	4.39	0.88	3.19	0.24	4.32	0.16
18	5.08	0.81	1.50	0.13	3.24	0.16
19	6.70	0.93	0.44	0.05	2.90	0.07
20	6.33	1.02	1.34	0.14	4.98	0.24
24	4.70	0.74	0.51	0.12	1.85	0.06
26	5.77	0.93	0.37	0.11	1.85	0.11
28	4.63	0.70	0.07	0.06	2.92	8.19
29	4.38	0.72	0.12	0.07	2.20	5.73
32	3.93	0.58	0.31	0.05	4.35	7.73
33	3.77	0.59	0.38	0.06	52.96	3.66
34	5.57	0.78	0.82	0.06	1.46	0.05
35	3.71	0.57	0.21	0.05	1.61	22.71
36	4.25	0.60	0.42	0.04	1.29	0.06
44	7.18	1.06	1.53	0.12	2.45	0.16
45	6.24	0.88	1.26	0.07	2.25	0.09
46	5.82	0.82	0.28	0.06	0.95	0.05

49	7.54	1.13	0.45	0.11	1.56	0.18
50	7.12	1.06	0.27	0.13	1.20	0.09
51	8.14	1.14	0.00	0.04	0.57	0.07
52	7.61	1.07	0.02	0.05	0.84	0.06
53	6.86	1.04	1.40	0.13	1.84	0.13
55	5.27	0.78	0.14	0.07	0.84	0.06

**SI table 4.3.** Results from RD fits of the  $\beta$  region combined for GB1<sub>dia</sub> at 14.1 and 16.4

$k_{ex}$ (s <sup>-1</sup> )	Error	$p_B$ (%)	Error			
14374	486	2.54	0.24			
Res	$\delta\Delta$ (ppm)	Error	$R_{1\rho,0}$ (s <sup>-1</sup> ) at 16.4 T	Error	$R_{1\rho,0}$ (s <sup>-1</sup> ) at 14.1 T	Error
12	4.18	0.90	1.88	0.19	7.29	0.27
17	3.17	0.74	3.16	0.25	4.30	0.16
18	3.64	0.75	1.50	0.13	3.24	0.17
19	4.77	0.93	0.43	0.05	2.90	0.07
20	4.57	0.93	1.30	0.13	4.95	0.24
44	5.12	1.02	1.53	0.12	2.46	0.16
45	4.47	0.89	1.26	0.07	2.24	0.09
46	4.17	0.82	0.26	0.06	0.94	0.05
49	5.38	1.08	0.44	0.10	1.56	0.16
50	5.08	1.01	0.28	0.11	1.19	0.09
51	5.81	1.15	0.00	0.04	0.56	0.07
52	5.44	1.07	0.00	0.05	0.82	0.06
53	4.90	1.00	1.39	0.13	1.84	0.13
55	3.79	0.74	0.11	0.07	0.82	0.07

**SI table 4.4.** Results from RD fits of the  $\alpha$  region combined for GB1<sub>dia</sub> at 14.1 and 16.4 T.

$k_{ex}$ (s <sup>-1</sup> )	Error	$p_B$ (%)	Error			
8750	546	0.90	0.07			
Res	$\delta\Delta$ (ppm)	Error	$R_{1\rho,0}$ (s <sup>-1</sup> ) at 16.4 T	Error	$R_{1\rho,0}$ (s <sup>-1</sup> ) at 14.1 T	Error
24	5.47	1.21	0.66	0.11	1.98	0.06
26	7.19	1.52	0.47	0.10	1.99	0.11
28	5.60	1.19	0.16	0.06	1.15	6.36
29	5.10	1.10	0.22	0.06	2.13	8.19
32	4.63	0.97	0.39	0.04	3.91	3.80
33	4.52	0.93	0.44	0.05	2.43	4.63



34	6.66	1.36	0.96	0.05	1.61	0.05
35	4.47	0.92	0.28	0.04	5.37	1.97
36	5.26	1.10	0.49	0.04	1.39	0.05

**SI table 4.5.** Results from RD fits of individual residues for GB1<sub>pre</sub> at 14.1 and 16.4 T

Res	$k_{\text{ex}}$ (s <sup>-1</sup> )	Error	$p_{\text{B}}$ (%)	Error	$\delta\Delta$ (ppm)	Error	$R_{1\rho,0}$ (s <sup>-1</sup> ) at 16.4 T	Error	$R_{1\rho,0}$ (s <sup>-1</sup> ) at 14.1 T	Error
12	22356	5972	4.49	1.28	4.09	3.03	6.16	0.34	3.30	0.33
17	24887	7785	0.89	1.27	7.95	5.08	7.14	0.39	4.38	0.42
18	15894	4908	3.15	1.26	3.43	1.56	6.27	0.26	5.40	0.36
24 <sup>[a]</sup>	1000	3069	3.24	5.22	6.74	4.75	6.85	0.26	4.89	0.28
26 <sup>[a]</sup>	1000	1667	21.58	3.87	3.87	4.09	3.36	0.14	2.29	0.17
28	3231	2234	25.44	3.79	1.77	5.82	3.17	0.13	2.49	0.15
29	15815	5163	9.19	1.10	1.66	0.63	3.25	0.16	2.41	0.17
32	23625	5465	6.49	0.95	2.25	0.87	3.51	0.16	2.33	0.16
33	28872	5851	6.97	1.71	2.37	1.95	2.43	0.15	2.03	0.18
35	8478	3409	3.41	2.47	2.54	1.29	4.23	0.16	3.12	0.18
36	1793	2429	7.95	7.50	2.79	11.71	4.07	0.07	2.99	0.10
44	16662	4421	5.79	1.68	2.79	0.96	3.27	0.19	2.54	0.20
45	35501	5714	9.14	3.04	3.03	2.04	2.44	0.22	1.87	0.22
46	19330	2711	7.03	0.52	2.80	0.55	2.01	0.12	1.33	0.13
49	18089	6223	7.54	1.02	3.50	1.14	5.04	0.37	3.54	0.43
50	4466	3875	4.02	3.52	3.89	8.66	5.69	0.31	3.96	0.36
51	11756	2156	5.31	0.32	3.87	0.72	3.24	0.27	2.44	0.32
52	15510	5224	7.43	1.08	2.51	1.24	1.96	0.17	2.00	0.18
53	20981	4940	5.82	2.11	3.06	1.30	2.95	0.23	2.29	0.27

[a] Residues did not reach a minima in the  $\chi^2$  fitting.

**SI table 4.6.** Results from RD fits of all residues combined for GB1<sub>pre</sub> at 14.1 and 16.4 T.

$k_{\text{ex}}$ (s <sup>-1</sup> )	Error	p <sub>B</sub> (%)	Error			
14988	814	1.95	0.22			
Res	δΔ (ppm)	Error	$R_{1\rho,0}$ (s <sup>-1</sup> ) at 16.4 T	Error	$R_{1\rho,0}$ (s <sup>-1</sup> ) at 14.1T	Error
12	5.78	1.49	6.41	0.24	3.52	0.27
17	4.54	1.20	7.53	0.26	4.74	0.31
18	4.28	1.14	6.29	0.22	5.42	0.34
24	3.74	1.13	6.69	0.31	4.71	0.32
26	4.86	1.23	3.05	0.16	2.01	0.17

28	4.51	1.16	2.86	0.15	2.19	0.16
29	3.45	0.92	3.27	0.13	2.42	0.17
32	3.55	0.91	3.69	0.11	2.48	0.13
33	3.53	0.89	2.72	0.10	2.30	0.14
35	3.45	0.94	4.10	0.16	3.02	0.18
36	3.44	0.86	3.86	0.08	2.79	0.10
44	4.67	1.20	3.30	0.15	2.57	0.18
45	4.59	1.15	3.12	0.13	2.48	0.15
46	4.98	1.24	2.14	0.10	1.44	0.12
49	6.63	1.70	5.15	0.31	3.65	0.38
50	4.96	1.34	5.32	0.32	3.69	0.38
51	6.39	1.64	3.07	0.24	2.29	0.32
52	4.75	1.21	1.97	0.13	2.01	0.17
53	4.84	1.26	3.13	0.18	2.44	0.21

**SI table 4.7.** Results from RD fits of the  $\beta$  region combined for GB1<sub>pre</sub> at 14.1 and 16.4 T.

$k_{\text{ex}}$ (s <sup>-1</sup> )	Error	$p_{\text{B}}$ (%)	Error			
19945	1320	3.73	0.21			
Res	$\delta\Delta$ (ppm)	Error	$R_{1\rho,0}$ (s <sup>-1</sup> ) at 16.4 T	Error	$R_{1\rho,0}$ (s <sup>-1</sup> ) at 14.1T	Error
12	4.37	0.89	6.25	0.26	3.37	0.30
17	3.66	0.80	7.31	0.28	4.54	0.33
18	3.32	0.74	6.16	0.23	5.31	0.36
44	3.52	0.70	3.19	0.15	2.48	0.18
45	3.69	0.68	2.92	0.14	2.31	0.16
46	3.80	0.68	1.99	0.11	1.31	0.12
49	4.91	1.03	4.98	0.32	3.48	0.38
50	3.72	0.86	5.22	0.33	3.57	0.38
51	4.78	0.92	2.90	0.25	2.09	0.33
52	3.51	0.70	1.89	0.14	1.94	0.16
53	3.73	0.75	2.98	0.19	2.31	0.23

**SI table 4.8.** Results from RD fits of the  $\alpha$  region combined for GB1<sub>pre</sub> at 14.1 and 16.4 T.

$k_{\text{ex}}$ (s <sup>-1</sup> )	Error	$p_{\text{B}}$ (%)	Error			
4176	804	1.66	0.16			
Res	$\delta\Delta$ (ppm)	Error	$R_{1\rho,0}$ (s <sup>-1</sup> ) at 16.4 T	Error	$R_{1\rho,0}$ (s <sup>-1</sup> ) at 14.1T	Error
24	5.08	1.20	6.80	0.26	4.84	0.28

26	6.64	1.30	3.30	0.14	2.24	0.18
28	5.56	1.10	3.14	0.12	2.46	0.15
29	3.90	0.88	3.50	0.12	2.62	0.15
32	4.01	0.84	3.94	0.10	2.70	0.12
33	3.68	0.76	3.01	0.08	2.58	0.13
35	3.93	0.90	4.35	0.13	3.20	0.17
36	4.30	0.86	4.03	0.07	2.95	0.10

**SI table 4.9.** Results from RD fits of individual residues for GB1 in complex with IgG at 16.4 and 20 T

Res	$k_{\text{ex}}$ ( $\text{s}^{-1}$ )	Error	$p_{\text{B}}$ (%)	Error	$\delta\Delta$ (ppm)	Error	$R_{1\rho,0}$ ( $\text{s}^{-1}$ ) at 20 T	Error	$R_{1\rho,0}$ ( $\text{s}^{-1}$ ) at 16.4 T	Error
11 <sup>[a]</sup>	1000	16317	12.67	5.92	12.57	8.48	8.43	2.64	8.34	2.58
17	15817	8270	8.89	1.28	4.62	1.94	6.89	1.76	4.76	1.94
18	22850	21418	5.05	2.02	3.75	5.25	9.28	1.92	6.51	1.49
19 <sup>[a]</sup>	1000	6240	3.64	4.55	14.33	5.65	9.66	0.85	5.72	0.55
20	32233	14668	14.88	2.44	3.52	3.38	11.63	2.36	6.18	1.91
38	16636	12793	6.17	1.91	3.93	3.08	11.32	1.60	9.27	1.45
44	16261	9414	4.83	1.22	4.29	1.44	8.56	1.15	5.85	1.16
49	19194	16830	7.20	2.36	4.31	4.79	11.49	2.29	7.15	1.99
50	24513	34153	4.20	3.73	3.89	7.63	9.47	2.71	7.58	2.19
51	8827	4969	7.64	1.90	4.66	4.22	10.64	0.88	5.36	0.82

[a] Residues did not reach a minima in the  $\chi^2$  fitting.

**SI table 4.10.** Results from RD fits of all residues combined for GB1 in complex with IgG at 16.4 and 20 T.

$k_{\text{ex}}$ ( $\text{s}^{-1}$ )	Error	$p_{\text{B}}$ (%)	Error			
13236	2812	4.73	0.73			
Res	$\delta\Delta$ (ppm)	Error	$R_{1\rho,0}$ ( $\text{s}^{-1}$ ) at 20 T	Error	$R_{1\rho,0}$ ( $\text{s}^{-1}$ ) at 14.1 T	Error
11	5.77	1.99	7.80	2.34	8.15	2.62
17	6.15	1.66	7.23	1.28	5.20	1.40
18	3.47	1.08	10.04	1.06	7.13	0.88
19	4.09	1.11	9.04	0.83	5.22	0.60
20	4.73	1.34	13.91	1.20	8.11	1.03
38	4.36	1.29	11.60	1.30	9.59	1.16
44	4.26	1.17	8.80	0.87	6.12	0.83
49	5.18	1.59	12.08	1.58	7.64	1.46

50	3.21	1.14	10.21	1.32	8.20	1.10
51	5.53	1.42	10.22	0.88	4.89	0.72

**SI table 4.11.** Results from RD fits of residues expected to bind the Fc fragment of IgG combined for GB1 in complex with IgG at 16.4 and 20 T.

$k_{ex}$ ( $s^{-1}$ )	Error	$p_B$ (%)	Error			
12274	4062	9.50	1.37			
Res	$\delta\Delta$ (ppm)	Error	$R_{1\rho,0}$ ( $s^{-1}$ ) at 20 T	Error	$R_{1\rho,0}$ ( $s^{-1}$ ) at 16.4 T	Error
44	3.10	1.27	8.87	0.91	6.21	0.85
49	3.80	1.61	12.17	1.62	7.72	1.43
50	2.33	1.10	10.27	1.30	8.26	1.15
51	4.05	1.55	10.31	0.89	4.99	0.81

**SI table 4.12.** Results from RD fits of residues expected to bind the Fab fragment of IgG combined for GB1 in complex with IgG at 16.4 and 20 T.

$k_{ex}$ ( $s^{-1}$ )	Error	$p_B$ (%)	Error			
14295	3832	3.63	0.63			
Residue	$\delta\Delta$ (ppm)	Error	$R_{1\rho,0}$ ( $s^{-1}$ ) at 16.4 T	Error	$R_{1\rho,0}$ ( $s^{-1}$ ) at 14.1T	Error
11	6.51	2.15	7.73	2.49	8.13	2.65
17	7.04	1.80	7.09	1.34	5.01	1.45
18	4.00	1.22	9.95	1.02	7.05	0.94
19	4.67	1.20	8.97	0.88	5.16	0.67
20	5.43	1.45	13.79	1.22	8.00	1.04
38	5.00	1.39	11.51	1.35	9.49	1.12

**SI table 4.13.** Number of spin-lock lengths, nutation frequencies and total duration of each experiment.

Sample	Spin-lock lengths	Nutation frequencies	Total duration
GB1 <sub>dia</sub> at 16.4 T	10	13	69.5 h
GB1 <sub>pre</sub> at 14.1 T	8	11	24 h
GB1 <sub>pre</sub> at 16.4 T	10	17	43 h
GB1:IgG at 16.4 T	7	10	231.5 h
GB1:IgG at 20 T	8	10	141 h

**SI table 4.14.** Statistical analysis of RD fits for all samples.

Sample	$\sum \chi^2$	Data points	Parameters	BIC
GB1 <sub>pre</sub>				

Single residue	1488.8	532	57	1846.6
All	1712.5	532	21	1844.3
$\alpha / \beta$	1609.3	532	23	1753.6
<b>GB1<sub>dia</sub></b>				
Single residue	3066.1	460	69	3489.2
All	3202.7	460	25	3356.0
$\alpha / \beta$	3190.0	460	27	3355.5
<b>GB1:IgG</b>				
Single residue	239.8	200	30	398.7
All	250.9	200	12	314.5
Fab / Fc	250.7	200	14	324.9

#### 4.5.3 References

- [1] N. Vajpai, M. Gentner, J.-R. Huang, M. Blackledge, S. Grzesiek, *J. Am. Chem. Soc.* **2010**, *132*, 3196–3203.
- [2] W. T. Franks, D. H. Zhou, B. J. Wylie, B. G. Money, D. T. Graesser, H. L. Frericks, G. Sahota, C. M. Rienstra, *J. Am. Chem. Soc.* **2005**, *127*, 12291–12305.
- [3] J. M. Lamley, D. Iuga, C. Öster, H.-J. Sass, M. Rogowski, A. Oss, J. Past, A. Reinhold, S. Grzesiek, A. Samoson, et al., *J. Am. Chem. Soc.* **2014**, *136*, 16800–16806.
- [4] J. R. Lewandowski, J. Sein, H. J. Sass, S. Grzesiek, M. Blackledge, L. Emsley, *J. Am. Chem. Soc.* **2010**, *132*, 8252–4.
- [5] D. H. Zhou, C. M. Rienstra, *J. Magn. Reson.* **2008**, *192*, 167–72.
- [6] O. Trott, A. G. Palmer, *J. Magn. Reson.* **2002**, *154*, 157–160.
- [7] A. J. Baldwin, L. E. Kay, *J. Biomol. NMR* **2013**, *55*, 211–218.
- [8] J. M. Lamley, C. Öster, R. A. Stevens, J. R. Lewandowski, *Angew. Chemie Int. Ed.* **2015**, *54*, 15374–15378.

## 5 Investigation of teixobactin-lipid II interactions using solution and solid state NMR

### 5.1 Abstract

Teixobactin is a new promising lipid II binding antibiotic discovered in uncultured soil bacteria with no detectable resistance in any bacteria where it targets cell wall biosynthesis by binding lipid II. However, its solubility and bioavailability are poor and analogues need to be constructed to address these issues. Structural studies of teixobactin itself and with its bacterial targets may give key information on the mode of action and could aid in structure-based design of teixobactin analogues to develop a new commercially available antibiotic. Here we present the solution NMR 3D structure of teixobactin in membrane mimetics and report on amino acids critical for the binding to lipid II. Moreover, we identified teixobactin regions that undergo conformational changes upon binding to lipid II by solution NMR titration experiments and solid state NMR of a sedimented teixobactin-lipid II complex.

### 5.2 Introduction and Discussion

The majority of antibiotics currently in clinical use have been discovered by screening cultivable soil bacteria. However, around 99% of microorganisms are uncultured, meaning that they do not grow under laboratory conditions. Recently, several methods to access potential antimicrobial compounds from uncultured microorganisms were developed<sup>[1-4]</sup>, of which the iChip technology<sup>[2]</sup> led to the discovery of teixobactin from a new species of  $\beta$ -proteobacteria called *Eleftheria terrae*. Teixobactin was shown to have very good activity against many difficult-to-treat bacterial infections and no resistant mutants were obtained by *in vitro* studies with various bacteria.<sup>[5]</sup> Teixobactin is simultaneously inhibiting the biosynthesis of peptidoglycan and teichoic acids triggering synergistic effects leading to increased cell wall damage and delocalization of autolysins. Additionally, teixobactin, in contrast to vancomycin, does not bind mature peptidoglycan, which enables it to efficiently kill bacteria with increased cell wall density such as

vancomycin-intermediate *Staphylococcus aureus* (VISA) against which vancomycin is ineffective.<sup>[6]</sup>

Since the discovery of teixobactin and identification of its biosynthetic pathway<sup>[5]</sup> a lot of research has been conducted to gain more understanding on the mode of action of teixobactin with the goal of developing analogues with better pharmacological properties to generate new powerful antibiotics against resistant strains for which there is now no efficient treatment. Several groups have synthesised teixobactin analogues to investigate the roles of the different residues in teixobactin and potentially find active compounds that are easier to synthesise and better suited for clinical use. An NMR study of seven analogues showed the importance of the D-amino acids for activity<sup>[7]</sup>. The residue in position 10, L-*allo*-enduracididine, is a non-proteinogenic amino acid, which has been difficult to synthesise and hence replacing it with a naturally available amino acid is an attractive approach. Arg10-teixobactin<sup>[7-9]</sup> and lys10-teixobactin<sup>[9]</sup> showed good activity and recently several other teixobactin analogues with different alternatives in position 10 were synthesised and found to have good activity against methicillin-resistant *Staphylococcus aureus* (MRSA), *Staphylococcus epidermidis* and *Bacillus subtilis*<sup>[10]</sup>. In this study, we focus on interactions between teixobactin and lipid II and structural changes to teixobactin upon binding of lipid II. We have determined the 3D structure of teixobactin in a membrane like environment using dodecylphosphocholine (DPC) micelles as membrane mimetics. We further investigated structural changes of teixobactin induced by binding of lipid II using titration experiments in solution NMR followed by solid state NMR of the aggregated complex formed between teixobactin and lipid II in DPC micelles.

Figure 5.1a shows the 20 lowest energy structures determined by structure calculations from NMR data of teixobactin in DPC micelles (see SI table 5.1 for details) and a crystal structure of the teixobactin analogue Ac- $\Delta_{1-5}$ Arg<sub>10</sub>-teixobactin as a hydrochloride salt<sup>[11]</sup>. The expected pyrophosphate binding cage is nearly identical in the NMR and crystal structures. The most obvious difference between the structures is

the side-chain of residue 10, where in the analogue the *allo*-enduracidine has been replaced by arginine. Additionally, the N-termini are different in the structures since residues 1-5 were replaced by an acetyl group in the crystal structure<sup>[11]</sup>.

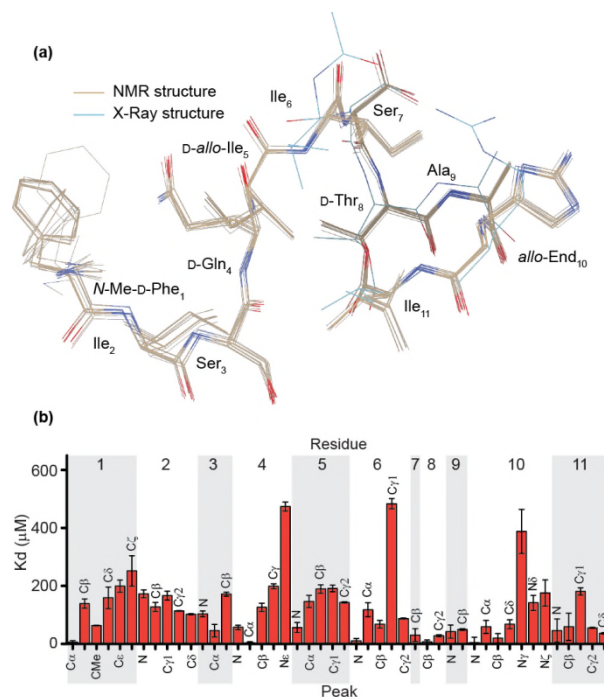


**Figure 5.1.** (a) Comparison between a solution NMR structure of teixobactin in DPC micelles with a crystal structure of teixobactin analogue Ac- $\Delta_{1-5}$ Arg<sub>10</sub>-teixobactin<sup>[11]</sup>. Beige backbone represents the solution structure and light blue represents the crystal structure. (b) Results from  $K_d$  fits of a 2:1 teixobactin:lipid II binding mode, based on titrations with lipid II to teixobactin in DPC micelles, measured by solution NMR.

The effect on teixobactin by binding to lipid II was investigated by NMR titrations. When lipid II was added to the teixobactin sample no changes in chemical shifts were observed but rather a decrease in intensities of the peaks, which is a behaviour characteristic for slow exchange. To determine binding affinities in the presence of slow exchange the peak intensities of the bound form are normally followed<sup>[12]</sup>. In this case that was not possible due to severe broadening (no peaks appearing for the bound form), probably caused by aggregation, so the intensities of the peaks from free teixobactin were fitted to extract dissociation constants ( $K_d$ ) (see equation 5.1 in SI). The fitting was performed with several different ratios of teixobactin:lipid II and the best fits were obtained using a 2:1 ratio (see SI tables 5.5-5.6), which was reported to be the



binding ratio previously<sup>[5]</sup>. It should be noted that the  $K_d$  values obtained by these fits may be lower than the actual  $K_d$  values due to the effect aggregation has on the NMR spectra. Even if the calculated  $K_d$  values may not be exact, they can give qualitative information on where the interaction takes place. Figure 5.1b shows the fitted  $K_d$  values for all isolated peaks in  $^1\text{H} - ^{15}\text{N}$  and  $^1\text{H} - ^{13}\text{C}$  spectra (for a carbon or nitrogen that have more than one proton the average  $K_d$  is reported). Overall, the peaks in the expected pyrophosphate binding cage, residues 7-11, are showing low  $K_d$  values indicating that these residues are involved in binding lipid II. Low apparent  $K_d$  values were also seen for Ca of residues 1, 3 and 4 ( $K_d$  for Ca of residue 2 is missing due to spectral overlap) suggesting allosteric effects upon binding.

To further investigate the interactions we measured spectra of the complex formed between teixobactin and lipid II. Due to aggregation this was not possible in solution NMR but the soluble aggregate was sedimented by ultracentrifugation and packed into a solid state NMR rotor. The increased line broadening seen in solution NMR due to large size of a molecule is not seen in solid state NMR and hence complexes of several hundreds of kDa may be studied. The sedimented complex between teixobactin and lipid II gave high quality spectra (See SI Fig. 5.1-5.2) and full chemical shift assignments were possible (SI table 5.4). Chemical shift perturbations (CSPs), Fig 5.2a, and secondary chemical shifts, Fig 5.2b-d, were calculated (described in the SI). The CSPs based on H-N peaks inform on binding and conformational changes, and we see large CSPs for residues 3-5 and 9-10 suggesting that not only the pyrophosphate binding cage is affected by binding of teixobactin to lipid II. The Ha-Ca CSPs suggest that conformational changes mostly affect residues 2-7. This is more obvious in secondary chemical shifts, which report on secondary structure deviations from random coil. Taken together the Ca, Ha and C $\beta$  secondary chemical shifts suggest that residues 2-6 change from random coil towards a more  $\beta$ -sheet like conformation while the back-bone conformation for residues 7-11 remains unchanged.

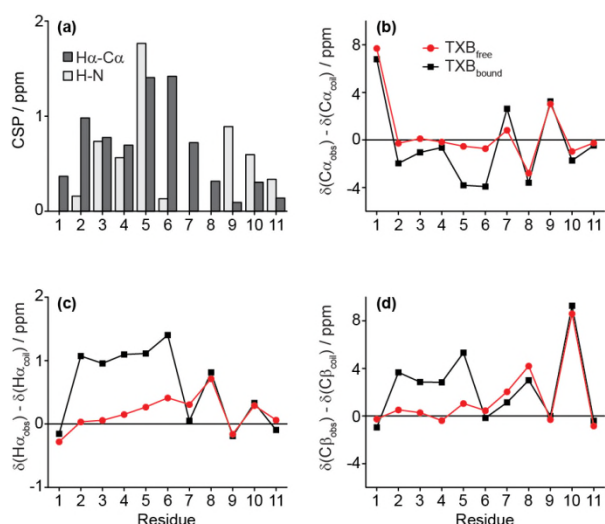


**Figure 5.2.** Comparison of chemical shifts between teixobactin in solution and teixobactin in complex with lipid II in solid state. (a) Chemical shift perturbations for H-N (light grey) and H $\alpha$ -C $\alpha$  (dark grey). Secondary chemical shifts based on C $\alpha$  (b), H $\alpha$  (c) and C $\beta$  (d).

All random coil chemical shifts used in these calculations are defined for L-amino acids<sup>[13]</sup>, and hence for the modified and unusual amino acids the chemical shifts from standard amino acids might not be representative. This needs to be considered for residue 1, with a methyl group attached to the amide nitrogen which will affect the C $\alpha$  chemical shift, for residue 10 which is significantly different from arginine which was used as comparison and residue 8 which forms a lactone bond with residue 11.

However, residues 1, 8 and 11 remained unchanged between free and bound teixobactin with chemical shifts that indicated the presence of secondary structure. In contrast, residues 2-6 showed deviations from random coil shifts only in complex with lipid II in the solid state. The chemical shift changes illustrated by CSPs and secondary chemical shifts agree generally with the  $K_d$  fits in Fig. 5.1 and together they complement each other well, as the involvement of residue 11 in binding is suggested by the  $K_d$  fits but is not clear from the comparison of chemical shifts. Furthermore, the low  $K_d$  values obtained for some residues outside the expected pyrophosphate binding cage can mostly be attributed to conformational changes in residues 2-6.

The N-terminus of teixobactin has been suggested to function as an anchoring point to the cell membrane, however our data suggest that it

could have a more involved role in the killing mechanism of teixobactin by promoting aggregation, which may explain the lower activity seen in analogues where residues 1-5 were replaced by a hydrophobic group.<sup>[11]</sup> The general chemical shift changes towards  $\beta$ -sheet formation for residues 2-6 and the large soluble aggregates formed by interactions between teixobactin and lipid II suggest that these residues may have an important role in the aggregation process, perhaps by fibril formation, as was previously reported for the ramoplanin:lipid II complex<sup>[14]</sup>. In the case of ramoplanin, addition of 20% DMSO prevented aggregation to some extent and the interactions could be studied in solution. That is not the case for the teixobactin:lipid II complex where attempts to measure interactions in solutions containing DMSO resulted in very poor quality spectra and addition of up to 80% DMSO was not sufficient to prevent aggregation.

The binding mode of teixobactin has previously been compared to that of nisin<sup>[15]</sup>, with regards to the pyrophosphate binding cage<sup>[9]</sup>. Nisin has a second killing mechanism, in addition to accumulation of peptidoglycan precursors, it forms pores by insertion of its elongated part into the cell membrane. It is possible that the large aggregates formed between teixobactin and lipid II in a micellar environment are related to some type of pore formation, however further investigations need to be done to confirm this.

In summary, we have solved the 3D structure of teixobactin confirming the presence of a pyrophosphate binding cage previously suggested in truncated teixobactin analogues. The combination of titrations in solution NMR and solid state NMR experiments reveals that teixobactin undergoes conformational changes upon binding to lipid II. Importantly, residues 2-6 are, from a structural point of view, relevant for the high activity of native teixobactin compared to truncated analogues. We suggest that residues 2-6 are important for the activity due to their involvement in aggregation of teixobactin – lipid II complexes, which in the cell would lead to accumulation of lipid II and inhibition of cell wall synthesis. Here we have, for the first time, used proton detected solid state NMR to obtain site-specific information on interactions between an antimicrobial

peptide and a cell wall precursor. And although further studies are required to fully determine the structure of the complex formed between teixobactin and lipid II, the advantages of using solid state NMR to study the interactions between an antibiotic and its target without the use of non-physiological solvents to solubilize aggregates are clear.

### 5.3 References

- [1] T. Kaeberlein, K. Lewis, S. S. Epstein, *Science* **2002**, 296, 1127–9.
- [2] D. Nichols, N. Cahoon, E. M. Trakhtenberg, L. Pham, A. Mehta, A. Belanger, T. Kanigan, K. Lewis, S. S. Epstein, *Appl. Environ. Microbiol.* **2010**, 76, 2445–2450.
- [3] A. D’Onofrio, J. M. Crawford, E. J. Stewart, K. Witt, E. Gavrish, S. Epstein, J. Clardy, K. Lewis, *Chem. Biol.* **2010**, 17, 254–264.
- [4] E. Gavrish, C. S. Sit, S. Cao, O. Kandror, A. Spoering, A. Peoples, L. Ling, A. Fetterman, D. Hughes, A. Bissell, et al., *Chem. Biol.* **2014**, 21, 509–518.
- [5] L. L. Ling, T. Schneider, A. J. Peoples, A. L. Spoering, I. Engels, B. P. Conlon, A. Mueller, D. E. Hughes, S. Epstein, M. Jones, et al., *Nature* **2015**, 517, 455–459.
- [6] T. Homma, A. Nuxoll, A. B. Gandt, P. Ebner, I. 4 Engels, T. Schneider, F. Götz, K. Lewis, B. P. Conlon, **2016**, 60, 6510–6517.
- [7] Parmar A., S. H. Prior, A. Iyer, C. S. Vincent, D. Van Lysebetten, E. Breukink, A. Maddar, E. J. Taylor, I. Singh, *Chem. Commun.* **2017**, DOI: 10.1039/c6cc09490b.
- [8] Y. E. Jad, G. A. Acosta, T. Naicker, M. Ramtahal, A. El-Faham, T. Govender, H. G. Kruger, B. G. de la Torre, F. Albericio, *Org. Lett.* **2015**, 17, 6182–6185.
- [9] H. Yang, K. H. Chen, J. S. Nowick, *ACS Chem. Biol.* **2016**, 11, 1823–1826.
- [10] A. Parmar, A. Iyer, D. G. Lloyd, C. S. Vincent, S. H. Prior, A.

- Madder, E. J. Taylor, I. Singh, *Chem. Commun.* **2017**, DOI 10.1039/C7CC04021K.
- [11] H. Yang, D. R. Du Bois, J. W. Ziller, J. S. Nowick, *Chem. Commun.* **2017**, 8–11.
- [12] M. P. Williamson, *Prog. Nucl. Magn. Reson. Spectrosc.* **2013**, 73, 1–16.
- [13] D. S. Wishart, *Prog. Nucl. Magn. Reson. Spectrosc.* **2011**, 58, 62–87.
- [14] P. Cudic, J. K. Kranz, D. C. Behenna, R. G. Kruger, H. Tadesse, A. J. Wand, Y. I. Veklich, J. W. Weisel, D. G. McCafferty, *Proc. Natl. Acad. Sci. U. S. A.* **2002**, 99, 7384–7389.
- [15] S.-T. D. Hsu, E. Breukink, E. Tischenko, M. A. G. Lutters, B. de Kruijff, R. Kaptein, A. M. J. J. Bonvin, N. A. J. van Nuland, *Nat. Struct. Mol. Biol.* **2004**, 11, 963–7.

## 5.4 Supplementary Information

### 5.4.1 Experimental Section

Sample preparation. Lipid II was obtained from the Dowson and Roper groups at the School of Life Sciences, University of Warwick. Natural abundance and [U-<sup>13</sup>C, <sup>15</sup>N]teixobactin was obtained from Kim Lewis and Dallas Hughes at Novobiotics.

Solution NMR. [U-<sup>13</sup>C, <sup>15</sup>N]teixobactin was dissolved to a concentration of 2 or 3 mM in 10 mM NaP buffer, pH 6.5, with 100 or 150 mM d<sub>38</sub> dodecylphosphocholine (DPC) (Eurisotop). For titrations lipid II was dissolved in 10 mM NaP buffer, pH 6.5, with 150 mM d<sub>38</sub> DPC. Natural abundance teixobactin was prepared in the same way as isotopically labelled teixobactin. All solution NMR experiments were performed on a Bruker Avance II 700 MHz spectrometer equipped with a cryo-probe, using 3 mm NMR tubes. Experiments were performed at 25 °C, additional <sup>1</sup>H-<sup>15</sup>N and <sup>1</sup>H-<sup>13</sup>C correlation experiments were performed at 37 °C so

that assignments could be compared with assignments obtained in solid state NMR experiments. Initial assignments were obtained from a natural abundance teixobactin using 2D experiments:  $^1\text{H}$ - $^{13}\text{C}$  HSQC (hsqcetgpsp.2, 16 scans, 256 t1 increments),  $^1\text{H}$ - $^{15}\text{N}$  SOFAST HMQC (sfhmqccf3gpqh, 0.3 s recycle delay, 64 scans, 62 t1 increments),  $^1\text{H}$ - $^1\text{H}$  TOCSY (mlevesgppg, 8 scans, 256 t1 increments, 70 ms mixing time),  $^1\text{H}$ - $^1\text{H}$  COSY (cosygpprpf, 8 scans, 512 t1 increments). Assignments were confirmed and completed from 3D experiments using  $[\text{U-}^{13}\text{C},^{15}\text{N}]$  teixobactin: BEST HNCACB (b\_hncacbgp3d, 0.3 s recycle delay, 24 scans, 44 increments in the  $^{15}\text{N}$  dimension, 80 increments in the  $^{13}\text{C}$  dimension),  $^{13}\text{C}$  HSQC-TOCSY (hcchdigp3d2, 2 scans, 96 increments in the HSQC dimension, 160 increments in the TOCSY dimension, 16.3 ms DIPSI-3 mixing time), CBCA(CO)NH (cbcaconhgpgw3d, 24 scans, 48 increments in the  $^{15}\text{N}$  dimension, 96 increments in the  $^{13}\text{C}$  dimension, 25% non-uniform sampling (NUS) reconstructed in TopSpin using the MDD algorithm<sup>[1]</sup>. 3D NOESYs were used for distance restraints in the structure calculations:  $^{13}\text{C}$  HSQC-NOESY (noesyhsqcetgpsi3d, 8 scans, 48 increments in the HSQC dimension, 96 increments in the NOESY dimension, 200 ms mixing time),  $^{15}\text{N}$  HSQC-NOESY (noesyhsqcf3gpsi3d, 8 scans, 64 increments in the HSQC dimension, 256 increments in the NOESY dimension, 200 ms mixing time). Titrations with lipid II to  $[\text{U-}^{13}\text{C},^{15}\text{N}]$  Teixobactin were measured using  $^1\text{H}$ - $^{15}\text{N}$  SOFAST HMQC (2 scans, 128 t1 increments) and  $^1\text{H}$ - $^{13}\text{C}$  HSQC (4 scans, 128 t1 increments). Lipid II was titrated to the following concentration (mM): 0.33, 0.79, 1.5, 2, 2.7, 3, 3.4, 3.7, 4, 4.3, 4, leading to a dilution of Teixobactin to a final concentration of 2 mM from an initial concentration of 3 mM. The dilution factor was accounted for in Kd fitting.

Solid State NMR. After titrations of lipid II to  $[\text{U-}^{13}\text{C},^{15}\text{N}]$ teixobactin the sample was transferred from the NMR tube, 10 mM NaP buffer pH 6.5, with 2% 2,2-dimethyl-2-silapentane-5-sulfonate (DSS) was added up to 500  $\mu\text{l}$  leading to a final concentration of approximately: 0.6 mM  $[\text{U-}^{13}\text{C},^{15}\text{N}]$  teixobactin, 1.4 mM lipid II, 45 mM  $\text{d}_{38}$  DPC. The sample was sedimented by ultracentrifugation (Beckmann Coulter Optima MAX-XP Ultracentrifuge) for 46 hours at  $700\,000 \times G$ , forming a solid paste. Most

of the liquid was removed and a small amount of 10 mM NaP buffer containing 2 mM gadolinium diethylenetriaminepentaacetic acid bismethylamide (Gd(DTPA-BMA)) and 2% DSS was added to the sediment. The sediment was packed into a 0.81 mm Samoson rotor. To keep the sample hydrated during packing small amounts of buffer with Gd(DTPA-BMA) and DSS was added to the rotor. All experiments were recorded at a 600 MHz Bruker Avance II spectrometer using a Samoson HXY 0.81 mm probe at 90 kHz magic angle spinning and a sample temperature of  $39 \pm 2$  °C measured from the water peak referenced to DSS. Proton detection with 30 ms acquisition time was used for all experiments. The addition of Gd(DTPA-BMA) enabled a recycle delay of 0.5 s. Water suppression was achieved by 100-150 ms sITPPM<sup>[2]</sup> at 22.5 kHz nutation frequency ( $\frac{1}{4}$  of the spinning speed). The following spectra were acquired: 2D  $^1\text{H}$ - $^{13}\text{C}$  inverse cross polarization (CP) (32 scans, 160  $t_1$  increments, 0.4 ms CP between  $^1\text{H}$ - $^{13}\text{C}$  and  $^{13}\text{C}$ - $^1\text{H}$ ), 2D  $^1\text{H}$ - $^{15}\text{N}$  inverse CP (32 scans, 112  $t_1$  increments, 1 ms CP between  $^1\text{H}$ - $^{15}\text{N}$  and 0.9 ms between  $^{15}\text{N}$ - $^1\text{H}$ ), 3D hCANH (64 scans, 48 increments in  $^{13}\text{C}$  dimension, 40 increments in the  $^{15}\text{N}$  dimension, 0.4 ms CP between  $^1\text{H}$ - $^{13}\text{C}$ , 11 ms between  $^{13}\text{C}$ - $^{15}\text{N}$ , 0.9 ms between  $^{15}\text{N}$ - $^1\text{H}$ ), 3D hCONH 64 scans, 28 increments in the  $^{13}\text{C}$  dimension, 44 increments in the  $^{15}\text{N}$  dimension, 2.5 ms CP between  $^1\text{H}$ - $^{13}\text{C}$ , 11 ms between  $^{13}\text{C}$ - $^{15}\text{N}$ , 0.9 ms between  $^{15}\text{N}$ - $^1\text{H}$ ). 3D hCCH TOCSY (16 scans, 108 increments in both  $^{13}\text{C}$  dimensions, 0.4 ms for  $^1\text{H}$ - $^{13}\text{C}$  and  $^{13}\text{C}$ - $^1\text{H}$  CP, 15 ms DIPSI-2 mixing time at 10 kHz nutation frequency) 3D hCOCACBHAHB DREAM (64 scans, 28 increments in the  $^{13}\text{CO}$  dimension, 52 increments in the  $^{13}\text{CA/CB}$  dimension, 2.5 ms CP between  $^1\text{H}$ - $^{13}\text{CO}$ , 0.4 ms CP between  $^{13}\text{CA/CB}$ - $^1\text{HA/HB}$ , 7 ms DREAM<sup>[3]</sup> between  $^{13}\text{CO}$  –  $^{13}\text{CA/CB}$  at 45 kHz nutation frequency,  $\frac{1}{2}$  of the spinning speed).

Data Analysis. TopSpin 3.2 was used to process all spectra. The spectra were assigned in Sparky. Structure calculation was performed using UNIO 10 with Cyana 2.1<sup>[4]</sup> as molecular dynamics software. Raw spectra ( $^{13}\text{C}$  HSQC-NOESY and  $^{15}\text{N}$  HSQC-NOESY) were used as input into the structure calculation. Automatic peak picking and NOE assignments were achieved by UNIO ATNOS-CANDID<sup>[5,6]</sup>. The results from the structure

calculation are shown in SI table 1. Cyana library entries for D-amino acids were produced using CyLib<sup>[7]</sup>: D-Glutamine (converted from DGN.cif), D-allo-Isoleucine (converted from 28J.cif), D-Threonine (converted from DTH.cif). A Cyana library entry for N-Methylated-D-Phenylalanine was initially converted by Cylib from ZAE.cif and slightly modified by producing a .cor file in cyana containing the new ZAE residue as first residue and a peptide bond to another amino acid. The amide proton was added in Chimera and a pdb file was exported and read in Molmol where coordinates were exported as a library file. The library file was edited manual in a text editor to fit to the Cyana library format. The .cif files were obtained from [http://www.bpc.uni-frankfurt.de/guentert/wiki/index.php/Cyana\\_Residue\\_Library\\_Entries](http://www.bpc.uni-frankfurt.de/guentert/wiki/index.php/Cyana_Residue_Library_Entries), except for D-allo-isoleucine (28J.cif), which was obtained from <http://www.ebi.ac.uk/pdbe-srv/pdbechem/chemicalCompound/show/28J>. A cyana library entry for allo-Enduracidine was produced from a drawing of the chemical structure in ChemSketch (ACDLabs Freeware 2012) including peptide bonds to residues before and after. The chemical structure was exported as a .mol file and converted to PDB in UCSF Chimera. MOLMOL was used to write coordinate files and the cyana library entry was finalized by manually rearranging the atoms and adding torsion angles in a text editor (PSPAD editor).

To determine binding affinities the peak intensities of free teixobactin were measured in the titration spectra and fitted to:

$$P = \frac{1}{2 \cdot n \cdot [P_t]} \cdot (-K_d - [L_t] + n \cdot [P_t] + \sqrt{4 \cdot K_d \cdot n \cdot [P_t] + (K_d + [L_t] - n \cdot [P_t])^2}) \quad (5.1)$$

where P is normalized peak intensity, n is molar ratio for binding (lipid II / teixobactin),  $[L_t]$  is ligand concentration (lipid II),  $[P_t]$  is protein concentration (teixobactin).  $K_d$  values were calculated for several different values of n (0.25, 0.5, and 1) representing a molar binding ratio of teixobactin:lipid II of 4:1, 2:1, and 1:1 (see SI table 6). The fitting of the data was done by minimization of the  $\chi^2$  target function:



$$\chi^2 = \sum \frac{(X_{i,calc} - X_{i,exp})^2}{\sigma_{i,exp}^2} \quad (5.2)$$

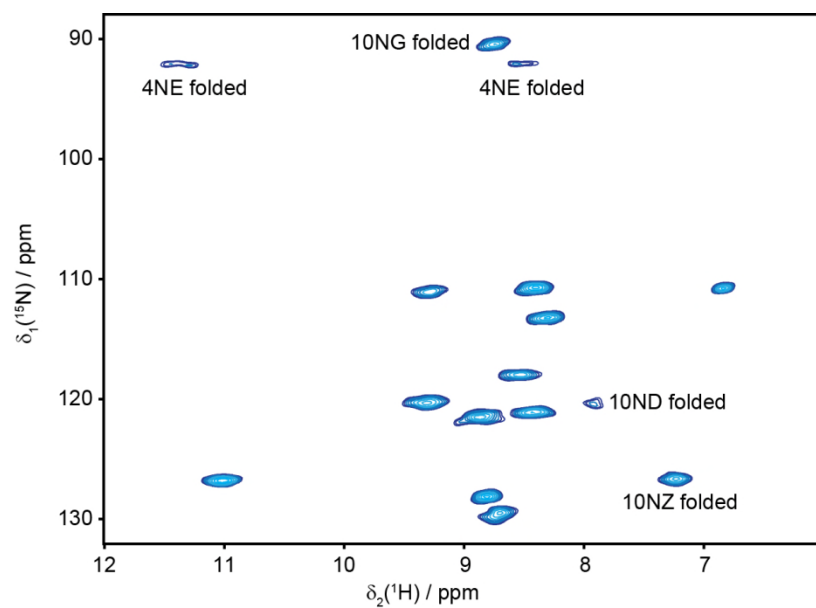
where  $X_i$  are the data sets and  $\sigma_i$  the corresponding error. Secondary chemical shifts were calculated from random coil chemical shifts from L-amino acids<sup>[8]</sup>, and hence for the modified and unusual amino acids D-N-Me-Phe (L-Phe was used as comparison) and L-allo-End (Arg was used as comparison) the chemical shifts from standard amino acids might not be representative. Chemical shift perturbations were calculated as Euclidian distances<sup>[9]</sup>:

$$CSP = \sqrt{\frac{1}{2}[\delta_H^2 + (\alpha \cdot \delta_X^2)]} \quad (5.3)$$

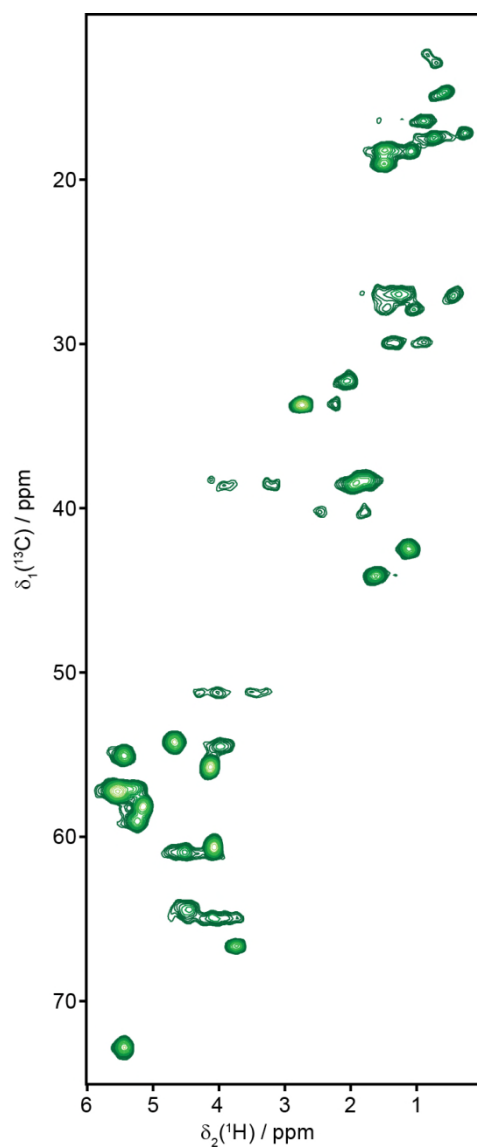
where  $\delta$  is the difference in chemical shift between teixobactin in solution and solid state,  $\alpha = 0.14$  if  $x = N$  and  $\alpha = 0.3$  if  $x = C$ .

#### 5.4.2 Results and Discussion

$^1H$ - $^{15}N$  and  $^1H$ - $^{13}C$  solid state NMR spectra of  $[U-^{13}C, ^{15}N]$ teixobactin in complex with natural abundance lipid II in  $d_{38}$  DPC micelles are shown in SI figures 5.1 and 5.2. Folded  $^{15}N$  side chains are indicated in SI figure 5.1. SI Table 5.1 contains information from the structure calculation of  $[U-^{13}C, ^{15}N]$ teixobactin in  $d_{38}$  DPC micelles. Resonance assignments for teixobactin are gathered in SI table 5.2 (25 °C, solution), SI table 5.3 (37 °C solution) and SI table 5.4 (solid state NMR). SI tables 5.5 and 5.6 contain results from  $K_d$  fits based on titrations of lipid II to teixobactin.



**SI figure 5.1.**  $^1\text{H}$ - $^{15}\text{N}$  solid state NMR spectrum of  $[\text{U-}^{13}\text{C}, ^{15}\text{N}]$ teixobactin in complex with natural abundance lipid II in  $\text{d}_{38}$  DPC micelles. Side chains are folded in the  $^{15}\text{N}$  dimension.



**SI figure 5.2.**  $^1\text{H}$ - $^{13}\text{C}$  solid state NMR spectrum of  $[\text{U-}^{13}\text{C}, ^{15}\text{N}]$ teixobactin in complex with natural abundance lipid II in  $d_{38}$  DPC micelles.

**SI table 5.1.** Results from structure calculation of  $[\text{U-}^{13}\text{C}, ^{15}\text{N}]$ teixobactin in  $d_{38}$  DPC micelles in solution.

Assigned cross-peaks	$^1\text{H} - ^{15}\text{N}$ HSQC NOESY	$^1\text{H} - ^{13}\text{C}$ HSQC NOESY
Total	100	159
Diagonal	0	1
Intraresidual ( $i = j$ )	40	111
Sequential ( $ i - j  = 1$ )	40	24
Medium range ( $1 <  i - j  < 5$ )	19	21
Long range ( $ i - j  \geq 5$ )	1	2
Distance restraints <sup>[a]</sup>		
Total	125	
Intraresidual ( $i = j$ )	37	

Sequential ( $ i - j  = 1$ )	47
Medium range ( $1 <  i - j  < 5$ )	38
Long range ( $ i - j  \geq 5$ )	3
No. of restraints per residue	11.4
Backbone rmsd	$0.09 \pm 0.01 \text{ \AA}$
Heavy-atom rmsd	$0.31 \pm 0.09 \text{ \AA}$
[a] only meaningful, non-redundant distance restraints are reported	

**SI table 5.2.** Chemical shifts (ppm) for  $[U^{13}C^{15}N]$ teixobactin in  $d_{38}$  DPC micelles, solution NMR at 25 °C. Non-standard amino acids: DNP = N-methylated-D-phenylalanine, DGN = D-glutamine, DAI = D-allo-isoleucine, DTH = D-threonine, END = *allo*-enduracidine.

Res	1 DNP	2 ILE	3 SER	4 DGN	5 DAI	6 ILE	7 SER	8 DTH	9 ALA	10 END	11 ILE
H		8.57	8.31	8.73	7.93	8.26			7.97	9.04	8.43
N		130.4	119.1	123.5	120.0	121.5			125.4	113.2	116.8
		7	2	8	0	4			7	5	0
CA	65.21	60.73	58.28	55.39	60.48	60.11	59.14	58.88	55.41	54.94	60.69
HA	4.25	4.07	4.40	4.36	4.31	4.47	4.66	4.96	4.03	4.50	4.10
CB	39.16	39.11	63.91	28.87	39.61	39.33	65.74	73.85	18.66	39.44	37.68
HB		1.45			1.87	1.92		5.51			1.90
HB2	3.04		3.78	1.91			3.89		1.41	1.93	
HB3	3.38		3.81	2.12			4.09			2.24	
CG				33.79						55.41	
CG1		27.10			28.50	27.49					27.91
CG2		17.61			17.14	18.55		18.05			17.72
HG										4.01	
HG12		0.61			1.13	1.22					1.18
HG13		0.91			1.44	1.57					1.53
HG2				2.27							
HG22		0.59			0.90	0.97		1.19			0.85
HG3				2.31							
CD										51.12	
CD1	62.70 <sup>a]</sup>	13.59			14.09	13.42					12.45
HD12		0.64			0.88	0.88					0.87
HD1	7.26									3.32	
HD2	7.31									3.89	
CE1	60.97 <sup>a]</sup>										
HE1	7.25										
HE2	7.31										
HE21				6.87							
HE22				7.57							
ND										89.99	
NE2				112.3 8							
NG										79.53	

NZ										68.41	
HND										8.17	
HNG										8.09	
HZ	7.13									7.64	
C-Met	34.44										
CZ	59.22 <sup>a]</sup>										
H12	2.66										
<sup>[a]</sup> Assignments of folded peaks											

**SI table 5.3.** Chemical shifts (ppm) for [U<sup>13</sup>C<sup>15</sup>N]teixobactin in d<sub>38</sub> DPC micelles, solution NMR at 37 °C. Non-standard amino acids: DNP = N-methylated-D-phenylalanine, DGN = D-glutamine, DAI = D-allo-isoleucine, DTH = D-threonine, END = *allo*-enduracidine.

Res	1 DNP	2 ILE	3 SER	4 DGN	5 DAI	6 ILE	7 SER	8 DTH	9 ALA	10 END	11 ILE
H		8.59	8.36	8.78	7.99	8.29			8.06	9.12	8.52
N		130.21	119.21	123.67	119.91	121.48			125.44	113.29	116.78
CA	65.41	60.82	58.40	55.54	60.56	60.37	59.11	59.01	55.52	55.05	60.85
HA	4.34	4.20	4.53	4.49	4.44	4.58	4.78	5.06	4.16	4.63	4.23
CB	39.35	39.31	64.09	29.02	39.85	39.25	65.85	74.01	18.81	39.51	37.98
HB		1.58			1.99	2.03		5.63			2.01
HB2	3.15		3.91	2.03			4.00		1.53	2.06	
HB3	3.49		3.93	2.24			4.21			2.36	
CG				33.95						55.52	
CG1		27.18			28.66	27.57					28.02
CG2		17.74			17.22	18.66		18.20			17.83
HG										4.14	
HG12		0.74			1.25	1.34					1.31
HG13		1.05			1.56	1.69					1.64
HG2				2.39							
HG22		0.72			1.02	1.09		1.32			0.97
HG3				2.44							
CD										51.27	
CD1	52.92 <sup>f]</sup>	13.67			14.05	13.64					12.62
HD12		0.77			1.00	1.00					0.99
HD1	7.38									3.45	
HD2	7.43									4.01	
CE1	51.18 <sup>f]</sup>										

HE1	7.42										
HE2	7.43										
HE21				6.93							
HE22				7.63							
ND										90.25	
NE2				112.1 0							
NG										79.53	
NZ										68.44	
HND										8.26	
HNG											
HZ	7.25									7.71	
C-Met	34.66										
CZ	49.48 <sup>[a]</sup>										
H12	2.78										

[a] Assignments of folded peaks

**SI table 5.4.** Chemical shifts (ppm) for [U<sup>13</sup>C<sup>15</sup>N]teixobactin in complex with lipid II in d<sub>38</sub> DPC micelles, solid state NMR at 600 MHz <sup>1</sup>H Larmor frequency, 90 kHz MAS and a sample temperature of 39 ± 2 °C. DNP = N-methylated-D-phenylalanine, DGN = D-glutamine, DAI = D-*allo*-isoleucine, DTH = D-threonine, END = *allo*-enduracidine.

Residue	1 DNP	2 ILE	3 SER	4 DGN	5 DAI	6 ILE	7 SER	8 DTH	9 ALA	10 END	11 ILE
H	6.84	8.71	9.30	8.86	8.30	8.42	11.02	8.39	8.81	9.29	8.53
N	110.7 6	129.7 0	120.3 7	121.5 6	113.2 9	121.1 5	126.8 5	110.7 6	128.1 5	111.0 9	118.0 5
CA	64.49	59.14	57.26	55.06	57.28	57.19	60.91	58.21	55.75	54.26	60.63
HA	4.47	5.24	5.43	5.44	5.28	5.57	4.52	5.16	4.13	4.67	4.08
CB	38.63	42.48	66.66	32.24	44.13	38.63	64.94	72.81	19.11	40.18	38.40
HB		1.12			1.62	1.94		5.44			1.75
HB2	3.13		3.74	2.05			3.82		1.47	1.79	
HB3	3.82		3.74	2.04			4.07			2.45	
CG				33.61						54.51	
CG1		27.03			29.92	27.11					27.80
CG2		17.18			16.45	18.24		18.19			17.45
HG										3.98	
HG12		0.44			0.90	1.39					1.47
HG13		1.19			1.32	1.01					1.02

HG2				2.22						
HG22		0.27			0.90	1.08		1.47		0.74
HG3				2.23						
CD									51.26	
CD1	62.85 <sup>[a]</sup>	14.70			14.88	12.45				12.90
HD12		0.58			0.67	0.77				0.71
HD1	6.99								3.33	
HD2	7.31								4.10	
CE1	60.37 <sup>[a]</sup>									
HE1	6.99									
HE2	7.34									
HE21				8.49						
HE22				11.37						
ND									70.23	
NE2				41.09						
NG									90.22	
NZ									76.39	
HND									7.91	
HNG									8.75	
HZ	6.99								7.24	
C-Met	33.70									
CZ	59.20 <sup>[a]</sup>									
H12	2.74									

[a] Assignments of folded peaks

**SI table 5.5.** Results from  $K_d$  fits (equation (5.1)) with a 2:1 ratio of teixobactin:lipid 2. Only isolated peaks included.  $K_d$  values for carbons and nitrogens with more than one proton are combined.

Atom	$K_d$ ( $\mu\text{M}$ )	Error
1CA	6.13	5.23
1CB	139.06	16.26
1C-Met	63.36	1.06
1CD1	159.19	37.06
1CE1	199.26	20.89
1CZ	251.64	52.65
2N	172.49	13.57

2CB	127.60	15.39
2CG1	166.34	15.57
2CG2	113.46	1.35
2CD1	102.40	1.79
3N	103.54	9.67
3CA	45.45	21.85
3CB	171.66	7.01
4N	56.79	7.99
4CA	3.58	3.53
4CB	125.99	14.12
4CG	198.85	8.58
4 NE	474.05	15.20
5N	56.69	17.15
5CA	146.34	21.06
5CB	189.50	14.75
5CG1	191.60	11.51
5CG2	142.99	1.86
6N	10.36	8.70
6CA	117.65	23.95
6CB	68.02	13.26
6CG1	483.53	17.81
6CG2	87.49	2.05
7CB	30.29	22.26
8CB	6.75	6.77
8CG2	27.97	3.50
9N	42.34	22.68
9CB	49.43	2.84
10N	3.71	19.02
10CA	58.82	22.51
10CB	19.68	15.99
10CD	68.14	15.45
10NG	388.01	75.98
10ND	141.43	25.73
10NZ	176.06	44.88
11N	45.78	40.07
11CB	58.95	46.84
11CG1	181.00	12.38
11CG2	55.28	1.66



11CD1	36.49	2.33
-------	-------	------

**SI table 5.6.** Comparison of  $K_d$  fits with different ratios of teixobactin:lipid II. All peaks included.

Txb:lipid II	2:1		1:1		4:1	
Peak	$K_d$ ( $\mu$ M)	$\chi^2$	$K_d$ ( $\mu$ M)	$\chi^2$	$K_d$ ( $\mu$ M)	$\chi^2$
1CD1-HD1	159.19	0.34	67.36	0.49	209.37	0.84
1CE1-HE1	199.26	0.11	81.21	0.68	266.56	0.42
1CZ-HZ	251.64	0.22	116.20	0.30	328.82	0.52
1CA-HA	6.13	3.83	0.00	60.15	7.31	5.14
1CB-HB3	120.02	0.33	46.98	1.02	159.33	0.93
1CB-HB2	158.11	0.11	60.68	1.18	213.40	0.50
1C-Met-H-Met	63.36	0.16	13.52	6.68	88.16	0.86
2CA-HA	144.65	0.26	56.52	0.58	192.62	0.75
2CB-HB	127.60	0.09	42.30	1.91	175.37	0.50
2CG1-HG13	158.75	0.27	64.64	0.64	211.06	0.73
2CG1-HG12	173.93	0.18	69.60	0.68	232.46	0.57
2CD1-HD12	102.40	0.56	41.02	0.80	134.82	1.25
2CG2-HG22	113.46	0.14	38.90	1.73	153.74	0.67
3CA-HA	45.45	3.92	13.32	4.64	61.28	4.99
3CB-HB3	149.61	0.25	59.79	0.63	198.84	0.74
3CB-HB2	193.71	0.21	82.45	0.40	255.94	0.60
4CA-HA	3.58	4.52	1.60	2.97	4.52	5.54
4CG-HG3	198.13	0.39	84.51	0.36	261.25	0.78
4CG-HG2	199.58	0.40	88.56	0.28	261.29	0.82
4CB-HB3	145.96	0.40	38.09	3.81	212.81	0.48
4CB-HB2	106.03	1.09	47.64	0.67	136.35	1.85
5CA-HA	146.34	0.58	42.90	2.69	209.87	0.76
5CB-HB	189.50	0.21	78.66	0.49	251.64	0.58
5CG1-HG13	202.14	0.17	85.19	0.57	268.44	0.51
5CG1-HG12	181.06	0.22	76.22	0.47	239.50	0.63
5CG2-HG22	142.99	0.23	56.07	0.94	191.42	0.70
5CD1-HD12	198.28	0.18	83.18	0.49	263.26	0.53
6CA-HA	117.65	1.83	32.87	5.82	180.47	1.94
6CB-HB	68.02	0.34	20.10	3.05	92.23	1.11
6CG1-HG13	483.53	0.14	240.07	0.60	627.98	0.12
6CG1-HG12	195.81	0.32	84.82	0.36	257.73	0.72
6CG2-HG22	87.49	0.38	31.38	1.62	116.60	1.10

6CD1-HD12	202.83	0.20	86.81	0.40	268.08	0.57
7CA-HA	3.36	29.91	0.04	91.59	17.77	5.57
7CB-HB3	50.87	0.79	15.60	2.17	66.70	1.74
7CB-HB2	9.71	3.03	2.18	8.47	13.12	4.19
8CB-HB	6.75	5.76	0.88	8.90	7.02	6.96
8CA-HA	6.60	5.70	0.00	186.08	32.25	5.75
8CG2-HG22	27.97	1.44	11.03	2.12	35.34	2.59
9CA-HA	104.30	1.28	48.56	0.34	133.01	2.04
9CB-HB2	49.43	1.18	20.04	1.09	63.18	2.19
10CA-HA	58.82	3.76	13.33	4.20	79.52	4.65
10CG-HG	62.49	1.28	27.14	0.99	79.53	2.25
10CD-HD2	52.47	1.15	20.85	1.43	67.06	2.16
10CD-HD1	83.81	0.58	31.20	1.92	110.63	1.36
10CB-HB3	19.68	3.24	8.08	3.21	25.01	4.38
10CB-HB2	134.13	0.31	46.61	1.16	182.55	0.76
11CA-HA	95.80	0.35	31.59	1.96	130.16	0.95
11CB-HB	58.95	1.68	23.57	1.76	76.60	2.61
11CG1-HG13	181.00	0.33	77.36	0.40	238.54	0.76
11CG1-HG12	146.48	0.25	58.06	0.84	195.48	0.72
11CG2-HG22	55.28	0.94	21.13	1.34	71.58	1.90
11CD1-HD12	36.49	2.06	12.80	1.41	48.11	2.95
2N-H	172.49	0.10	14.96	15.85	222.30	0.52
3N-H	103.54	0.37	11.04	10.16	155.00	0.56
4N-H	56.79	0.78	5.78	11.22	86.96	1.28
5N-H	56.69	0.29	1.06	54.34	83.26	0.77
6N-H	10.36	2.36	0.00	10492.62	9.42	4.06
9N-H	42.34	0.48	0.00	108.95	68.51	0.72
10N-H	3.71	3.79	1.23	1.19	4.96	4.80
11N-H	45.78	1.68	0.00	31.27	97.24	1.18
4NE-HE22	346.32	0.25	95.28	0.76	458.80	0.31
4NE-HE21	601.77	0.12	208.66	0.29	757.32	0.11
10ND-HND	141.43	0.15	12.15	16.32	191.97	0.50
10NG-HNG	388.01	0.60	41.47	7.27	434.51	1.16
10NZ-HZ	176.06	1.15	0.00	38.58	184.37	2.14

### 5.4.3 References

- [1] V. Y. Orekhov, V. A. Jaravine, *Prog. Nucl. Magn. Reson. Spectrosc.*

- 2011**, 59, 271–292.
- [2] J. R. Lewandowski, J. Sein, H. J. Sass, S. Grzesiek, M. Blackledge, L. Emsley, *J. Am. Chem. Soc.* **2010**, 132, 8252–4.
  - [3] R. Verel, M. Baldus, M. Ernst, B. H. Meier, *Chem. Phys. Lett.* **1998**, 287, 421–428.
  - [4] P. Güntert, C. Mumenthaler, K. Wüthrich, *J. Mol. Biol.* **1997**, 273, 283–298.
  - [5] T. Herrmann, P. Güntert, K. Wüthrich, *J. Biomol. NMR* **2002**, 24, 171–89.
  - [6] T. Herrmann, P. Güntert, K. Wüthrich, *J. Mol. Biol.* **2002**, 319, 209–27.
  - [7] E. M. Yilmaz, P. Güntert, *J. Biomol. NMR* **2015**, 63, 21–37.
  - [8] D. S. Wishart, *Prog. Nucl. Magn. Reson. Spectrosc.* **2011**, 58, 62–87.
  - [9] M. P. Williamson, *Prog. Nucl. Magn. Reson. Spectrosc.* **2013**, 73, 1–16.